TECHNISCHE UNIVERSITÄT WIEN

isas

Ferroelectric and energy storage characterization of PVDF-based thin films and nanocomposites

DISSERTATION

Zur Erlangung des Grades
des Doktors der technischen Wissenschaften (Dr. Techn.)
an der Fakultät für Elektrotechnik und Informationstechnik
am Institut für Sensor- und Aktuatorsysteme E366
der Technische Universität Wien

Davide Disnan, MSc
Matrikelnummer: 12031889

Wien, 2025

Rigorosum: Wien, 31. Januar 2025

Supervisor: Univ.-Prof. Dr.rer.nat. Ulrich Schmid
Technische Universität Wien

Reviewer: Univ.-Prof. Dr.rer.nat. Alexander Bergmann
Technische Universität Graz

Reviewer: Univ.-Prof. Dr.sc. Silvan Schmid
Technische Universität Wien

Abstract

Functional materials, such as lead zirconate titanate (PZT) and barium titanate (BTO), are widely used in microelectromechanical systems (MEMS) due to their strong piezoelectric properties. However, the inherent stiffness of these ceramics limits their applicability where high mechanical flexibility is required. This limitation has led to the growing interest in piezoelectric polymers, particularly in ferroelectric poly(vinylidene fluoride) (PVDF) and its copolymer with trifluoroethylene (P(VDF-TrFE)). These polymers offer a soft alternative to traditional piezoceramics, making them suitable for flexible MEMS applications. This thesis investigates the electromechanical behaviour of PVDF and P(VDF-TrFE) thin films within the context of polymer science. It specifically explores how processing parameters, surface microstructure, and crystalline phases influence the piezoelectric and ferroelectric properties of these materials. For this purpose, capacitor-type test structures were fabricated by depositing thin films of PVDF and P(VDF-TrFE) via spin-coating. Additionally, capacitors can be applied as energy storage devices, an area where ferroelectric polymers have gained significant interest due to their superior dielectric strength compared to conventional ceramics and higher dielectric permittivity than standard polymeric materials. To leverage these advantageous properties even further, this work focuses on developing P(VDF-TrFE)-based nanocomposites loaded with carboxymethyl cellulose nanofibers mixed with BTO polydopamine-based functionalized high-permittivity nanoparticles (CCNF-BTO@PDA). These nanocomposites were incorporated into spin-cast thin films of 2 μm thickness, which is ten times thinner than those typically reported. Despite challenges such as nanoparticle agglomeration, which became more pronounced in these thinner films and significantly affected the breakdown strength, these findings offer valuable insights for further research in spin-cast fluoropolymer-based nanocomposite thin films, especially when targeting the micrometre thickness range for MEMS applications.

Acknowledgments

This thesis marks the culmination of a significant chapter in my life, made possible by the invaluable support, guidance, and encouragement of many remarkable people, whom I am deeply grateful to acknowledge here.

Foremost, I want to express my gratitude to my supervisor, Prof. Ulrich Schmid, for his continuous support and invaluable advice. I am particularly thankful for the opportunity he provided me to work on this interesting and exciting research topic at his institute.

I would also like to thank Dr. Michael Schneider for his meaningful guidance throughout this thesis. I have benefited greatly from his expertise and appreciated the time and effort he put into discussing and solving scientific issues with me.

Special thanks go to my friend Jonas, whose invaluable support at the beginning of my thesis was crucial. His experience and insightful advices helped me to organize my work effectively and navigate the challenges of pursuing a PhD successfully. The transition from colleagues to good friends strengthened our work experience, leading to a supportive and creative environment that enabled me to achieve a number of scientific works I am really proud of.

I had the fortune to collaborate with many talented people on my publications. In addition to those already mentioned, I would like to recognize Fabian Bacher, Simone Benaglia, Stephan Berger, and Marco Theuschel for their valuable contributions. Special thanks also to Mauro and Borislav for their amazing work and publications I was proud to support during my PhD. In particular, I am grateful to call Mauro a friend. His support, both in work and in life, has been priceless: our meaningful conversations and mutually inspiring approach toward life have continually pushed each other to be the best versions of ourselves.

I would like to thank Prof. Alexander Bergmann and Prof. Silvan Schmid for their availability in agreeing to take on the role of reviewers for my thesis.

For funding my project, I would like to acknowledge the Federal Ministry for Climate Action, Environment, Energy, Mobility, Innovation, and Technology. I also thank the TU Wien Bibliothek for financial support through its Opens Access Funding Program.

I would like to thank our project partners from Shanghai University, Prof. Xin Feng, Hermione Wu, Xinxin Zhang, Kunpeng Qian, and Yin Zhao, for their contribution to my work related to P(VDF-TrFE)-based nanocomposite thin films.

I extend my acknowledgments to USTEM for providing access to their advanced electron microscopy facilities, which were instrumental in the completion of this research.

Many thanks go to my friends and colleagues in university with whom I spent most of my free time and working hours over the last four years, engaging in both fruitful academic discussions and relaxing conversations. Especially to Andre, Giorgio, Kostas, Paolone, Paolo, Philipp, Matthias, and all the others in our research group, as well as those previously mentioned.

I also want to give special recognition to all my friends outside of university, whether near or far, who listened to me, provided advice, and shared meaningful moments with me. The balance between work and free time is crucial for being successful in life, and good friends outside of the work environment play a key role in achieving it. Special thanks to Alex, Bofa, Checco, Depa, Mengo, Peter, Poldo, Shahrom, Sofia and Uolli.

In particular, I would like to express my deep gratitude to my family. I thank my dad and my mum for their support, encouragement, and education, which guided me to all the accomplishments of my academic journey. I also want to show my appreciation to my brother Marco for his generosity and affection in the little things and important moments of my life. Special thanks also to my aunt Carla, my uncle Marco, and my cousin Lara for their presence, support, and advice throughout my life. Lastly, I am grateful to my grandparents, both who is still here and who have passed, all of them significantly contributed to my success.

Table of Contents

1 Introduction

1.1 Motivation and Objectives

The discovery of piezoelectricity in 1880[1] marked a significant milestone in material science and electrical engineering. This phenomenon, extensively studied since its discovery, refers to the ability of materials with a non-centrosymmetric crystalline structure to generate an electric charge in response to an applied mechanical stress, and *vice versa*[2,3,4]. In 1921, ferroelectricity, a subset of piezoelectricity, was discovered, introducing a new field in material science and engineering[5]. Ferroelectrics are a class of materials distinguished by a spontaneous nonlinear polarization that can be reversed by applying an external electric field. This characteristic allows ferroelectrics to maintain two stable polarized states, called remnant polarization, even after the external field is removed[6]. The piezoelectric behaviour observed in ferroelectric materials enabled efficient electromechanical energy conversion and signal transformation[3], leading to their widespread integration into microelectromechanical systems (MEMS). As a consequence, ongoing research has been stimulated to explore applications like sensors, actuators, energy harvesters, and energy storage devices[4,7,8,9,10,11,12,13]. Barium titanate (BTO) and lead zirconate titanate (PZT) are among the most studied ferroelectrics and are part of the so-called piezoceramic materials, that, over time, have achieved widespread use and reliability. However, the stiffness and lack of flexibility of traditional piezoceramics prompted interest in finding softer, more flexible alternatives for MEMS applications.

In 1969, the discovery of strong piezoelectricity in uniaxially drawn and poled poly(vinylidene fluoride) (PVDF) thin films by Kawai revolutionized the field by introducing polymers as viable ferroelectric materials[14]. Since then, PVDF and its copolymer, poly(vinylidene fluoride and trifluoroethylene) (P(VDF-TrFE)), have dominated electroactive polymer technology. They have garnered significant interest due to their noteworthy mechanical and dielectric properties when compared to piezoceramics[3,15,16,17]. The integration of polymer science into ferroelectric research introduced new complexities, such as macromolecules, a wide range of processing techniques, and polymer degradation, thus

necessitating continuous research in the field. Despite these challenges, the ability to avoid high-temperature processing required for piezoceramic thin film fabrication, address the health risks with lead-containing materials, and reduce manufacturing costs has favoured the adoption of ferroelectric polymers across various industrial sectors[18,19,20,21,22,23,24]. In particular, the usage of ferroelectric polymers in energy storage devices has attracted in the last decades strong interest due to their higher electric breakdown field compared to the common ceramics. However, since the energy storage capacity is directly proportional to the dielectric permittivity, which is typically low in polymeric materials, researchers have turned to nanocomposite technology to enhance these devices[25]. Dielectric nanocomposites, consisting of polymer matrices loaded with inorganic or organic nanofillers, aim to leverage the properties of both components to enhance the energy density of the material. Therefore, by introducing high permittivity nanofillers, such as BTO or titanium dioxide (TiO_2), the energy storage capacity of the polymer matrix has been shown to increase. On the downside, the high surface energy of nanoparticles can cause them to agglomerate, potentially reducing the breakdown strength due to an uneven electric field distribution within the material[26,27,28]. This poses challenges, especially in submicron spin-cast thin films, which are a key focus of this work.

Due to these partially counteracting requirements when targeting the improvement of material properties in soft ferroelectric thin films, this thesis focuses on evaluating the electrical as well as electromechanical properties of spin-cast PVDF and P(VDF-TrFE) thin films, considering parameters associated with polymer science, such as microstructure, crystalline phase, and fabrication process. Special attention is also given to the energy storage capability, exploring the potential and challenges for spin-cast ferroelectric nanocomposite thin films compared to the current state-of-the-art in the fluoropolymers field. Additionally, the utilization of nanocomposite technology, including the integration of organic and inorganic nanoparticles and its potential applications into MEMS, is explored to develop polymer thin films for future highly flexible energy storage devices.

1.2 Thesis Outline

The objectives of this thesis involve different disciplines: polymer science and electrical engineering. Polymer science plays a pivotal role, as it is essential for understanding the physical and chemical transformations of the materials, particularly in response to factors like temperature or electric field, which subsequently influence the electromechanical response. The electrical engineering aspects focus on the integration of ferroelectric polymer and nanocomposite thin films into MEMS fabrication processes, along with their electrical characterization, thereby completing the scope of the thesis.

The following offers a brief introduction to the different topics addressed in this thesis, organized by chapters. Chapter 2 provides an overview of the current state-of-the-art in ferroelectric polymers and nanocomposite thin films. It encompasses various aspects of polymer science, including morphology, crystalline phases, and processing techniques in ferroelectric polymers. Chapter 2 also introduces nanocomposite technology, exploring both current applications, especially energy storage, and potential future markets.

Chapter 3 presents the fundamentals of electroactive polymers, providing a detailed discussion on piezoelectricity, electrostriction, ferroelectricity, and energy storage characteristics.

Chapter 4 focuses on fabrication details, presenting the integration of ferroelectric polymers (PVDF and P(VDF-TrFE)) and nanocomposite (P(VDF-TrFE)-based) thin films into a standard silicon MEMS fabrication process.

These fabricated structures are subsequently subjected to characterization techniques, which are presented in Chapter 5. These characterization techniques include X-ray diffraction and electromechanical studies, among others, offering insights into their crystalline as well as piezo- and ferroelectric properties.

Chapter 6 highlights the results and discussion of the electromechanical studies conducted on semi-crystalline polymers PVDF and P(VDF-TrFE). It investigates various aspects of polymer science, including chain conformations, crystalline phase transitions, and microstructure characteristics. Chapter 6 explores how these factors influence the piezo- and ferroelectric activity of these materials.

Chapter 7 concentrates on the study of P(VDF-TrFE)-based nanocomposite thin films, investigating nanofillers, surface functionalization, and final thin-film characteristics, such as

nanoparticle dispersion. This chapter bridges chemistry with ferroelectricity in the context of energy storage characterization, covering aspects such as dielectric studies, electric breakdown field, and energy density.

Concluding, Chapter 8 summarizes the findings of this thesis and offers an outlook on potential future developments in the field.

2 State-of-the-art

2.1 Ferroelectric polymers: PVDF and P(VDF-TrFE)

PVDF and P(VDF-TrFE) belong to the category of polar polymers, drawing increasing interest for their application into MEMS devices thanks to their unique advantages over traditional piezoceramics, such as flexibility, non-toxicity, and biocompatibility[18,22,23]. This chapter provides a comprehensive examination of PVDF and P(VDF-TrFE) molecular structures, crystalline phases, and ferroelectric properties according to the current state-of-the-art, highlighting their significance in material science. It underscores the dynamic nature of ferroelectric polymers and their potential for driving innovation across industries.

2.1.1 Ferroelectric polymers

Polymers are a class of materials composed of long molecular chains, known as macromolecules, that in turn are made up of repeating molecule fundamental units called monomers. Polymers characterized by a single type of monomer unit are termed homopolymers, while those composed of two or more different types of monomeric units are referred to as copolymers. Within the broad category of polymers, there exists a distinct subset known as polar polymers, defined as polymers constituted by monomers containing polar chemical groups with a nonzero net polarization within the fundamental unit. A simplified scheme is presented in Fig. 2.1. It should be noted that polymers present diverse

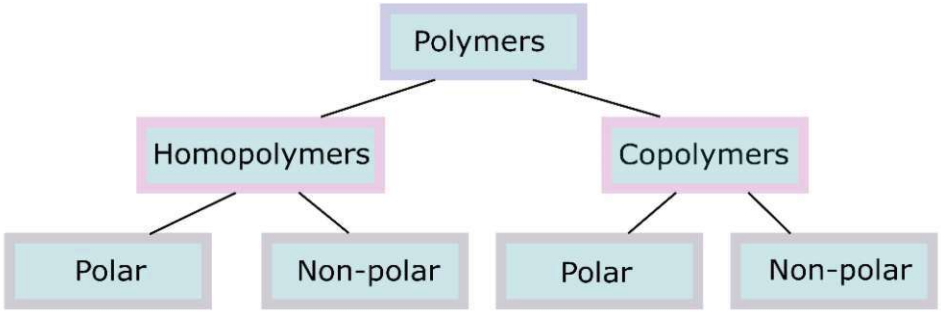

Figure 2.1 Schematic diagram illustrating the subsets of polymers focused in this study: homopolymers and copolymers (distinguished by the presence of a single or multiple monomer units, respectively) divided in polar and non-polar whether or not they possess a nonzero net polarization within the monomer unit.

characteristics and can be further classified into numerous categories. For the purpose of this thesis, this simplified categorization is used.

However, to achieve an effective macroscopic piezoelectricity from polar polymers, their constituents must not be overly large or voluminous. This is because excessive bulkiness can inhibit the crystallization of the macromolecules or force them into shapes that induce compensation of internal dipoles, leading to a zero net macroscopic polarization[29]. Considering these factors, fluorocarbons emerge as highly suitable monomers for generating piezoelectric and ferroelectric characteristics. Among the most common polyfluorocarbons is the homopolymer PVDF. In 1969, Kawai first observed the piezoelectric effect in PVDF[14], which quickly gained interest for its electroactive properties, originating from the high polar dipole -CH_2-CF_2- presented in its single monomer unit, illustrated in Fig. 2.2a. The fluorine atoms, being more electronegative compared to hydrogen atoms, tend to attract the bonding electrons, resulting in a dipole moment within the monomeric structure[16].

The study of polymers has evolved significantly with growing molecular complexity, exemplified by the development of sequence-defined polymers. This progress has led to the synthesis of a diverse range of polymers known as copolymers. One of the most prominent PVDF copolymers is the random copolymer P(VDF-TrFE). Random copolymers are copolymers whose monomer units are randomly distributed along the polymer chain. Specifically, P(VDF-TrFE) is constituted by two monomers randomly distributed: VDF and TrFE. As shown in Fig. 2.2b, the difference between VDF and TrFE monomers lies in the presence of a fluorine atom instead of a hydrogen atom. This modification, as discussed later, significantly impacts the final crystalline phase and properties of the material.

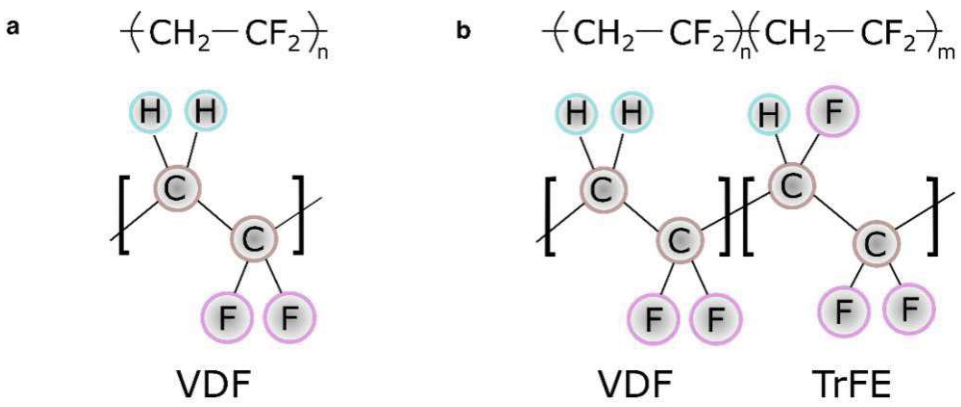

Figure 2.2 Chemical structure of **a** PVDF and **b** P(VDF-TrFE) with a schematic representation of the monomer units.

In polymer science, the crystalline phase (or polymorph) refers to a specific arrangement of the molecules within the material. Within polar polymers, the crystalline phase can be classified as either polar or non-polar, depending on whether it results in a net polarization within the fundamental unit cell. As will be discussed more in detail in Chapter 2.1.2, PVDF may exhibit both polar and non-polar crystalline phases, with the non-polar being the most thermodynamically stable polymorph in solution-processed thin films[30,31]. However, the non-polar PVDF phase can be subsequently transformed into a polar phase through methods such as uniaxial stretching or electric poling[16,29,30,31]. The advantage of the copolymer P(VDF-TrFE) lies in the presence of the bulkier TrFE groups into PVDF chains, which weakens the intermolecular interaction and causes thermodynamic destabilization, leading to the formation of a polar, and thus ferroelectric, crystalline phase without any further treatment[22,26,32]. Additionally, P(VDF-TrFE) presents a higher relative permittivity compared to PVDF, with the former approximately equal to 13, while the latter 9[26,33].

A major material parameter of most ferroelectric crystals is the Curie temperature, defined as the temperature at which spontaneous polarization is lost through either order-disorder or a displacive-type transition, resulting in a paraelectric state[29]. The Curie temperature of P(VDF-TrFE) varies depending on the VDF content, which ranges from 55 to 88 mol% and is below its melting point, which ranges between 150 °C and 170 °C. Specifically, the Curie temperature of P(VDF-TrFE) varies from 55 to 128 °C. In contrast, in PVDF, the melting point is reached at 172 °C before such transition[26]. In this work, the copolymer P(VDF-TrFE) with a VDF-to-TrFE molar ratio of 70:30 has been used, and it will be implicitly assumed throughout the study.

Over time, several other copolymers have been synthesized, expanding the range of possibilities in polymer science applied to ferroelectrics. One example is poly(vinylidene-hexafluoropropylene) (P(VDF-HFP)), which contains bulkier CF_3 groups and can be deposited in an amorphous or elastomeric form[26]. Another notable copolymer is poly(vinylidene-chlorotrifluoroethylene) (P(VDF-CTFE)), which, unlike other copolymers, does not undergo a Curie transition and can become amorphous based on VDF content. P(VDF-CTFE) presents improved flexibility and a higher relative permittivity than PVDF, approximately equal to 13[26]. As technology advances, new possibilities such as P(VDF-TrFE)-based ternary copolymers continue to emerge[33]. All in all, polymer science remains a broad, dynamic, and

multifaceted field that enables the exploration of increasingly complex molecular architectures and is expected to drive further developments in advanced ferroelectric materials with tailored properties.

2.1.2 Morphological, crystalline, and ferroelectric characteristics

The deposition of ferroelectric polymer thin films can be achieved through various techniques, including spin-coating, doctor-blade, and Langmuir Blodgett techniques[34,35]. Among these, spin-coating is the most popular for its ability to produce uniform, adherent, and smooth thin films in an easy and repeatable manner. In spin-coating, the thickness of the final thin film depends on several parameters, such as rotation speed, viscosity of the polymer solution, and solvent-evaporation rate[36,37]. This technique is extensively used for MEMS device fabrication in this study.

Once the polymer thin film has been spin-coated on the substrate, annealing is carried out. The annealing step involves subjecting the material to high temperatures, usually between 130 °C and 170 °C for PVDF and P(VDF-TrFE), to enhance crystallinity and optimize the electrical properties. Crystallization is a mechanism not fully understood yet, and many of its details are still unknown due to the involvement of many variables and complex phenomena, such as molecular diffusion processes, lamellar thickening growth, and chain folding[38,39,40]. In general, crystallization represents a phase transition from a disordered, random, and coiled state typical of polymer solutions to an ordered and regular crystalline state. Polymer materials, such as PVDF, can crystallize into various molecular conformations or polymorphs. PVDF, for instance, may exhibit at least four distinct phases: α-, β-, δ-, γ-phase[29,33,41]. In each phase, PVDF molecular chains possess a dipole moment perpendicular to the polymer chain. However, the arrangement of these chains within the unit cell

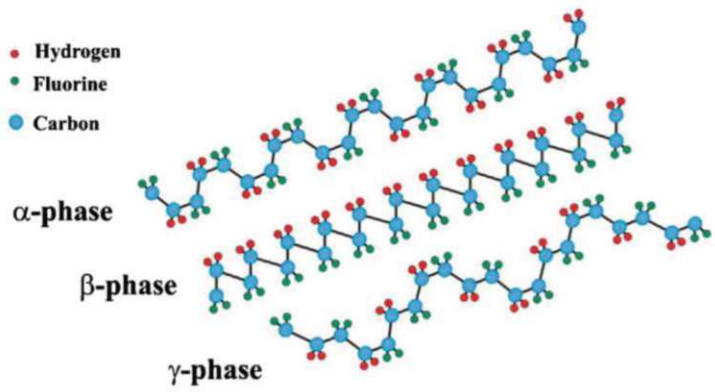

Figure 2.3 Molecular conformations of the α (tg^+tg^-), β ($tttt$) and γ ($tttg^+tttg^-$) polymorphs[33].

determines whether a crystalline phase exhibits a polar or non-polar characteristic, influencing the presence of net macroscopic polarization and piezoelectric effects. Polar polymorphs of PVDF include β-, δ- and γ- phases, while α-phase is not.

Typically, as previously mentioned, solution-processed PVDF thin films are non-ferroelectric, since the most thermodynamically stable polymorph is the non-polar α-phase. In this phase, the polymer chains crystallize in a *trans gauche*$^+$ *trans gauche*$^-$ (tg^+tg^-) conformation, visible in 2D in Fig. 2.3[33]. This conformation presents an antiparallel packing of the chains within the unit cells, which causes the dipole moments to cancel each other out resulting in a zero global dipole moment, as illustrated in Fig. 2.4[29].

Different treatments can convert α-PVDF into electroactive polymorphs. For instance, δ-PVDF can be achieved by electroforming[30,42], while β-PVDF requires mechanical stretching[16] and γ-PVDF specific annealing conditions[43]. Alternatively, the copolymer P(VDF-TrFE) is often utilized as it prefers to crystallize in a highly polar phase similar to that of the β-PVDF, that is a trans (*tttt*) chain conformation, displayed in Fig. 2.3[33], where dipoles in the crystalline unit cell are parallel oriented, as shown in Fig. 2.4[29]. Therefore, The β-phase results in a highly polar crystal structure with the strongest ferroelectric and piezoelectric response among the PVDF polymorphs. Depicted in Fig. 2.3[33] there is also the γ-phase, which shows a chain arrangement between the α- and β-phases in a $tttg^+tttg^-$ conformation. γ-PVDF possesses a polar nature, but smaller than that of the β-phase[44]. More precisely, the alignment of the dipoles in the same direction normal to the axis gives the β-phase a dipole moment of 7.0 x 10^{-30} C·m per unit. In contrast, the γ-phase, due to the inclination of dipoles to the molecular axis, has components of the net moment both perpendicular (4.0 x 10^{-30} C·m) and

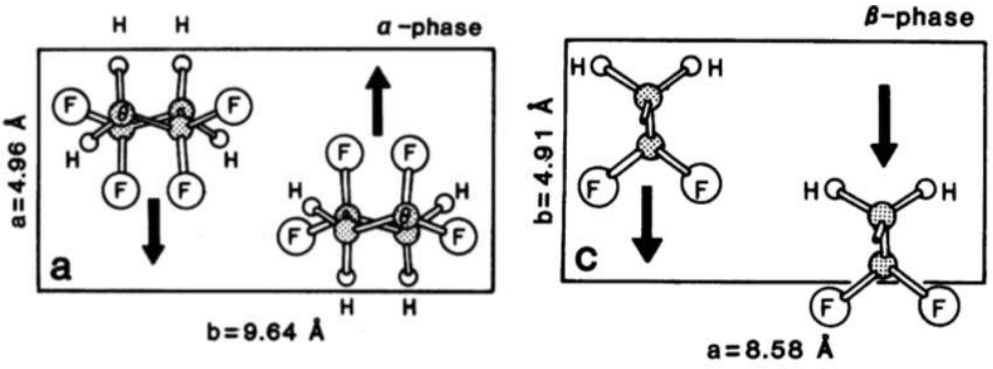

Figure 2.4. Unit cells with their dimensions of α-phase and β-phase in PVDF with antiparallel and parallel dipole directions indicated by the arrows[29].

parallel (3.4 x 10^{-30} C·m) to the chain[29]. The δ-phase instead presents the tg^+tg^- conformation of the α-phase, but with ferroelectric properties, for this reason, is defined as the polar α-phase, also referred to as α_p-phase[45]. The ferroelectric characteristics of δ-PVDF are discussed in detail in Chapter 6. It should be noted that in literature PVDF polymorphs are also called in order of their discovery form I, II, III, and IV, respectively β-, α-, γ-, and δ-phase[30,46].

PVDF and P(VDF-TrFE) are semi-crystalline polymers, *i.e.* consisting of both amorphous and crystalline regions. Typically, during the crystallization process in polymers, not all regions of the material become fully crystallized, resulting in some areas remaining in a disordered state. This partial crystallization is why these polymers are referred to as semi-crystalline. PVDF exhibits a degree of crystallinity of around 50%, while P(VDF-TrFE) can reach up to 80%[47]. The presence of TrFE promotes the formation of the β-P(VDF-TrFE), whose *tttt* conformation results in a more ordered semi-crystalline structure compared to α-PVDF.

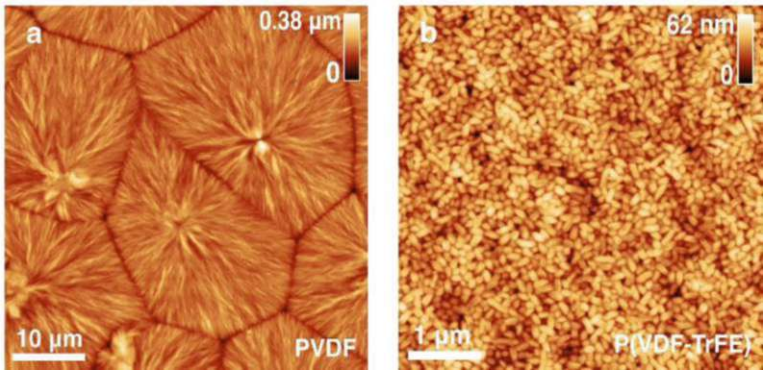

Figure 2.5. AFM height images of **a** PVDF spherulites and **b** P(VDF-TrFE) rice-like domains microstructures in spin-cast thin films. It is worth noticing the scale bar on the bottom left of the figures, which highlights the dimensions of the crystalline domains in the two polymer thin films.

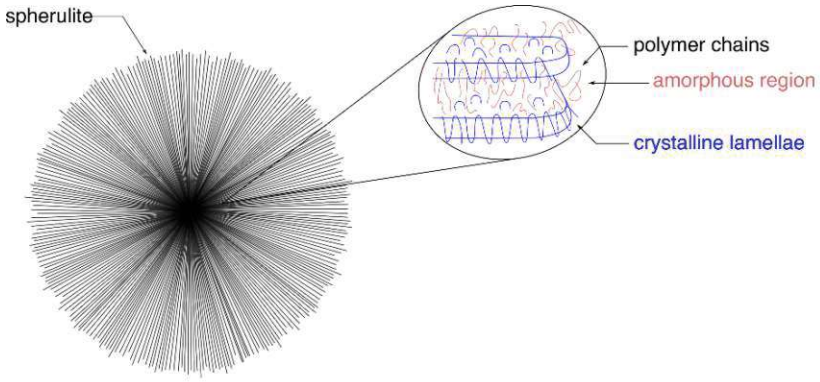

Figure 2.6 Schematic illustration of the spherulite structure, consisting of crystalline lamellae. The lamellae represent sheets of crystalline phases that grow outward from a central nucleation point. The interlamellar areas are filled with amorphous regions.

The addition of the TrFE monomer within the VDF chains does not only influence the crystalline phase but also the microstructure of spin-cast polymer thin films. For instance, in PVDF, the semi-crystalline regions are shaped as large spherulites[29,30,31,48,49], whereas, in P(VDF-TrFE), they are generally shaped as small rice-like crystalline domains[50,51,52,53]. These two microstructures are illustrated in Fig. 2.5. In general, the semi-crystalline regions consist of folded molecular chains arranged in highly ordered platelet-like crystal structures called lamellae (see Fig. 2.6)[29,54]. The organization of the lamellae during the crystallization process leads to morphological differences in the microstructure of PVDF and P(VDF-TrFE). As previously mentioned, PVDF crystallizes into spherulitic structures with dimensions ranging up to several micrometers. In PVDF, during crystallization the lamellae grow outward from a central nucleation point towards the grain boundary, forming the dendrite-like characteristic of the spherulites. The dendrite-like structure, perfectly represented by PVDF microstructure in Fig. 2.5a, visually resembles a branched, tree-like pattern composed of lamellae approximately 10 nm thick[55,56]. In the spaces between the lamellae, polymer chains adopt disordered conformations, resulting in amorphous interlamellar regions (see Fig. 2.6). Due to the folding of a single polymer chain back and forth multiple times through the same lamella and/or across different lamellae, the crystalline and amorphous parts are strongly intertwined within a single spherulite. In Chapter 6.1.1, a detailed morphology study of α-PVDF from micro- to sub-nanometre scale using atomic force microscopy is presented, revealing the organization of polymer chains inside the crystalline lamellae.

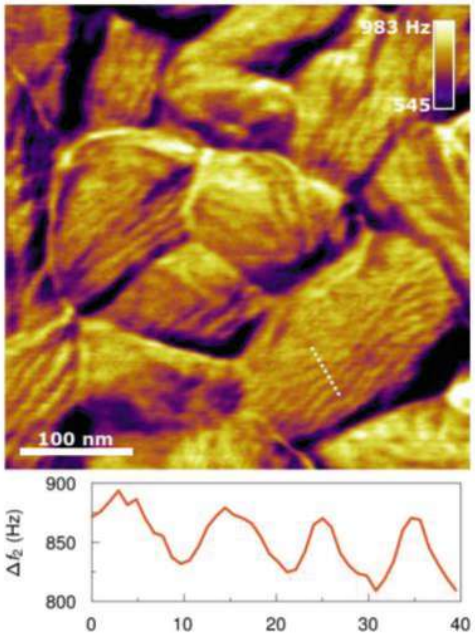

Figure 2.7 High resolution bimodal AFM images of P(VDF-TrFE) thin film with rice-like domains. The profile of the line scan across the lamellar structure of the crystalline domains is shown under the image[52].

P(VDF-TrFE) typically crystallites instead into small rice-like domains (see Fig. 2.5b), each also consisting of stacks of lamellae like the spherulites. However, these rice-like domains have significantly smaller dimensions compared to spherulites, ranging from 100 nm to 200 nm[41,52]. Through high-

resolution bimodal AFM, our research group directly observed the lamellar structure within the P(VDF-TrFE) crystalline domains, indicated by the line scan in Fig. 2.7[52]. The lamellae of the copolymer were found to have a thickness of about 5-8 nm, with a distance between each other within one single domain of approximately 10 nm[48,52,54,57]. However, it has been demonstrated that the microstructure of P(VDF-TrFE) thin films is highly sensitive to fabrication conditions, which can result in a variety of morphological characteristics that can differ significantly from the rice-like domains. For instance, literature reports the appearance of large needle-shaped crystals formed by melt recrystallization when the annealing temperature exceeds the melting point[58]. In general, given its strong association with crystallization processes, the microstructural arrangement of the polymer surface morphology is a complex topic, involving structural configurations like "edge-on" lamellae, where chain crystals stand predominantly on their edges, or "face-on", where molecular chains are preferentially oriented perpendicular to the substrate. These configurations have been deeply studied to explain variations in film morphology and their dependence on different fabrication procedures[59,60,61,62]. In this work, a detailed analysis of the factors influencing the microstructure of P(VDF-TrFE) thin films is conducted, drawing from the existing literature to provide a comprehensive understanding. Specifically, in Chapter 6.1.2, the so-called spherulite-like microstructure observed in P(VDF-TrFE) thin films is introduced and its characteristics are studied, highlighting the morphological similarities with the

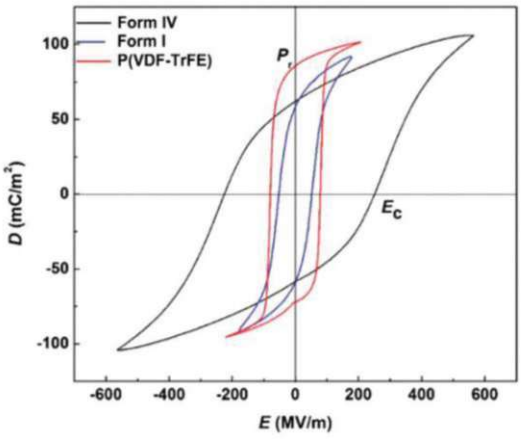

Figure 2.8 Comparison of the ferroelectric characteristics between β-PVDF (Form I), δ-PVDF (Form IV), and β-P(VDF-TrFE) thin films by means their *D-E* hysteresis loops[62].

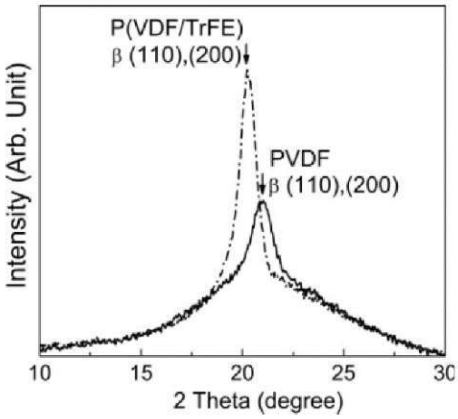

Figure 2.9 XRD patterns of β-PVDF and β-P(VDF-TrFE) thin films, highlighting the crystalline differences between the β-phases in the two polymeric thin films[64].

spherulite microstructure of PVDF. The spherulite-like thin films are also compared with the well-known rice-like P(VDF-TrFE) thin films in terms of ferroelectric characteristics. By conducting this comparison, insights into the relationship between microstructure and ferroelectric properties can be gained, contributing to a deeper understanding of the material behavior for potential applications into MEMS devices.

PVDF and P(VDF-TrFE), belonging to the semi-crystalline polar polymers group that exhibit ferroelectric behavior, possess an inherent electric polarization that can be reversed by an external electric field, enabling the switching between two stable polarized states, known as remnant polarization, in the absence of an electric field. This results in a hysteretic response between the polarization and the electric field, which was first observed in PVDF in 1974[63]. Fig. 2.8 provides an example of electric displacement hysteresis loops as a function of the applied electric field, the so-called *D-E* curve, taken from literature[62]. These curves illustrate the various shapes of the PVDF hysteretic responses achievable depending on the crystalline phase characterizing the material, in comparison with the typical hysteretic response of P(VDF-TrFE). Particularly, Fig. 2.8[62] presents the δ-PVDF (labeled as Form IV) and the β-PVDF (labeled as Form I) alongside β-P(VDF-TrFE). Despite their similar nomenclature, β-PVDF and β-P(VDF-TrFE) exhibit slightly different ferroelectric characteristics. As shown in Fig. 2.9, their X-ray diffraction patterns reflect these differences[64]: the peak of β-PVDF is shifted to higher degree values and its intensity is lower compared to β-P(VDF-TrFE). Generally, the all-trans conformation characteristic of the low-temperature phase of P(VDF-TrFE) is also called β-phase due to its similarity to the β-phase of pure PVDF.

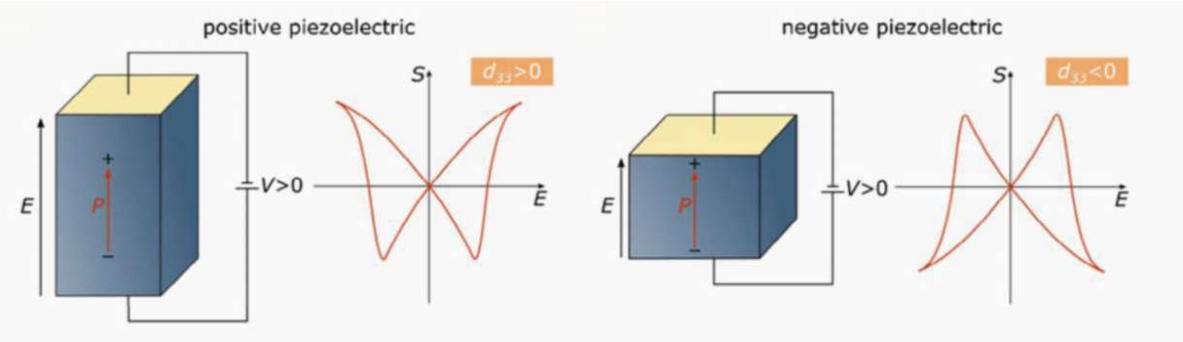

Figure 2.10 Positive piezoelectric effect: applying an electric field along the polarization direction results in an expansion of the material (e.g. BTO). Negative piezoelectric effect: applying an electric field along the direction of the polarization results in a contraction of the material (e.g. PVDF)[47].

Remnant polarization (P_r) and coercivity (E_c) are two fundamental parameters in ferroelectric materials. P_r represents the electric polarization that remains in a material when the external electric field is removed, while E_c refers to the field required to change its polarization. Typically, δ-PVDF presents an E_c value of 115 V·μm^{-1} and a *Pr* value of 7.0 μC·cm^{-2} [16,30]. The remnant polarization of δ-PVDF is comparable to that of β-PVDF and P(VDF-TrFE), but the coercive field is higher than both β-PVDF (approximately 90 V·μm^{-1}) and P(VDF-TrFE) (approximately 60 V·μm^{-1})[51,52,65]. It is important to note that in general the values of these two parameters are influenced by the amplitude of the electric field applied during the measurement, and any comparison with literature must consider this. Specifically, a higher applied electric field results in more aligned dipoles in its direction, leading to higher values of remnant polarization value and coercivity[66].

Another important parameter to consider in ferroelectric materials is the Curie point (T_c), which is defined as the temperature at which ferroelectric materials undergo a phase transition from ferroelectric to paraelectric state. As mentioned in Chapter 2.1.1, the homopolymer PVDF does not exhibit a Curie transition because it melts (at approximately 172 °C) before reaching this point. In contrast, P(VDF-TrFE), which shows both Curie and melting points depending on the VDF content, as shown in Fig. 2.11[67], exhibits a Curie transition at around 100 °C with a 70:30 mol% ratio of VDF and TrFE. More details about Curie's transition can be found in Chapter 3.1.4.

When a ferroelectric material presents an electric displacement response as a function of the electric field in a hysteresis loop, a mechanical strain response occurs simultaneously. This electrostrain characteristic, the so-called *S-E* curve, is commonly referred to as the butterfly curve, due to its distinctive shape resembling a butterfly, as illustrated in Fig. 2.10[47].

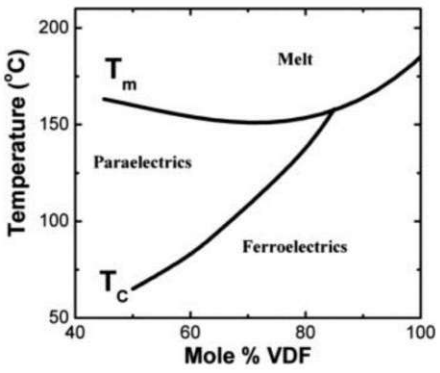

Figure 2.11 Melting and Curie temperatures in P(VDF-TrFE) as a function of the %VDF content[67].

Understanding and characterizing the butterfly response is crucial for optimizing the performance of ferroelectric materials according to the specific technical application. The *S-E* curve is used to study the piezoelectric coefficient, which describes the relationship between the electric field and mechanical strain. In this context, the longitudinal piezoelectric coefficient, denoted as d_{33}, represents this relationship. Typically, ferroelectric materials show a positive d_{33}, meaning they expand when subjected to an electric field aligned with the polarization direction. However, PVDF-based ferroelectric polymers exhibit a negative piezoelectric effect due to the Van der Waals forces acting as intermolecular bonds, which cause contraction when an electric field is applied[52,65,68] (see Chapter 3.1.3 for further details). This phenomenon is directly reflected in the orientation of the butterfly curve, as illustrated in Fig. 2.10. Typically, the longitudinal piezoelectric coefficient d_{33} of δ-PVDF is equal to -36 pm·V^{-1}, while β-PVDF reports -26 pm·V^{-1}. P(VDF-TrFE) exhibits a similar piezoelectric coefficient, approximately -26 pm·V^{-1} [52,65,44].

The fundamentals of the electric displacement hysteresis loop, butterfly response, and negative piezoelectric behaviour are discussed in detail in Chapter 3.

2.1.3 Applications

Throughout the 1970s and 1980s, PVDF began to find its first applications[16], thanks not only to its greater mechanical flexibility compared to standard piezoceramics, but also to its ease of processing, environmental compatibility, and biocompatibility[18,22,23]. For instance, PZT, despite its high d_{33} value up to 500-600 pm·V^{-1} [69], faces limitations in its application due to its mechanical stiffness and high lead content, which can be up to 60% by weight. Moreover, the high chemical resistance, resistance to microorganisms, and UV resistance[70,71] of ferroelectric polymers like PVDF and P(VDF-TrFE) have positioned them as ideal candidates for energy harvesting applications, particularly in wearable electronic textiles, where mechanical energy must be efficiently converted into electrical energy by piezoelectric nanogenerators[72,73]. Additionally, polymers exhibit a higher dielectric breakdown strength than piezoceramic materials, enabling them to withstand higher electric fields and therefore more electrical energy (see Table 2 Chapter 3.2.1)[74]. Ferroelectric materials such as PVDF and P(VDF-TrFE) typically possess higher energy density than linear polymer dielectrics, rendering them well-suited for energy storage applications[75]. Another application area for PVDF-based polymers is in sensors, including tactile sensors capable of detecting mechanical deformations such as

bending, stretching, and pressing and transforming them into digital signals[74,76]. In the sensors field, PVDF has also demonstrated its capability to monitor dynamic and static pressure changes, exhibiting high-pressure sensitivity in biomedical applications[77]. These examples offer only a small insight into the current and prospective applications of PVDF and P(VDF-TrFE), which has paved the way for the fabrication of polymers capable of meeting increasing standards of evaluation and expanding their applications in MEMS.

Ferroelectric polymer science represents a dynamic and evolving discipline that offers a diverse array of scientific and technological opportunities. It encompasses the study of increasingly complex macromolecular structures and holds the potential to drive innovation across a wide range of applications, from advanced materials to biomedical devices and beyond. In addition to the industry of macromolecular structures, to further enhance desired performances in fluoropolymers, nanocomposite technology has been introduced. This is the main focus of the next chapter.

2.2 Nanocomposite based on ferroelectric polymers

This chapter explores the state-of-the-art in fluoropolymer-based nanocomposite thin films, focusing on the integration of nanofillers into polymer matrices and examining the distinctions and advantages of both organic and inorganic nanofillers, particularly within PVDF and P(VDF-TrFE) polymer matrices. The discussion also emphasizes critical challenges like dispersion and nanoparticle-matrix interface quality, essential in realizing the full potential of this technology for industrial applications. Through this comprehensive analysis of the state-of-the-art, this chapter highlights the importance of overcoming these obstacles in the field of energy storage devices.

2.2.1 Nanocomposite technology

The concept of composite materials, involving the mixing of materials with different characteristics, has been practiced for centuries. However, the term “nanocomposite” was first mentioned in 1940 by C. Bower, who developed a nanocomposite material consisting of a suspension of nanoparticles into a reinforcement metal matrix material, a combination of Al/SiC and Al/BN[25]. Despite the early introduction of this term, it wasn’t until the early 1990s that the nanocomposite technology experienced widespread commercial applications[78].

Initially, the research on polymer composites based on nanoparticles primarily focused on improving processability. However, as the potential benefits of incorporating nanofillers into polymer matrices became evident, research efforts shifted toward enhancing their properties. This shift in focus has led to significant attention from industries such as aerospace, automotive, and electronics, where polymer nanocomposites are now utilized for various applications including biomedical devices, energy storage systems, structural components, and sensors[79,80,81].

Nanocomposite technology has played a crucial role in enhancing the capabilities of fluoropolymers like PVDF and P(VDF-TrFE). The incorporation of nanofillers into these polymers has enabled improvements in their mechanical, thermal, electrical, and piezoelectric properties, expanding their potential applications. In the following chapters, the role of the nanofillers, their interface with the polymer matrix, and the challenges faced by this technology are discussed in detail. Understanding these aspects is essential for optimizing the performance of nanocomposite materials and unlocking their full potential across various industries.

2.2.2 Nanofillers and polymer matrix

Both industry and academia have driven extensive research aimed at enhancing the properties of the materials to meet increasingly ambitious goals in the MEMS field. The integration of nanofillers into polymer matrices represents a significant advancement, enabling the customization of mechanical, dielectric, and piezoelectric properties. Nanofillers have notably improved the performance of various polymers, including poly(methyl methacrylate) (PMMA), polydimethylsiloxane (PDMS), and polyimides, particularly in biomedical, optical, and sensor applications[82,83,84,85,86]. The selection of appropriate fillers based on type, shape, and size is crucial in tailoring material properties. Commonly used filler types include conductive fillers like graphene[87,88], carbon black[89,90], and carbon nanotubes[91,92], as well as non-conductive ceramics like barium titanate (BTO)[93,94], titration dioxide (TiO_2)[95], and zinc oxide (ZnO)[96]. These ceramics, acting as insulators, possess high dielectric permittivity compared to polymer materials, making them suitable for applications such as energy storage. Furthermore, the shape, such as zero-dimensional (spheres, dots), one-dimensional (tubes, wires), and two-dimensional (sheets, platelets), as well as the size of the fillers, significantly influence the material quality and performance[97,98,99]. All these factors impact fundamental

phenomena in the nanocomposite technology like the percolation limit, which represents the critical concentration where continuous channels begin to form across the entire system, thus limiting further filler addition[26].

In the fabrication of nanocomposite materials, careful attention must be paid to considerations such as the dispersion of nanoparticles and their compatibility with the polymer matrix. While the general approach of incorporating nanofillers to enhance the properties of the base material is promising, an often overlooked but essential aspect is the interface between the nanofiller and the polymer matrix. External stimuli, such as mechanical stress or electric fields, act on the embedding material (matrix) rather than directly on the embedded material (nanofiller). Therefore, the quality of the interface between them is pivotal in realizing improvements from the nanocomposite compared to the pure embedding material. For instance, the addition of ceramic nanofillers like BTO or TiO_2 into the polymer matrix may introduce structural defects at the interface, such as pores, which deteriorate the mechanical properties, increase leakage current as well as dielectric loss[100,101]. Moreover, in nanocomposites for energy storage devices, where high-permittivity nanofillers are used, a significant difference in dielectric permittivity between the filler and the matrix may lead to a substantial increase in the local electric field density at the interface, reducing the breakdown strength of the nanocomposite[28]. In addition, due to the large specific surface area and high surface energy, the nanoparticles tend to agglomerate forming micrometer-sized clusters, undermining the concept and the desired performance of a homogenous nanocomposite material. To address these issues, methods for improving the dispersion and compatibility of the nanoparticles within the polymer matrix have been extensively studied. These methods include, beyond the optimization of processing conditions, the specific surface modification of the nanoparticles.

In the last decades, various surface modification approaches have been reported in literature to achieve better dispersion and compatibility between nanoparticles and matrices. These include hydrogen peroxide (H_2O_2) treatment[102,103,104], titanate coupling agent utilization (TC-2)[105,106], and phosphonic acid functionalization[107,108]. Overall, the addition of H_2O_2 resulted in improved morphology of the composite due to the hydrogen bonding between the hydroxyl group (-OH) formed on the surface of the nanoparticles and the fluorine atoms on the PVDF molecular chains, as shown in Fig. 2.12a[102]. Titanate coupling

agent (TC-2) was presented as an improvement over the previously described surface modification and is used immediately after hydroxylation, as illustrated in Fig. 2.12b[105]. Adding TC-2 showed enhanced compatibility and dispersion of the nanoparticles compared to single hydroxylation treatment, with beneficial results in terms of energy density[105,106]. Similarly, surface modification with polyvinylpyrrolidone (PVP), presented in Fig. 2.12c, has been effective in PVDF-based nanocomposite thin films[109]. Nevertheless, it is always essential to consider potential trade-offs associated with various functionalization techniques. This is exemplified in certain modifications, such as phosphonic acid functionalization, where, for instance, the dipole orientation with the electric field may be limited[110]. In response, an innovative and more sophisticated approach, such as using soft carbon chains, was proposed as an improvement in the field of phosphonic acid functionalization (see Fig. 2.12d)[111].

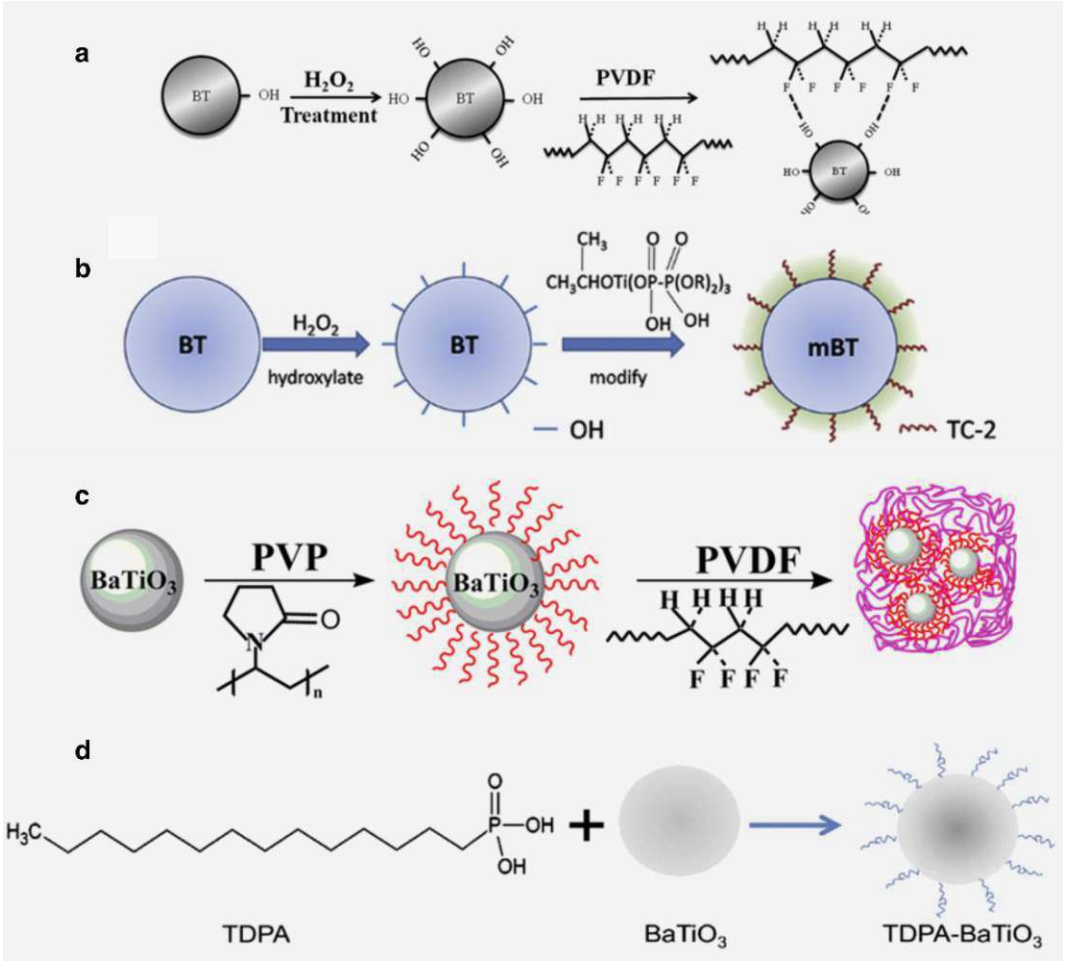

Figure 2.12 a. Schematic diagram of the hydroxylation of BTO nanoparticles and the hydrogen bonds in the PVDF-based nanocomposite[102] **b.** Schematic image of nanoparticle surface modification with TC-2[105] **c.** Schematic diagram of PVP-modified BTO nanoparticles and the PVDF-based nanocomposite[109] **d.** Schematic representation of TDPA modified BTO nanoparticles[111].

Among the functionalization agents presented in literature, polydopamine (PDA) has emerged as a highly versatile and biocompatible polymer for surface functionalization. Initially introduced in 2007 by Lee and Messersmith, PDA coating has gained significant attention for its unique properties and ease of application[112]. Inspired by the adhesive proteins secreted by mussels for attachment to wet surfaces[113], the primary advantage of polydopamine is that it can be easily deposited with controllable thickness and durable stability on virtually all types of inorganic and organic substrates, including superhydrophobic surfaces[114]. Simple immersion of substrates in a dilute aqueous solution of dopamine, buffered to a pH equal to 8.5 typical of marine environments, results in spontaneous deposition of a thin adherent polymer film whose thickness is a function of the immersion time, as shown in Fig. 2.13[112]. Compared to the other functionalization methods, PDA coating offers excellent biocompatibility, making it suitable for a wide range of biological applications, and versatility, allowing effective functionalization of diverse substrates[115]. As a consequence, PDA gained a wide range of applications, ranging from polymeric nanoparticles and diamonds to ceramics and graphene[116,117,118,119]. A schematic diagram of PDA functionalization is reported in

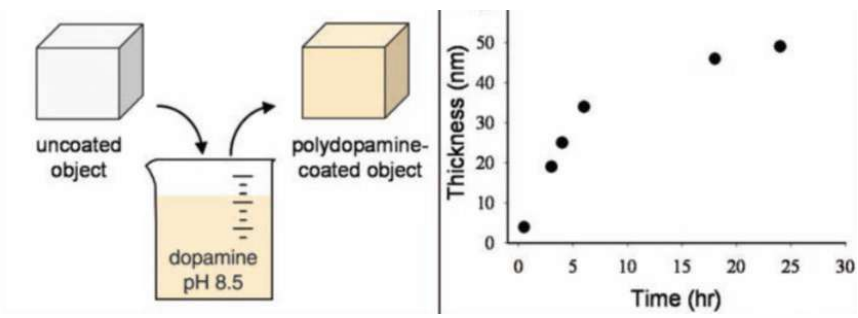

Figure 2.13 On the left a schematic illustration of film deposition of polydopamine by dip-coating in an alkaline dopamine solution. Thickness evolution of polydopamine coating as a function of reaction time for a given concentration of dopamine in alkaline solution[112].

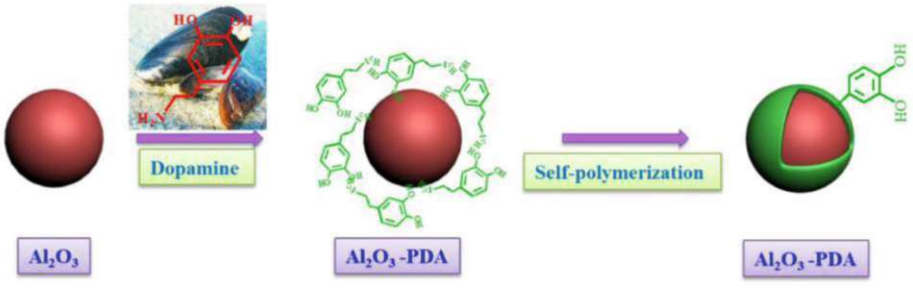

Figure 2.14 Schematic diagram of polydopamine functionalization by dopamine polymerization on top of on Al_2O_3 nanoparticles[120].

Fig. 2.14[120]. Moreover, the PDA synthesis process is simple, involving the only autoxidation of dopamine in alkaline conditions. This leads to the spontaneous polymerization of dopamine molecules on surfaces, resulting in a coating that can be tailored by adjusting polymerization conditions[121]. This simple process makes PDA functionalization cost-effective and accessible for various research fields[122], making it the surface modification of choice in this work.

Although inorganic nanofillers like alumina, barium titanate, graphene, and titanium dioxide are commonly used and studied for their properties and scalability in production, organic nanofillers such as nanocellulose and nanoclays offer unique advantages compared to their inorganic counterparts. These advantages extend beyond enhancing the properties of the polymer materials and include factors such as biocompatibility, sustainability, and green manufacturing. The promising characteristics of organic nanofillers have driven research into their industrial applications in polymer nanocomposites. For instance, the use of clay montmorillonite (MMT), which can be easily exfoliated into nanolaminates and used as filler, has been shown to promote the nucleation of β-phase in PVDF, thereby enhancing its piezoelectric properties and energy storage capabilities[123]. Meanwhile, cellulose, recognized

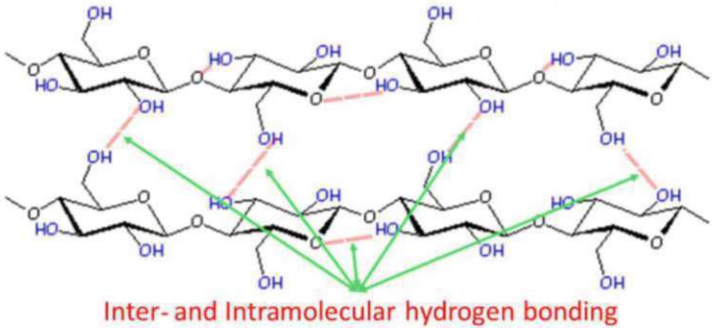

Figure 2.15 Schematic diagram of nanocellulose chemical structure and hydrogen bonding[124].

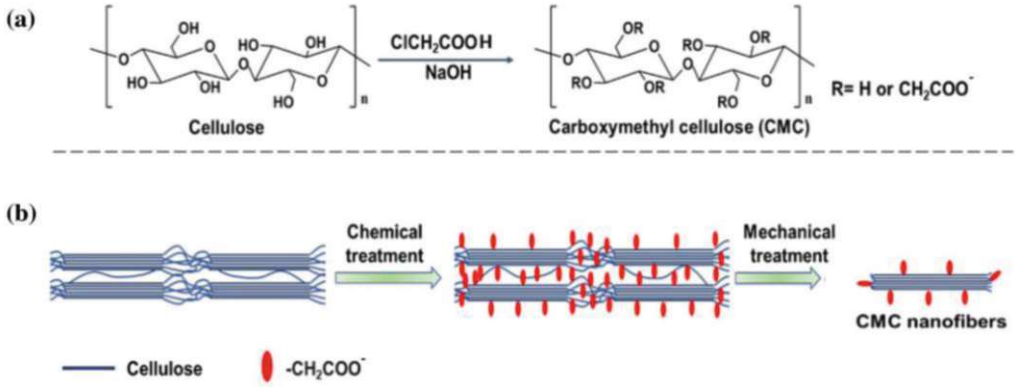

Figure 2.16 a. Reaction scheme of carboxymethylation for cellulose **b.** Schematic illustration of the fabrication of CMC nanofibers[127].

as the most ubiquitous and abundant biopolymer in nature, has also attracted significant attention for both its biosynthesis and applications in nanoparticle form[124]. Cellulose nanoparticles are considered promising fillers due to their anisotropic character (large aspect ratio), renewability, cost-effectiveness, low density, compostability, and mechanical stability[125]. In particular, cellulose nanofibers (CNF) have already demonstrated their effectiveness as green binders for a variety of composite polymer materials. This is attributed to their high crystallinity, unique long polymer chain molecular structure, abundant function groups, and subtle physiochemical properties[126]. However, CNF possesses a strong tendency to high self-association due to the interaction of surface hydroxyl groups, as shown in Fig. 2.15[124], leading to nanofiller aggregation and challenging homogenous dispersion. To address this issue, carboxymethyl cellulose nanofibers (CCNF) have been introduced as cellulose derivatives, substituting hydroxyl groups with carboxymethyl groups, as illustrated in Fig. 2.16[127]. This modification enhanced the dispersibility of CNF without compromising their physical properties[128]. The introduction of cellulose nanoparticles in PVDF to enhance the performance of the polymer matrix has been already studied. For example, the addition of small amounts of cellulose nanoparticles has been shown to improve tensile strength and storage modulus, and additionally, a thermal stabilizing effect at high temperatures was observed[129]. Moreover, in the field of triboelectric textile sensors, cellulose nanocrystals have been demonstrated to enhance the β-phase fraction and membrane properties in PVDF[130,131,132]. Recent advancements in the field of energy storage devices have highlighted the potential of cellulose-based nanocomposites as well[133]. Specifically, the incorporation of cellulose nanoparticles in PVDF-base nanocomposites has been found to increase the dielectric permittivity[125], further intensifying the interest in energy storage applications.

Together with the appropriate selection of nanofillers and proper functionalization of their surfaces, the role of the polymer matrix is highly relevant as its characteristics must suit the desired application. For instance, for the packaging, construction, and insulation industries, polymers like polyethylene and polystyrene are ideal choices due to their chemical resistance and thermal properties[134]. On the other hand, in electronic applications such as energy storage and sensors, PVDF and P(VDF-TrFE) emerge as suitable candidates owing to their piezoelectric properties and high dielectric permittivity compared to non-polar polymers. Generally, non-polar polymers exhibit high breakdown fields but possess low

relative permittivity, typically ranging from 2 to 3, which imposes limitations in energy density performance[28]. In non-polar polymers individual dipole moments cancel out each other due to the symmetry, resulting in a lower permittivity. In contrast, in polar polymers presenting a macroscopic polarization, the dipoles typically do not cancel out, leading to higher dielectric permittivity[26]. In energy storage applications, polymers with both high breakdown strength and dielectric permittivity are essential, as the electrostatic energy stored in a dielectric material is proportional to both the dielectric permittivity and the square of the electric field applied to the material. This inherent polarity and the high breakdown strength have prompted extensive research into fluoropolymers, such as PVDF and P(VDF-TrFE)[135,136]. The relative permittivity of common non-polar and polar polymers is reported in Table 1. For instance, PMMA, though a polar polymer, does not exhibit a macroscopic polarization, resulting in a relative permittivity higher than that of non-polar polymers like HDPE, PP, or PDMS, but lower than that of PVDF and P(VDF-TrFE). Further details about dielectric characteristics and electric breakdown strength mechanism in PVDF and P(VDF-TrFE) are discussed in Chapter 3.1.1 and Chapter 3.2.1.

In the fabrication of MEMS devices, the performance of the nanocomposites is related to the synthesis process as well. In contrast to this work, where the deposition technique is spin-casting, scientific reports available in literature, focusing on the energy storage characteristics of fluoropolymer-based nanocomposites, have predominately used the casting technique. This method results in thicker layers, typically ranging between 10 and 40 μm[98,146,120,147,148], that consequently require extremely high voltages, often in the kilovolt (kV)

Material	Relative permittivity (1 kHz)
High-density polyethylene (HDPE)	2.3[137,138]
Polypropylene (PP)	2.2[139]
PMMA	4.5[140,141]
PDMS	2.6[138,142]
PVDF	8-10[48,143]
P(VDF-TrFE)	10-15[51,144,145]

Table 1 Dielectric permittivity measured at 1 kHz of various polar and non-polar polymers at room temperature. Notably, PMMA, although a polar polymer, has a lower dielectric permittivity than PVDF and P(VDF-TrFE) due to the absence of a macroscopic polarization.

range, for polarization. Even though theoretically thinner films should withstand higher voltages, they suffer more from processing defects which could compromise their dielectric strength. This limitation created a research gap in literature regarding studies on energy density capability in fluoropolymers-based nanocomposite with thicknesses below 10 μm. Chapter 7 proposes a novel study on the ferroelectric properties of P(VDF-TrFE)-based nanocomposite thin films with a thickness of approximately 2 μm and a nanofiller content of up to 15% by weight, highlighting a significant improvement compared to previous reports available in literature[149,150].

2.2.3 Energy storage as an application example

Nanocomposites are advanced materials that offer a wide range of benefits and have seen widespread adoption across industries from aerospace to healthcare and biomedical devices[151,152]. This thesis explores nanocomposites tailored for energy storage applications, particularly in fabricating thin films used as dielectric capacitors. Dielectric capacitors, when compared to fuel cells, batteries, and supercapacitors, hold significant promises due to their higher power density, higher charge and discharge rate, and longer cycle time[27,28]. In applications where the accumulation and instantaneous release of energy to achieve high power outputs is of utmost importance, nanocomposite capacitors are extensively employed[26,153]. However, despite their high power density, dielectric capacitors have relatively poor energy density compared to other energy storage systems, as shown in Fig. 2.17[28]. Over the past decade, there has been an exponential increase in the number of

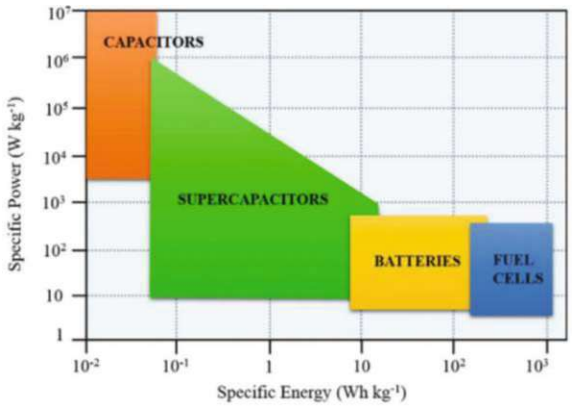

Figure 2.17 Energy and power density of four mainstream energy storage techniques[28].

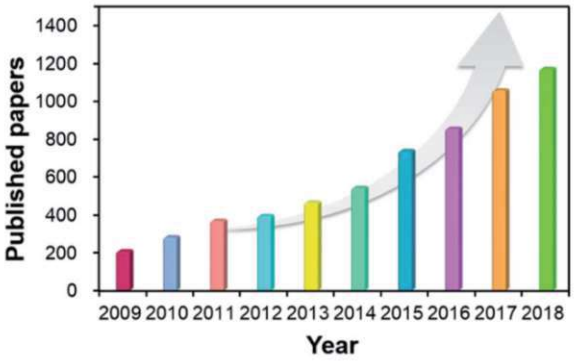

Figure 2.18 Number of publications related to dielectric energy storage materials over the past decade[28].

scientific works, as illustrated in Fig. 2.18[28], aiming to enhance the energy density of polymer nanocomposites. This found is especially crucial for applications like automotive inverters, electrotherapy, particularly in defibrillators, and defense systems, where compact size and high performance are critical[26,154,155,156]. Additionally, significant efforts have been also made to develop highly flexible nanocomposite materials for wearable devices, which require small size, lightweight design, low power consumption, and portability[157]. The rapid advancement of technology in this field has led to the emergence of textiles with novel functionalities, including power generation from movement, vibration and pressure detection, heat regulation, luminescence, and touch sensitivity, offering substantial benefits in healthcare, sports, transports, space exploration, and beyond.

In general, improving dielectric properties in ferroelectric nanocomposites is crucial for enhancing their energy density. Nevertheless, several challenges still need to be overcome in the near future to further advance the technology. These challenges include, for instance, tailoring the polarization mechanism, mitigating the interfacial polarization, reducing dielectric losses, and enhancing surface modification of nanoparticles to minimize aggregation and improve interfacial adhesion. Additionally, the choice of suitable polymer materials is crucial, as the final dielectric properties depend on both the fillers and the matrix. Engineering the appropriate polymer matrix involves facing the complexities of polymer science and macromolecular construction, also previously mentioned. Addressing these challenges is pivotal for unlocking the full potential of flexible nanocomposites in high-energy-density applications.

3 Fundamentals of Electroactivity and Energy Storage

3.1 Electroactivity

In electroactive polymers, fundamental concepts such as polarization, energy density, and the interplay between mechanical, thermal, and electrical properties are of outmost importance for industrial applications. Dielectric polymers, categorized into subclasses like piezoelectrics, pyroelectrics, and ferroelectrics, exhibit diverse functional behaviours. Ferroelectrics, in particular, with their spontaneous electric polarization and reversible nature, are integral in modern technology. This chapter provides the fundamentals on the relationship between electric fields, materials properties, and functional capabilities of dielectric materials.

3.1.1 Dielectricity

Dielectricity is a fundamental concept in electromagnetism and refers to the property of materials enabling them to generate a polarization as response to an external electric field.

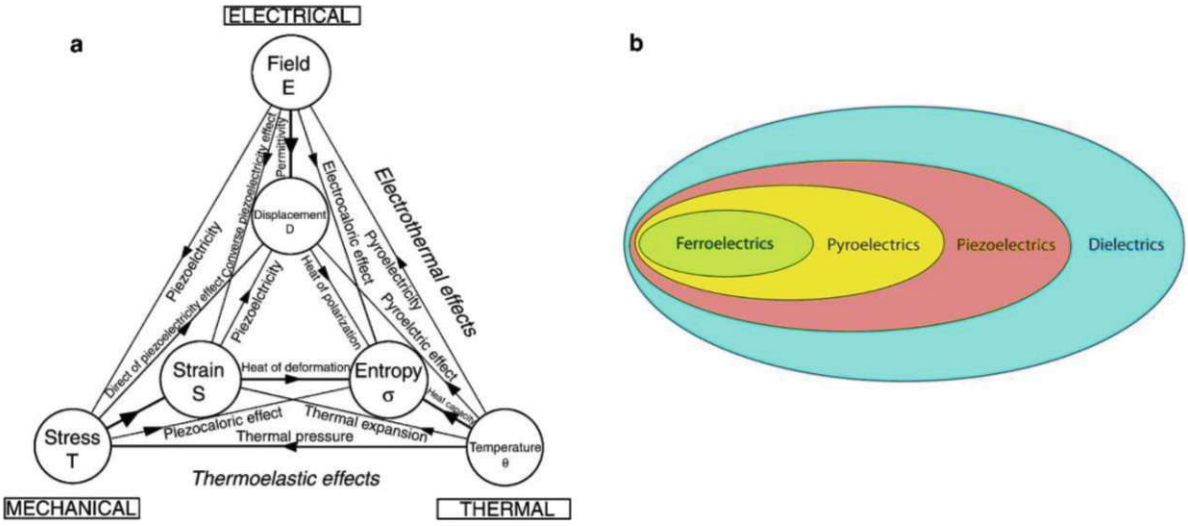

Figure 3.1 a The Heckmann diagram illustrating the interplay between thermal, mechanical, and electrical properties in dielectrics[158]. **b** Representation of the subdivision of dielectrics into subclasses of piezoelectrics, pyroelectrics, and ferroelectrics.

In the study of dielectrics, understanding the interplay between their thermal, mechanical, and electrical properties is crucial. To illustrate these relationships, scientist G. Heckmann created a schematic diagram known as the Heckmann diagram, displayed in Fig. 3.1a[158]. This diagram illustrates the coupling between elastic, electric, and thermal variables in dielectric solids, including the electromechanical response by linking the electric field and the mechanical strain, a central topic of this thesis. Depending on their functionality or crystal structure, dielectric materials can be divided into three subclasses: piezoelectrics, pyroelectrics, and ferroelectrics, as shown in Fig. 3.1b. The diverse functional behavior of these material classes provides a wide range of capabilities, making dielectric materials suitable for various applications, from electrical insulation to the functioning of capacitors and other electronic devices.

Understanding dielectricity involves exploring how materials respond to electric fields, resulting in phenomena like polarization and energy storage. When a dielectric material is exposed to an electric field, it undergoes polarization, where positive and negative charges within the material align in response to the external field, as shown in Fig. 3.2. This polarization effect reduces the overall electric field within the material, thereby influencing its capacitance and allowing for the storage of more electric energy. As a consequence, the external field induces a local displacement in the average equilibrium position of the electrical charges within the material. This electric displacement is described by:

$$D = \varepsilon_0 E + P \tag{3.1}$$

where $\varepsilon_0 = 8.854 \cdot 10^{-12}$ F·m^{-1} is the vacuum permittivity, E denotes the external electric field applied, measured in V·m^{-1}, and P represents the electric polarization[159], measured in C·m^{-2}. The electric displacement D is measured in C·m^{-2}.

The electric polarization P induced by an electric field within the material is defined as the total dipole moments in the dielectric per unit volume, expressed by the equation:

$$P = (\varepsilon_r - 1)\varepsilon_0 E \tag{3.2}$$

where ε_r is the relative permittivity, defined as the permittivity of the material ε as a ratio with the vacuum permittivity ε_0.

The degree of polarization of a dielectric under the influence of an applied electric field is measured by a term called susceptibility χ:

$$\chi = (\varepsilon_r - 1) = \frac{P}{\varepsilon_0 E} \tag{3.3}$$

In general, four main types of polarizations can be found in dielectric materials: electronic, ionic, molecular, and interfacial, as shown in Fig. 3.3[160]. Electronic polarization is associated with the displacement of the electric cloud with respect to the nucleus of the atoms. The negatively charged atomic shell is shifted against the direction of the electric field, while the positive is in the same direction, resulting in an electric-field-induced dipole moment. On the other hand, ionic polarization describes the motion of cations and anions in an electric field. In ionic materials, the cations are displaced in the direction of the field, while the anions are displaced in the opposite direction. Both electronic and ionic polarization exhibit resonance at frequencies in the optical and infrared (IR) range, respectively, as depicted in Fig. 3.4[26], which places them in the so-called resonance regime[161]. These two phenomena are temperature-independent, as they are phenomena of intramolecular nature[162]. Molecular and interfacial polarizations have instead different characteristics. Typically, the molecules composing a dielectric material possess an asymmetric distribution of charges between atoms due to

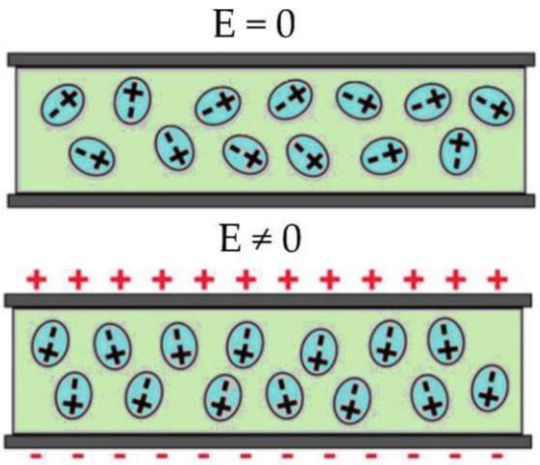

Figure 3.2 Representation of dielectric polarization response through the application of an external electric field.

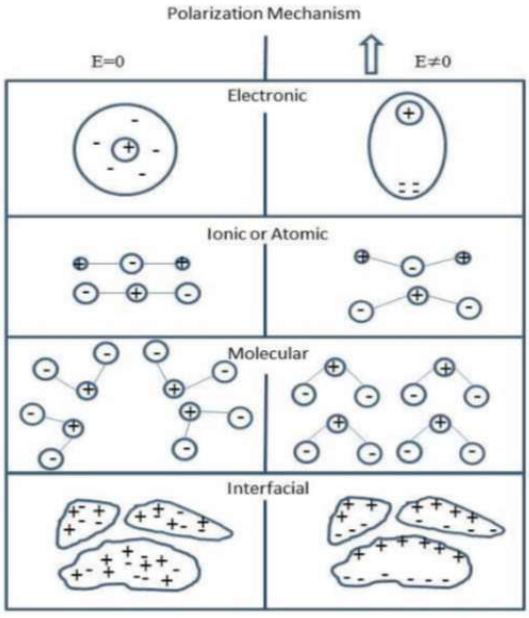

Figure 3.3 The four types of polarization mechanism in a dielectric material: electronic, ionic, molecular and interfacial[160].

different electronegativity. This leads to the presence of a dipole moment within the molecules, as seen in materials like PVDF and P(VDF-TrFE). These molecules can therefore orientate the dipoles in the direction of an applied electric field leading to molecular polarization. Additionally, as molecules need energy to overcome the resistance the surrounding molecules offer, this phenomenon is temperature-dependent. When the external field is removed, the molecules require time to relax back to equilibrium, resulting in molecular polarization falling into the relaxation regime. This process typically occurs with frequencies in the radio band[163], as depicted in Fig. 3.4[26]. In real capacitors, local inhomogeneities such as impurities or incomplete contact of the film with the electrodes lead to regions of accumulated trap charges within the dielectric, resulting in the Maxwell-Wagner-Sillars interfacial polarization[26]. These regions create a dipole moment that adds to the total polarization of the dielectric. This phenomenon also depends on temperature, and since it is the slowest process, the relaxation frequency is approximately 10 Hz, as shown in Fig. 3.4[26].

When a dielectric material is subjected to an alternating electric field, its electrical characterization involves the use of complex permittivity, which covers real and imaginary parts of the dielectric response. The real part reflects the material's ability to store electric

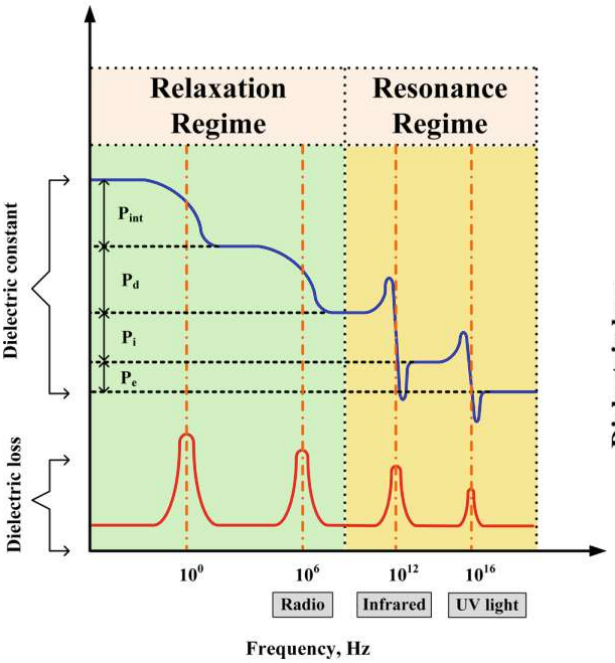

Figure 3.4 The four types of polarizations and their frequency dependences. Dielectric permittivity (dielectric constant) and corresponding losses are depicted with blue and red lines, respectively[26].

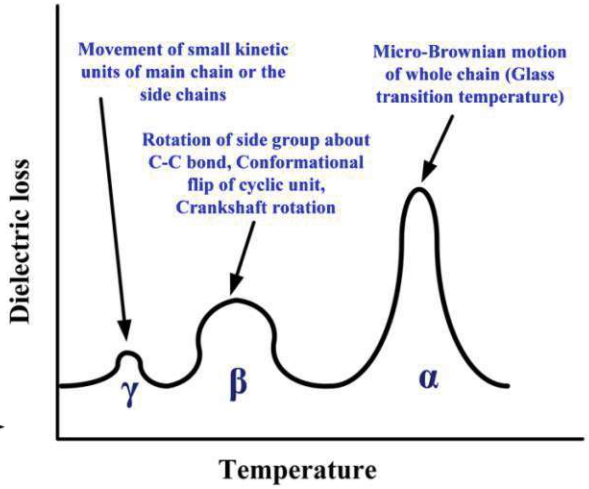

Figure 3.5 Different types of dielectric relaxations with a qualitative scale on the x-axis representing the temperatures related to the maximum dielectric loss[26].

energy, *i.e.* the polarization, while the imaginary part represents the dissipation of electrical energy as heat, known as dielectric losses. These losses are typically divided into two categories: frequency-independent ohmic conduction losses, which arise from the material's resistance to electric current flow, and frequency-dependent dielectric losses, occurring as energy is absorbed to move the charges in the direction of the field[164]. The polarization mechanisms are associated with the latter.

In the relaxation regime, dielectric relaxation processes are the fundamental mechanisms behind dielectric losses and, specifically in polymer dielectrics, two types of molecular relaxations exist: dipolar segmental relaxation, associated with the micro-Brownian motion of the entire chain, known as α relaxation, and dipolar group relaxation, linked to the localized motion of the molecules as small chain units, known as β and γ[162,165,166]. The β relaxation typically involves side groups or conformational shifts, while γ relaxation entails the movement of small units of the chains, occurring at lower temperatures. Fig. 3.5 illustrates the various relaxations and their corresponding qualitative activation temperatures as peaks of dielectric losses in polymers[26].

Dielectric materials can be classified into linear and non-linear based on their response to an applied electric field. In the case of a linear relationship between polarization and the electric field, by combining equations (3.1) and (3.2), the electric displacement follows a linear function of the electric field as well:

$$D = \varepsilon E \tag{3.4}$$

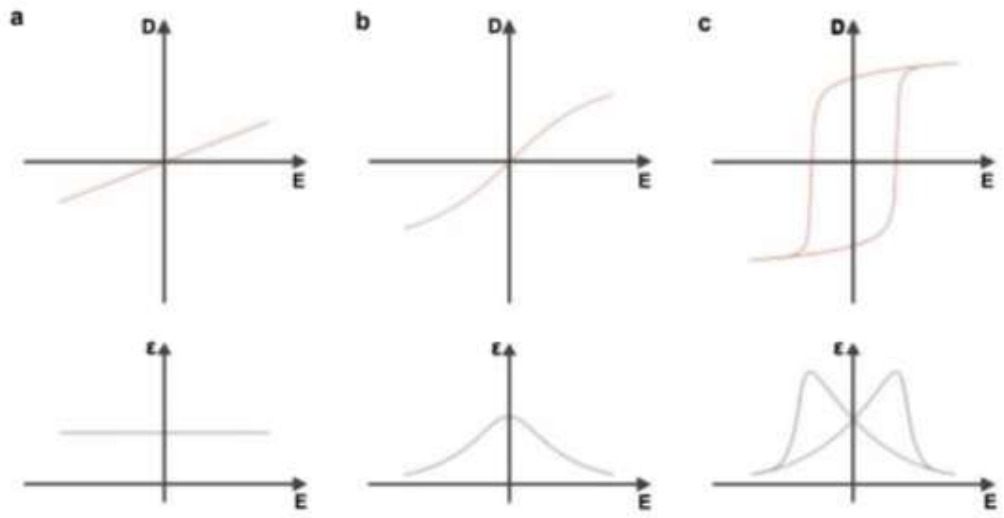

Figure 3.6 Schematic diagram of displacement-field (*D*-*E*) and permittivity field (ε-*E*) characteristics in **a** linear dielectrics, **b** paraelectrics, and **c** ferroelectrics[47].

Linear dielectrics maintain their electric polarization as long as the electric field is applied. Electric susceptibility, dielectric permittivity, and relative permittivity are constant, as illustrated for ε in Fig. 3.6a[47]. However, in non-linear dielectrics, these properties are dependent on the electric field, and more generally, the dielectric permittivity is expressed as:

$$\varepsilon = \frac{\partial D}{\partial E} \tag{3.5}$$

Non-linear dielectrics contain permanent dipoles, and the distinct electrical responses of molecular and electronic polarization mechanisms result in non-linear behavior of dielectric properties (see Figs. 3.6b and c). For example, materials exhibiting paraelectric behavior possess permanent dipoles randomly distributed within the material, leading to a zero net macroscopic polarization. When subjected to an external electric field, these permanent dipoles align in the direction of the field, resulting in the electric displacement becoming a non-linear function of the electric field (see Fig. 3.6b[47]). Ferroelectric materials, on the other hand, also possess permanent dipoles but exhibit macroscopic polarization even in the absence of an external electric field, showing remnant polarization, as illustrated in Fig. 3.6c[47]. Ferroelectric characteristics are discussed in detail in Chapter 3.1.4.

Applying an electric field not only induces electric polarization but also leads to a mechanical strain in the material. Materials that undergo mechanical deformation in response to an electric field are called electroactive materials. Chapter 3.1.2 and Chapter 3.1.3 will delve into the principles of electrostrictive and piezoelectric effects.

3.1.2 Electrostriction

Electrostriction is a non-linear electromechanical coupling phenomenon and is observed in all dielectric materials, including amorphous ones[159,167,168,169,170]. Essentially, electrostriction represents a second-order property, characterized by a quadratic dependence of the strain S on the electric field and can be expressed as:

$$S = ME^2 \tag{3.6}$$

where M is the field-related electrostrictive coefficient measured in units of $m^2 \cdot V^{-2}$. It is important to note that equation (3.6) is only valid for linear dielectrics. Ferroelectric and paraelectric materials exhibit highly non-linear dielectric properties and do not demonstrate a quadratic change of an electric-field-induced mechanical strain. Instead, they display a

quadratic change of the mechanical strain as a function of the electric displacement. The strain-field (*S-E*) curve of the electrostrictive effect of a linear dielectric is reported in Fig. 3.7a[47]. At higher fields, a saturation effect in the mechanical strain is observed due to the saturation of field-induced polarization within the material. The discrepancy caused by the saturation with respect to the quadratic behavior can be modeled by expanding equation (3.6) with even higher orders of the electric field.

Since the electromechanical effect arises from the electric polarization within the material, there exists an electric polarization-related electrostrictive effect, where the electric field is replaced by the electric displacement as the independent variable:

$$S = QD^2 \tag{3.7}$$

here, Q represents the polarization-related electrostrictive coefficient, measured in units of $m^4 \cdot C^{-2}$. The strain-displacement (*S-D*) characteristic is represented in Fig. 3.7b[47]. Unlike the case with the electric field, saturation is not visible since it is already included in *D*. In general, using *D* instead of *E* as the independent variable proves more useful. This is because the field-related electrostrictive coefficient *M* tends to depend on the amplitude of the field, while the polarization-related coefficient *Q* does not. Therefore, focusing on the intrinsic material properties related to polarization, as represented by *D*, reduces the influence of field strength variations.

Electrostriction is attributed to the anharmonicity of chemical bonds[159,167,168,169,170] and leads to either an expansion or compression of the material, contingent upon the sign of the electrostrictive coefficient *M* or *Q*. Notably, ferroelectric polymers like PVDF or P(VDF-TrFE)

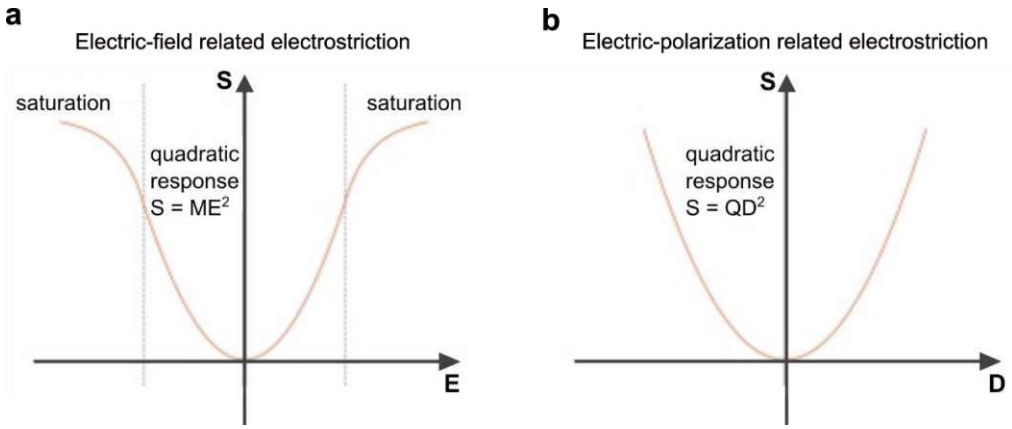

Figure 3.7 Schematic diagram of **a** strain-field (*S-E*) characteristic of the electric-field related electrostrictive effect in linear dielectrics, showing its quadratic nature, and **b** strain-displacement (*S-D*) characteristic of electric-polarization related electrostrictive effect[47].

exhibit a negative electrostrictive effect, causing them to compress when subjected to an external electric field. Electrostriction is a phenomenon present in all dielectrics, including piezoelectric materials; however, the strain it induces is generally minor compared to that induced by piezoelectricity. As a result, the contribution of electrostriction-induced strain is often neglected for pure piezoelectric materials, the effect of which is analyzed in the next Chapter 3.1.3.

3.1.3 Piezoelectricity

Piezoelectricity is an electromechanical phenomenon wherein mechanical stress induces the generation of an electric charge on the surfaces of the material, and conversely, the application of an electric field results in mechanical deformation. This effect has become a well-established transducer mechanism in MEMS, allowing for its utilization as an actuating and sensing element due to its reversibility, as shown in Fig. 3.8[171].

The piezoelectric effect is characterized by a linear electromechanical coupling between mechanical and electric quantities and is only present in materials with a non-centrosymmetric crystal structure[159]. The constant governing this linear relationship is known as the piezoelectric coefficient. In the case of the direct piezoelectric effect, the linear relation between the mechanical stress T and electric displacement D is given by:

$$D = d\,T \tag{3.8}$$

where d represents the piezoelectric coefficient, measured in $C{\cdot}N^{-1}$. The value of the piezoelectric coefficient is dependent on the material and the direction of the applied mechanical stress.

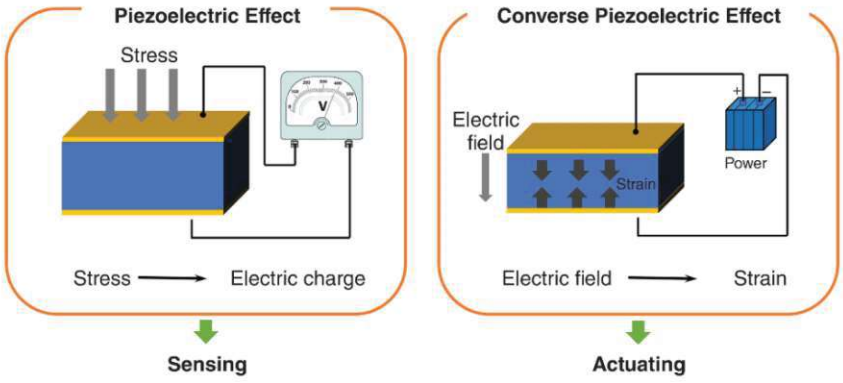

Figure 3.8 Direct piezoelectric effect generates an electric charge from mechanical stress, while the converse (or inverse) piezoelectric effect generates strain under an applied electric field[171].

The equation representing the inverse piezoelectric effect, where S represents the mechanical strain and E denotes the electric field, is given by:

$$S = d\,E \tag{3.9}$$

here d is again the piezoelectric coefficient, but in this case measured in $m \cdot V^{-1}$.

The piezoelectric response depends on the direction of the applied mechanical or electrical stimulation, and it is represented by a matrix. Based on this direction, specific components of the piezoelectric coefficient matrix become significant. In technological applications, the components d_{33} and d_{31} are of particular interest. These are referred to as the longitudinal (33-mode) and transverse (31-mode) piezoelectric coefficients, respectively. Considering the inverse piezoelectricity, in the case of the longitudinal effect, a mechanical deformation occurs in the same direction as the applied electric field, whereas in the transverse effect, the mechanical deformation arises perpendicular to the direction of the applied field. Importantly, the longitudinal and transverse effects are interrelated; that is, when a piezoelectric material is mechanically or electrically stimulated, both effects are present. In practical applications, these effects can influence each other due to the clamping of the piezoelectric material to metallic electrodes or a rigid substrate. Clamping can restrict the ability of the piezoelectric thin film to deform to an applied electric field, leading to a reduction in the measured piezoelectric constant[47]. It should be noted that the longitudinal piezoelectric coefficients d_{33} given in this work are mostly effective values, *i.e.* they are determined under the influence of clamping effects and the intrinsic transverse piezoelectric coefficient d_{31}.

In general, piezoelectricity describes a linear relation between electrical and mechanical observables. However, a non-linear behavior is observed at high mechanical stresses or electric fields due to the saturation of the dipole motion. In this case, a linear relation is only observable around the zero value of the mechanical stress or the electric field. Therefore, the direct piezoelectric coefficient is experimentally determined using the relation:

$$d = \left.\frac{\partial D}{\partial T}\right|_{T=0} \tag{3.10}$$

while for the inverse piezoelectric effect:

$$d = \left.\frac{\partial S}{\partial E}\right|_{E=0} \tag{3.11}$$

As discussed above, the piezoelectric response is a characteristic found in non-centrosymmetric crystal structures. However, the presence of electrostriction in all dielectrics plays a crucial role in field-induced piezoelectricity[53]. When an electric field is applied to a dielectric, it causes a redistribution of charges, leading to a loss of center of symmetry in the dielectric, enabling a piezoelectric mechanism to operate. This phenomenon, known as field-induced piezoelectricity, can be controlled by applying a DC field[53]. The magnitude of the field-induced piezoelectric effect is strongly influenced by the electrostrictive response of the material. For instance, in strong piezoelectric materials like aluminum nitride (AlN), this effect is negligible, whereas in ferroelectric materials, which typically exhibit a large electrostrictive response, it can be significant (see Chapter 3.1.4).

Quartz (α-quartz) was one of the first materials in which piezoelectricity was observed. Subsequently, polycrystalline piezoelectric ceramics such as BTO and PZT have been introduced, offering significantly improved piezoelectric characteristics compared to quartz. These ceramics exhibit strong piezoelectric responses with d_{33} values reaching 145 pm·V^{-1} for BTO and even 593 pm·V^{-1} for PZT[172]. Piezoelectricity has also been observed in semi-crystalline polymers like PVDF and P(VDF-TrFE), where the piezoelectric coefficients are negative (see Chapter 2.1.2), in contrast to the positive coefficients seen in piezoceramics. These polymers in fact contract when subjected to an electric field aligned with the polarization direction. This characteristic is attributed to the one-dimensional molecular chains bonded together by weak van der Waals forces where the strong intramolecular bonds within the chains and the weaker intermolecular bonds result in highly anisotropic physical properties. When an electric field is applied, the softness of the intermolecular bond leads to enhanced dipole-dipole interaction, causing the van der Waals gap to shrink more than the expansion of the intramolecular bond, resulting in the macroscopic contraction of the material[68].

In this study, MEMS devices based on PVDF and P(VDF-TrFE) are fabricated, and their piezoelectric coefficients are investigated. It is imperative to acknowledge that reported piezoelectric coefficient values in literature may vary significantly for the same material due to factors such as differences in material synthesis methods.

3.1.4 Ferroelectricity

Ferroelectrics are a subclass of dielectric materials that embraces all phenomena of piezoelectricity, and pyroelectricity. These characteristics make ferroelectrics an exciting field for both research and application-related activities.

First observed in Rochelle salt ($KNaC_4H_4O_6$) by Valasek in 1921, the term "ferroelectricity" was coined due to its formal analogy with ferromagnetic properties[5]. Ferroelectric materials exhibit a spontaneous electric polarization P_s which can be reversed by an external electric field, *i.e.* $P_s = P_s(E)$ is a function of E. Consequently, in ferroelectrics the total polarization is the sum of the induced and spontaneous polarization $P = P_i + P_s$ and the ferroelectric displacement is given by:

$$D = \varepsilon_0 E + P = \varepsilon_0 E + (P_i + P_s) = \varepsilon E + P_s \tag{3.12}$$

As ferroelectrics can reverse the direction of the spontaneous polarization P_s, two stable polarized states can be found at zero-field conditions:

$$D(E = 0) = P(E = 0) = P_s(E = 0) = \pm P_r \tag{3.13}$$

where P_r is the remnant polarization.

Switching between the two opposite polarized states requires a sufficiently high electric field to be applied which is called coercive field E_c:

$$E(D = 0) = \pm E_c \tag{3.14}$$

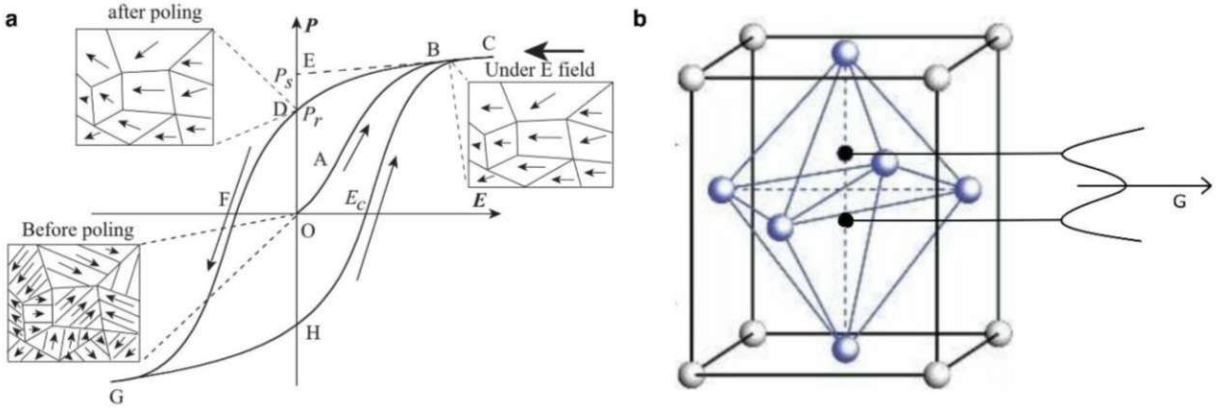

Figure 3.9 a Typical hysteresis loop in ferroelectrics and corresponding domain reversal[175]. **b** The tetragonal perovskite structure of BTO with the two thermodynamically equivalent states within the unit cell[173].

In ferroelectric materials, spontaneous polarization exists within the single-unit cell. For instance, in the tetragonal perovskite structure of BTO, the tetravalent titanium ion (Ti^{4+}) is displaced from the center of the unit cell. This non-centrosymmetric crystalline structure results in spontaneous polarization where the titanium ion has two thermodynamically equilibrated states within the unit cell as shown in Fig. 3.9b[173]. These states are described by the electric Gibbs potential. According to the thermodynamic model of ferroelectrics, related to the Landau-Devonshire theory[174,175,176], the two local equilibrium states of *G* correspond to the two possible polarization states of the ferroelectric, as depicted on the right side of Fig. 3.9b. Consequently, the unit cell exhibits a remnant polarization even without any applied field. In general, from a macroscopic point of view, spontaneous polarization is typically observed in single crystals[47]. In polycrystalline materials instead, the permanent dipoles are arranged in ferroelectric domains, which are regions of equivalent aligned dipoles. Materials characterized by a polycrystalline nature may not exhibit a macroscopic net polarization, as the random orientation of dipoles with opposite directions can result in a net polarization of zero. These domains can only be rotated by applying a sufficiently strong electric field, known as a coercive field. Therefore, to induce a macroscopic polarization, a poling procedure in polycrystalline materials is required, typically involving the prolonged application of a sufficiently high electric field, *i.e.* above coercive value, along the desired polarization axis.

Fig. 3.9a schematically illustrates a standard *P-E* hysteresis loop of a polycrystalline ferroelectric material[177]. It begins from an unpolarized state (O), where all the ferroelectric domains are randomly oriented within the material. As the applied electric field increases, it reaches the saturation point (C), where all the domains are aligned in the same direction. Subsequently, upon decreasing the external electric field, the polarization reduces until reaching the remnant polarization P_r at point (D) under zero-field conditions ($D(E=0) = \pm P_r$). Then, the applied electric field reverses, reaching the negative coercivity point (F), from which the polarization is inverted. This leads to the negative saturation point (G), and from here the inverse process begins, tracing the hysteretic response. For more details, Chapter 5.4 delves into how the ferroelectric hysteresis loop is measured using a Sawyer-Tower circuit and how parameters like E_c or P_r are extracted using empirical models.

The presence of spontaneous polarization in ferroelectrics enables electrostriction to induce piezoelectric activity within the material, as discussed earlier in the context of field-induced piezoelectricity in Chapter 3.1.3. However, ferroelectrics exhibit highly non-linear dielectric behavior, characterized by a strong electrostrictive response that results in electromechanical deformation much more complex than observed in non-ferroelectric piezoelectric materials. Fig. 3.10 provides both typical hysteresis (Fig. 3.10a) and butterfly (Fig. 3.10b) curves of ferroelectric polymer P(VDF-TrFE), facilitating the comprehension of the relationship between ferroelectric displacement and macroscopic strain[52]. While the polarization process in Fig. 3.10a is analogous to that described in Fig. 3.9a, the electrostrain behaviour in Fig. 3.10b, referred to as the butterfly curve, is described as follows considering that, in this case, it does not start from an unpolarized state. Segment (1) denotes the initial stage where the applied electric field increases from its zero-value, resulting in a corresponding increase in the mechanical strain. The initial zero-field value of the strain is called remnant strain ($S(E=0) = S_r$), similar to the remnant polarization ($D(E=0) = -P_r$) of the *D-E* characteristic. As the external electric field increases, the strain reaches a maximum at the coercivity ($E(D=0) = +E_c$), corresponding to a zero-displacement value in the *D-E* hysteresis loop. Subsequently, with further increments in the applied electric field, the strain gradually decreases and becomes negative, reaching a minimum at the saturation point of the polarization. Transitioning to segment 2, as the external electric field begins to decrease, the strain once again decreases until it reaches the remnant strain as the applied field approaches

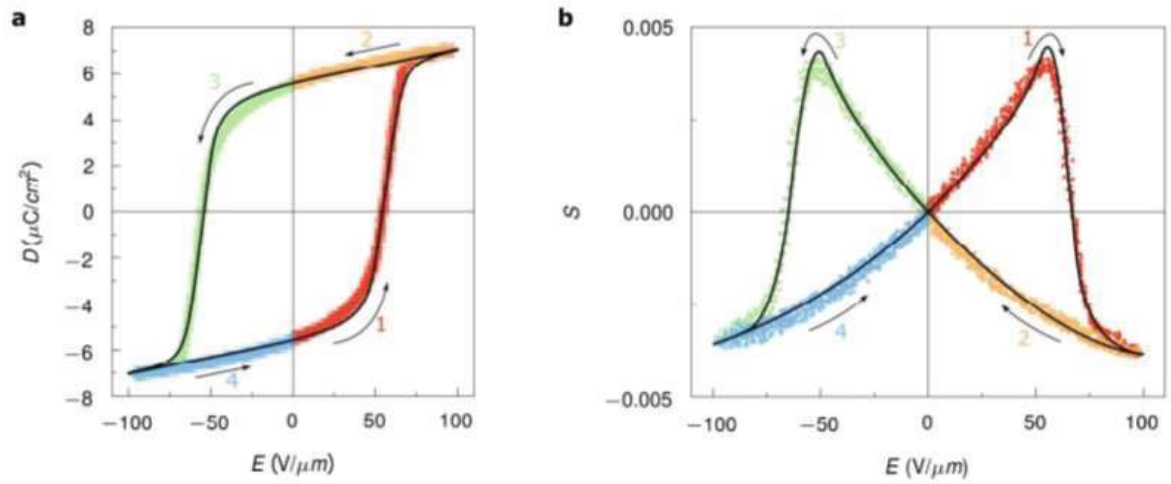

Figure 3.10 a Polarization and **b** strain characteristics of P(VDF-TrFE), with arrows indicating the direction of the electric field applied and colors representing the four key segments corresponding to both characteristics[52].

zero. Following this, the inverse process starts. Typically, the remnant strain value is set to zero, as after the ferroelectric is polarized once, the remnant strain remains and does not contribute to the field-varying strain.

In general, the electrostrain in ferroelectrics can be expressed as:

$$S = QD(E)^2 = Q(\varepsilon E + P_s(E))^2 = Q\varepsilon^2 E^2 + 2Q\varepsilon P_s(E)E + QP(E)_s^2 \quad (3.15)$$

where the first term, $Q\varepsilon^2E^2$ corresponds to the pure electrostrictive effect, the second term $2Q\varepsilon P_sE$ is referred to as the linear piezoelectric effect, and the last term $Q_{33}P_s^2$ represents the spontaneous strain. The piezoelectric coefficient can be calculated with equation (3.11):

$$d = \frac{\partial S}{\partial E}\Big|_{E=0} = 2Q\varepsilon_0\varepsilon_r P_r \quad (3.16)$$

where ε_r is the relative permittivity at zero-field. The sign of the piezoelectric coefficient d is defined by the sign of the electrostrictive coefficient Q. Typically, ferroelectric materials like BTO exhibit a positive piezoelectric coefficient value, while ferroelectric polymers tend to have a negative one. It is important to note that the orientation of the butterfly curve is related to the sign of the electrostrictive coefficient. In the case of piezoceramics like BTO, the *S-E* strain-field characteristic is inverted compared to ferroelectric polymers. This means that at the coercivity point, there will be a minimum of electrostrain, and at the maximum electric field value, there will be a maximum of electrostrain, as shown in Fig. 2.10.

Equation (3.15) does not represent a quadratic function of E, since both spontaneous polarization P_s=$P_s(E)$ and the dielectric permittivity ε=$\varepsilon(E)$ are highly non-linear functions of the electric field (see Fig. 3.6). In general, due to the electrostrictive nature of the electrostrain in ferroelectrics, a linear relation between S and D^2 is observed (see Chapter 6.2.2.1).

The spontaneous polarization in ferroelectrics is not observed at all temperatures. At a critical temperature known as Curie temperature (T_c), ferroelectric materials undergo a phase transition. During this transition, they lose their ferroelectric properties and become paraelectrics and the spontaneous electric polarization disappears. This phase transition can be described by the Landau-Devonshire theory with the electric Gibbs potential[174]. Generally, the calculations indicate that at T_c three local minima of the Gibbs potential become equally probable. This implies that the ferroelectric and paraelectric phases coexist. Consequently, a double-hysteresis loop, combining properties of the ferro- and paraelectric states, is observed

experimentally in P(VDF-TrFE) thin films (see Fig. 3.11b[52]). This phenomenon is a characteristic feature of a discontinuous phase transition. Above T_c the two local minima of the ferroelectric phase disappear, and the remnant polarization vanishes, as shown in Fig. 3.11a[52]. For example, in BTO a phase transition occurs at around T_c = 125 °C, where the non-centrosymmetric tetragonal crystal structure transforms into a centrosymmetric cubic crystal structure. This transition in BTO is categorized as being of a displacive nature. In contrast, in P(VDF-TrFE), it has been demonstrated that the transition from ferroelectric to paraelectric state is associated with micro- or macroscopic electromechanical responses[52]. At its Curie temperature of approximately 100 °C, the electrostrain behavior of the P(VDF-TrFE) within the crystalline domains still exists, but macroscopically it is mechanically compensated by the amorphous matrix, resulting in an undetectable butterfly response[52]. PVDF instead exhibits a Curie temperature above 172 °C, *i.e.* higher than its melting point, making the transition not observable[33]. Last, but not least, it is always important to consider that external influences, such as an electric field or mechanical stress, might alter the Curie temperature of a ferroelectric material[162].

3.2 Energy storage

For energy storage applications the electric breakdown strength is a parameter of utmost importance. This chapter highlights its pivotal role in various applications and the factors influencing it. Subsequently, energy density, energy loss, and energy efficiency are

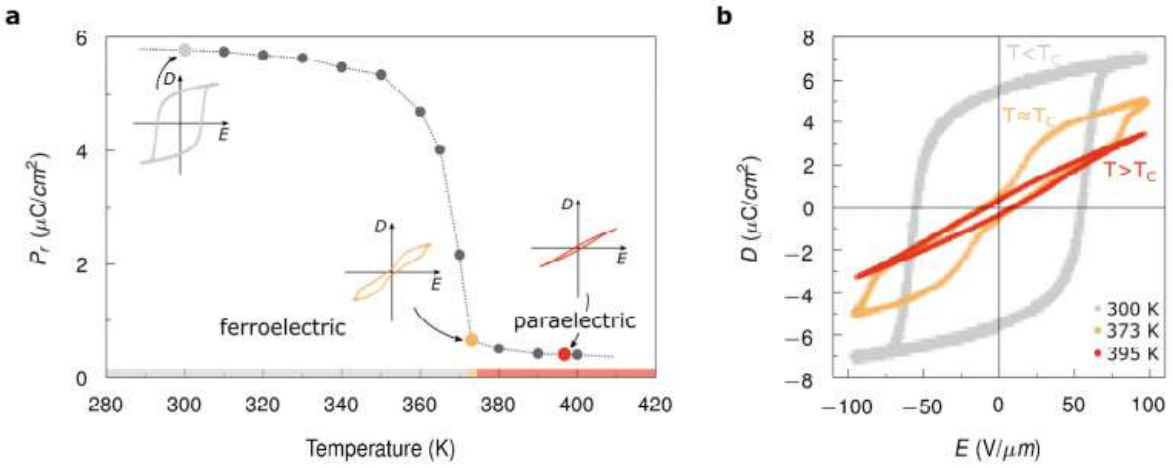

Figure 3.11 a Remnant polarization values as a function of temperature and **b** *D-E* hysteresis loops at temperatures below, around, and above the Curie point, showing the transition from ferroelectric to paraelectric of P(VDF-TrFE)[52].

investigated as fundamental key indicators in energy storage evaluation. Overall, the essential insights into characterizing energy storage devices are presented.

3.2.1 Electric breakdown strength

Electric breakdown strength in dielectrics is a fundamental property defining the threshold at which dielectric materials transition from an insulating to a conducting state under electrical stress. This property plays a crucial role in various applications requiring reliable electrical component insulation. For instance, in high-energy density applications, avoiding breakdown is essential as it significantly impacts both the capacitor's capability to store energy and the lifespan of the device. Expressed in $V \cdot \mu m^{-1}$, electric breakdown strength, also termed dielectric strength or breakdown field, is notably high in dielectric polymers compared to their inorganic counterparts. Table 2 reports dielectric strength, expressed in $V \cdot \mu m^{-1}$, and relative permittivity values for typical piezoceramics and polymers, providing valuable insights. Within the polymer class, ferroelectric polymers, with their superior relative permittivity, are particularly suitable for energy storage applications.

In general, the breakdown strength under DC voltage tends to exceed that under AC fields, since the breakdown is a phenomenon strongly related to various breakdown mechanisms: thermal breakdown, breakdown due to space-charge effect, and electromechanical breakdown[135]. Thermal breakdown results from thermal energy associated with dielectric losses, while the space-charge effect involves electron-hole recombination energy, potentially dissociating polymer molecules into radicals affecting dielectric strength. Electromechanical breakdown instead is related to the increase in mechanical stress within the material when subjected to an AC field, comprising Maxwell stress and electrostrictive stress. Maxwell stress arises from the Coulombic attraction of the electrodes carrying opposite charges, while the electrostrictive stress is the sum of all electric-field-induced mechanical stresses within the material. In this case, the breakdown strength of polymers can be theoretically estimated when the total electromechanical stress equals the yield stress of the polymer[145].

Moreover, the dielectric breakdown strength of a material is also influenced by factors such as traces of impurities, micro defects, porosity, electrode sizes and arrangement, environmental conditions, and stress application characteristics, such as the electric field ramp

rate[6,28]. Geometrical design is also critical as it can cause stress amplification in certain areas, leading to electric field enhancements and hence, premature device failure.

In the case of polymer nanocomposites, additional elements play a crucial role in the dielectric strength of the material such as differences in the relative permittivity between individual fillers and polymer matrix. A significant contrast in these values can lead to local inhomogeneity of the electric field within the material, reducing the breakdown strength. To enhance the breakdown field, it is important to achieve a homogenous dispersion of the nanofillers, necessitating surface modification to prevent the interconnection or even agglomeration of nanofillers, which could result in electrically conductive channels and the formation of voids, respectively.

In general, achieving high-performance energy storage devices requires careful consideration of factors such as relative permittivity and electric breakdown fields. Energy storage characteristics are further discussed in the following Chapter 3.2.2, focusing on energy density, loss, and efficiency.

Material	Dielectric strength (V· μm^{-1})	Relative permittivity (1kHz)
PZT	12[178]	200-5000[3,178]
BTO	15[138,179]	1235[180]
PMMA	250[141]	4.5[140,141]
Polyamide	240[181]	3[181]
PVDF	150-500[143,182]	8-10[48,143]
P(VDF-TrFE)	200-300[103,183]	10-15[51,144,145]

Table 2. Dielectric strength and relative permittivity of typical piezoceramics and polymers at room temperature. It is worth noting that the higher dielectric strength of polymers is juxtaposed with their lower relative permittivity compared to the piezoceramics. This discrepancy forms the basis for the development, study and fabrication of nanocomposites for energy storage applications.

3.2.2 Energy density, loss, and efficiency

Energy density, energy loss, and energy efficiency are fundamental parameters in energy storage characterization, crucial for evaluating the performance and effectiveness of various energy systems and materials. Specifically, energy density quantifies the amount of energy that can be stored within a material per unit volume, while energy loss represents the

dissipation of energy, thereby representing the reduction of the usable energy output. In literature, both are typically measured in J·cm^{-3}. Energy efficiency instead evaluates how effectively energy is converted from one form to another, indicating the efficiency of the energy charge-discharge process.

To measure the energy density (U_e) of ferroelectric materials, it is necessary to perform first the ferroelectric characteristic *D-E*, then to integrate the area between the displacement axis and discharge curve, as shown in Fig. 3.12[28], using the equation:

$$U_e = \int EdD \tag{3.17}$$

In linear dielectrics, where permittivity is not a function of *E* and the displacement exhibits a linear relationship with *E*, the electrical energy density is given by:

$$U_e = \frac{1}{2}\varepsilon_0\varepsilon_r E^2 \tag{3.18}$$

Energy loss (U_l) is represented by the area within the hysteresis loop (see Fig. 3.12[28]). By using energy density and energy loss, it is possible to calculate the energy efficiency of a capacitor using the formula:

$$\eta = \frac{U_{discharge}}{U_{charge}} = \frac{U_e}{U_e + U_l} \tag{3.19}$$

It is worth noting from equation (3.18) that energy density has a squared relationship with breakdown strength, highlighting the need for higher breakdown strength to achieve greater energy density. In the case of polymer nanocomposites, energy density largely

Material	Energy density (J·cm^{-3})
Poly(phthalazine ether ketone)	1.6[184]
PMMA	1.5[140]
Polyamide	1.4[181]
PVDF	2.8[143]
P(VDF-TrFE)	2.1[185]

Table 3. Energy density measured in J·cm^{-3} of various dielectric polymers at room temperature. Among these, the fluoropolymers appear to be the most promising matrix for developing nanocomposite materials with high energy density.

depends on the matrix material, while improvements in permittivity are sought with the introduction of nanofillers. However, as discussed previously, improper dispersion or functionalization of nanofillers can significantly reduce the breakdown strength of the nanocomposite. Table 3 presents the energy density values, expressed in $J \cdot cm^{-3}$, taken from literature of different polymer matrices, measured between 200 and 250 $V \cdot \mu m^{-1}$. The upcoming Chapter 4 delves into ferroelectric polymer-based capacitor fabrication. Additionally, the chapter discusses the functionalization and dispersion techniques used in this work to enhance nanocomposite energy storage performance.

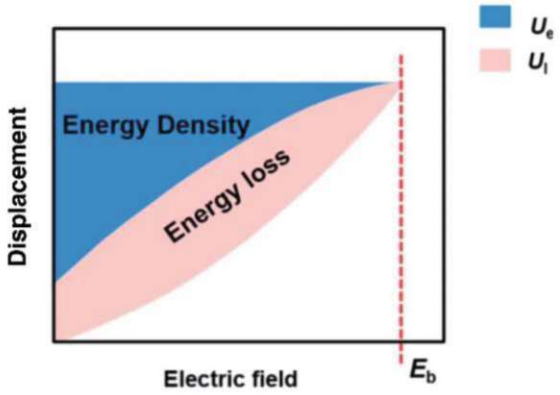

Figure 3.12 Graphical representation of a *D-E* loop used for energy density and energy loss calculations[28].

4 Fabrication Details

4.1 PVDF and P(VDF-TrFE)

To characterize the ferroelectric polymers PVDF and P(VDF-TrFE), solution-processed thin films were fabricated via spin-coating under cleanroom and humidity-controlled conditions. Structural analysis, including AFM, FTIR, DSC, and XRD measurements, primarily focused on spin-cast thin films on silicon substrates. In addition, to investigate potential substrate influences on the microstructure and crystallinity of the spin-cast polymer thin films, silicon substrates with an electron-beam evaporated gold layer were used as an alternative. Gold was chosen to mimic the micromachined capacitors' bottom electrodes for electrical and electromechanical characterization. The following sections provide a detailed analysis of the synthesis of PVDF and P(VDF-TrFE) thin films on silicon and gold-covered substrates, as well as the fabrication of the capacitor-type test structures for ferroelectric and electromechanical analysis.

4.1.1 Synthesis of polymer thin films

The synthesis of PVDF and P(VDF-TrFE) thin films is summarized in Fig. 4.1. Following this summary, every single step will be analyzed in detail.

Thin films of PVDF and P(VDF-TrFE) (ratio VDF and TrFE 70:30 mol%), were deposited via spin-coating from polymer solutions. For that purpose, high-purity powders of PVDF and P(VDF-TrFE) were purchased from Sigma-Aldrich and Piezotech/Arkema Group and were dissolved at a weight ratio of 4% and 8% in the solvents dimethylformamide (DMF) and 2-butanone (methyl ethyl ketone (MEK)), respectively. To increase the dissolution rate and to prevent polymer agglomerations, the dissolution process was carried out at 60 °C for PVDF and 50 °C for P(VDF-TrFE). While DMF has a boiling point of 153 °C under standard conditions, MEK has a boiling point of approximately 80 °C, therefore a small measure was applied during the dissolution process of the latter solvent. A glass cover was used to prevent the possible evaporation of the MEK, so to ensure that the 8% weight ratio between solvent and polymer remained unaffected. The required utensils for the synthesis of the solutions are

shown in Fig. 4.2a. The dissolution of the polymer powder was facilitated by magnet stirring within the solution as depicted in Fig. 4.2b. Visible in Fig. 4.2b is also the temperature sensor immersed in the solution. When the polymer powder appeared to be fully dissolved by the naked eye, the solution was stirred for an additional 10 minutes to ensure complete dissolution. Typically stirring of the polymer solution may lead to the formation of air bubbles, strongly depending on the stirring intensity, which can result in pinholes within the deposited thin film. To avoid this, the solution was degassed in a vacuum desiccator. It is important to note that while P(VDF-TrFE) can be dissolved in both DMF and MEK, PVDF is soluble at room conditions only in the former[186]. In this thesis, P(VDF-TrFE) has been deposited only from MEK solution. Choosing a more volatile solvent like MEK for P(VDF-TrFE) was advantageous due to the cumbersome spin-coating process, discussed in the following paragraph, involved in depositing polymer thin films from a high boiling point solvent, like DMF.

The usage of DMF as solvent requires spin-coating deposition at a high substrate temperature (above 100 °C). Films deposited at low substrate temperatures exhibit high roughness and a phenomenon called vapor-induced phase separation (VIPS)[187] (further details can be found in Chapter 6.1.1), resulting in electrically short-circuited capacitors[80].

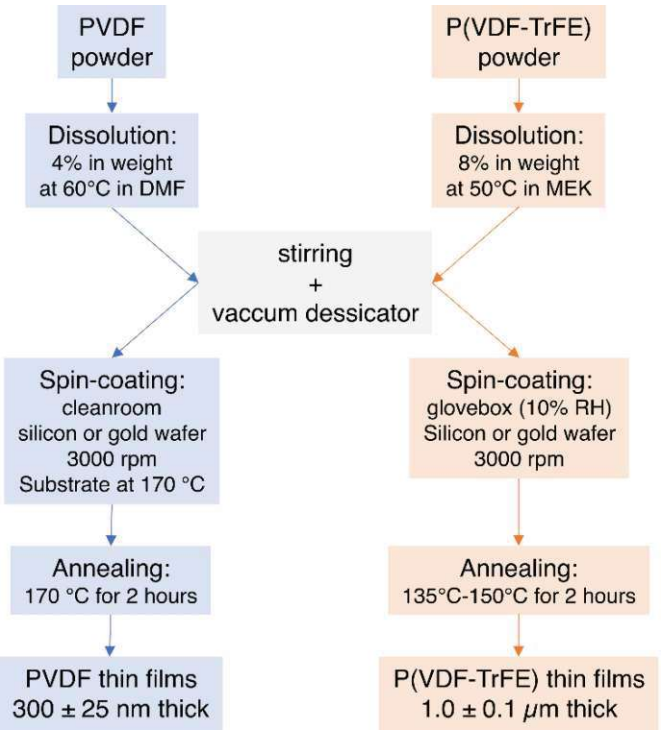

Figure 4.1 Schematic diagram showing the key steps involved in the synthesis of PVDF and P(VDF-TrFE) thin films.

High substrate temperatures prevent VIPS and reduce the roughness of the layer by suppressing PVDF crystallization through faster evaporation of the solvent and by the difference between the substrate temperature and the crystallization temperature[30]. This process requires preheating of the spin-coater chuck, which subsequently heats the wafer used as the deposition substrate. However, obtaining a uniform distribution of temperature across the chuck could be challenging and may require several attempts, which is why, if possible, the use of MEK for P(VDF-TrFE) is preferred. In this work, the chuck, and subsequently the substrate, were heated up to 170 °C to ensure high-quality deposition of PVDF thin films.

Once prepared, PVDF and P(VDF-TrFE) solutions were spin-cast on a 4", 100 nm (100) silicon (Si) wafer, typically at 3000 rpm, resulting in homogenous polymer thin films. Alternatively, as previously mentioned, to investigate the potential influences of the substrate on P(VDF-TrFE) microstructure and crystalline phase, a 100 nm layer of gold thermally evaporated was deposited on the silicon wafer before spin-coating.

After spin-coating, any residual solvent of MEK or DMF within the thin films was subsequently evaporated in the annealing process, which is crucial for improving the electrical and mechanical properties of the polymers and promoting crystallization. PVDF samples were annealed for 2 hours at 170 °C in air to ensure a high degree of crystallinity[188]. In P(VDF-TrFE) thin films instead, the annealing temperature plays a more crucial role in determining the final microstructural and ferroelectric characteristics (as discussed in

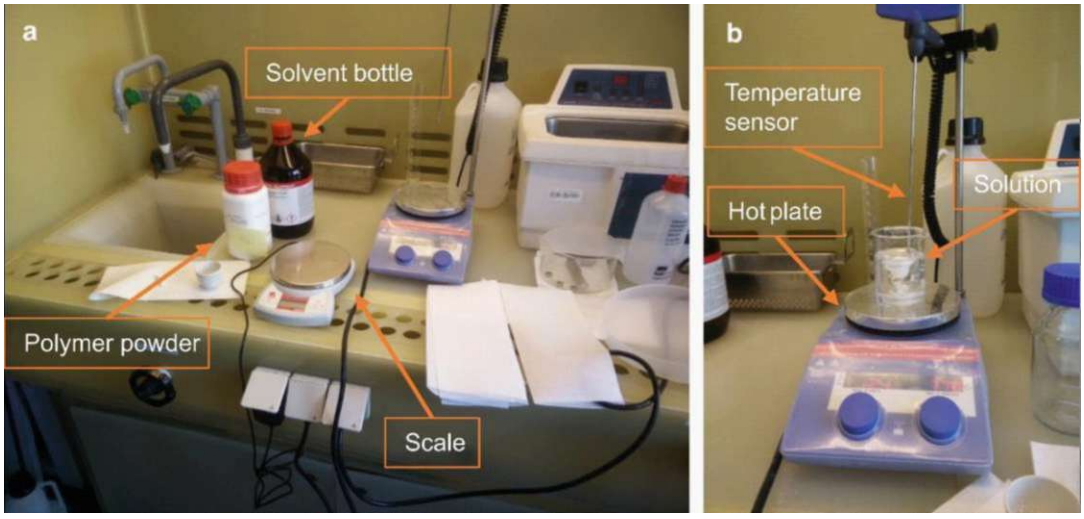

Figure 4.2 a Required utensils for the synthesis of polymer solution, including the solvent bottle, a plastic white box containing the polymer powder, and a scale; **b** The magnet-driven stirring process for dissolving the polymer powder in the solvent, including the temperature sensor that monitors the heat transfer from the hotplate to the solution, facilitating an increased the dissolution rate.

Chapter 6.2.2.1). In this work, the effects of annealing temperature on P(VDF-TrFE) thin films, ranging between 135 °C and 150 °C, were studied. It is important to note that every step described here was carried out under cleanroom conditions for PVDF and humidity-controlled conditions using a glovebox supplied by dehumidified air for P(VDF-TrFE). The use of a glovebox, depicted in Fig. 4.3, maintained at 10% relative humidity (RH) during the deposition of P(VDF-TrFE) thin films, served a similar purpose to the heated-up chuck used in PVDF processing, aiming to prevent phase separation phenomena induced by the water in the air, *i.e.* VIPS[187]. Although VIPS is particularly common in DMF due to its high boiling point, MEK can also be affected, especially during summer when the lab's relative humidity is around 50%.

The film thicknesses obtained were 300 ± 25 nm for PVDF and 1.0 ± 0.1 µm for P(VDF-TrFE), measured with a DEKTAK surface profilometer. In general, various parameters can be adjusted to control the final thickness of the ferroelectric polymer thin films. These parameters include for instance the weight ratio of polymer powder dissolved in the solvent, which influences the viscosity of the solution, the rotational speed, and the acceleration of the spin-coating. Furthermore, previous research has demonstrated that the geometry of the chuck can also impact the film thickness[47]. By modulating these parameters, polymer films with a

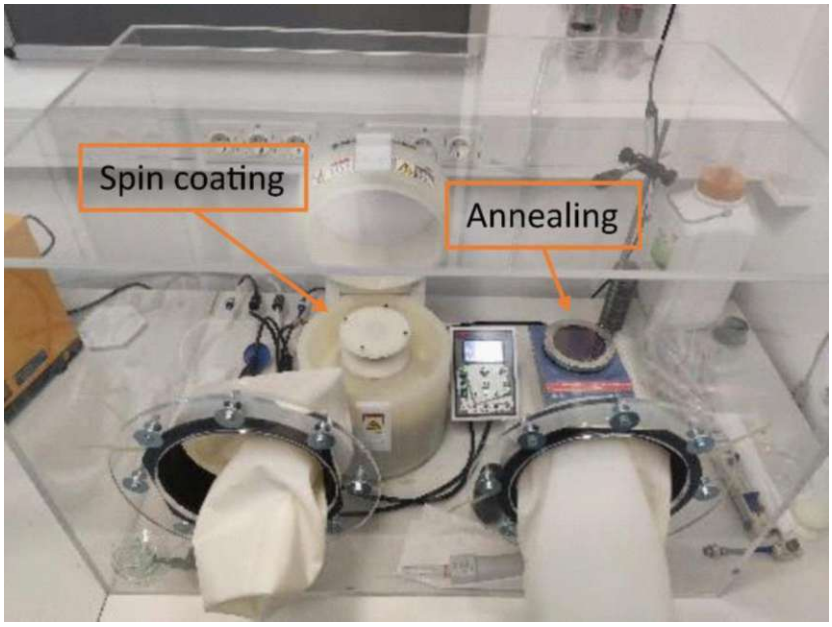

Figure 4.3 Custom-made glovebox based on Plexiglas walls. Dehumidified air was circulated inside to maintain a 10% RH level. Both spin coating and annealing of P(VDF-TrFE) thin films were conducted within this glovebox environment.

thickness ranging from single monolayer to several microns are feasible via spin-coating[50]. The duration of the spin-coating process is primarily essential for achieving homogenous thin films. While the initial seconds are critical for dispersing the polymer solution evenly on the substrate, the duration beyond this point becomes less relevant in influencing the final thickness.

4.1.2 Fabrication of capacitor-type test structure

The electrical and electromechanical characterization of PVDF and P(VDF-TrFE) involved the integration of the polymer thin films in micromachined capacitor-type test structures. These structures are metal-ferroelectric-metal (MFM) capacitors, where the ferroelectric is either PVDF or P(VDF-TrFE) and the thin film electrodes are made of gold (Au). The fabrication process, previously detailed by our research group[47], is outlined step by step below and illustrated in Fig. 4.4a.

1) A 4″ 100 nm (100) Si wafer coated with 250 nm LPCVD silicon dioxide (SiO_2) and 80 nm silicon nitride (Si_3N_4) was used as substrate.
2) The bottom electrodes were formed by the lift-off process. For that purpose, 50 nm of chromium (Cr) was deposited by electron-beam evaporation as an adhesion promoter for a 100 nm thermally evaporated gold (Au) layer.
3) A thin film of PVDF or P(VDF-TrFE) was spin-coated on the wafer, as described in Chapter 4.1.1, and annealed.
4) On top of the polymer, a 150 nm thermally evaporated Au layer was deposited.
5) The top electrodes were fabricated using a wet-chemical etching process. Since standard photoresist solvents, like acetone, can damage the polymer and irreparably alter its structure, lift-off techniques were not employed for patterning the top electrodes.
6) The capacitor-type test structure was finally obtained.

On the Si wafer, the resulting capacitor-type test structures, shown in Fig. 4.4b, typically presented diameters ranging from 6 mm to 8 mm, corresponding to areas between 0.3 cm^2 and 0.5 cm^2. These specific values were selected to ensure a sufficiently large area capable of storing a significant quantity of charges, facilitating the electrical measurements. Capacitors potentially affected by short circuits were tested with a multimeter.

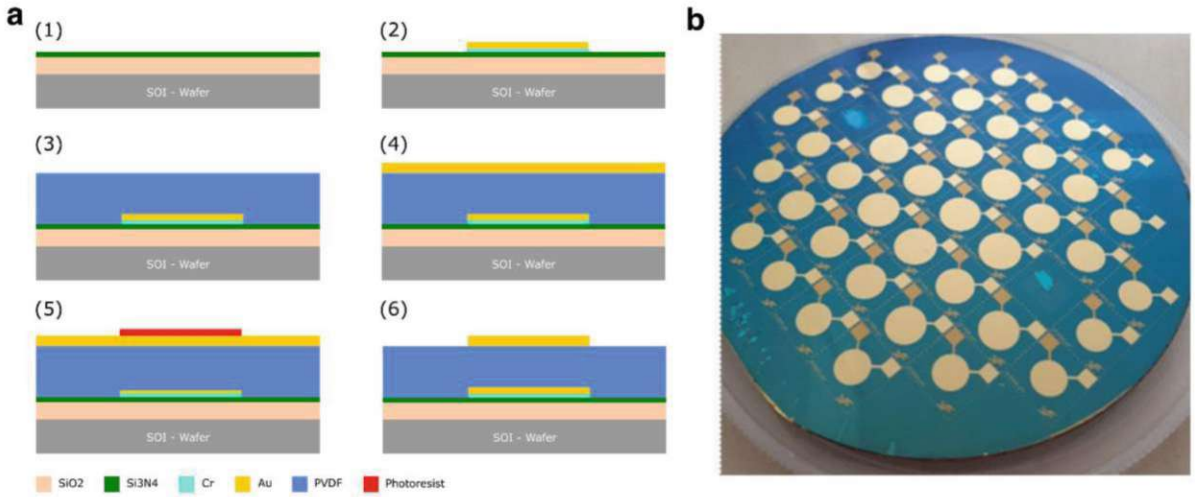

Figure 4.4 a Process steps for the fabrication of the ferroelectric polymer-based metal-ferroelectric-metal capacitors. **b** Picture of the final capacitor-type test structures on a Si wafer.

4.2 P(VDF-TrFE)-based nanocomposite

Functionalization of nanofillers is a fundamental step in processing nanocomposite thin films. In this thesis, commercially purchased BTO, henceforth referred to as BTO$^{(C)}$, powder was initially employed and functionalized with PDA (BTO$^{(C)}$@PDA). At a later stage, a mixture of BTO@PDA and CCNF (CCNF-BTO@PDA) provided by the Research Center of Nano Science and Technology of Shanghai University served as nanofillers for P(VDF-TrFE)-based nanocomposite thin films. The following sections detail the experimental procedures for the PDA functionalization of the BTO$^{(C)}$ powder, the synthesis of the nanofillers mixture (CCNF-BTO@PDA) provided by Shanghai University, and the dispersion of these nanofillers into the P(VDF-TrFE) polymer solution. This process is finalized for the synthesis of P(VDF-TrFE)-based nanocomposite thin films, for ultimately fabricating the capacitor-type test structures for energy storage characterization.

4.2.1 Functionalization of nanofillers

A commercially available BTO$^{(C)}$ powder, 99.95% pure with a cubic structure and mean dimension of 90 nm, was purchased from Nanografi. As detailed in Chapter 2.2.2, PDA was identified as the most suitable candidate for the functionalization of BTO$^{(C)}$ nanoparticles. Functionalizing nanoparticles with PDA require a pH 8.5 Tris buffer solution. To achieve this, 200 mg of Tris Base (Trizma-Base) and 100 mg of Tris HCl (Trizma Hydrochloride), both purchased from Sigma-Aldrich, were added to 230 ml of deionized water and dissolved using

magnet stirring. Once a stable pH value of 8.5 was reached, the nanoparticles were introduced into the solution and sonicated for 30 minutes using a UP400S sonicator from Hielscher. This step was performed to break up any agglomeration formed due to physical interactions between the nanoparticles within the powder. SEM images, shown in Fig. 4.5, illustrate the difference in nanoparticle powders before (Fig. 4.5a) and after (Fig. 4.5b) pre-sonication step. Failure to disperse such clusters, as visible in Fig. 4.5a, may lead to the functionalization of the entire agglomerated structure, resulting in the introduction of micrometer-sized agglomerated nanoparticles within the nanocomposite thin films, thus making the capacitors more prone to localized breakdown and poor electrical performance.

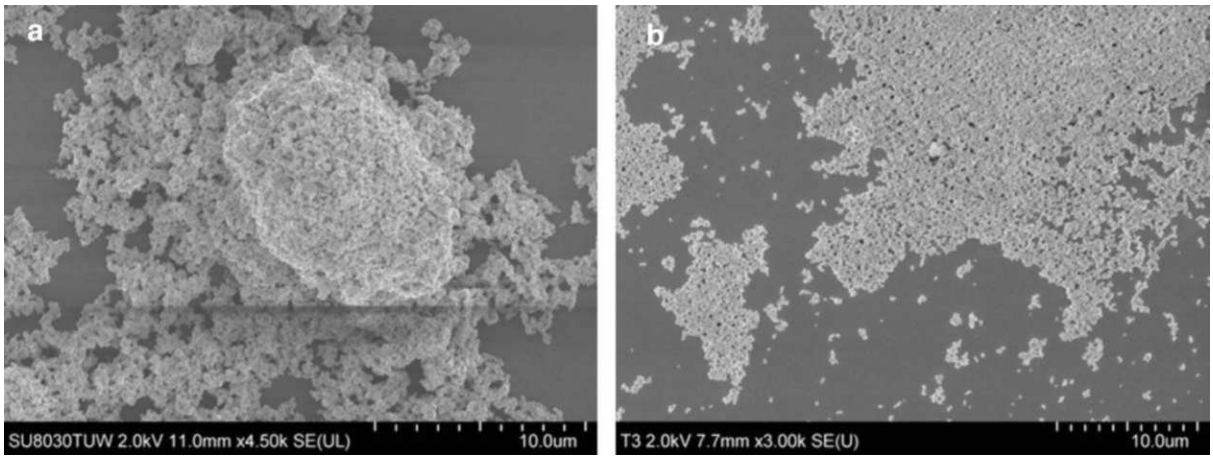

Figure 4.5 BTO$^{(C)}$ nanoparticles before **a** and after **b** pre-sonication step. The pre-sonication step was necessary for breaking up any clusters in the powder, thus improving the dispersion of nanoparticles in the polymer solution for the subsequent deposition of the nanocomposite thin films.

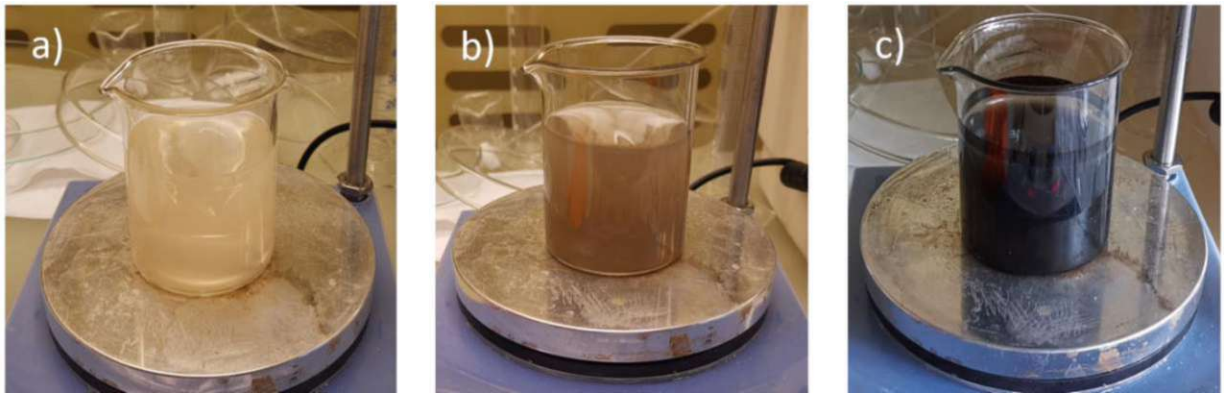

Figure 4.6 Three stages of the PDA polymerization of the BTO$^{(C)}$ nanoparticles: **a)** Dopamine hydrochloride just introduced in the solution: transparent colour **b)** After 5 minutes, the reaction starts, and the colour changes to light brown **c)** After 10 hours, the solution turns completely black, indicating that the polymerization is reaching the saturation stage (see Fig. 7.3).

After the pre-sonication step, 160 mg of dopamine hydrochloride, purchased from Sigma-Aldrich, was introduced into the water solution. The alkaline conditions, combined with the oxygen in the air, promoted the polymerization of dopamine, resulting in the formation of a PDA layer on the surface of the nanoparticles. The occurrence of the polymerization could be observed by the naked eye, as the color of the solution changes from a brown to a dark hue within a few hours, as shown in Fig. 4.6. In this work, the quantities of deionized water and dopamine hydrochloride were chosen based on literature (2 mg of dopamine per milliliter of 10 mM tris, pH 8.5)[112], allowing us to establish a reference for the functionalization layer thickness as a function of the reaction time, as previously presented in Chapter 2.2.2 and visible in Fig. 2.13. Results and discussion can be found in Chapter 7.1.

Once the desired functionalization thickness was achieved, the BTO$^{(C)}$@PDA nanoparticles were separated from the solution through centrifugation (see Fig. 4.7a). After centrifugation, the collectible nanoparticles could be observed settled at the bottom of the glass, as shown in Fig. 4.7b. The collected powder was then washed with isopropanol and centrifugated three times for 2 minutes each at 5000 rpm to further remove any residual dopamine within the supernatant. Finally, the nanoparticles underwent a drying process for 24 hours at room temperature in the glovebox with a RH of roughly 10%.

The nanofillers provided by Shanghai University were instead an already prepared mixture of CCNF-BTO@PDA. The CCNF, with a solid content of 3% in weight, was obtained

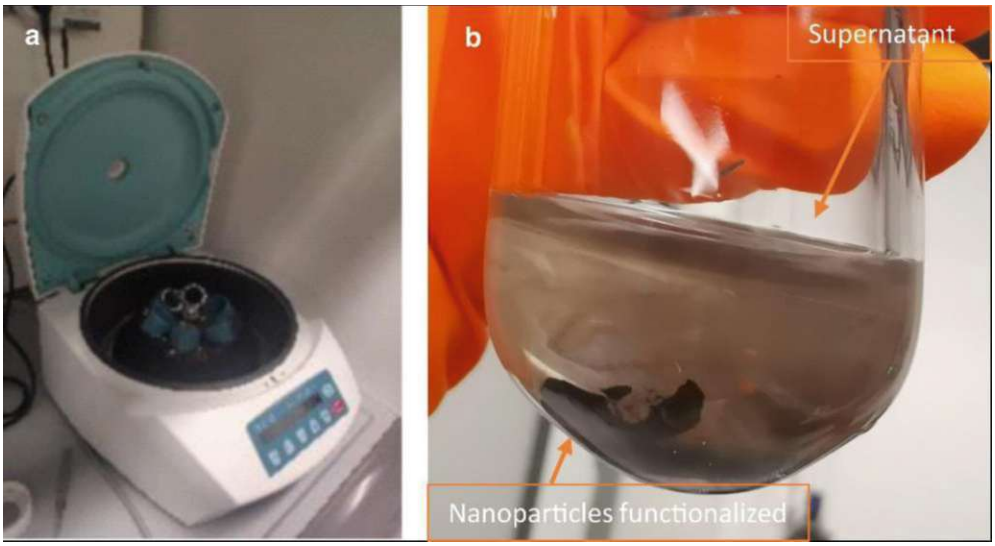

Figure 4.7 a Centrifuge used to separate the commercially purchased and functionalized nanoparticles (BTO$^{(C)}$@PDA) from the aqueous solution and reagent residuals. **b** The BTO$^{(C)}$@PDA powder, deposited at the bottom of the centrifuge tube, was separated from the supernatant.

via ammonium persulfate (APS) oxidation method by using cotton fiber as source materials[189]. In this case, the BTO nanoparticles powder was prepared by a hydrothermal method[190] and presented an average size of 145 nm, as shown in Figs. 4.8a and b. The BTO nanofillers were functionalized with PDA in a tris buffer solution at a pH value of 8.5 prepared with Tris (hydroxymethyl) aminomethane, bought from Adamas Reagent Com, and deionized water. The functionalization has been performed using dopamine hydrochloride obtained from Sinopharm Group Chemical Reagent Co. The functionalized BTO nanoparticles were separated from the liquid 5 times by high-speed centrifugation for 10 minutes, and the upper liquid of the BTO@PDA solution was removed, similar to what is shown in Fig. 4.7b. The wet sediment composed of BTO@PDA at the bottom of the centrifuge tube was further treated by sonication for 1 hour and then transferred to the CCNF solution by intensive mixing with magnetic stirring for 12 hours. Subsequently, the CCNF-BTO@PDA wet sediments were obtained by washing and centrifuging with deionized water for 5 minutes at 10000 rpm twice. An exemplified schematic process of the synthesis of the nanofiller mixture

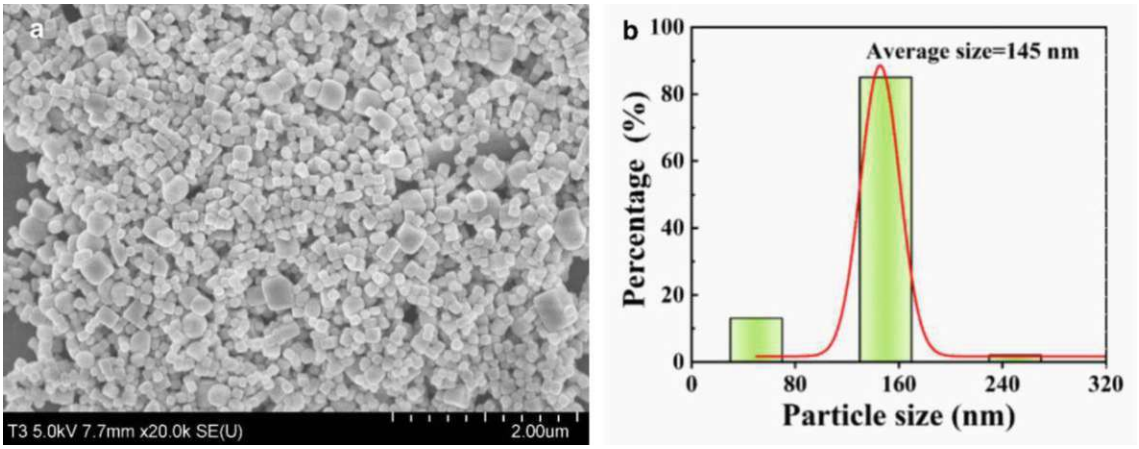

Figure 4.8 a SEM image of the BTO nanoparticles provided by Shanghai University and **b** their particle size distribution determined by Nano Measurer[150].

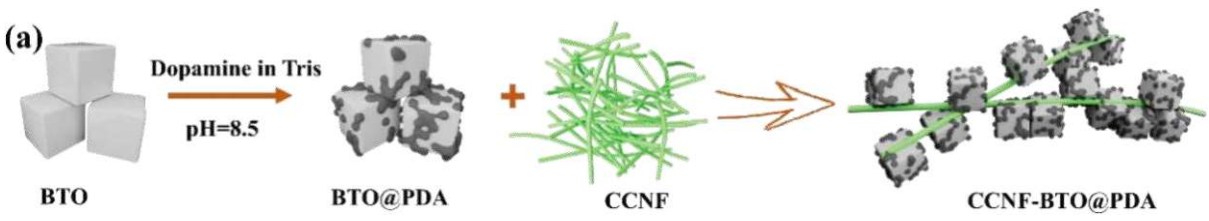

Figure 4.9 Schematic process of synthesizing the CCNF-BTO@PDA nanoparticles mixture, as provided by Shanghai University: first the BTO nanoparticles were functionalized with PDA in a Tris buffer solution and afterwards mixed with the CCNF[150].

CCNF-BTO@PDA is presented in Fig. 4.9. The nanofillers were then collected and delivered to our research group dispersed in MEK.

Once both BTO$^{(C)}$@PDA and CCNF-BTO@PDA nanoparticles were prepared, the subsequent step involved their integration into the P(VDF-TrFE) polymer solution to finally deposit P(VDF-TrFE)-based nanocomposite thin films. The following chapter provides a comprehensive description of the synthesis process for P(VDF-TrFE)-based nanocomposite thin films.

4.2.2 Synthesis of nanocomposite thin films

Similarly to the synthesis of pure PVDF and P(VDF-TrFE) thin films, P(VDF-TrFE)-based nanocomposite thin films were prepared via spin-coating on silicon wafers. This process was conducted to investigate the influence of nanofillers on the structural characteristics and crystalline phase of the polymer matrix. Optical microscopy, FTIR, and XRD were applied for analysis.

A crucial consideration before depositing nanocomposite thin films involves selecting the appropriate quantity of nanoparticles to introduce into the polymer solution typically expressed as volume fraction v_f or weight fraction w_f. In this study, the objective is to enhance energy storage characteristics, so the chosen v_f or w_f aimed to increase permittivity while minimizing any significant reduction in the electric breakdown field.

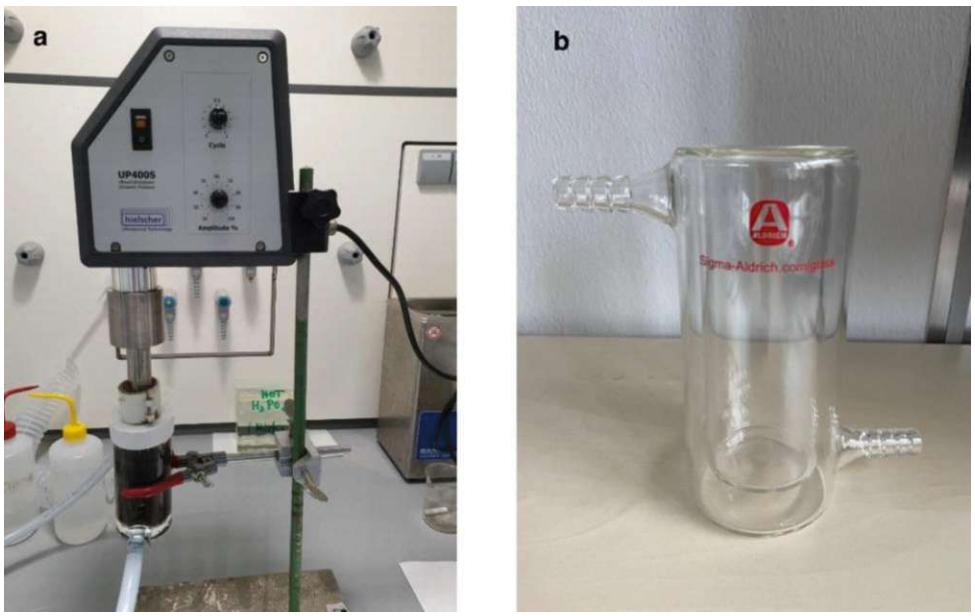

Figure 4.10 a Ultrasonication process with a UP400S from Hielscher acting on the polymer solution with nanoparticles in a double-walled glass contained with water cooling capability, represented in **b**.

To deposit nanocomposite thin films, P(VDF-TrFE) was employed as a polymer matrix. The procedure outlined in Chapter 4.1.1 was utilized to prepare the P(VDF-TrFE) polymer solution, after which the desired v_f or w_f of nanoparticles was added. The nanoparticles used in this study, as mentioned before, included commercially purchased BTO$^{(C)}$ functionalized with PDA and the CCNF-BTO@PDA mixture provided by Shanghai University. It should be noted that in literature v_f is commonly applied for inorganic nanoparticles, while w_f is typically used for organic nanoparticles, where determining density is more challenging, such as with the CCNF-BTO@PDA mixture. Therefore, v_f was used for the BTO$^{(C)}$@PDA, and w_f was used for the CCNF-BTO@PDA mixture.

Once the nanoparticles were introduced into the P(VDF-TrFE) solution, they were dispersed by sonicating for 1.5 hours. The setup, presented in Fig. 4.10a, involved placing the solution inside a glass vessel equipped with a mantel jacket (see Fig. 4.10b). This jacket allowed a water-cooling system, supplied by city water, to regulate the solution's temperature during sonication, preventing MEK evaporation. Excessive temperature increases in fact could cause the solvent to reach its boiling point, leading to evaporation. This would have increased the solution's viscosity, thus making the dispersion of the nanofillers more difficult.

After sonication, the nanocomposite thin film was deposited via spin-coating at 1000 rpm, following a procedure similar to that used for pure P(VDF-TrFE) thin films as described in Chapter 4.1.1. The resulting homogenous thin film was then annealed for 2 hours at 140 °C and then cooled down to room temperature. Both spin-coating and annealing were carried out under humidity-controlled conditions in the custom-built glovebox (see Fig. 4.3) to prevent VIPS and to ensure the reproducibility of layer quality[187]. The final film thickness was measured to be 1.8 ± 0.2 µm for each sample using a DEKTAK surface profilometer.

For this work, various volume and weight fractions were added to the P(VDF-TrFE) solutions, ranging from 0.5% to 15%. However, enhanced energy storage characteristics were observed for percentages above 5%, specifically in thin films loaded with the nanofiller mixture CCNF-BTO@PDA. Chapter 7 discusses the findings and characterization regarding P(VDF-TrFE)-based nanocomposite thin films in detail.

4.2.3 Fabrication of capacitor-type test structures

For determining the energy storage characteristics of the P(VDF-TrFE)-based nanocomposite thin films, micromachined capacitor-type test structures were used. Therefore, metal-ferroelectric-metal (MFM) structures based on P(VDF-TrFE)-based nanocomposite thin films, deposited according to the process exposed in Chapter 4.2.2, were fabricated as described in Chapter 4.1.2 using a 4" (100) Si wafer with 500 nm thermal silicon dioxide (SiO_2) as substrate. The introduction of nanofillers in the matrix generally acts as pre-defined impurities, which could lead to premature electric breakdown of the nanocomposite material. In 2 μm thick thin films, surface and bulk defects can have a significant impact on the device performance compared to thicker films. As a result, the diameters of the capacitors used for the nanocomposite thin films were slightly adjusted compared to those used for pure P(VDF-TrFE) thin films, with diameters ranging from 1 mm to 8 mm being explored. The dispersion process is generally considered random, and as the v_f or w_f of nanofillers increases, the probability of encountering clusters within the electrodes, potentially compromising the performance of the entire capacitor, also increases. Large capacitor diameters, such as those used for pure PVDF and P(VDF-TrFE) thin films, offer the potential for high-quality measurements but are more prone to premature breakdown voltage due to the higher likelihood of encountering large clusters. Conversely, smaller capacitor diameters are expected to reduce the likelihood of including clusters within the electrodes. However, they exhibited poor ferroelectric performance, compromising both the functionality and the measurability of the ferroelectric properties. Ultimately, a capacitor diameter of 5 mm was adopted for electrical and energy storage characterizations for P(VDF-TrFE)-based nanocomposite thin films, balancing the need for reliable measurements with the risk of defects. Chapter 7 delves into detail on the topic, providing measurements and an explanation of the process.

5 Characterization Techniques

5.1 Microstructural characterization

The microstructural characterization of PVDF and P(VDF-TrFE) spin-cast thin films is a crucial aspect of this study, particularly due to the diverse surface morphologies that P(VDF-TrFE) thin films may exhibit. The crystallization process of the copolymer P(VDF-TrFE), as previously mentioned in Chapter 2.1.2, is significantly influenced by the annealing temperature, resulting in the formation of either a rice-like or a spherulite-like microstructure (see Chapter 6.1.2 Fig. 6.8). In this thesis, the effects of these variations on the final electroactive properties are investigated, thus necessitating a comprehensive examination of those microstructures.

Optical microscopy, with its ease of use, serves as a primary tool for identifying the microstructure of the polymer thin films after annealing. The micrometre-scale spherulite structure of PVDF can be easily identified by employing optical microscopy, as presented in Fig. 5.1a. However, due to the potential for P(VDF-TrFE) to exhibit two distinct microstructures, the structural properties of P(VDF-TrFE) cannot always be revealed with optical microscopy alone. Spherulite-like and rice-like microstructures feature different crystalline domain sizes. While the former consists of spherulite-shaped crystalline domains,

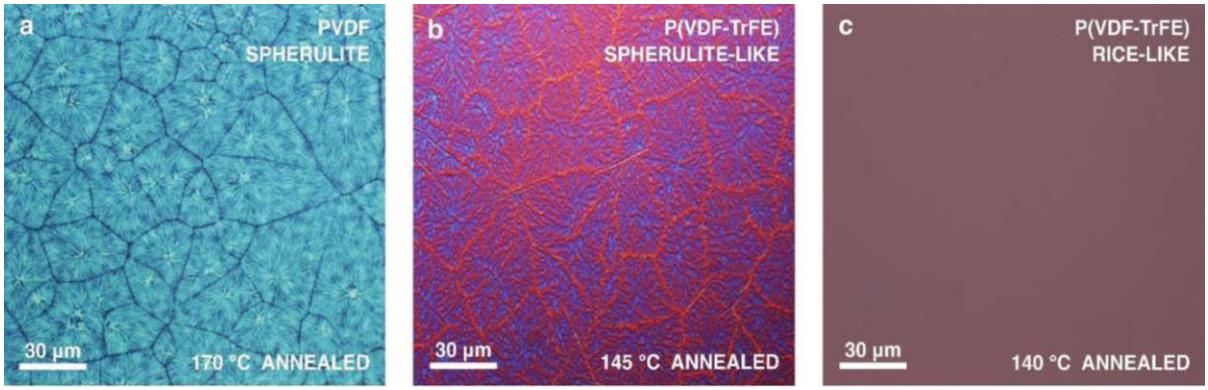

Figure 5.1 Optical microscope images of **a** PVDF spherulite, **b** P(VDF-TrFE) spherulite-like, and **c** P(VDF-TrFE) rice-like microstructures. The crystalline domains of P(VDF-TrFE) rice-like microstructure are too small to be detected with visible light, highlighting the limits of optical microscopy. These limitations emphasize the need for more advanced instruments, such as AFM.

resembling the spherulite structure of PVDF and visible under optical microscopy as shown in Fig. 5.1b, the latter features rice-like crystalline domains that are too small to be detected by optical microscopy (see Fig. 5.1c).

Beyond crystalline domain characteristics, a first examination by optical microscopy is fundamental to evaluate the quality of the ferroelectric polymer surface. The presence of impurities, VIPS phenomena (see Chapter 6.1.1), or pin holes formed during spin-coating may lead to poor performances or short-circuited capacitors. Furthermore, in the case of P(VDF-TrFE)-based nanocomposite, optical microscopy provides an evaluation of whether the nanoparticles have been homogenously dispersed within the polymer matrix, as discussed in detail in Chapter 7.2.

For higher quality and detailed studies of the PVDF and P(VDF-TrFE) thin film surface microstructure, atomic force microscopy (AFM) measurements were conducted. The AFM instrument utilized in this work was a Dimension Edge from Bruker, and for imaging the tapping mode with a silicon cantilever (NCHV-A, Bruker, f_1 = 320 kHz, k_1 = 40 N·m^{-1}) was used. AFM imaging provided clear visualization of both P(VDF-TrFE) microstructures, facilitating a comparison with PVDF surface morphology. Further discussion of these observations is provided in Chapter 6.1.2. Moreover, this study additionally includes a high-resolution AFM phase image depicting the chain organization within a PVDF spherulite at the sub-nanometre scale (see Fig. 6.4b). The AFM phase image here presented was performed at the Institute of Materials Science of Madrid and was obtained by operating in the amplitude modulation mode[191], employing small oscillation amplitudes ranging from 100 to 500 pm applied to the cantilever. Previous studies have demonstrated that small and ultra-small amplitudes enable the acquisition of molecular resolution images of polymer thin films[192]. Operating with small amplitudes enhanced sensitivity to short-range interaction forces, thereby providing higher spatial resolution. The experiments utilized PPP-FM-AuD cantilevers (NanoAndMore, Germany) driven in their second flexural mode with typical parameters f_2 = 448 kHz, k_2 = 158 N·m^{-1}, and Q_2 = 575.

Since one of the primary focuses in the characterization of P(VDF-TrFE)-based nanocomposites was the analysis of the nanofillers, scanning electron microscopy (SEM) was used for this purpose. Unlike techniques reliant on cantilever deflection or visible light imaging, SEM utilizes a beam of electrons to probe samples and generate images, necessitating

high vacuum conditions. Upon interaction with the sample's atoms, the electrons generate various signals including the emission of secondary electrons, back-scattered electrons, and X-rays, providing information about surface topography and chemical composition. SEM predominantly uses secondary electrons for imaging due to their low energy and limited mean free path within the sample, resulting in high resolution in the range of 10 nm. Back-scattered electrons and X-rays are utilized in energy-dispersive X-ray analysis (EDX), which enables the identification of the chemical elements within the sample. In this work, an SEM from Hitachi SU8030 was used for high-resolution imaging, typically applying an acceleration voltage between 2-5 kV with a current between 2-10 µA. To study the characteristics of the nanofillers under high vacuum conditions, the nanoparticles were affixed to a silicon substrate using Aquatar. Aquatar is a water-based anti-reflective coating commonly employed in the semiconductor industry. In this study, it was applied by spin-coating onto a silicon wafer at 5000 rpm to form a nanometer-thick film layer. The Aquatar layer was then soft-baked at 90 °C for 30 seconds to partially evaporate the solvent and promote the adhesion to the silicon wafer. This process created a sticky surface onto which the nanoparticles, previously sonicated in isopropanol to break up any agglomerates formed by physical bonding, were deposited before SEM analysis. SEM imaging served to examine nanoparticle characteristics, including the imaging of $BTO^{(C)}$ and BTO particles, the detection of any agglomerates, and an initial assessment of the PDA functionalization.

In Chapter 2.2.2, the process of PDA functionalization on the nanofiller surface and its dependence on reaction time were introduced. For a detailed analysis of functionalization layers, transmission electron microscopy (TEM) is typically the most appropriate technique. TEM uses a beam of electrons that passes through electromagnetic lenses to ensure coherence and uniformity. The electrons are then transmitted through an ultra-thin specimen, providing detailed information about the internal structure of the material at atomic and nanoscale levels by analysing the scattering and absorption of the electrons by the sample. In this study, a FEI TECNAI TF 20 with X-FEG and GATAN Rio16-CMOS camera was employed. For local carbon mapping, a GATAN GIF Tridiem Energy filter was used, and a three-window method was applied. For conducting the study, the nanofillers were placed on a lacy carbon grid.

5.2 Crystalline phase characterization

The ferroelectric characteristics of PVDF and P(VDF-TrFE) thin films, as well as the energy storage characteristics of the P(VDF-TrFE)-based nanocomposite thin films, are strongly correlated to the conformation assumed by the polymer chains. Therefore, identifying the polymorphs (α-, β-, γ-, δ-phase, see Chapter 2.1.2) present within the synthesized polymer thin films is crucial. To achieve this, both Fourier-transform infrared spectroscopy (FTIR) and X-ray diffraction (XRD) techniques were used.

FTIR spectroscopy analyzes the infrared-active spectrum of a sample to identify its vibrational modes, thus allowing it to conclude the binding situation of the chemical elements when their presence is known in advance. This technique relies on the absorption of infrared radiation by chemical bonds, specifically the vibrations within the molecules at specific frequencies. The resulting absorption pattern provides a spectrum divided into two regions: one representing the functional groups and the other known as the fingerprint region. The fingerprint region is crucial for identifying the chain conformation and hence, the phase present in the polymer. In this study, an FTIR Tensor 27 from Bruker was used for characterizing both pure ferroelectric polymers PVDF and P(VDF-TrFE), as well as P(VDF-TrFE)-based nanocomposites.

XRD served as the second measurement technique used in this thesis to characterize crystalline structures. In this method, X-rays are generated by a cathode ray tube, filtered to produce monochromatic radiation, collimated to concentrate, and then directed toward the sample. The technique relies on the principle that when X-ray beams interact with the lattice planes in a crystal, they undergo diffraction, producing a characteristic pattern of constructive interferences. This phenomenon is governed by Bragg's law, which describes the conditions under which constructive interference of the diffracted X-rays occurs:

$$2d\sin(2\theta) = n\lambda \tag{5.1}$$

where d is the lattice distance, θ is the incident angle, n is an integer number, and λ is the wavelength of the X-rays. In this work, an X-ray diffractometer X'Pert Pro from Molvern Panalytic in Bragg-Brentano configuration was employed, with a Cu-$k_{\alpha1\text{-}\alpha2}$ source at wavelengths of 1.540598 Å and 1.544426 Å, respectively. The pattern obtained from the measurement, known as the diffraction pattern, is used to identify the crystalline structure of

the material and determine its lattice parameters. In XRD, silicon and gold-covered substrates, commonly used in this work, provide high-intensity diffraction peaks, which can interfere with the analysis of the polymer crystalline phase. For this reason, the investigation was limited to the angles of interest of PVDF and P(VDF-TrFE) chain conformations, typically ranging between 2θ values of 16° and 30° for the pure ferroelectric polymer thin films. For the P(VDF-TrFE)-based nanocomposite thin films instead, the 2θ range was expanded up to 60° to enable the detection of peaks associated with the nanofillers.

5.3 Thermoanalytical technique

Thermoanalytical techniques are widely used in polymer engineering since they provide valuable insights into phase transitions, thermal transitions, such as melting and glass transition points, the presence of impurities, as well as decomposition. In this work, the thermoanalytical technique employed was differential scanning calorimetry (DSC). This technique involves recording and plotting the difference in heat flow between the sample and a selected reference material as they are heated or cooled at a controlled rate. The reference material is chosen primarily for its stability and suitability within the desired temperature operating range. DSC operates on the principle that alterations in the physical or chemical state of a material lead to either absorption or release of heat. Consequently, when a material undergoes a physical transformation like glass transition, melting, or crystallization, there are corresponding changes in enthalpy, which are reflected in characteristic peaks on the DSC curve. Position, shape, and area under the peaks provide information about the transition temperature, enthalpies, and kinetics. In this thesis, a DSC 250 from TA instruments was used with a ramp of 10 °C·min^{-1} up to 250 °C to determine the melting temperature (T_m) of the rice-like and spherulite-like P(VDF-TrFE) microstructures. Results and discussion can be found in Chapter 6.1.2.

5.4 Ferroelectric characterization

PVDF and P(VDF-TrFE) show highly non-linear dielectric characteristics, as discussed in Chapter 3. Specifically, when exposed to an alternating electric field, they exhibit a hysteresis loop in polarization or displacement, revealing two remnant polarization states. Accurately determining the values of these polarization states and plotting the hysteresis loop is crucial for device applications and technology advancements. In this thesis, to evaluate the ferroelectric properties of the polymer and nanocomposite thin films, a custom-built Sawyer-Tower circuit[47,193,194,195] was utilized together with an MFM capacitor incorporating the material under investigation.

The Sawyer-Tower circuit is a setup that utilizes a linear reference capacitor with a known capacitance $C_R = 1$ µF to measure the non-linear dielectric properties of the MFM capacitor through its capacitance C_S. The fabrication processes of MFM devices for both pure ferroelectric polymers and P(VDF-TrFE)-based nanocomposites are detailed in Chapter 4.1.2 and Chapter 4.2.3, respectively. Fig. 5.2a illustrates the circuit diagram of the Sawyer-Tower circuit. Using a KEYSIGHT 33600A function generator, an AC voltage at a frequency of 100 Hz was applied to the two capacitors connected in series, the MFM capacitor and the reference capacitor. Due to the necessity of high field strengths (up to 200 V·µm^{-1}) for the characterization, the function generator's signal was amplified through a TREK 2100HF amplifier with a fifty-fold gain. The applied electric field induced electric polarization on both capacitors, which was compensated by the free charges at the electrodes. Since the capacitors were connected in series, the charge Q_S stored in the MFM capacitor and Q_R stored in the reference capacitor must be identical at the electrostatic equilibrium:

$$Q_S = Q_R \tag{5.2}$$

In general, a capacitor's charge is directly proportional to the voltage drop, so for both capacitors was valid:

$$Q_S = U_S C_S \qquad Q_R = U_R C_R \tag{5.3}$$

By combining equations (5.2) and (5.3), the following relationship is obtained:

$$Q_S = Q_R \rightarrow \frac{U_R}{U_S} = \frac{C_S}{C_R} \tag{5.4}$$

The reference capacitance C_R was chosen such that $C_R >> C_S$, considering that the capacitance C_S of the MFM capacitor typically falls within the nanofarad range. It should be noted that, despite the capacitance of the MFM capacitor is not constant as a function of the applied voltage, the previous comparison must always hold, regardless of the voltage applied. Therefore, according to equation (5.4), the voltage drop at the sample U_S must be much higher than that at the reference capacitor U_R, *i.e.* $U_S >> U_R$. Hence, U_S can be considered nearly equal to the amplified supply voltage. Consequently, the electric field E applied to the ferroelectric thin film is given by the equation:

$$E = \frac{U_S}{t} \tag{5.5}$$

where t is the distance between the capacitor plates, *i.e.* the thickness of the polymer thin film. To avoid high voltage measurements by the oscilloscope, a voltage divider consisting of two resistors R_1 = 1 kΩ and R_2 = 10 kΩ was used. Knowing that the same voltage must drop across

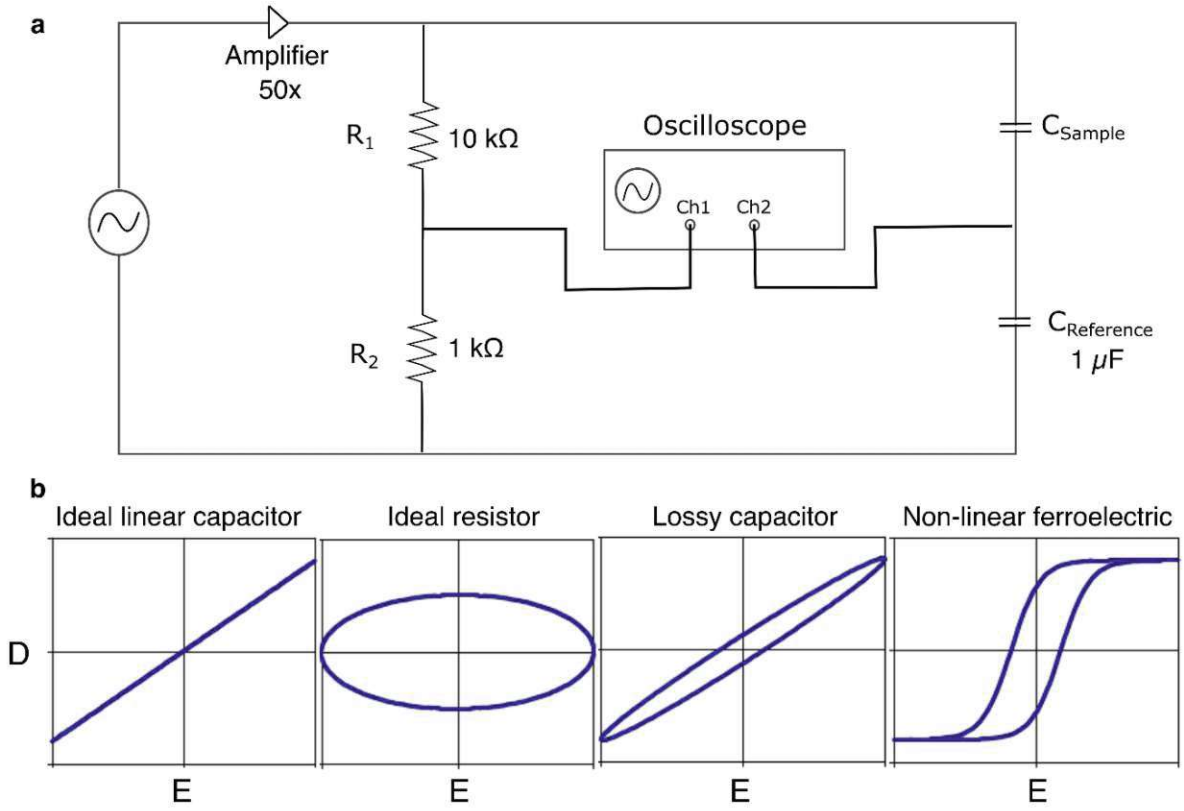

Figure 5.2 a Schematic diagram of the Sawyer-Tower circuit, consisting of two resistors R_1 = 1 kΩ and R_2 = 10 kΩ, serving as a voltage divider, a reference capacitor with C_R = 1 μF and the MFM capacitor (C_{Sample}) containing the ferroelectric polymer under investigation. **b** Typical ferroelectric responses of MFM capacitors which can be measured using a Sawyer-Tower circuit.

the resistances and the capacitors since they are in parallel, the voltage at channel 1 *CH1* of the oscilloscope is obtained as follows:

$$U_{CH1} = \frac{R_1}{R_1+R_2}\,(U_S + U_R) \tag{5.6}$$

Considering that $U_S >> U_R$ and assuming a homogenous applied electric field within the capacitor plates, equation (5.6) with equation (5.5) can be semplified to:

$$U_{CH1} \approx \frac{R_1}{R_1+R_2}\,E\,t \tag{5.7}$$

Therefore, the electric field across the ferroelectric thin film can be expressed as:

$$E = \frac{R_1+R_2}{R_1\,t}\,U_{CH1} \tag{5.8}$$

To obtain the displacement of the MFM capacitor, the voltage at channel 2 *CH2* of the oscilloscope was observed. The voltage U_{CH2} is equal to the voltage drop U_R at the reference capacitor. Given the generalized equation for the capacitance of a parallel plate capacitor:

$$C_S = \frac{\varepsilon_0 \varepsilon_r A}{t} \tag{5.9}$$

where A is the area of the MFM capacitor, using equations (5.4), (5.5), and (5.9), the voltage U_{CH2} can be expressed as:

$$U_{CH2} = U_R = U_S\,\frac{C_S}{C_R} = \varepsilon_0 \varepsilon_r \frac{A\,E}{C_R} \tag{5.10}$$

According to Gauss's law of the Maxwell equation, the density of free charges at the electrodes of the MFM capacitor is equal to the electric displacement D of the ferroelectric material. The Sawyer-Tower circuit aims to measure the non-linear response of D through the linear reference capacitor C_R, which is independent of U_R. Since the stored charge of the reference capacitor is equal to the stored charge in the ferroelectric material, as expressed in equation (5.2), the electric displacement of the sample is determined by:

$$D = \frac{Q_S}{A} = \frac{Q_R}{A} = \frac{C_R U_R}{A} = \frac{C_R}{A}\,U_{CH2} \tag{5.11}$$

By combining equations (5.10) and (5.11), equation (3.4) is obtained.

Finally, using equations (5.8) and (5.11), the displacement D of the ferroelectric thin film can be measured as a function of the applied field E. Essentially, the Sawyer-Tower circuit reveals the characteristic *D-E* hysteresis loop, which, as discussed in hapter 3.2.2, is also

fundamental for investigating the energy storage characteristics of the ferroelectric polymers and nanocomposite thin films. In general, the Sawyer-Tower circuit allows for the measurement of any dielectrics, such as linear dielectrics or paraelectrics. In Fig. 5.2b, typical *D-E* characteristics measured from MFM capacitors are presented. For instance, MFM capacitors with high leakages show a dielectric response that is similar to ideal resistors or lossy capacitors, which often indicates defects within the ferroelectric thin film. In such cases, conducting a successful dielectric study on the MFM capacitor is not feasible.

Referring to equation (3.12), it is important to note that the difference between P and D is not that significant, and typically $P = D$ is a sufficiently good approximation. In this work, apart from conceptual descriptions, there will be no emphasis on the difference between polarization and displacement.

In the characterization of ferroelectric materials, determining the value of parameters like remnant polarization P_r and coercive field E_c from the hysteresis loop is of utmost importance. The empirical model developed by Miller *et al.*[196] aids in this step by fitting the ferroelectric *D-E* hysteresis loop recorded by using the Sawyer-Tower circuit setup. This model represents the spontaneous polarization P_s in the equation (3.12) and distinguishes between two parts of the hysteresis curve: one from negative to positive electric field P_s^+, and the other from positive to negative field P_s^-, such that:

$$P_S^-(E) = -P_S^+(-E) \tag{5.12}$$

For instance, the hysteresis branch P_s^+ fitting equation is given by:

$$P_s^+(E) = P_{max}\tanh\left(\frac{E-E_c}{\delta}\right) + \frac{P_{max}}{2}\left(\tanh\left(\frac{E_{max}+E_c}{\delta}\right) - \tanh\left(\frac{E_{max}-E_c}{\delta}\right)\right) \tag{5.13}$$

where E_{max} is the maximum applied electric field, P_{max} is the maximum electric polarization, and δ is defined as:

$$\delta = 2\,E_c\left(\ln\left(\frac{1+\frac{P_r}{P_{max}}}{1+\frac{P_r}{P_{max}}}\right)\right)^{-1} \tag{5.14}$$

Using equations (5.12), (5.13), and (5.14), the *D-E* characteristic of a ferroelectric material is fitted. Miller's model has been widely used in Chapter 6.2 and Chapter 7.4.3 to model the ferroelectric displacement D as a function of the electric field E. It is noteworthy

that while the AC voltage applied is typically a sinusoidal signal, in this thesis, a triangular waveform is chosen instead to minimize the duration of high voltage amplitudes.

In this thesis, ferroelectric characterizations under different temperatures ranging from room temperature to 90 °C were conducted to investigate the thermal stability and hysteretic response of both the spherulite-like and rice-like P(VDF-TrFE) microstructures, as well as P(VDF-TrFE) nanocomposite thin films (see Chapter 6.2.2.2 and Chapter 7.4.3) To perform such measurements a climate chamber VCL 4006 from Vötsch-Industrietechnik was employed.

In ferroelectric characterization determining the dielectric permittivity is fundamental. For this purpose, a commercial LCR meter (Hioki IM35533-01) was employed. The capacitance of the MFM capacitor was measured at low alternating voltages and the dielectric permittivity ε was subsequently determined from equation (5.9). Moreover, in the studies conducted on P(VDF-TrFE)-based nanocomposite thin films, the dielectric response as a function of frequency, from 100 Hz to 10 kHz, was evaluated using the same setup.

5.5 Electromechanical characterization

The analysis of the electromechanical response in ferroelectric thin films holds fundamental importance for MEMS applications. It facilitates the measurement of piezoelectric coefficients and provides insight into electromechanical phenomena like the electrostrictive effect. When exposed to an alternating electric field, an MFM capacitor exhibits a deflection due to the field-induced strain within the polymer thin film. Given the micrometre thickness of the polymer films, very small vertical displacements, typically in the order of a few nanometres, induced by the driving signal needed to be recorded. In this thesis, the electromechanical characterization has been conducted at low frequencies, specifically at 100 Hz, according to the *D-E* measurements. As a result, the highly sensitive optical lever readout, commonly employed in commercial AFM setups, proved to be a suitable tool for detecting the electrostrain behaviour of PVDF and P(VDF-TrFE) in the low-frequency regime[191,197,198]. It is worth noticing that since piezoelectric and electrostrictive coefficients are not directly related to the energy storage characterization, such electromechanical investigations have been conducted only on pure PVDF and P(VDF-TrFE) thin films.

The process of measuring the electrostrain using an AFM setup is referred to as cantilever-based deflection measurement[47]. In this work, a Bruker Dimension Edge AFM equipped with commercial Nanoworld PNP-TR AFM probes (with a spring constant of 0.32 $N \cdot m^{-1}$) was utilized. These probes feature silicon nitride as both the tip and cantilever material, thereby mitigating any electrical interference typically associated with probes made from more conductive materials like doped silicon, which are commonly used for standard AFM imaging recording (refer to Chapter 5.1). During the cantilever-based deflection measurements, the MFM capacitor was also integrated into the Sawyer-Tower circuit, allowing the ferroelectric characterization of the sample in parallel.

Aligned with the Sawyer-Tower circuit setup, the measurement process involved applying an alternating electric voltage generated by the KEYSIGHT 33600A function generator and amplified by a TREK 2100HF amplifier. The vertical displacement of the capacitor was then recorded and observed through the vertical microcantilever deflection via a laser beam reflection on the backside of the probe. Prior research conducted by our group extensively explored this characterization technique, and a detailed description is provided in the following[52]. First, the deflection needs to be calibrated by recording the deflection signal against the movement of the z-axis positioning element in the scanning head. This step is crucial since it calibrates the sensitivity of the AFM system, which is necessary to accurately measure the deflection of the cantilever. Upon the tip making hard contact with the sample surface, a linear response curve is obtained, as shown in Figs. 5.3a and b. The inverse of the slope of this linear response, known as inverse optical lever sensitivity (InvOLS), was

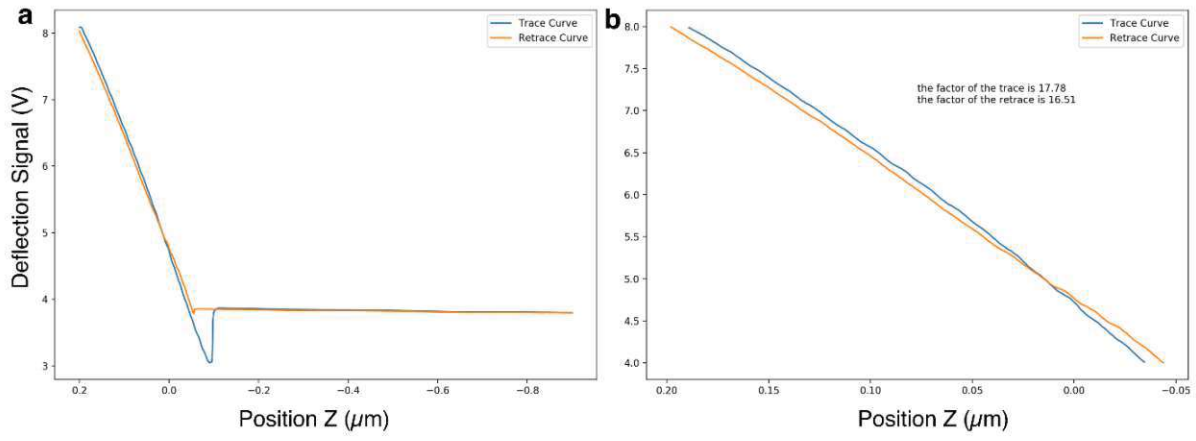

Figure 5.3 a Linear response obtained by recording the deflection signal against the movement along the z-axis for the calibration. **b** Enlarged image of the linear response with the values of inverse of the slope, known as inverse optical lever sensitivity (InvOLS).

extracted and served to convert the voltage signal from the photodetector into vertical displacement in length units. It is important to note that this calibration is sensitive to the compliance of the sample surface against which the AFM probe presses, thereby impacting the measured InvOLS. To avoid significant indentation effects, the silicon wafer surface surrounding the capacitor structure was used to land the probe for determining the calibration factor. After calibration, the probe was retracted and landed in contact mode on the top electrode of the capacitor. The probe was placed in an area close to the centre of the electrode to ensure that any substrate bending during the electrical stimulation of the device remained negligible. Fig. 5.4a displays raw data from a cantilever-based deflection measurement performed on an MFM capacitor while applying an alternating electric voltage. The data is presented as a deflection signal (V) plotted against the tip voltage (V). By using the InvOLS previously calculated, the time-dependent strain behaviour of the MFM was obtained. This is illustrated in Fig. 5.4b, which depicts the strain response to the voltage applied as a function of measuring time. The simultaneous recording of the *D-E* characteristic through the Sawyer-Tower circuit enabled plotting the applied electric field as a function of time as well. By synchronizing the strain recorded from the AFM with the electric field recorded from the oscilloscope (see Fig. 5.5a), the butterfly curve *S-E* was obtained, as depicted in Fig. 5.5b. In general, the mechanical strain is expressed as $S=\Delta l/l_0$ and is calculated as the relative change in thickness of the polymer thin film, where Δl is the variation in thickness from its zero-field value l_0 after initial polarization. To complete the electrostrain study, according to the

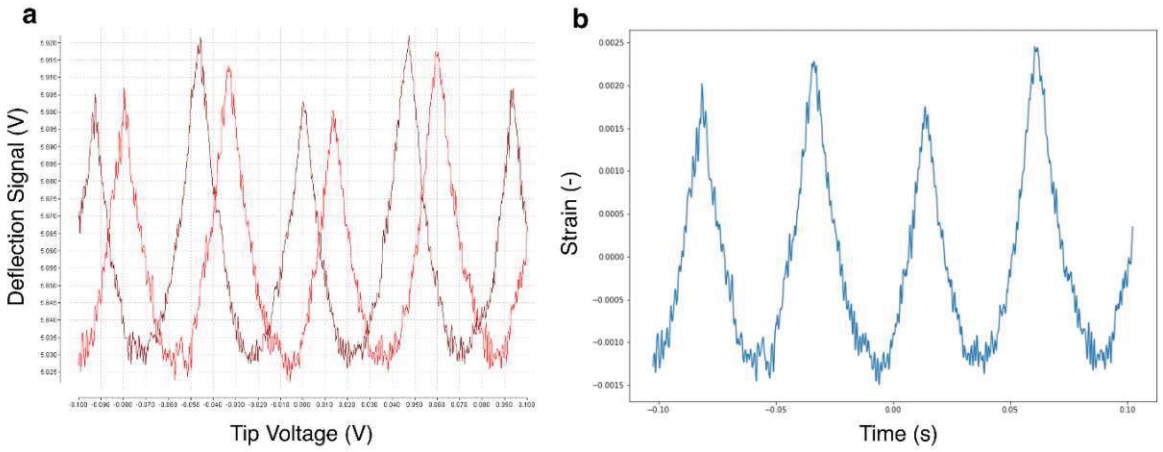

Figure 5.4 a Representation of the raw data measured with the AFM on the MFM expressed as deflection signal (V) against tip voltage (V), afterward converted in appropriate units in **b** where the strain is plotted as a function of time.

equations (3.15) and (3.16) the electrostrictive coefficient Q_{33} and the piezoelectric coefficient d_{33} were then extracted from the *S-E* characteristic.

In addition to the high field electrostrain measurements, the cantilever-based deflection measurement methodology was also employed to measure the electrostrain at low electric fields. After polarizing the ferroelectric thin film with a sufficiently large DC voltage, meaning above the coercivity, a direct measurement of the piezoelectric coefficient d_{33} is possible to perform. By applying an AC voltage, below the coercive field, on the ferroelectric thin film after polarization, a linear *S-E* response is obtained. The slope of this linear curve represents the piezoelectric coefficient d_{33} of the thin film. Moreover, in this thesis, another method for the piezoelectric coefficient calculation is proposed and explained in the following. After polarization through DC voltage as described above, the ferroelectric thin film was subjected to different and increasing DC voltages, below coercivity, while recording the corresponding vertical displacement through AFM. By plotting the corresponding vertical displacement against the DC electric field applied, a linear correlation was obtained, and the slope of this correlation represents the piezoelectric coefficient d_{33}. Further details regarding high field measurements, *i.e.* butterfly response, curve fitting, and electrostrictive coefficient Q_{33}, along with low field measurements for determining the piezoelectric coefficient d_{33} can be found in Chapter 6.2.

Last but not least, it is important to note that the cantilever-based deflection measurements are typically affected by clamping the film onto a rigid substrate. This means

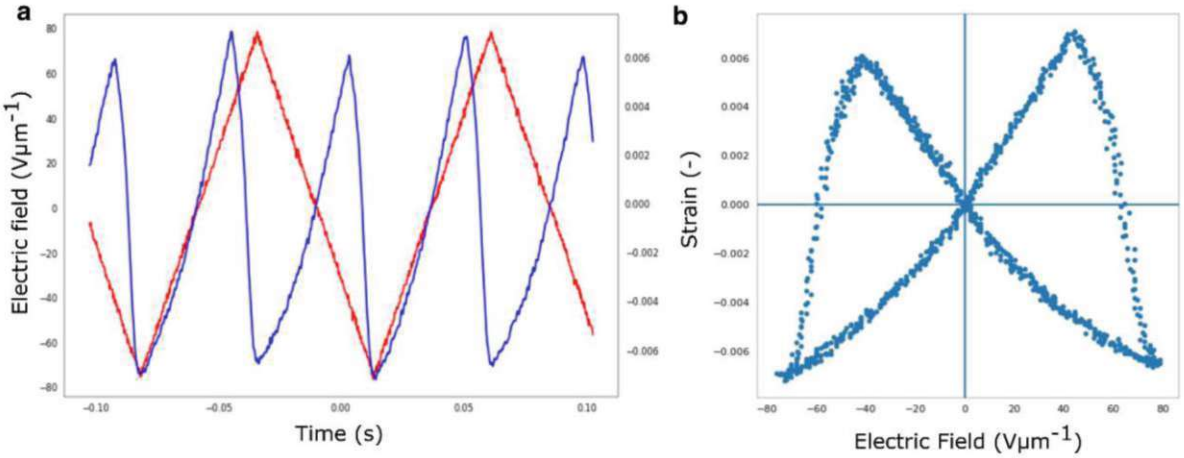

Figure 5.5 a Plot of the AFM recorded deflection signal (blue coloured) expressed as strain, alongside the electric field applied in triangular waveform (red coloured), both plotted as a function of time. **b** Butterfly curve obtained from **a** by plotting the strain as a function of the electric field.

that the clamped film can expand or contract only in the direction perpendicular to the sample surface. Consequently, the electromechanical characterization described here can only yield an effective piezoelectric coefficient. To determine the true piezoelectric coefficient, it is necessary to consider clamping effects[47].

5.6 Electric breakdown field

The electric breakdown field refers to the maximum electric field strength that an insulator can withstand before the formation of a conductive path. As already discussed in Chapter 3.2, the electric breakdown strength is a fundamental characteristic of energy storage devices. The electric breakdown field was measured by applying a step-increasing voltage to the sample while monitoring the current value. When the breakdown occurred, a sudden increase in the current was detected, determining the breakdown voltage. A Süss PM8 manual wafer prober, consisting of a moving chuck for the wafer, a movable microscope, and vacuum-powered needle arm holders (see Fig. 5.6), was employed in conjunction with a Stanford Research Systems PS325 source meter. The source meter has a maximum voltage of 2.5 kV, a minimum voltage of 1 V, a maximum current of 10 mA, and a minimum current of 10 μA, respectively. The testing of MFM capacitors was conducted using a controlled electrical setup interfaced through a GPIB (General Purpose Interface Bus) connection.

To determine the dielectric strength, an I/V measurement was conducted, sweeping between 1V and up to 500V. The applied voltage was ramped up in a loop in 1V steps every 3 seconds to ensure that the sample had enough time to stabilize, allowing for accurate current readings. Given the high voltages required for this measurement, the Stanford Research Systems PS325 was identified as the most suitable and available source meter. However, it is important to note that the measurement is limited by the resolution limits of the minimum and maximum current range. Consequently, the I/V graphs recorded did not show any activity until the breakdown occurred, since the current values below the minimum resolution threshold were not plotted. As illustrated in Fig. 5.7, the current only became visible after the breakdown event. Notably, after the initial breakdown at 650 V, as shown in Fig. 5.7, the I/V graph exhibited gaps in the current readings. This absence of continuous current values, resulting in current peaks, was due to the self-healing phenomenon. Specifically, as the layers of the capacitor get damaged by the high energy, the metallic electrode evaporates at the point

of failure, making further electrical arcs unlikely at that exact location. Therefore, despite the initial breakdown, the capacitor goes back to behaving normally (self-healing), although with reduced general electrical stability and lifetime. As the voltage increased, the capacitor experienced further breakdowns at other points all over the electrode with the current exceeding the minimum detectable range, further leading to the evaporation of more material.

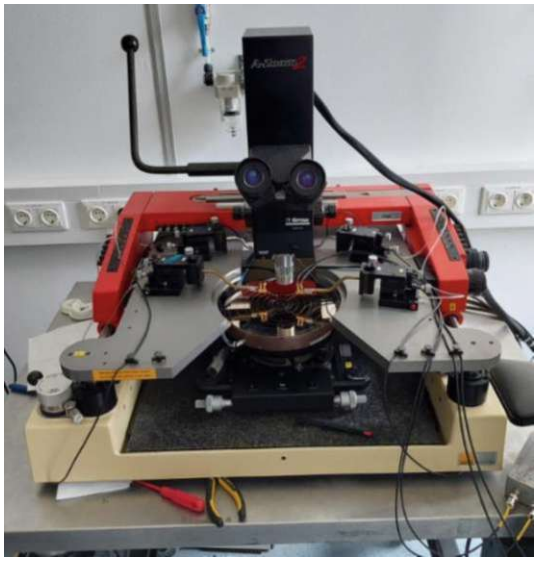

Figure 5.6. Süss PM8 wafer prober for dielectric strength measurements equipped with needles, microscope and movable chuck.

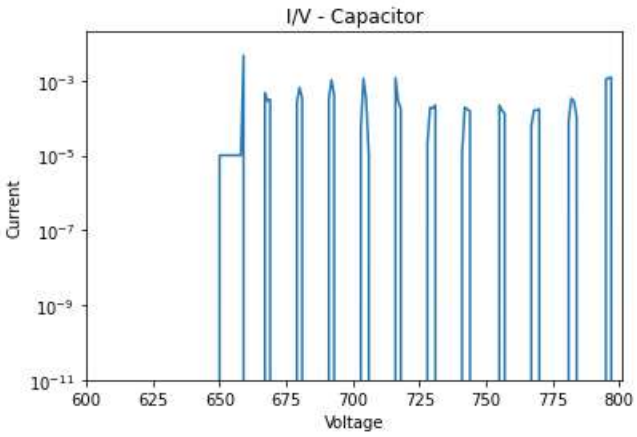

Figure 5.7. I/V measurement of an MFM polymer thin film. The appearance of the first current peak at 650 V indicates the dielectric breakdown voltage of the material. The self-healing phenomenon is evidenced by the presence of consecutive current peaks at higher voltages.

6 Ferroelectric Polymers PVDF and P(VDF-TrFE)

6.1 Crystalline phases and microstructure

Chapter 2.1 introduced the fundamental characteristics of ferroelectric polymer thin films, covering aspects such as crystalline phases and microstructures. Studying these features is a fundamental starting point in ferroelectric characterization since they may significantly influence the final properties of PVDF and P(VDF-TrFE) thin films. This chapter provides an in-depth analysis of the crystalline phases and microstructures, explaining the importance of the fabrication process and its influence on the final thin film characteristics. The findings from this chapter have already been published in references 31, 41, and 49.

6.1.1 PVDF

PVDF exhibits different polymorphs (α-, β-, δ- and γ-phase), each characterized by a different chain conformation (see Chapter 2.1.2). Solution-processed pristine PVDF thin films are typically not ferroelectric, as the α-phase is the most thermodynamically stable[80]. As evidence, in this work, FTIR and XRD measurements were conducted on solution-processed pristine PVDF thin films, fabricated as presented in Chapter 4.1.1. In particular, Fig. 6.1a shows the FTIR spectrum obtained, which exhibits the characteristic bands at 615 cm^{-1}, 764 cm^{-1}, 796 cm^{-1}, 854 cm^{-1}, 976 cm^{-1}, and 1209 cm^{-1} representing the non-polar α-phase absorption peaks[33,199]. Absorption peaks related to γ-PVDF are absent, while a weak absorption band at 1071 cm^{-1} suggests a small presence of β-phase[80,52]. The absorption bands at 876 cm^{-1} and 1184 cm^{-1} are instead less sensitive to chain conformation and are formed by contribution from both α- and β-phase[200]. In addition, Fig. 6.1b depicts the corresponding XRD pattern, fitted using a Split Pearson VII function to extract the peak positions. It identifies peaks at 2θ values of 17.9° and 20.1°, corresponding to the (100) and (110) orientation planes of the non-polar tg^+tg^- α-phase, thus confirming the FTIR findings[201,202,203].

In addition to studying crystalline phases, the characterization of spin-cast α-PVDF thin films also included microstructural analysis. Initially, optical microscopy was used to verify the surface quality and presence of the spherulite characteristics typical for α-PVDF thin films[31,48]. The morphological features may significantly impact device performances: thin films with a cloudy appearance and rough surface typically exhibit poorer ferroelectric activity compared to those with high optical quality and smooth surface topography[187]. In Chapter 4.1.1 the synthesis of spin-cast α-PVDF thin film was presented, emphasizing the usage of substrate preheated at 170 °C during spin-coating to prevent the VIPS, which causes opaque surface appearance[187]. As schematically represented in Fig. 6.2a, during spin-coating at room conditions, water from the air diffuses into the film while DMF evaporates. DMF, being a high boiling point solvent fully miscible with water, undergoes evaporation at a different rate compared to water absorption. This disparity in evaporation and absorption rates during spin-coating leads to variations in film quality and can result in the occurrence of vapor-induced phase separation (VIPS). This phenomenon can be explained utilizing an isothermal ternary phase diagram of PVDF/DMF/H_2O, as presented in Fig. 6.2b[187]. To determine the occurrence of vapor-induced phase separation in a ternary phase diagram, the so-called binodal and spinodal lines play a crucial role (see Fig. 6.2b)[204,205]. The binodal curve represents the boundary between regions where a single homogenous phase is stable and where two immiscible liquid phases coexist in a stable configuration. This boundary is depicted by the left and the right sides, respectively, of the binodal curve in Fig. 6.2b. The spinodal curve, on the other hand, separates regions where two immiscible liquid phases stably coexist and where they do not, leading to a spontaneous phase separation. These

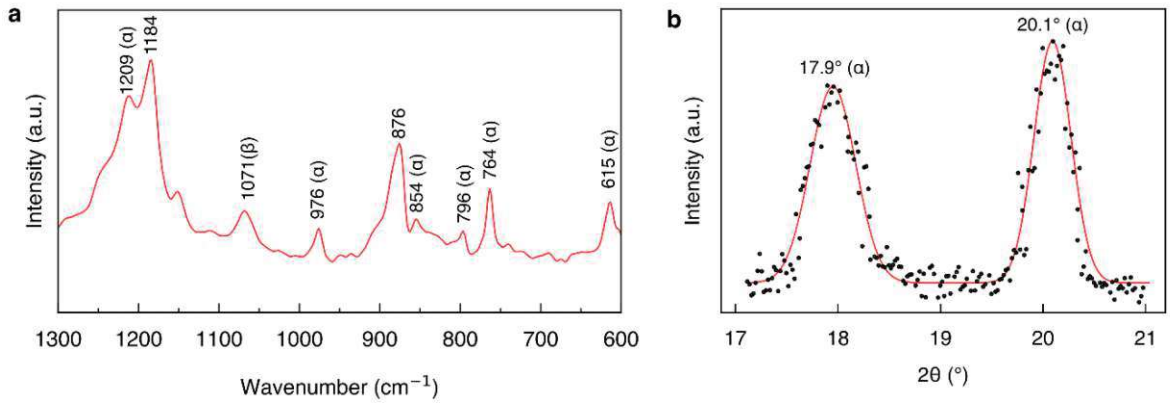

Figure 6.1. a FTIR spectrum (absorbance) and **b** XRD pattern, fitted by a Split Pearson VII, of solution-processed PVDF thin films presenting a predominant non-ferroelectric α-phase[31].

regions can be found in Fig. 6.2b with respect to the spinodal curve on the left side, up to the binodal curve, and on the right side. The pink, purple, and orange lines in the schematic represent three potential concentration evolutions of PVDF/ DMF/H_2O during spin-coating. Each line corresponds to a scenario with different levels of water absorption: low (pink), medium (purple), and high (orange). All scenarios begin with a homogeneous solution and illustrate how varying water absorption rates influence the final thin film morphology at the end of the spin-coating process. For instance, the pink line (low water intake) remains entirely within the single-phase region, avoiding the binodal line. This results in a high-quality homogenous microstructure, as shown in the pink outlined image in Fig. 6.2c. The purple line, representing medium water intake, crosses into the region between the binodal and spinodal lines, leading to a metastable phase. This transition results in a coarse and rough polymer thin film surface, shown in the purple framed picture in Fig. 6.2c. The orange line instead, associated with high water intake, crosses the spinodal line, indicating phase separation and

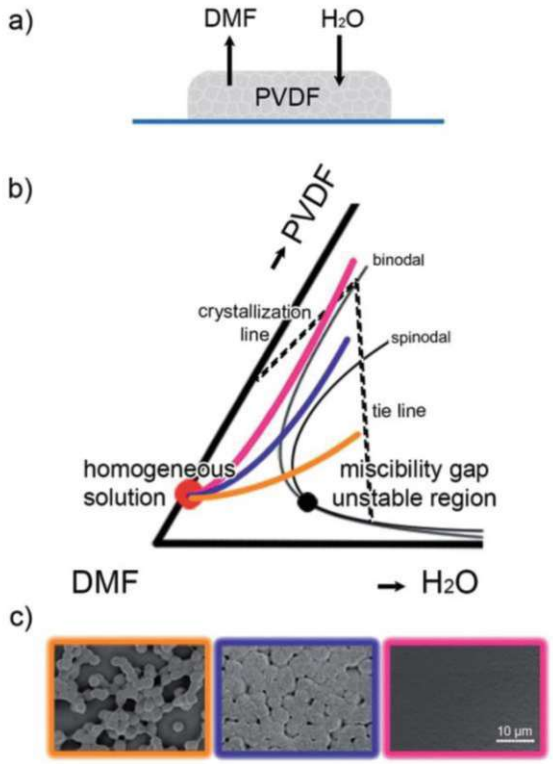

Figure 6.2. a) Illustration depicting water intake and DMF evaporation during PVDF thin film deposition. **b)** Isothermal ternary phase diagram of PVDF/DMF/H_2O, with the starting homogenous solution indicated by the red dot and the three trajectories representing environments at low, medium, and high levels of water absorption during the spin-coating process. **c)** SEM micrographs showing the corresponding morphology of the resulting PVDF thin films according to the three enviroments[187].

resulting in the microstructure depicted in the orange framed picture in Fig. 6.2c. In general, when high boiling solvents like those used for PVDF (*e.g.* DMF) cannot be avoided, smooth thin films can still be fabricated by increasing the substrate temperature. Figs. 6.3a and b present optical micrographs of spin-cast α-PVDF thin films. In Fig. 6.3a, spherulite nucleation is observed, corresponding to the scenario described by the pink line in Fig. 6.2b. In contrast, Fig. 6.3b shows the coexistence of dual immiscible liquid phases, aligning with the purple line in Fig. 6.2b.

Additionally to optical microscopy, a more detailed characterization of the spherulite microstructure was conducted with AFM. In Fig. 6.4a, an AFM height image of a spin-cast α-PVDF thin film is presented, displaying the spherulite crystalline domains in more detail. As discussed in Chapter 2.1.2, within the spherulites, the polymer chains are organized into platelet-like crystals known as lamellae, with a thickness of approximately 10 nm. These lamellae contain the fundamental crystalline unit cell. For α-PVDF, as depicted in Fig. 6.6, the unit cell has lattice constants of a = 4.96 Å, b = 9.64 Å and c = 4.62 Å. These fundamental values were determined through spectroscopy techniques, such as XRD, but never directly observed through a morphological surface map. Fig. 6.4b presents a high-resolution AFM phase image in the sub-nanometre regime, enabling for the first time a direct observation of the polymer chain packing within the lamellae in the crystalline unit cell dimension. More in detail, the image provides a close-up view of the dendrite-like structure typical of the spherulites. This structure is identifiable by the three raised bands pointing in the same direction, where the

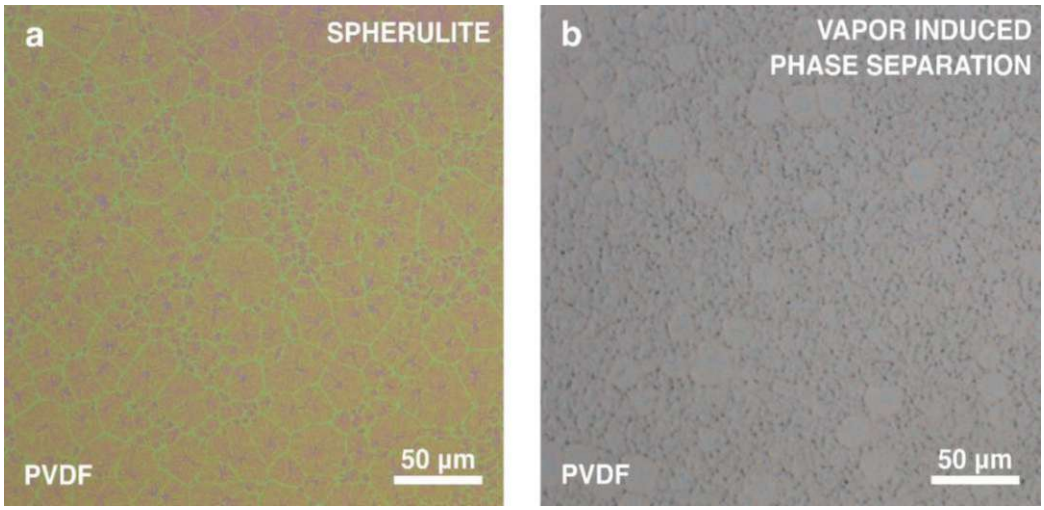

Figure 6.3. Optical micrographs of PVDF thin films deposited **a** on a high-temperature substrate, resulting in a homogenous stable phase, and **b** on a low temperature substrate, resulting a coarse microstructure of the metastable region between binodal and spinodal lines.

polymer chains are placed perpendicularly. The AFM measurement section in the bottom right corner of Fig. 6.4b, indicated by the white line drawn perpendicular to the polymer chains, displays the height profile of the raised band surface, revealing distinct ridges. The half peak-to-peak amplitude width of a representative ridge was measured as an approximation of one polymer chain dimension, resulting in a value of 0.47 nm (equivalent to 4.7 Å). This value aligns with the projection onto the *ab* plane of the α-PVDF crystalline unit-cell[46,206], as shown in Fig. 6.5, where the *a*-value, corresponding roughly to the dimension of a polymer chain, is 4.96 Å. Additionally, the distance peak-to-peak along the y-axis (*x(nm)*) was measured to be approximately 0.98 nm, thereby aligning with the *b*-dimension of the crystalline unit-cell. Given that the crystalline unit-cell has lattice constants equal to $a = 4.96$ Å, $b = 9.64$ Å, and $c = 4.62$ Å, Fig. 6.4b confirms the direct microscopic observation of these unit cell dimensions. Each ridge on the raised band represents therefore a polymer chain packed in parallel within crystalline lamellae. However, due to the semi-crystalline nature of PVDF, the ordered crystals also contain amorphous parts (see Fig. 2.6 in Chapter 2.1.2), resulting in an expected non-periodic and irregular profile. The high-resolution AFM phase image in Fig. 6.4b presented in this work was obtained in previous research conducted by our group in collaboration with the Institute of Materials Science in Madrid[31].

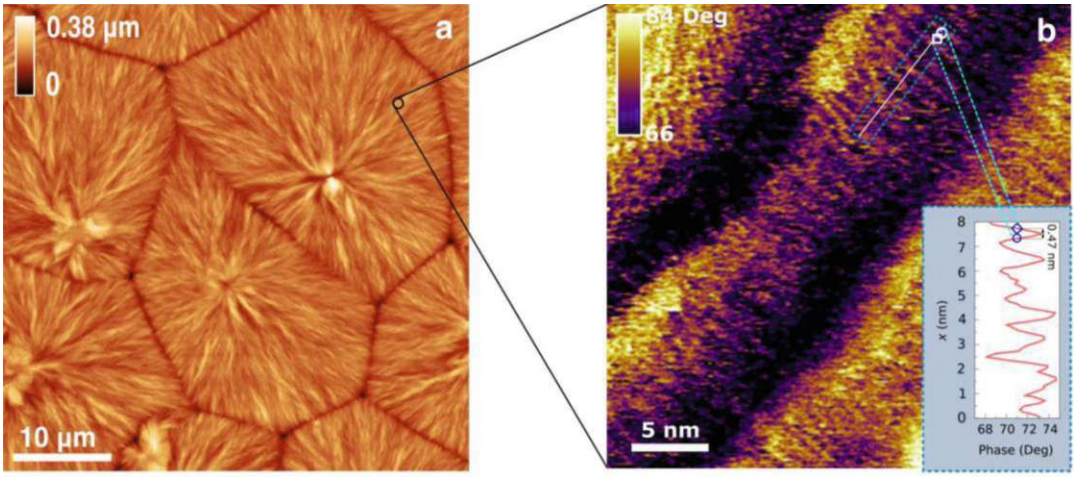

Figure 6.4. a AFM height image was conducted with a scan range of 50 µm, revealing in detail the spherulite microstructure typical of α-PVDFthin films. **b** Close-up view of the PVDF raised bands, depicted through a high-resolution AFM phase image, showing the chain organization within a spherulite at the sub-nanometre scale. The height profile shown in the bottom right corner provides insights into the chain dimension and unit cell values of the polymer thin film[31].

In general, α-PVDF can be converted into electroactive polymorphs through different treatments, such as mechanical stretching, exposure to a high electric field, and temperature and pressure treatments. Among these, electro-forming is particularly effective in inducing the transition from α- to δ-phase. At the molecular level, applying a sufficiently high voltage to the non-polar α-PVDF causes a reversal of the dipole components in every second chain, leading to the molecular packing characteristic of the δ-phase[46]. Fig. 6.6 illustrates the unit cell of both the α-phase and the electro-formed δ-phase, with arrows representing dipole directions. In the α-phase, the arrows point in opposite directions, cancelling each other out and representing its non-polar nature, while in the δ-phase, they align, resulting in a net macroscopic polarization. The reversal of the dipole components during the α-δ transition can occur through various mechanisms, including the reorientation of every second chain by 180° through the propagation of a twist along the molecule, or a 90° rotation about every gauche and gauche minus bond of alternate chains[42,46,207,208,209,206]. As depicted in Fig. 6.6, these reversal phenomena do not affect the molecular conformation and the unit-cell dimensions. δ-PVDF and α-PVDF share the same chain conformation, resulting in no differences in peak positions observed in both FTIR and XRD spectra[80,201,210,211]. As a consequence, it is reasonable to assume that an AFM microscopy-based measurement, similar to that conducted on α-PVDF depicted in Fig. 6.4b, on the δ-PVDF surface would yield the observance of the same crystalline unit-cell values.

Following this section, Chapter 6.2.1 discusses the piezo- and ferroelectric properties of the electro-formed δ-PVDF thin films. This includes electromechanical characterization at both high-field, to explore non-linear electrostrictive behaviour, and low-field measurements, to investigate the linear piezoelectric effect.

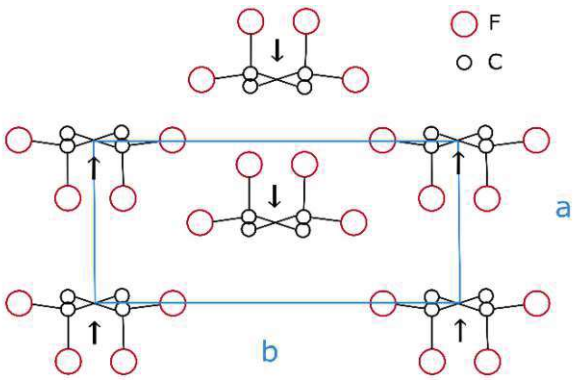

Figure 6.5. c-axis projection of the α-PVDF chain onto the *ab* plane of the unit cell[31].

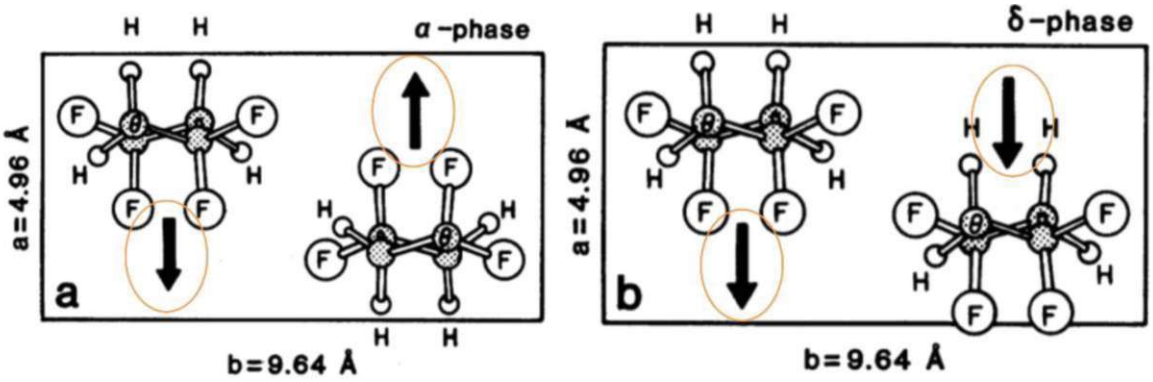

Figure 6.6. Visual representation of the crystalline unit cell of non-polar α-PVDF and electro-formed ferroelectric δ-PVDF with arrows indicating the dipole directions: in α-PVDF, the dipoles cancel each other out, while in δ-PVDF, they align uniformly[29].

6.1.2 P(VDF-TrFE)

P(VDF-TrFE) is a ferroelectric random copolymer composed of VDF and TrFE monomers. Unlike solution-processed PVDF thin films, which typically crystallize in the non-polar α-phase, P(VDF-TrFE) preferentially crystallizes in the highly polar β-phase, similar to β-PVDF. This eliminates any additional treatment needed to convert the α-PVDF into an electroactive phase, making P(VDF-TrFE) a convenient choice for integration into MEMS devices. Additionally, PVDF and P(VDF-TrFE) differ in how they organize their lamellar structure during the crystallization process, resulting in strong morphological distinctions in their microstructure.

Spin-cast P(VDF-TrFE) thin films exhibit varying microstructures depending on the annealing temperature. When annealed at 145 °C, a microstructure characterized by large spherulite-shaped crystalline domains is observed. Figs. 6.7a and b show an optical micrograph and an AFM height image of this morphology. Although this microstructure strongly resembles the spherulites found in α-PVDF (see Fig. 6.7c), the organization at the nanometre scale differs, leading to its classification as a spherulite-like microstructure. In detail, P(VDF-TrFE) spherulite-like features needle-shaped crystals (NSC in Fig. 6.7a), which are absent in the α-PVDF microstructure. Typically, lamellae exhibit "edge-on" orientation, where the polymer backbone is parallel to the substrate, or "face-on" orientation, with the backbone oriented perpendicular to the substrate. These needle-shaped crystals are more likely associated with "edge-on" microcrystalline domains, while spherulite-like microstructure generally displays "face-on" characteristics, which are also linked to a more

irregularly packed structure[59,60,61]. In α-PVDF spherulites, the lamellae are evenly distributed throughout the entire crystalline domain, growing dendrite-like from a central nucleation point (NC in Fig 6.7d) towards the grain boundary (BG in Fig. 6.7d), presenting a high degree of regularity[29]. In contrast, the lamellae in P(VDF-TrFE) spherulite-like crystalline domains grow in a less regular pattern: instead of extending straight from the central nucleation point (NC in Fig. 6.7b) towards the grain boundary (BG in Fig. 6.7b), they form windings structures that are irregularly distributed across the crystalline domain. Another notable difference is the mean surface roughness. The spherulite-like microstructure of P(VDF-TrFE) has a mean surface roughness of 36 nm, compared to 18 nm for the spherulite microstructure of α-PVDF. This slightly rougher surface in the spherulite-like microstructure is likely attributed to the irregular growth of the lamellae.

Instead, when the annealing temperature is lowered to 140 °C, P(VDF-TrFE) thin films present a microstructure characterized by small rice-like crystalline domains. The transition

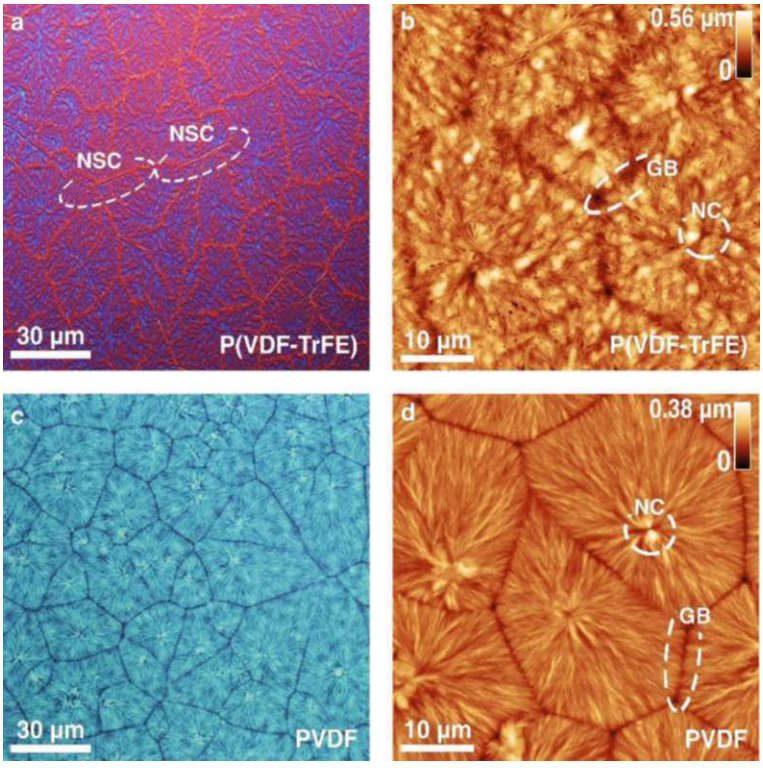

Figure 6.7. a,b Optical micrograph and AFM height image of the P(VDF-TrFE) spherulite-like microstructure. Notable features such as needle-shaped crystals (NSC), nucleation centres (NC), and grain boundaries (GB) are highlighted on the surface. **c,d** Similarly present optical micrograph and AFM height image of α-PVDF spherulite microstructure, showcasing features analogous to those observed in P(VDF-TrFE)[41].

from rice-like to spherulite-like as a function of annealing temperature is illustrated in Fig. 6.8. In general, rice-like domains form when the annealing occurs at temperatures of 140 °C or lower (see Figs. 6.8a, b, c, and d), while the spherulite-like domains emerge at temperatures of 145 °C or higher (see Figs. 6.8e, f, g, and h). Further investigation into any potential mixed states between these two microstructures within the 140–145 °C range was not conducted due to limitations concerning the hotplate used for annealing, which has an accuracy ± 1.5 °C. This lack of precision hindered the ability to accurately monitor and control temperature fluctuation. Accompanying this shift in morphology, changes in surface roughness were observed: thin films annealed at or above 145 °C possessed a mean roughness of approximately 23 nm, while rice-like structures exhibited a mean roughness of about 5 nm. Additionally, unlike spherulite-like domains, the size of rice-like domains was observed to increase proportionally with the annealing temperature, as shown in Fig. 6.9.

Fig. 6.10 presents detailed spherulite-like AFM height images obtained at different scan ranges. Notable morphological features such as central nucleation point (NC), grain boundaries (GB), and needle-shaped crystals (NSC) are highlighted in Fig. 6.10a, similar to Fig. 6.7b. Figs. 6.10b, c, and d display the spherulite-like microstructure with progressively decreasing scan area sizes, offering a more detailed view. By zooming in on the crystalline

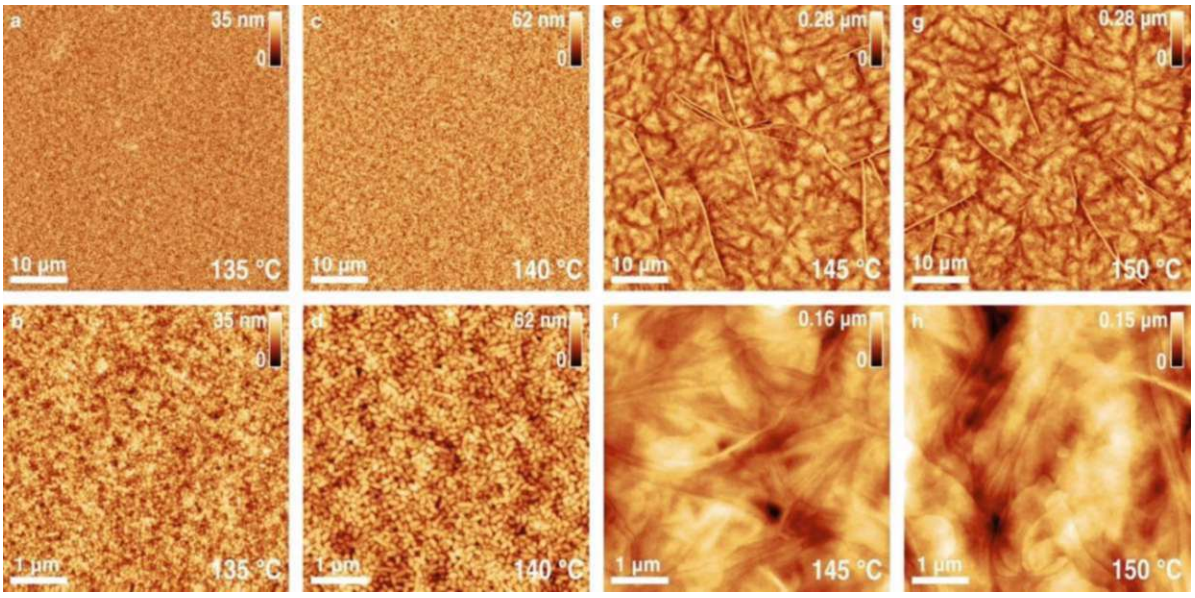

Figure 6.8. AFM height images of P(VDF-TrFE) thin films annealed at different temperatures, revealing the morphological phase transition from rice-like to spherulite-like crystalline domains. **a,b,c,d** Annealed at 135 °C and 140 °C, displaying rice-like domains **e,f,g,h** Transition to spherulite-like microstructure when annealed at 145 °C and 150 °C[41].

features within the single spherulite-like domain, multiple winding-like conformations are observed, indicating the characteristic irregular lamellar growth.

The influence of the fabrication process on P(VDF-TrFE) surface morphology has been extensively explored in literature. For example, D. Singh *et al.* demonstrated that the cooling rate after annealing significantly affects P(VDF-TrFE) microstructure[61]. D. Guo *et al.* showed that ultrathin films (40 nm thick) of P(VDF-TrFE) when annealed at 145 °C and cooled under natural convection to room temperature, exhibit needle-like morphology[60,212]. J.-H. Kim *et al.* reported similar findings for thicker films up to 150 nm, although they did not provide information about the cooling-down conditions[58]. Conversely, D. Mao *et al.* observed a rice-like microstructure in 200 nm thick P(VDF-TrFE) films annealed at 144 °C and cooled down naturally[213]. In general, it is well established that the rice-like microstructure can be obtained in thin films with a thickness ranging between 500 nm and 1 μm when annealed at 140 °C. However, a precise point of morphology transition is not specified, as it seems that various factors such as cooling rate, film thickness, and fabrication conditions may influence this transition. In general, the formation of spherulite-like crystals is likely related to a melt-

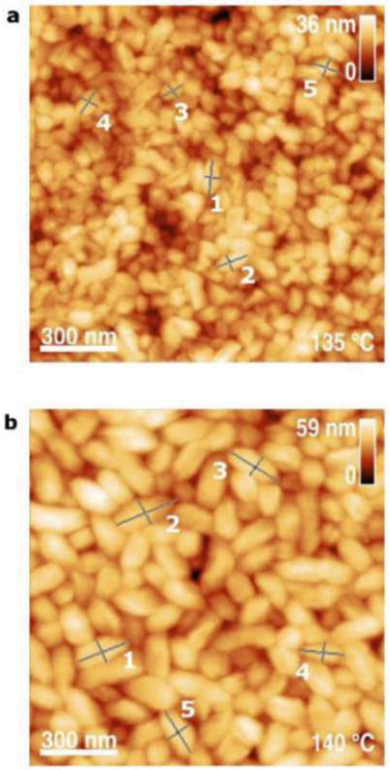

Grain	Length (nm)	Width (nm)
1	150	65
2	140	70
3	100	75
4	115	72
5	120	75
Average	**125**	**71**

Grain	Length (nm)	Width (nm)
1	225	95
2	270	120
3	185	80
4	235	95
5	200	115
Average	**223**	**101**

Figure 6.9. a,b Width and length measurement lines are drawn on the rice-like crystalline domains of P(VDF-TrFE) thin films annealed at 135 °C and 140 °C. The corresponding values were measured using Gwyddion software and are reported in the tables to the right[41].

recrystallization process, suggesting that annealing close to the melting temperature of the thin film is crucial for obtaining such microstructure.

The comparison of electroactive β-phase presence in rice-like and spherulite-like P(VDF-TrFE) thin films in this work was studied using FTIR and XRD analysis. The FTIR spectra, shown in Fig. 6.11a, correspond to P(VDF-TrFE) thin films deposited on silicon and annealed at four different temperatures, ranging from 135 °C to 150 °C. Despite the morphological transition, all thin films exhibit the same conformational characteristics. In particular, strong absorption bands are identified at 850 cm^{-1}, 1073 $cm^{-1,}$ and 1277 cm^{-1}, attributed to the CF_2 vibration and CH_2 rocking modes of the *all-trans* conformation characteristic of the low-temperature phase of P(VDF-TrFE) (also known as the β-phase due to its similarity to the PVDF β-phase)[51,52,62]. The absorption bands at 880 cm^{-1} and 1183 cm^{-1} are less sensitive to chain conformation, with contributions from both α- and β-phase and the amorphous phase[200].

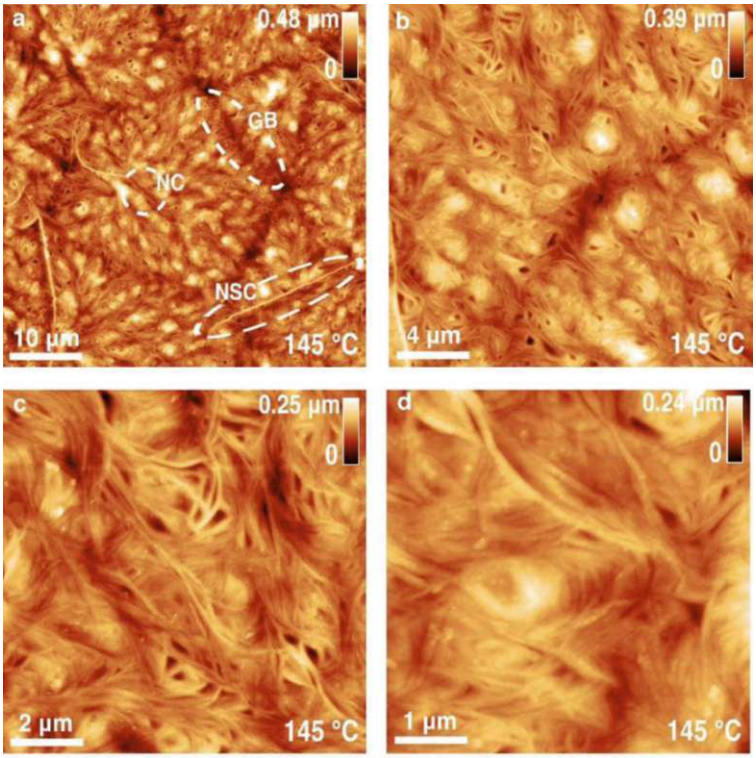

Figure 6.10. a AFM height image performed at a scan range of 50 µm, highlighting key features of P(VDF-TrFE) spherulite-like microstructure: nucleation centre (NC), grain boundary (GB), and needle-shaped crystal (NSC). **b**,**c**,**d** Zoomed-in view, showcasing details of the morphology at the nanometre scale. AFM height images were performed with a scan range of 20 µm, 10 µm, and 5 µm, respectively[41].

XRD measurements performed on the same samples (see Fig. 6.11b), revealed a characteristic diffraction peak at a 2θ value of 19.8° for all of them. This diffraction peak is attributed to the (110) and (200) orientation plane of the pseudohexagonal crystal structure of the low-temperature ferroelectric phase, also known as β-phase[214]. However, a significant decrease in peak intensity was observed for spherulite-like thin films compared to rice-like ones, indicating a poorer ferroelectric film quality. Interestingly, XRD measurements conducted on spherulite-like P(VDF-TrFE) thin films deposited on gold substrate showed instead an increase in the β-phase peak intensity compared to those spin-coated on a silicon substrate (see Fig. 6.12), despite AFM investigation, shown in Fig. 6.14, did not reveal any noticeable differences in the surface morphology of the P(VDF-TrFE) thin films. Further investigations are required to understand the underlying cause of this phenomenon.

Since P(VDF-TrFE) thin films annealed above the melting point typically exhibit a melt-recrystallization microstructure and poor ferroelectric activity, previous studies associated the melt-recrystallization process with a decrease in the ferroelectric β-phase and subsequent performance degradation[52,213]. Therefore, the melting temperatures of both microstructures in this study were investigated. The melting temperature of the spherulite-like microstructure was measured to be approximately 152 °C, below the annealing temperature, confirming the avoidance of any adverse effect on ferroelectricity[58,213]. The melting points of both microstructures, as determined through DSC measurements, are presented in Fig. 6.13.

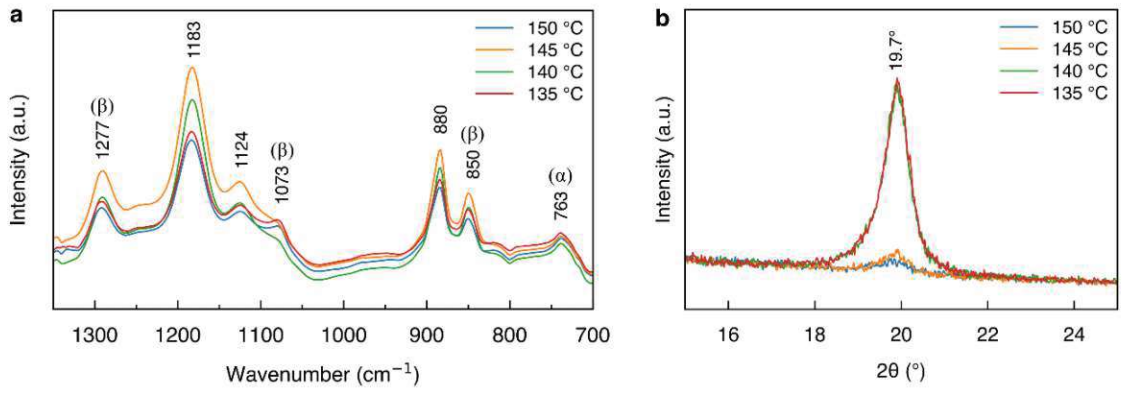

Figure 6.11. a FTIR spectrum (absorbance) and **b** XRD pattern of P(VDF-TrFE) thin films annealed at different temperatures showing the ferroelectric β-phase chain conformation[41].

Although the spherulite-like microstructure thin films deposited on a silicon substrate exhibited a low-intensity β-phase XRD peak, the high-intensity peak observed for those deposited on a gold-coated substrate suggested promising electromechanical and ferroelectric characteristics. In Chapter 6.2.2, the piezoelectric and ferroelectric properties of the spherulite-like microstructure are measured and compared to those of rice-like P(VDF-TrFE) and PVDF thin films. This includes electromechanical characterization at both high-field, to explore non-linear electrostrictive behaviour, and low-field measurements, to extract fundamental parameters such as the piezoelectric coefficient. Additionally, the thermal stability of the spherulite-like ferroelectric phase is investigated and compared with that of rice-like P(VDF-TrFE) microstructure with further ferroelectric studies.

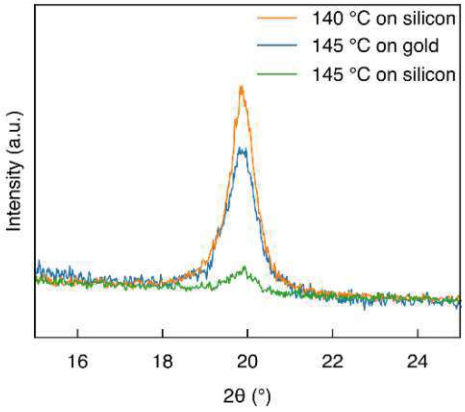

Figure 6.12. XRD patterns of P(VDF-TrFE) thin films annealed at 140 °C and 145 °C on silicon and gold substrates revealed a notable increase in the β-phase peak in the spherulite-like microstructure when using gold substrate[41].

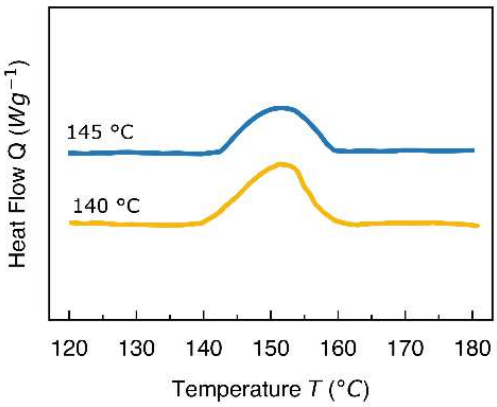

Figure 6.13. DSC thermogram of P(VDF-TrFE) thin films annealed at 140 °C and 145 °C revealing the melting point to be approximately 152 °C for both[41].

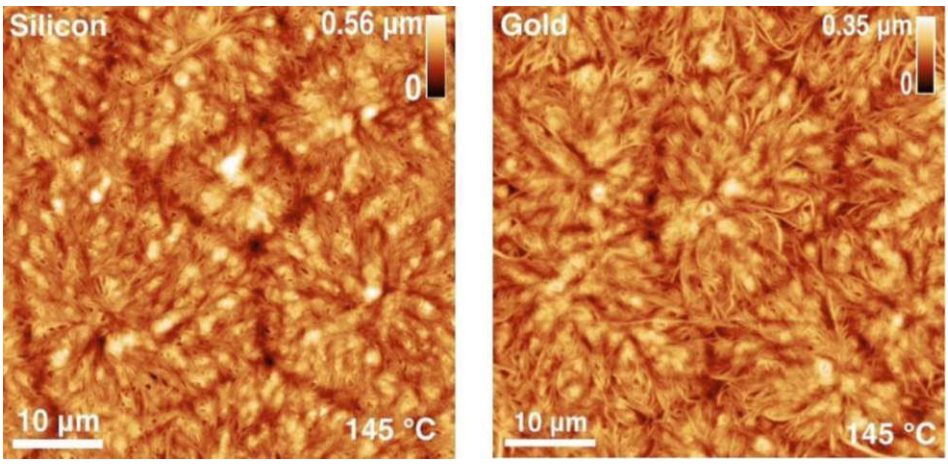

Figure 6.14. AFM height images of spherulite-like P(VDF-TrFE) thin films deposited on silicon and gold substrates do not show any relevant difference[41].

6.2 Ferroelectric and electromechanical characteristics

Determining the electromechanical characteristics of ferroelectric polymers is crucial for their application scenarios. This chapter delves into the piezo- and ferroelectric properties of δ-PVDF and P(VDF-TrFE). Specifically, it presents the transition from the non-polar α-PVDF to the polar δ-PVDF through electro-forming and discusses its ferroelectric *D-E* and electrostrain *S-E* characteristics. Furthermore, in P(VDF-TrFE) thin films, it compares the ferroelectric characteristics of the spherulite-like and rice-like microstructures, providing also insight into the ferroelectric thermal stability of these two microstructures. This final analysis highlights the importance of annealing and microstructural characteristics for real-world device applications in P(VDF-TrFE) thin films.

6.2.1 PVDF

The transition of solution-processed α-PVDF thin films into δ-phase occurs when a sufficiently high electric field is applied to the polymer, causing a reversal of the dipole components in every second chain. This transformation from a non-polar to ferroelectric phase was observed by measuring the hysteretic response of displacement *D* as a function of the electric field *E* using a custom-built Sawyer-Tower circuit, as described in Chapter 5.4. Additionally, the transition was observed through the electrostrain behavior of the thin films, by recording the strain *S* as a function of electric field *E* using the highly sensitive optical lever

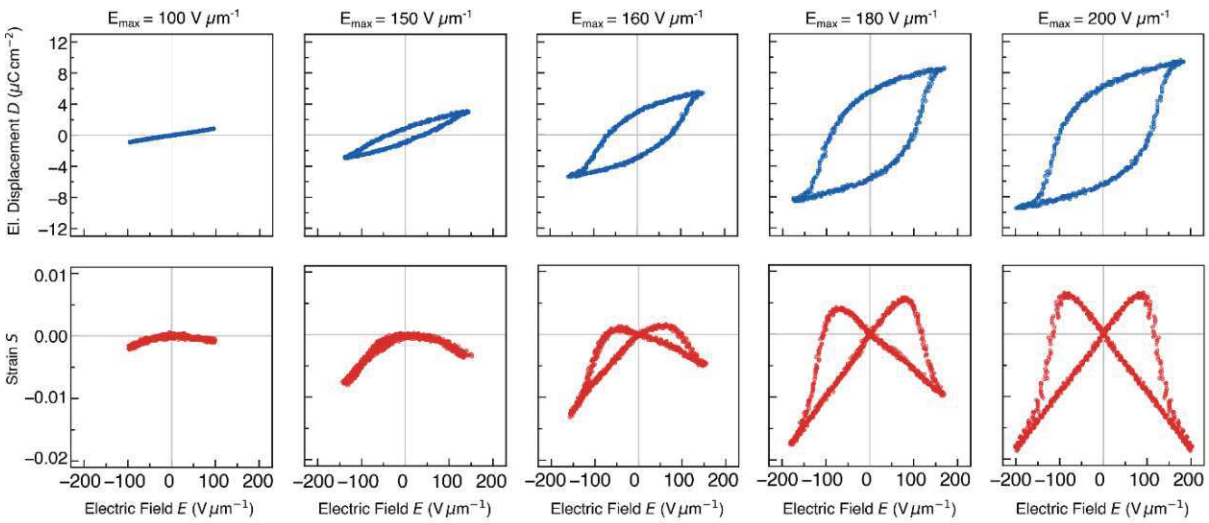

Figure 6.15. *D-E* (blue) and *S-E* (red) characteristics as a function of the electric field applied. As the electric field increases, a transformation from the α- to δ-phase is observed, transitioning from linear dielectric to ferroelectric behavior[31].

readout of the AFM, as described in Chapter 5.5. Micromachined capacitors fabricated according to the process outlined in Chapter 4.1.2 were used for these measurements. Fig. 6.15 illustrates the electro-forming process of the δ-phase, represented by the *D-E* hysteresis loop and *S-E* electrostrain characteristic. As shown in Fig. 6.15, when starting from a pristine film with an amplitude of E_{max} = 100 V·µm^{-1} applied, the *D-E* curve exhibited a linear dielectric behavior, and the *S-E* characteristic showed a parabola-shaped behavior typical of a pure electrostrictive response, both as expected from the non-polar α-PVDF. By stepwise increasing E_{max}, the hysteresis and the butterfly curves slowly appeared, indicating the transformation into the ferroelectric δ-phase. The full *D-E* loops, along with a constant value of P_r, in conjunction with a stabilized and symmetric *S-E* response, were reached at E_{max} of about 200 V·µm^{-1}. To evaluate coercive field E_c and remnant polarization P_r, the empirical model developed by Miller *et al.* was used, where two parts composing the hysteresis curve are distinguished: P_S^+ and P_S^- (see Chapter 5.4 for more details). The *D-E* curve was fitted, as displayed in Fig. 6.16a, yielding fitting parameters E_c and P_r of 113 ± 3 V·µm^{-1} and 6.1 ± 0.2 µC·cm^{-2}, respectively. The uncertainties of these values were derived from repeated measurements and were consistent with previously published data[30,44,215]. The reported coefficients of determination (R^2) of about 95% indicated a high-quality fit.

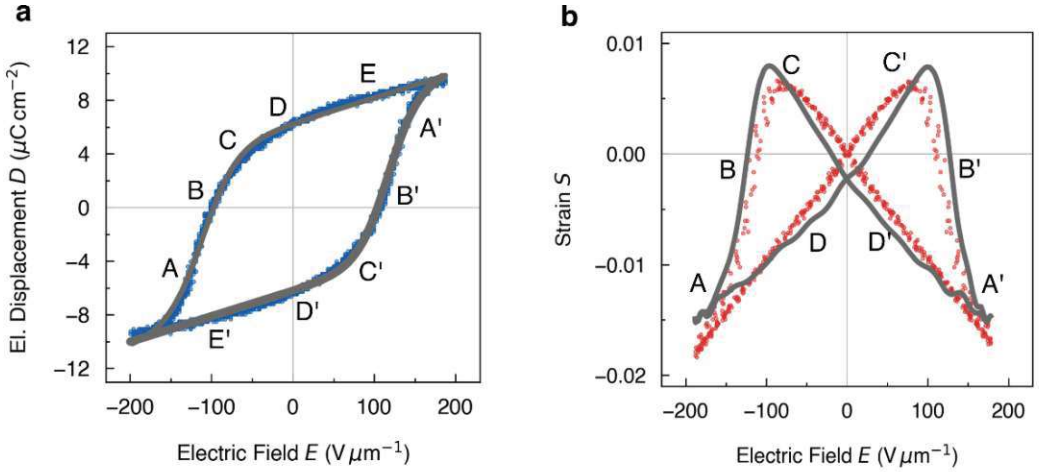

Figure 6.16. a Fit, with an R^2 of about 95%, of measured *D-E* data (blue circles) according to the Miller model (grey line). The error bars, representing the standard deviation in an interval Δx = 1.8, are too small to be visualized in the graph. Therefore, they are reported here for selected key points: 0.48 in **AA'**, 0.30 in **BB'**, 0.20 in **CC'**, 0.14 in **DD'**, and 0.16 in **EE'**. **b** Fit, with an R^2 of about 94%, of measured electromechanical response (red circles) according to the electrostrictive model (grey line). The error bars, representing the standard deviation in an interval Δx = 2.5, analogous to those in the *D-E* loop, are reported as follow: 0.0015 in **AA'**, 0.0016 in **BB'**, 0.0005 in **CC'**, 0.0004 in **DD'**[31].

According to the electrostriction model (see Chapter 3.1.4), the strain S in ferroelectric polymers varies as the square of the electric displacement D, expressed by a Taylor series with the first non-vanishing term. By applying equation (3.15), the S-E data at high fields, measured from a representative sample reflecting the average ferroelectric characteristics across the dataset, were fitted as shown in Fig. 6.16b. From the fitting, a negative Q_{33} electrostrictive coefficient was extracted, and the corresponding d_{33} piezoelectric coefficient was calculated from the derivative of the strain with respect to the electric field at zero (see equation (3.16)). This resulted in values of Q_{33} = -3.7 $m^4 \cdot C^{-2}$ and d_{33} = -39 $pm \cdot V^{-1}$. The negative value of the piezoelectric coefficient arises from the Van der Waals forces acting as intermolecular bonds, as discussed in Chapter 3.1.3. The R^2 value of approximately 94% reflected a high-quality fit.

Generally, when the applied electric field exceeds the coercive value E_c, performing high field measurements, the ferroelectric material undergoes polarization reversal, exhibiting the highly non-linear behavior of electrostrain, known as the butterfly curve. To isolate and study the pure piezoelectric response of δ-PVDF, as explained in Chapter 5.6, the material must first be polarized and subjected to low-field measurements. This was achieved by applying a positive DC voltage well above E_c for 5 minutes, resulting in a macroscopically positively polarized state of the δ-PVDF thin films. Following polarization, six low-field measurements were conducted by applying progressively increasing DC electric fields, ranging from -80 V·µm to + 80 V·µm, all below E_c, to analyze the piezoelectric response. The results, illustrated in Fig. 6.17b, indicate that when DC electric fields below E_c were applied to the positively polarized δ-PVDF thin film, a corresponding strain S was observed. Upon

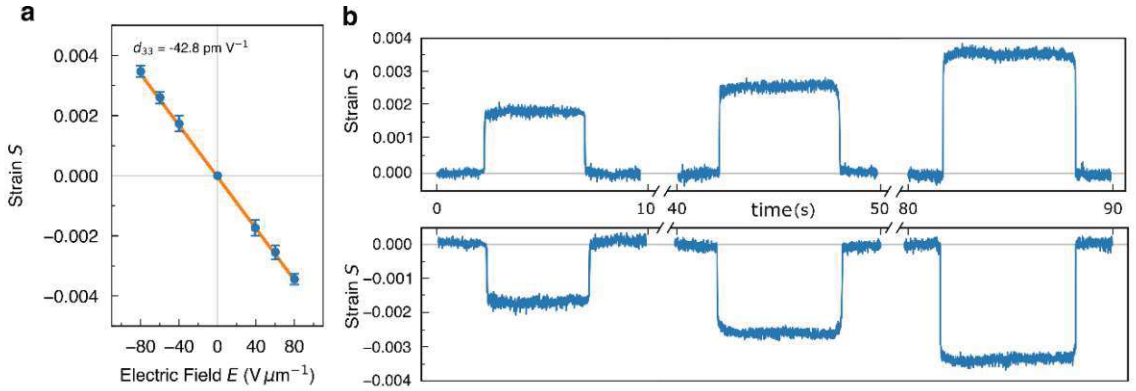

Figure 6.17. a Plot of the corresponding S-E values collected from **b** where the strain response to the applied DC step voltage is shown. The linear fitting in **a** gives the piezoelectric coefficient d_{33}. The error bars in **a** refer to the values from **b**. Despite the uncertainties, a linear piezoelectric correlation was found[31].

removal of DC electric fields, the strain returned to its initial zero position. As the DC electric field increased during the three measurements (from left to right in Fig. 6.17b), the corresponding strain also increased. By gathering the corresponding *S-E* values and plotting them as shown in Fig. 6.17a, a linear correlation was found, with the piezoelectric coefficient d_{33} serving as the proportionality factor. It should be noted that the sign of the slope between the strain *S* and the electric field *E* depends on the sign of the remnant polarization. Positively polarized thin films exhibit a negative slope, whereas negatively polarized thin films show a positive slope. Hence, through a linear fit, a d_{33} = - 42.8 pm·V^{-1} was extracted, in good agreement with d_{33} = - 39 pm·V^{-1} determined from high field measurements. The d_{33} values presented in this work are also comparable to those of biaxially stretched β-PVDF (-31 pm·V^{-1}) and solid-state processed δ-PVDF (-36 pm·V^{-1})[44].

6.2.2 P(VDF-TrFE)

The addition of the monomer TrFE to PVDF aims to stabilize the polar β-phase as the most thermodynamically stable polymorph in solution-processed thin films. Ferroelectricity and electrostrain behavior of the copolymer P(VDF-TrFE) have been extensively studied, with annealing temperature being one of the parameters most considered for optimizing the ferroelectric properties of the material. Specifically, it was demonstrated that annealing at 130 °C results in a substantial rise in β-phase crystallinity, up to 80% compared to non-annealed thin films[216]. Further annealing above 130 ° leads mostly to a growth in the thickness of the crystalline lamellae, which is reflected in the dimension of the crystalline domains (see Fig. 6.9). As a consequence, the ferroelectricity of the thin films is improved, and 140 °C in P(VDF-TrFE) has been selected as the annealing temperature for ferroelectric characterization[48,52]. P(VDF-TrFE) thin films annealed at 140 °C exhibit a rice-like microstructure. When annealed at 145 °C, a morphological transition to spherulite-like microstructure has been observed. This chapter demonstrates that the morphological transition obtained via annealing at temperatures below the melting point does not necessarily imply a decrease in ferroelectricity. Additionally, the thermal stability of rice-like and spherulite-like thin films is investigated, highlighting the impact of thermal loadings up to 90 °C on ferroelectric characteristics, particularly in their energy storage characteristics, of both P(VDF-TrFE) microstructures.

6.2.2.1 Ferroelectric characteristics of rice-like and spherulite-like P(VDF-TrFE) microstructures

Chapter 6.1.2 discussed the morphological transition observed in P(VDF-TrFE) thin films, approximately 1 μm thick, from a rice-like to a spherulite-like microstructure when annealed from 140 to 145 °C, respectively. Given that the melting point, as estimated by DSC, was around 152 °C, and considering the presence of the highly polar β-phase as shown by FTIR and XRD analyses in Chapter 6.1.2, a good piezo- and ferroelectric response is expected. This raises the question of how the significant change in microstructure influences the ferro- and piezoelectric activity of P(VDF-TrFE). To address this, an in-depth analysis of the piezo- and ferroelectric characteristics of the spherulite-like microstructure of P(VDF-TrFE) thin films was conducted. This analysis was performed using micromachined capacitors, fabricated as described in Chapter 4.1.2. The Sawyer-Tower bridge circuit, detailed in Chapter 5.4, was used to plot the hysteretic responses of the electric displacement D as a function of electric field E, as illustrated in Fig. 6.18a. To extract parameters such as the coercive field E_c and remnant polarization P_r, the Miller model was used for fitting the D-E loops, as displayed in Fig. 6.19a for a representative sample. The analysis yielded a remnant polarization $P_r = 4.7 \pm 0.2$ μC·cm^{-2}, and a coercive field $E_c = 53 \pm 2$ V·μm^{-1}, with uncertainties derived from repeated measurements. These values are consistent with literature (refer Table 4), reflecting the precision of the Sawyer-Tower circuit and Miller model fitting. Additionally, the coefficient of determination R^2 of 96% proved the accuracy of the fit.

Fig. 6.18a provides insights into the polarization steps and dipole orientation as a function of the applied voltage. The hysteresis curve is here divided into four key segments, each highlighted by a different color. The direction of the electric field is indicated by arrows and corresponding numbers. Starting from a negatively polarized thin film (illustrated by the green line), the electric field was gradually increased from zero. At the coercivity (E_c), the polarization switched to a positive dipole orientation, reaching saturation at the highest voltage within this segment. Upon decreasing the electric field along segment 2 (depicted in blue), displacement is reduced until reaching the remnant polarization value ($D = P_r$) at zero field. Segments 3 and 4 represent the same process but in the opposite field direction.

The butterfly curve, shown in Fig. 6.18b, was observed in the S-E characteristic of spherulite-like P(VDF-TrFE) thin films. An analogous representation using colored segments

is presented here for the electrostrain behaviour. Following arrow 1 (green line), the electric field was increased from an initial strain value equal to zero, until reaching the maximum expansion achieved in correspondence with the coercivity. From here, the polarization was inverted until the maximum contraction was obtained at the saturation point when the dipoles were fully aligned in the same direction as the electric field. From this point, the electric field intensity decreased until returning to zero-deformation condition (blue line).

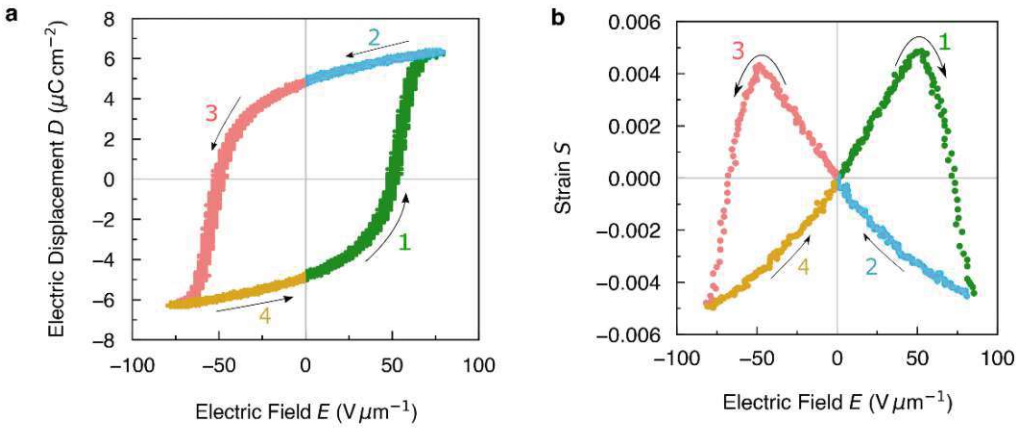

Figure 6.18. a Electric displacement as a function of the electric field (*D-E* hysteresis) and **b** strain response as a function of the electric field applied (*S-E* butterfly curve) of spherulite-like microstructure P(VDF-TrFE) thin films[41].

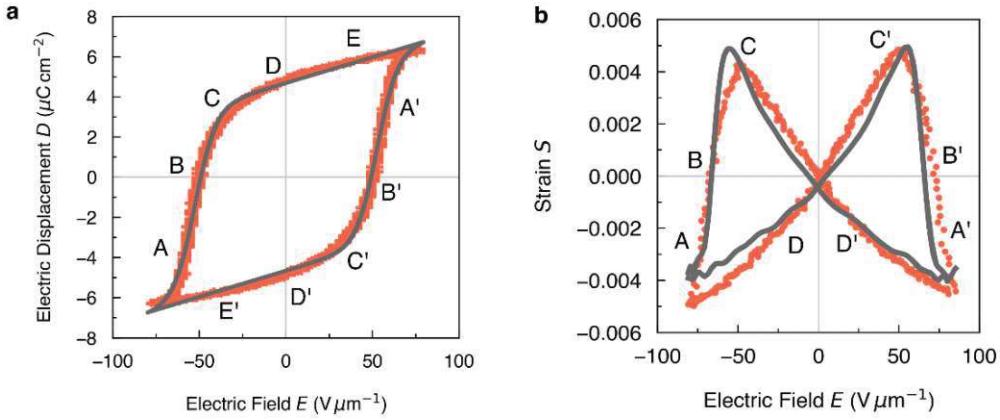

Figure 6.19. Fitting curves according to **a** the Miller model for the *D-E* hysteresis loop (R^2 of about 96%) and **b** to the electrostrictive model for the *S-E* butterfly response (R^2 of about 94%) in spherulite-like P(VDF-TrFE) microstructure thin films. Red circles represent the measured data, while the grey line represents the fit. The error bars for *D-E*, representing the standard deviation in an interval $\Delta x = 1.2$, are too small to be visualized in the graph and are therefore reported for selected key points: 0.64 in **AA'**, 0.57 in **BB'**, 0.14 in **CC'**, 0.06 in **DD'**, 0.06 in **EE'**. Similarly, the error bars for *S-E*, representing the standard deviation in an interval $\Delta x = 1.5$, are reported as follows: 0.00005 in **AA'**, 0.00006 in **BB'**, 0.00004 in **CC'**, 0.00009 in **DD'**[41].

Using the electrostrictive model, a nonlinear fit to the *S-E* characteristic at high fields was performed on a sample representative of the average ferroelectric properties measured across the dataset, as shown in Fig. 6.19b. This analysis allowed for the extraction of both the electrostriction and the piezoelectric coefficients at high fields, resulting in values of Q_{33} = -2.4 $m^4 \cdot C^{-2}$ and d_{33} = -29.8 $pm \cdot V^{-1}$, respectively. In general, the ferroelectric strain *S* can be described as proportional to the square of the electric displacement *D*. The proportionality factor between *S* and D^2 represents the longitudinal electrostrictive coefficient Q_{33}. According to equation (3.15), the electrostrictive coefficient Q_{33} can be extracted as the proportionality factor from the linear fit of S-D^2, as illustrated in Fig. 6.21 for one branch. The value reported Q_{33} = -2.4 $m^4 \cdot C^{-2}$ is the mean value of the two branches.

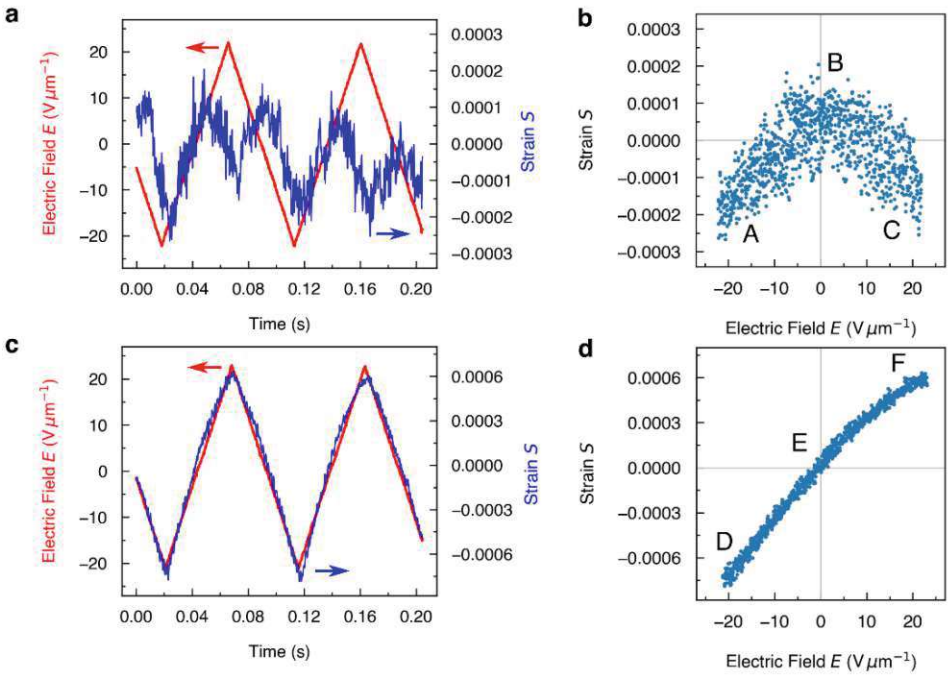

Figure 6.20. By applying an electric field in a triangular waveform with an amplitude of ±20 $V \cdot \mu m^{-1}$ (depicted in red in **a** and **c**) low-field measurements were conducted to study the electrostrictive and piezoelectric *S-E* curves of **a** unpolarized and **c** polarized spherulite-like microstructure P(VDF-TrFE) thin films. The recorded parabolic deflection signal in **a**, measured by AFM, represents the quadratic behaviour typical of an electrostrictive response, as shown in **b**. In contrast, when a polarized thin film, *i.e.* turned into a ferroelectric state, was measured, a linear deflection signal was recorded in **c**, leading to a linear *S-E* characteristic in **d** that demonstrates piezoelectric behaviour. **b** and **d** report also error bars representing the standard deviation in an interval Δx = 1.5 for selected key points: 0.00016 in **A**, 0.00014 in **B**, 0.00011 in **C**, 0.00005 in **D**, 0.00005 in **E**,0.00003 in **F**[41].

Additionally, electrostrain measurements at low fields were carried out to characterize the piezoelectric nature of the spherulite-like P(VDF-TrFE) thin film. To demonstrate that piezoelectricity can be measured only in polarized thin films, while in the case of unpolarized thin films an electrostrictive response is obtained, low field measurements were performed for both unpolarized and polarized thin films. Fig. 6.20a illustrates the deflection signal (blue colored), labeled as strain *S*, depicted as vertical displacement in response to an applied voltage (red colored) of an unpolarized thin film. The strain, shown as a function of time, exhibited a series of parabola-shaped behaviors, characteristic of the electrostrictive response. From the data provided in Fig. 6.20a, the *S*-*E* curve in Fig. 6.20b was obtained, confirming the purely electrostrictive nature of the response, with the strain *S* varying quadratically as a function of the electric field *E*. On the other hand, to transition macroscopically the polymer thin film into a ferroelectric state, a DC voltage exceeding the coercive value must be applied. Polarization generally occurs due to the re-orientation of dipoles in alignment with the applied electric field. This phenomenon involves a nucleation-growth mechanism that begins with a single-chain molecule and progresses through the propagation of a kink along the chain direction[16]. In this study, an electric field of 90 V·μm^{-1} for 5 minutes at room temperature,

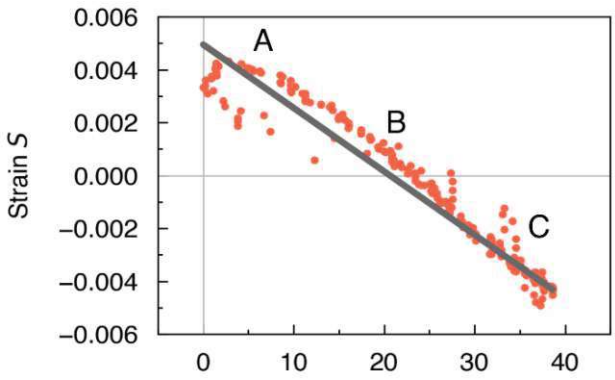

Figure 6.21. Strain characteristic *S* of the spherulite-like P(VDF-TrFE) thin film as a function of the squared electric displacement D^2 (red circles). The linear fit $S = Q_{33}D^2$is presented (grey line). The fitting parameter is the longitudinal electrostriction coefficient Q_{33}. The error bars, representing the standard deviation in an interval Δx = 0.7, are reported for selected key points: 0.0008 in **A**, 0.0002 in **B**, 0.0004 in **C.** The fit presents an R^2 equal to 95%[41].

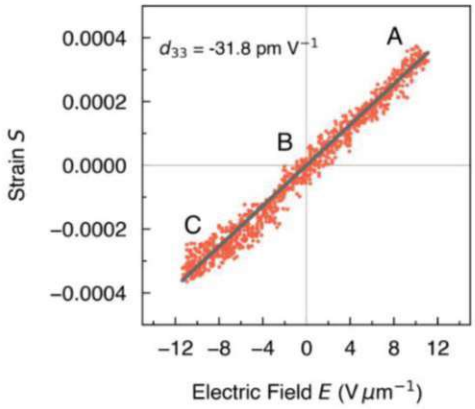

Figure 6.22. Linear fitting of a piezoelectric response at low electric field conditions measured from a polarized spherulite-like P(VDF-TrFE) thin film to estimate the longitudinal piezoelectric coefficient d_{33}. The error bars, representing the standard deviation in an interval Δx = 0.1, are reported for selected key points: 0.00004 in **A**, 0.00002 in **B**, and 0.00003 in **C.** The fit presents an R^2 equal to 98%[41].

i.e. above coercivity, was applied. It can be assumed that the system has been given enough energy to become negatively polarized. As a result, a linear deflection pattern was obtained, as shown in Fig. 6.20c. In contrast to the parabolic behavior of the electrostriction, polarized thin film exhibited a linear piezoelectric response, where the strain S was linearly proportional to the electric field E, as seen in Fig. 6.20d. The proportionality factor of the linear relation between electromechanical strain S and electric field E is the piezoelectric coefficient d_{33} of the P(VDF-TrFE) thin film, as illustrated in Fig. 6.22. Applying a linear fit with an R^2 equal to 98%, a piezoelectric coefficient of d_{33} = -31.8 pm·V^{-1} was obtained. This low field d_{33} value closely matched the d_{33} = - 29.8 pm·V^{-1} extracted at high fields through fitting the butterfly curve, indicating consistency across different measurement regimes.

A final comparison of the ferroelectric characteristics from different microstructures observed in P(VDF-TrFE) and PVDF phases is presented in Table 4. Coercive fields E_c, remnant polarizations P_r, piezoelectric coefficients d_{33}, and electrostrictive coefficients Q_{33} from literature are reported alongside the results obtained in this work for the spherulite-like P(VDF-TrFE) thin films and electro-formed δ-PVDF. This study reveals that there is no significant difference observed in the electromechanical response between the spherulite-like microstructure and the rice-like domains[48,52] and the spherulite microstructure of β-PVDF[65]. However, there is a notable contrast with the δ-PVDF, where significant differences in the coercive field are observed compared to spherulite-like P(VDF-TrFE) thin films, likely due to their distinct chain conformations.

Material	Microstructure	Thickness (μm)	E_c (V·μm^{-1})	P_r (μC·cm^{-2})	d_{33} (pm·V^{-1})	Q_{33} (m^4· C^{-2})
P(VDF-TrFE) This work	Spherulite-like	1.1	53 ± 2	4.7 ± 0.2	-29.8	-2.4
P(VDF-TrFE)[52]	Rice-like	1	55	5.8	-26.2	-1.7
P(VDF-TrFE)[48]	Rice-like	0.45	55	4.3	-31.4	-1.5
β-PVDF[65]	Spherulite	10-30	58	5.6	-26	-2.4
δ-PVDF This wok	Spherulite	0.3	113 ± 3	6.1 ± 0.2	-39	-3.7
δ-PVDF[44]	Spherulite	30	110	7	-36	-

Table 4. Ferro- and piezoelectric properties of P(VDF-TrFE) microstructures and PVDF thin films. The results obtained in this work are included and compared with values reported in literature[41].

6.2.2.2 Microstructural influence on thermal stability of P(VDF-TrFE) ferroelectricity

The thermal stability of ferroelectric polymers holds significant importance in applications requiring precise and reliable device performance. This pre-requisite across a wide temperature range is crucial for specific material selection. Literature indicates a thermal hysteresis effect on the behaviour of P(VDF-TrFE) ferroelectricity, where the remnant polarization during thermal cycling follows a slightly different path in heating and cooling down curves, but its value is ultimately restored[16,198]. However, existing literature on thermal hysteresis behaviour in P(VDF-TrFE) thin films has not thoroughly investigated microstructure specifics. In particular, there is a lack of comprehensive studies on the behaviour of the spherulite-like microstructure. This research gap underscores the need to explore how distinct microstructures influence the thermal response of P(VDF-TrFE) thin films during cyclic temperature changes. For this purpose, this work presents a study on the ferroelectric characteristics of P(VDF-TrFE) thin films with spherulite-like and rice-like microstructures before and after thermal loading. The thermal loading process was conducted in a climate chamber, described in Chapter 5.4, where the temperature was raised close to the Curie point (at approximately 90 °C) and then cooled down to room temperature. This process aimed to emulate potential operating conditions, such as cold lamination operating temperatures in the smart-textile field[217], where fluoropolymers are increasingly used.

For this purpose, micromachined capacitors were fabricated according to the procedure outlined in Chapter 4.1.2, with rice-like and spherulite-like microstructures

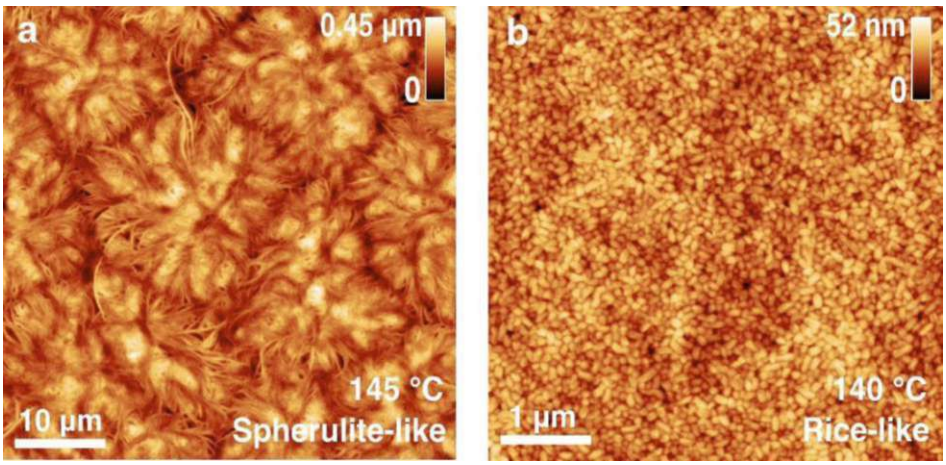

Figure 6.23. AFM height images of P(VDF-TrFE) thin films with **a** spherulite-like microstructure and **b** rice-like microstructure obtained after annealing at 145 and 140 °C, respectively[49].

obtained by annealing the thin films at 140 °C and 145 °C, respectively. The emergence of the two distinct microstructures is illustrated in Fig. 6.23 by AFM height images. By applying an electric field of amplitude E_{max} = ±100 V·µm^{-1}, the ferroelectric characteristics *D-E* of pristine P(VDF-TrFE) thin films with spherulite-like and rice-like microstructures were measured using a Sawyer-Tower circuit, as described in Chapter 5.4. The results are illustrated in Figs. 6.24a and c. To determine the remnant polarization and coercive field values, the fitting procedure employing a hyperbolic tangent function following the Miller model, as explained in Chapter 5.4, was utilized. The pristine P(VDF-TrFE) thin films exhibited remnant polarization values of P_r = 6.2 µC·cm^{-2} and 6.4 µC·cm^{-2} and coercive field values of E_c = 56 V·µm^{-1} and 59 V·µm^{-1}, for the spherulite-like and rice-like respectively, consistent with values reported in previous literature (see Table 4). The corresponding fitted curves of the *D-E* loops are shown in Figs. 6.25a and b, while Figs. 6.26a and c confirmed the presence of the ferroelectric crystalline β-phase.

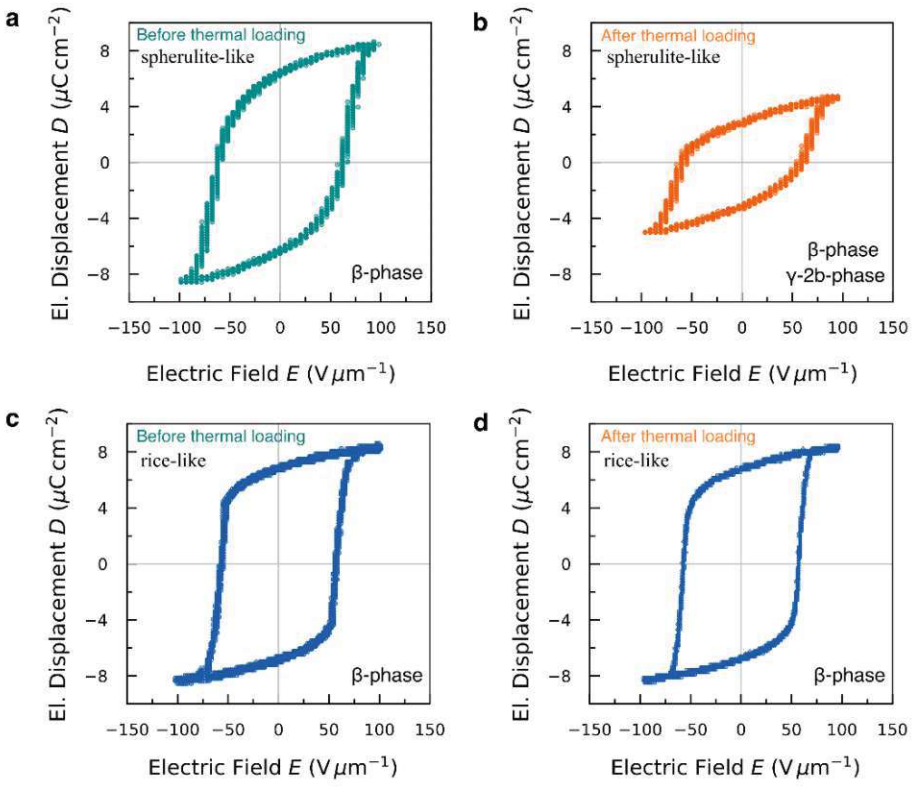

Figure 6.24. *D-E* characteristics of the P(VDF-TrFE) spherulite-like and rice-like microstructures thin films **(a-c)** before and **(b-d)** after thermal loading. The phase detected by XRD measurements is reported in the bottom right of the plot. After thermal loading, the spherulite-like sample underwent a chain conformation transition to the γ-phase, affecting its ferroelectric activity[49].

As a second step, the MFM capacitors were placed into the climate chamber, and after thermal loading, their hysteretic response was again measured by applying the same voltage as before (E_{max} = ±100 V·μm^{-1}). As shown in Fig. 6.24b, a reduction in the ferroelectric activity

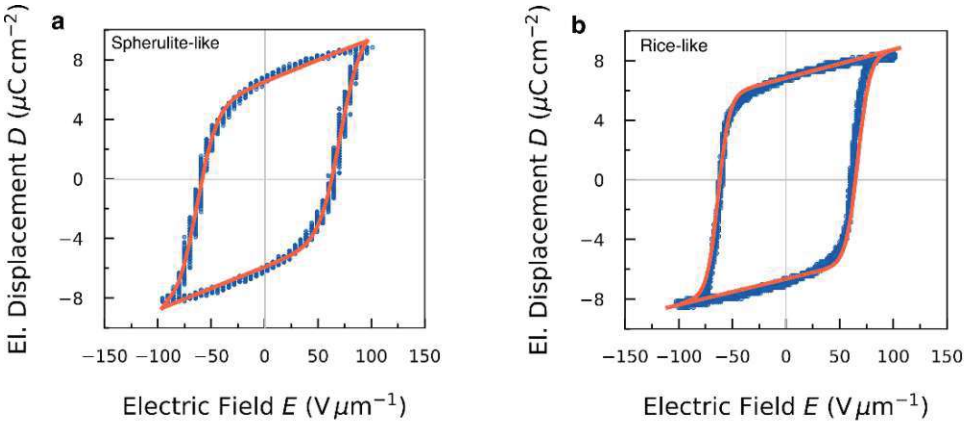

Figure 6.25. Fit according to the Miller model (orange line) for the measured electric displacement data (blue circles) of **a** the spherulite-like and **b** rice-like P(VDF-TrFE) thin films for determining remnant polarization P_r and coercive field E_c values[49].

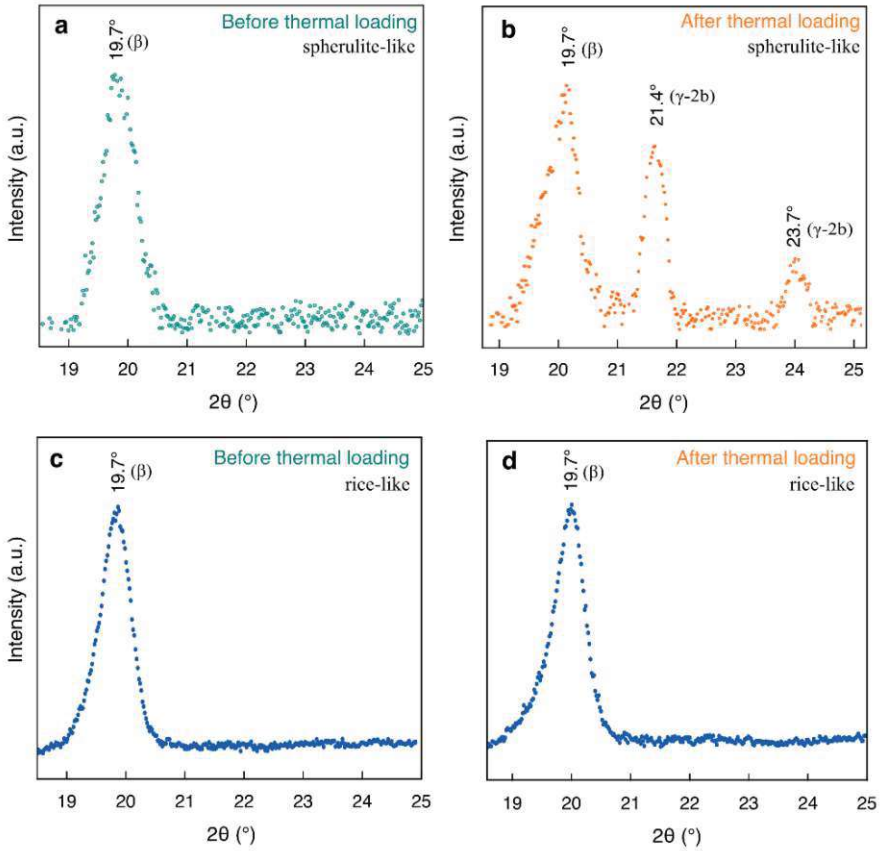

Figure 6.26. XRD pattern of the P(VDF-TrFE) thin films spherulite-like and rice-like microstructures **(a-c)** before and **(b-d)** after thermal loading. Notably in spherulite-like P(VDF-TrFE), thermal loading led to the appearance of γ-2b crystalline phase, whose effects on ferroelectricity are visible in Fig. 6.24[49].

in the spherulite-like thin films was observed. Conversely, this phenomenon was not observed in the case of the rice-like microstructure (see Figure 6.24d). XRD analysis proved that the decrease in ferroelectricity was associated with changes in the crystalline phase within the polymer thin film. Fig. 6.26b presents the XRD pattern of P(VDF-TrFE) thin films with spherulite-like microstructure after thermal loading, revealing the emergence of two new peaks at 2θ = 21.4° and 2θ = 23.7°. These peaks correspond to the γ-2b (022) and (032) crystallographic planes, respectively. In contrast, the XRD pattern of P(VDF-TrFE) thin films with the rice-like microstructure, as shown in Fig. 6.26d, revealed no new peaks after thermal loading, with only β-phase being detected. The γ-2b phase, observed in the spherulite-like microstructure, is characterized as the crystalline γ-phase with a double unit cell perpendicular to the chain axis. From literature, this phase was first identified by M. Remskar *et al.* in PVDF/molybdenum disulphide nanotube composites through XRD and AFM measurements[218]. The first ferroelectric investigation on this phase was performed by G. Peng *et al.*, who identified it in blend films composed of P(VDF-HFP) and PMMA after thermal treatment under vacuum[219]. Generally, the γ-2b phase exhibits lower polarity compared to the β-phase[219], which is consistent with the findings of this study. Recently, X. Zhao *et al.* also observed the γ-2b phase in SiC/P(VDF-CTFE) composites with X-ray diffraction[220]. However, the presence of the γ-2b phase in P(VDF-TrFE) has never been previously reported in literature, marking this a novel finding.

By applying a higher electric field with an E_{max} = ± 150 V·μm^{-1} to the γ-2b phase P(VDF-TrFE) thin films, and subsequently measuring the *D-E* characteristic again with an electric

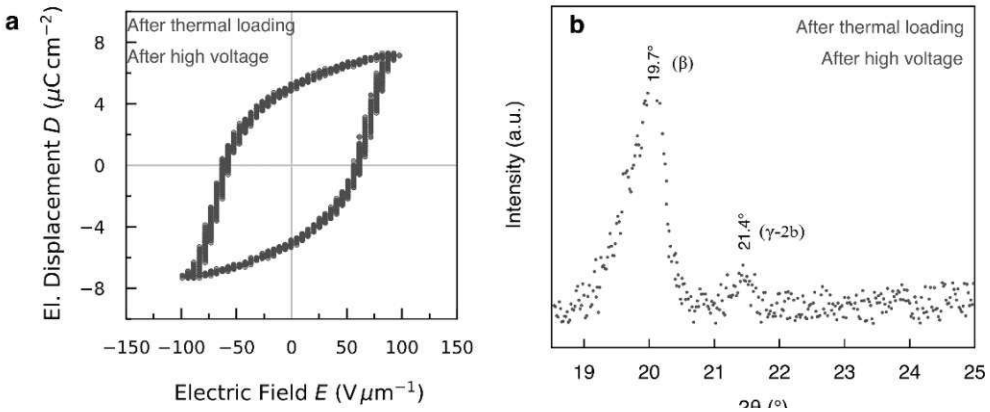

Figure 6.27. (a) Hysteretic response and **(b)** XRD pattern of the P(VDF-TrFE) spherulite-like microstructure thin films after thermal loading and subsequent application of a high electric field (E_{max} = ± 150 Vμm^{-1}). A partial restoration of the ferroelectric activity is observed, coinciding with a reduction in the γ-phase as detected by XRD, along with an increase in remnant polarization[49].

field E_{max} = ± 100 V·μm^{-1}, a hysteretic response similar to that observed in non-thermally treated spherulite-like samples was observed, as shown in Fig. 6.27a. XRD analysis, displayed in Fig. 6.27b, demonstrated that applying higher voltage (in this case E_{max} = ± 150 V·μm^{-1}) led to an almost complete restoration back to the β-phase. However, the remnant polarization P_r, determined using the Miller model, showed a slight decrease to 5.3 μC·cm^{-2} compared to the previous value of 6.2 μC·cm^{-2} in pristine samples. This reduction indicates that spherulite-like microstructure may be sensitive to thermal cycles, exhibiting a decrease in ferroelectric activity. More in detail, Fig. 6.28 depicts the ferroelectric behaviours of both microstructures after several thermal loadings. Prior to *D-E* plotting, all samples were subjected to higher voltage levels (E_{max} = ± 150 V·μm^{-1}) for a clear comparison, to restore the β-phase in the spherulite-like thin films. The results highlight the superior stability of the rice-like microstructure compared to the spherulite-like one. This difference is likely attributed to the annealing process, which promotes the formation of thicker crystals with higher thermostability in the rice-like, compared to the melt recrystallization process characterizing the spherulite-like samples. The values of the remnant polarization are detailed in Fig. 6.29. After the third loading cycle, the spherulite-like microstructure exhibited a decrease in remnant polarization of about 20%, declining from P_r = 6.2 μC·cm^{-2} to P_r = 4.9 μC·cm^{-2}. This effect can hold significant implications for device performance in environments characterized by a wide range of operating temperatures.

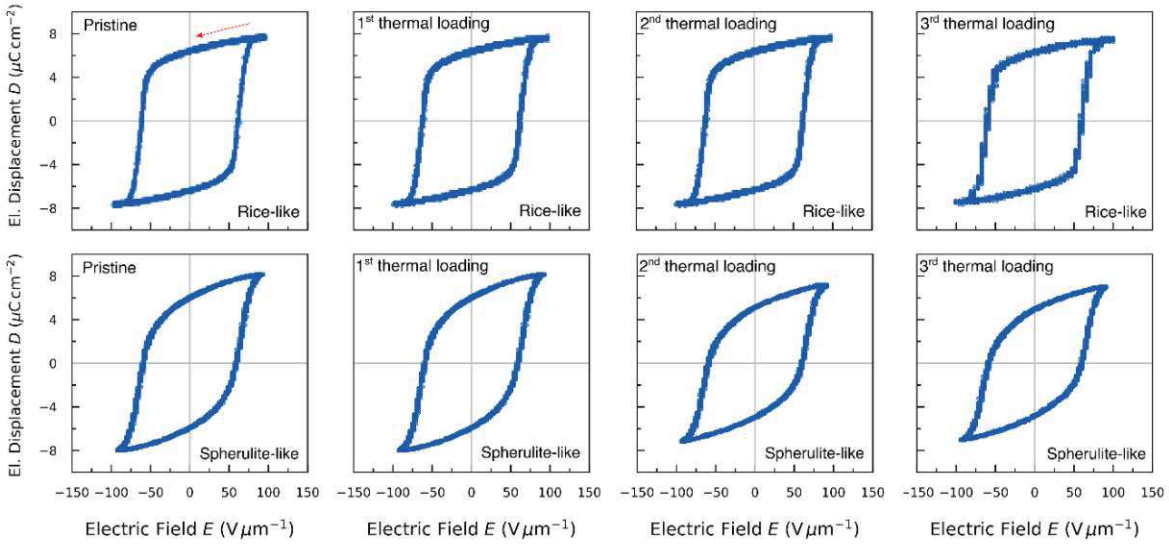

Figure 6.28. Hysteretic response of P(VDF-TrFE) thin films with spherulite-like and rice-like microstructures from pristine samples up to the electrical performance after three thermal loadings. Notably, the spherulite-like sample demonstrated lower thermal stability, evidenced by a gradual reduction in the remnant polarization[49].

Any impact of the microstructure on energy storage characteristics was also studied. Using the *D-E* loop of the pristine samples, the energy density was calculated by integrating the area between the discharge curve (indicated by a red arrow in the pristine rice-like hysteresis loop in Fig. 6.28) and the ordinate (see Chapter 3.2 for further details). Subsequently, energy efficiency was determined together with energy loss. The calculated data, as presented in Table 5, indicate that the spherulite-like microstructure generally exhibited higher energy density and efficiency values compared to the rice-like microstructure. This is likely attributed to the less pronounced shape of the hysteretic loop in the spherulite-like microstructures, which resulted in a larger area associated with the energy density. However, despite these advantageous characteristics, the instability of the spherulite-like microstructure under thermal loading cycles must be considered, as energy properties may change. Conversely, the rice-like microstructure, although exhibiting lower energy storage characteristics, proved to be a more reliable choice due to its greater stability.

Material	Microstructure	Energy Density ($J \cdot cm^{-3}$)	Energy Loss ($J \cdot cm^{-3}$)	Energy Efficiency
P(VDF-TrFE)	Spherulite-like	1.4	4.2	25 %
P(VDF-TrFE)	Rice-like	0.9	5.0	15 %

Table 5. Energy storage characteristics of P(VDF-TrFE) thin films with spherulite-like and rice-like microstructures indicate that spherulite-like P(VDF-TrFE) capacitors generally exhibit higher energy storage performance[49].

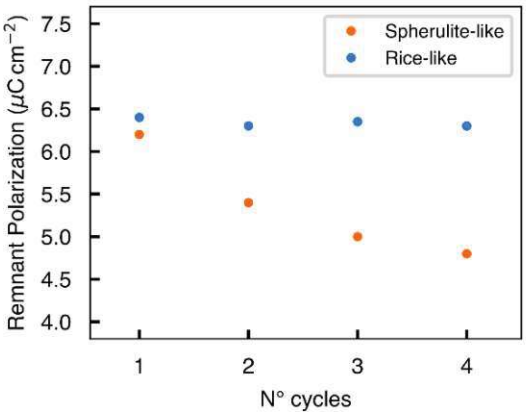

Figure 6.29. Remnant polarization values of the P(VDF-TrFE) spherulite-like and rice-like thin films from pristine through the three thermal loadings performed. After the third thermal loading, the spherulite-like sample presented a reduction of approximately 20% in P_r[49].

7 P(VDF-TrFE)-based Nanocomposite

7.1 Nanoparticles

Chapter 2.2.2 introduced the concept of nanoparticle surface functionalization, highlighting its significance in achieving the desired nanocomposite performances. Among the various techniques discussed, polydopamine-based functionalization was selected for this study due to its ease of use, cost-effectiveness, and versatility in adhering to inorganic surfaces. Following the procedure outlined in Chapter 4.2.1, commercially available BTO$^{(C)}$ nanoparticles underwent PDA functionalization. SEM and TEM were employed to characterize the functionalization layer. Some findings of this chapter are in reference 150.

Figs. 7.1a and b present SEM images of the BTO$^{(C)}$ nanoparticles before and after PDA functionalization, respectively. Fig. 7.1a illustrates the distinctive cubic shape of the unfunctionalized BTO$^{(C)}$ nanoparticles. In contrast, Fig. 7.1b shows the nanoparticles appearing more rounded, which is attributed to the deposition of the PDA layer. Additionally, the occurrence of surface modification is evident from the alterations in the electron scattering observed in imaging.

To determine the thickness of the PDA layer, TEM microscopy was used. As discussed in Chapter 2.2.2, the thickness of the PDA layer deposited varies with the duration of the

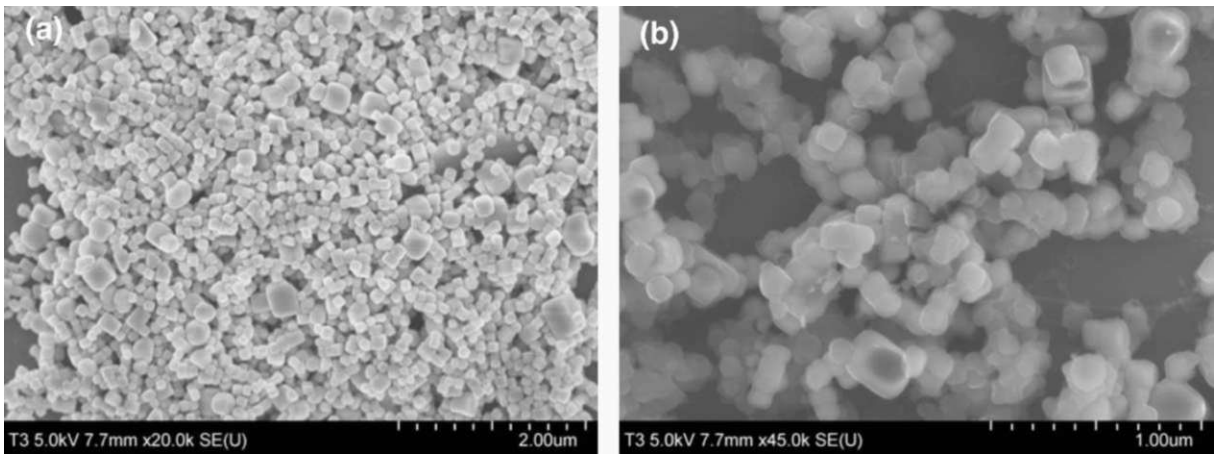

Figure 7.1. SEM images of BTO$^{(C)}$ nanoparticles (**a**) before and (**b**) after PDA functionalization. Functionalization is visible from the BTO$^{(C)}$ cubic structures becoming more rounded and from the changes observable in electron scattering.

dopamine polymerization, *i.e.* the reaction time. Longer reaction times result in a thicker PDA layer as shown from previous research in Fig. 2.13[112]. By employing the same quantity of reactants as reported in the referenced publication in Fig. 2.13[112], a comparable investigation was conducted in this study. Three samples of BTO(C) nanoparticles, each weighing 150 mg, were functionalized in a tris buffer solution at 8.5 pH, as described in Chapter 4.2.1. The functionalization was carried out using 165 mg of dopamine hydrochloride (2 mg of dopamine per millilitre of 10 mM tris, pH 8.5[112]) for durations of 2 hours, 7 hours, and 22 hours, respectively. Afterward, TEM images were performed (see Fig. 7.2) and the mean value of the PDA layers was measured (displayed in the top right corner of each image). The results, represented by the blue, orange, and green lines projecting the coordinates, were then compared in Fig. 7.3a with those from literature[112], showing a good consistency. The parabolic shape of the PDA thickness as a function of time is also evident in this work, attesting to the reliability of the results obtained. This parabolic trend serves as an indirect representation of the typical first-order chemical reaction in a closed system (see Fig. 7.3b), where the concentration of reactants diminishes over time, in contrast to the increase in the concentration of chemical products, until the chemical equilibrium is reached. The parabolic trend observed here therefore traces the typical behaviour of the concentration of the reaction products as a function of time.

In addition to the BTO(C), a second batch of CCNF-BTO@PDA nanoparticle mixture was investigated in this work. These nanoparticles were synthesized and characterized by the Research Center of Nano Science and Technology at Shanghai University. The average particle size of the BTO was analysed (see Fig. 4.8). Additionally, SEM images, XRD patterns, and FTIR

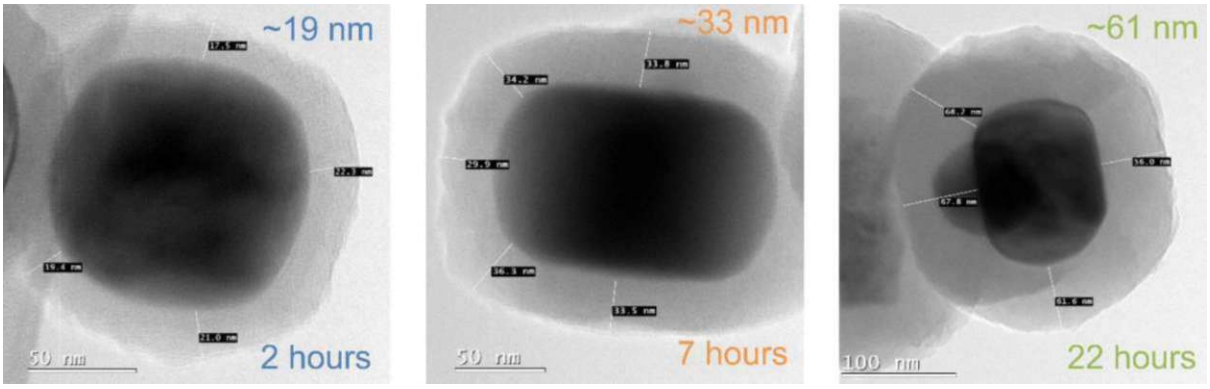

Figure 7.2. TEM images of the BTO(C) nanoparticles functionalized with PDA at different reaction times. The mean value of the measured PDA layer, displayed in the top right corner of each image, noticeably increases with the reaction time, displayed in the bottom right corner.

spectra were performed at Shanghai University to provide a comprehensive characterization of the nanoparticle mixture.

Fig. 7.4 presents the SEM images of the CCNF-BTO@PDA mixture. This characterization aims to highlight the filament network between the BTO cubic structures, indicative of the successful integration of the cellulose fibers (especially visible in Fig. 7.4(b3)).

The XRD patterns of both pure BTO (red coloured) and BTO@PDA (blue coloured) nanoparticles, presented in Fig. 7.5a, exhibit the characteristic diffraction peaks of BTO's crystallographic microstructure[221]. In particular, the XRD pattern of BTO@PDA did not show any difference from that of pure BTO, indicating that the crystalline structure of the ceramic

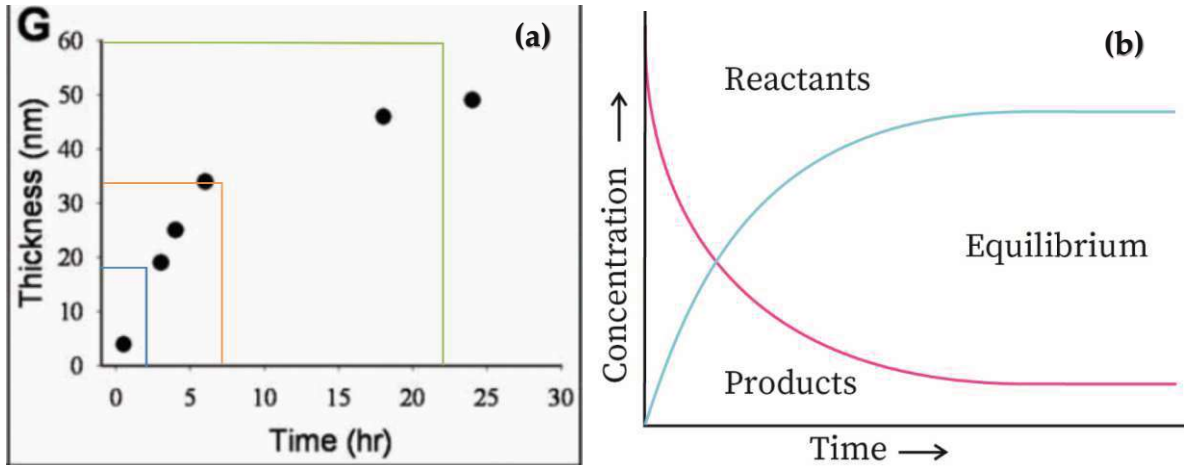

Figure 7.3. (a) Comparison of the time evolution of the PDA layer thickness formed on BTO(C) nanoparticles with literature data[113]. The blue, orange, and green lines represent the thicknesses measured in this work via TEM at different reaction times (see Fig. 7.2). The data show a good correlation with those from literature. **(b)** Representation of a first-order reaction in a closed system where the concentration of reactants diminishes while that of products increases in parallel with time until the chemical equilibrium is reached.

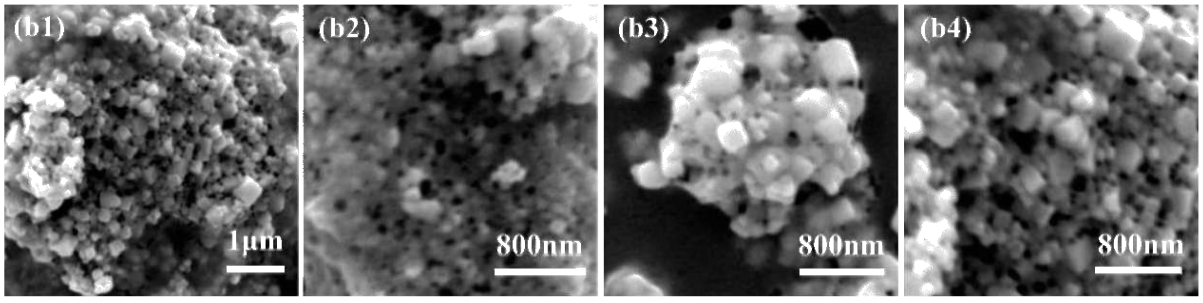

Figure 7.4. (b1-b4) SEM images of CCNF-BTO@PDA mixture performed at Shanghai University, illustrating the successful integration of the CCNF with the BTO@PDA. The network of filaments connecting the BTO cubic structures PDA functionalized demonstrates the effective incorporation of cellulose fibers[150].

nanoparticles remained unaltered after polydopamine functionalization[222]. The characteristic peaks of pure CCNF presented in Fig. 7.5a (black coloured) at 2θ values of 16°, 22.7°, and 34.5° correspond to the (110), (200) and (004) lattice planes, respectively[223]. After mixing BTO@PDA with CCNF, the distinct CCNF diffraction peaks of (110) and (200) mentioned above became less prominent due to the high-intensity peaks of BTO in the XRD pattern of CCNF-BTO@PDA (green coloured).

The corresponding FTIR spectrum is shown in Figs. 7.5b and c. When comparing the unmodified BTO with the BTO@PDA spectrum in Fig. 7.5c, new characteristic absorption peaks at 1291 cm^{-1} and 1625 cm^{-1} were observed in the latter material system. These peaks are attributed to the bending and stretching vibrational modes of -C-O and -N-H bonds in PDA, demonstrating that BTO was successfully modified by PDA[224]. In addition, the broad characteristic absorption peak at 3432 cm^{-1} of -OH and -NH bonds indicated the presence of hydrogen bond interaction between PDA and BTO. With the introduction of CCNF, the CCNF-BTO@PDA sample inherited all the characteristic absorption peaks of CCNF. In

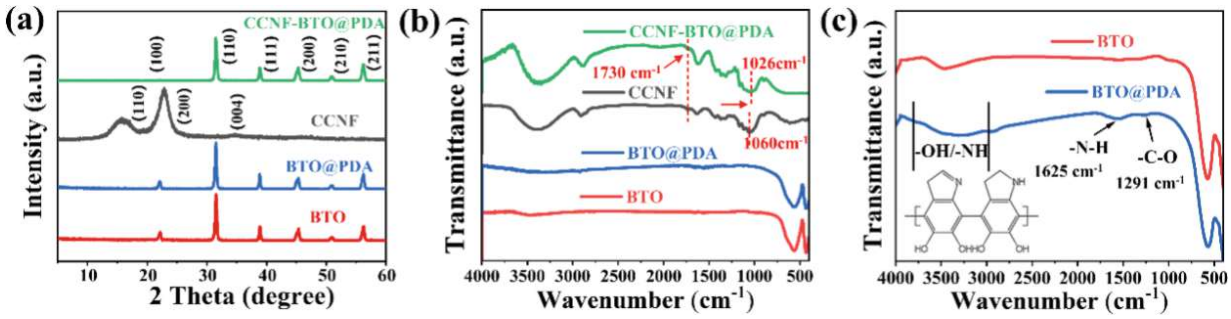

Figure 7.5. XRD patterns of **(a)** BTO, BTO@PDA, CCNF and CCNF-BTO@PDA and FTIR spectra of **(b-c)** BTO, BTO@PDA, CCNF and CCNF-BTO@PDA[150].

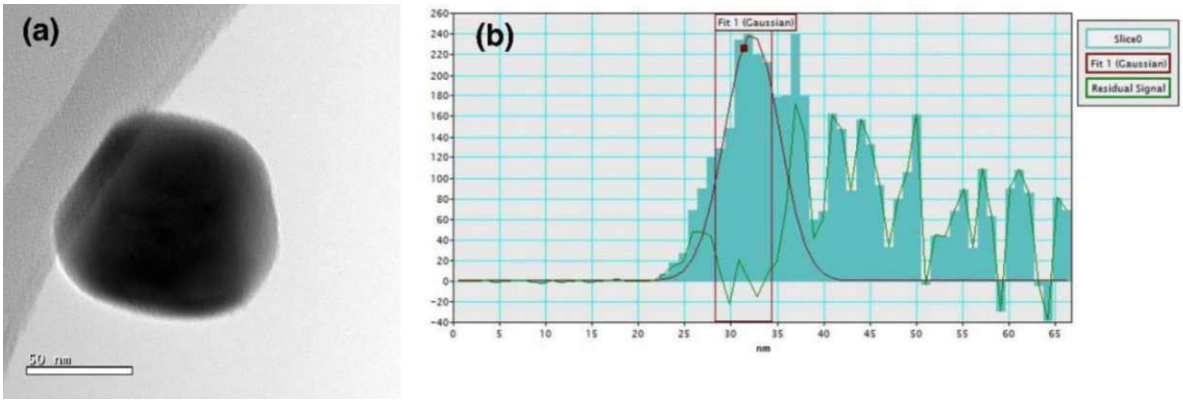

Figure 7.6. (a) BTO@PDA single nanoparticle in CCNF-BTO@PDA mixture at TEM microscope, where no PDA layer is visibly apparent. (**b**) Spectrum profile of carbon performed at TEM, revealing that the PDA layer is approximately 6 nm thick.

particular, the absorption peak at 1730 cm^{-1} highlighted in Fig. 7.5b, attributed to the C=O stretching vibration of -COOH in CCNF, confirmed the successful introduction of CCNF[225]. Moreover, compared to the pure CCNF infrared spectrum, the absorption peak in CCNF-BTO@PDA shifted from 1060 cm^{-1} to 1026 cm^{-1}. This blue shift is likely due to the hydrogen bond interactions and physical electrostatic interactions between the -COOH groups in CCNF and -OH in PDA[226].

For direct observation of the PDA layer on the surface of the BTO nanoparticles, the CCNF-BTO@PDA mixture was analysed by TEM at TU Wien. Fig. 7.6a shows a TEM image of a BTO nanoparticle from the CCNF-BTO@PDA mixture. Although the TEM analysis did not detect any visible PDA layer, a carbon spectrum profile was conducted, revealing a 6 nm thick PDA layer on top of the nanoparticles, as shown in Fig. 7.6b. This finding further confirms the successful functionalization with the PDA of BTO in the CCNF-BTO@PDA mixture.

7.2 Nanoparticles dispersion in P(VDF-TrFE) matrix

Properly dispersing the nanoparticles within the polymer solution before spin-coating is crucial for obtaining high-quality nanocomposite thin films. As discussed in previous chapters, surface functionalization is suggested in literature to improve nanoparticle dispersion. However, functionalization alone may not be sufficient to achieve optimal dispersion. Other parameters must be also considered, such as the viscosity of the polymer

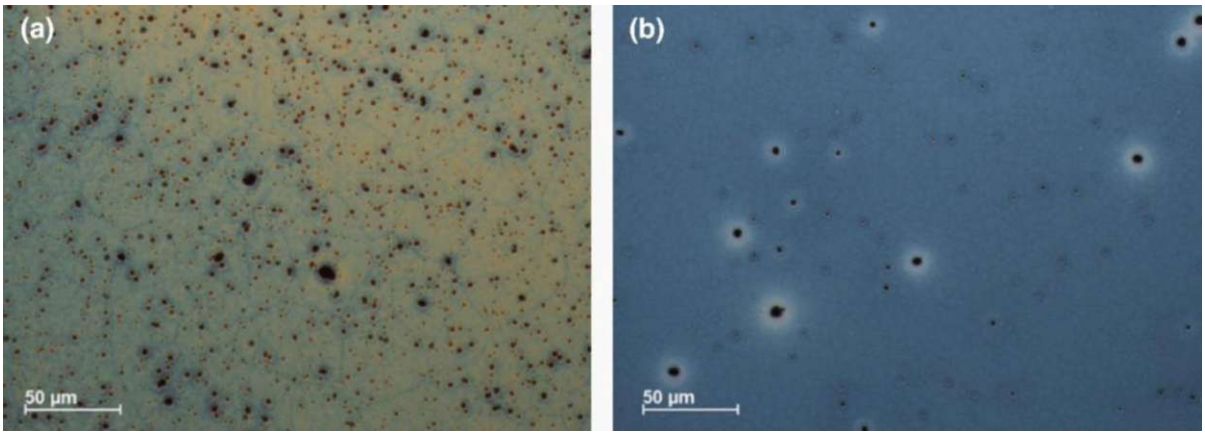

Figure 7.7. Optical micrograph of P(VDF-TrFE)-based nanocomposite thin films showing the dispersion quality of the nanoparticles within the polymer thin film. (**a**) and (**b**) present the improvement in dispersion before and after optimization of parameters such as viscosity of the polymer solution, sonication power, and its duration.

solution (proportional to the amount of P(VDF-TrFE) powder dissolved within the MEK), and the duration and power supplied during the sonication process. Figs. 7.7a and b illustrate the impact of these parameters on nanoparticle dispersion. Specifically, Fig. 7.7a presents an optical micrograph showcasing poor dispersion, where micrometre-sized clusters of BTO$^{(C)}$@PDA are visible within the P(VDF-TrFE) matrix. In contrast, Fig. 7.7b shows that by reducing the viscosity of the polymer solution (achieved by decreasing the P(VDF-TrFE) powder concentration from 8% to 6% by weight) and by increasing the power (from 100 W to the maximum 150 W) and duration (from 1 hour to 1.5 hours) of the sonication, the number of visible clusters was substantially reduced. Nevertheless, the sonication process has limits on maximum power supply and duration, with practical processing time usually set to 1.5 hours. Additionally, preliminary investigation showed that the viscosity cannot be decreased below 6% by weight to ensure the realization of sufficiently thick and homogenous thin films for electrical characterization[227].

To further improve dispersion, it is important to consider that BTO$^{(C)}$ nanoparticles are stored in plastic containers, where they tend to agglomerate due to physical bonding, such as Van der Walls forces. It was demonstrated (see Chapter 4.2.1) that magnet stirring used during PDA functionalization does not provide sufficient energy to break these bonds, resulting in the functionalization of entire agglomerates of BTO$^{(C)}$ nanoparticles. Fig. 7.8a shows a SEM image where the functionalization occurred on agglomerated nanoparticles rather than on individual ones. To address this issue, a pre-sonication step was added before PDA

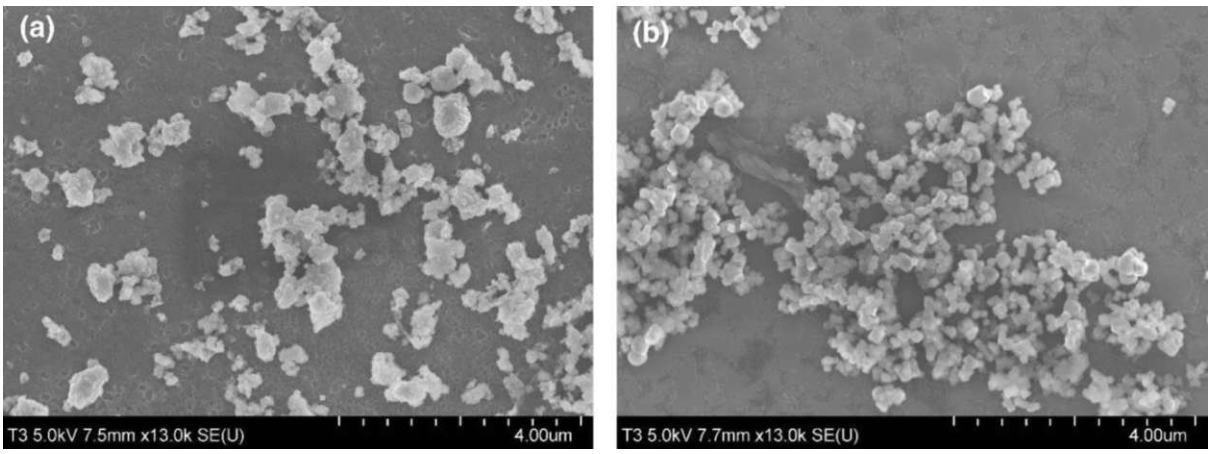

Figure 7.8. SEM images displaying the BTO$^{(C)}$ nanoparticles functionalized without (**a)** and with (**b)** pre-sonication. The pre-sonication step provided sufficient energy to break the agglomerations within the nanoparticle powder, allowing for effective functionalization of the individual nanoparticles.

polymerization. By introducing this step before functionalization, as described in Chapter 4.2.1 and illustrated in Fig. 4.5, the nanoparticles were functionalized in a non-agglomerated state. The results are shown in Fig. 7.8b, where properly functionalized BTO$^{(C)}$ cubic shape crystals are visible. This integration further improved the reduction of clusters, leading to a more uniform distribution of nanoparticles within the polymer thin film, as evidenced by the optical micrograph images in Fig. 7.9.

Once a homogenous dispersion of the nanoparticles was achieved, electrical characterizations of nanocomposite thin films were conducted. However, despite the improved dispersion, P(VDF-TrFE)-based nanocomposite thin films loaded with BTO$^{(C)}$@PDA nanoparticles exhibited poor electrical performances and, as a result, were never fully characterized. The MFM capacitors fabricated frequently suffered from short circuits, which hindered a proper scientific investigation. The underlying reason for the low-quality outcome, however, remained unclear.

In contrast, the nanoparticle batch provided by Shanghai University, *i.e.* the CCNF-BTO@PDA mixture, resulted in the fabrication of working and effectively measurable micromachined capacitors. These capacitors allowed for a comprehensive analysis, including crystalline phase analysis, dielectric properties, breakdown field studies, and energy storage characterization of the nanocomposite thin films. Due to the successful results with the Shanghai University batch, the BTO$^{(C)}$@PDA nanoparticles commercially purchased were thus abandoned.

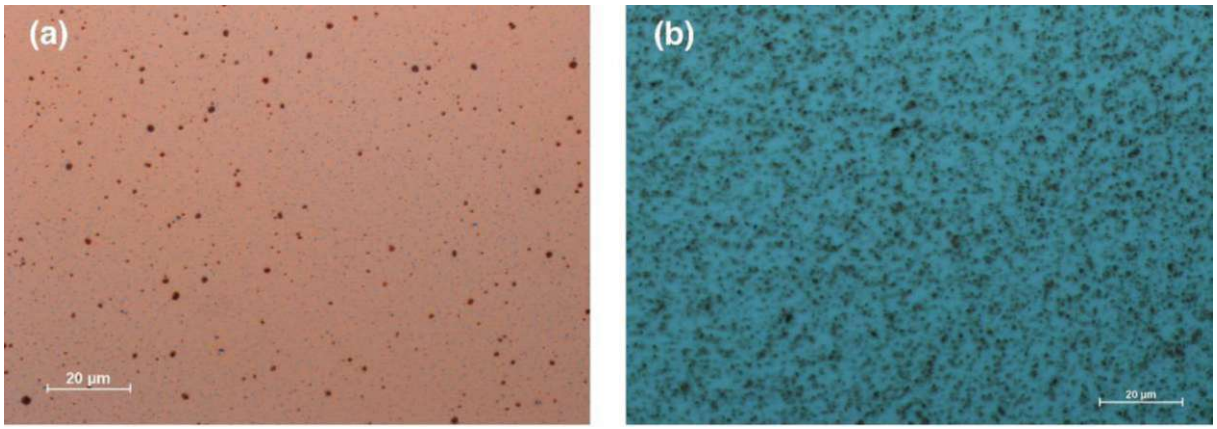

Figure 7.9. Optical microscope images illustrating the improvements in nanoparticle dispersion comparing (**a**) without and (**b**) with pre-sonication step in P(VDF-TrFE)-based nanocomposite thin films.

7.3 P(VDF-TrFE)-based nanocomposite crystalline phase analysis

P(VDF-TrFE)-based nanocomposites loaded with CCNF-BTO@PDA nanoparticles were subjected to crystalline phase analysis. Fig. 7.10a presents the FTIR spectra of pure and nanocomposite P(VDF-TrFE) thin films with different CCNF-BTO@PDA weight fractions. Notably, no distinct new absorption peaks emerged in the nanocomposite films. The spectra revealed two strong absorption bands at 845 cm^{-1} and 1277 cm^{-1}, which can be attributed to the CF_2 vibration and CH_2 rocking modes of the all-trans conformation characteristic of the low-temperature P(VDF-TrFE) phase (also called β-phase due to the similarity to the β-phase of pure PVDF). The typical β-phase peak at 1073 cm^{-1} is likely masked by the high intensity SiO_2 peak at 1091 cm^{-1} present in the substrate. The absorption bands at 880 cm^{-1}, 1183 cm^{-1}, and 1406 cm^{-1} are instead barely sensitive to chain conformation, showing a contribution of both α- and β-phase to their intensity[200]. Peaks related to the α-phase, such as at 763 cm^{-1}, have not been detected, likely due to the presence of the SiO_2 layer, which exhibits a broad peak at 795 cm^{-1} [228]. This overlap created an indistinct region, rendering the already low intensity α-phase and SiO_2 peaks unidentifiable[41]. In conclusion, according to the FTIR analysis, the addition of CCNF-BTO@PDA nanoparticles did not alter the chain conformation of the P(VDF-TrFE) matrix confirming the presence of the ferroelectric β-phase.

Fig. 7.10b shows the XRD patterns of the same samples. At a 2θ value of 19.7°, the diffraction peak corresponding to the (110) and (200) orientation plane of the pseudohexagonal crystallographic microstructure of the low-temperature ferroelectric

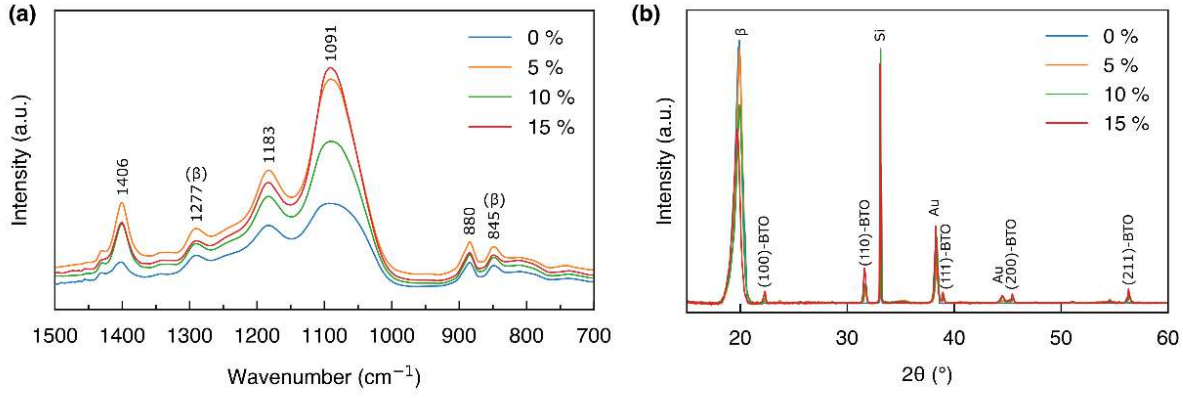

Figure 7.10. (**a**) FTIR spectrum (absorbance) and (**b**) XRD pattern of P(VDF-TrFE)-based nanocomposite thin films with different CCNF-BTP@PDA weight fractions[150].

β-phase was identified[41]. However, a noticeable decrease was observed in the intensity of such peak as the weight fractions of CCNF-BTO@PDA nanofillers increased. While previous research demonstrated an increase in the β-phase content with the introduction of BTO@PDA in P(VDF-TrFE) thin films[149], no reports have addressed the impact of introducing CCNF in P(VDF-TrFE). The observations reported in this study suggest a potential reduction in the ferroelectric β-phase of P(VDF-TrFE) likely due to the presence of CCNF. Additionally, a detailed comparison between the XRD patterns in Fig. 7.10b and Fig. 7.5a identified all the peaks corresponding to the presence of BTO. The peaks at 2θ values of 33°, 38.2°, and 44.6° were detected and attributed instead to silicon and gold components, representing the wafer substrate and the electrode material, respectively.

7.4 Energy Storage Characterization

7.4.1 Dielectric analysis

The dielectric permittivity is a fundamental parameter in energy storage characterization. In this work, its value was measured at a frequency of 100 Hz as a function of the nanoparticle weight fraction using micromachined capacitors with a diameter of 5 mm. The results obtained from multiple samples with respective error bars are shown in Fig. 7.11a. It was observed that the permittivity increases almost linearly with the nanoparticle weight fraction with an acceptable degree of uncertainty. This trend provides a significant advantage

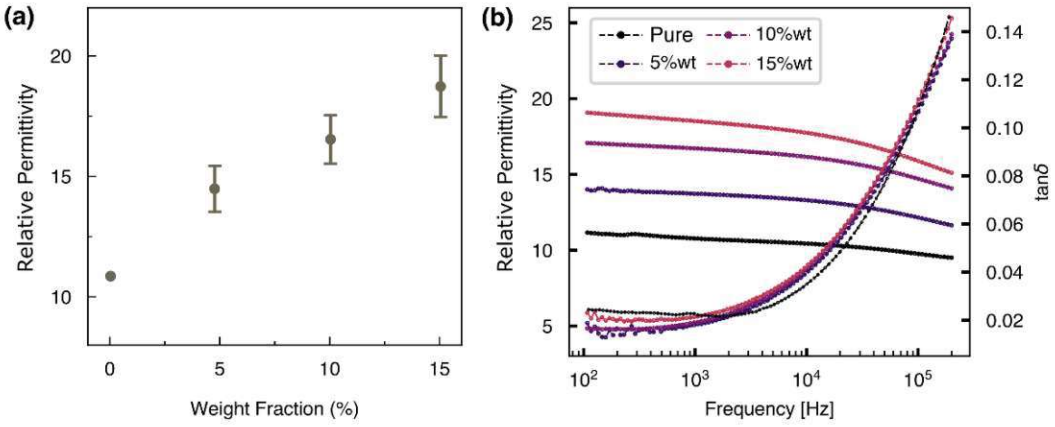

Figure 7.11. Dielectric characterization of nanocomposite thin films, in particular (**a**) variation of the relative permittivity measured at 100 Hz with filler loading and the corresponding error bars, and (**b**) relative permittivity and dielectric loss of CCNF-BTO@PDA nanocomposites as a function of frequency, both at room temperature. The permittivity increases with nanoparticle weight fraction, showing acceptable uncertainty[150].

for energy storage applications[229] and demonstrates consistency with previous findings in similar P(VDF-TrFE) nanocomposite thin films[230]. In particular, starting with a measured relative permittivity of 11 for pure P(VDF-TrFE), the introduction of BTO@PDA mixed with CCNF resulted in an increased relative permittivity, reaching a maximum value of 19 at a 15% weight fraction.

Additional characterization is shown in Fig. 7.11b, where both the dielectric permittivity and the dielectric loss of the nanocomposite thin films at varying CCNF-BTO@PDA loadings are presented as a function of the frequency. Representative samples, which closely aligned with the repeated permittivity measurements at 100 Hz were used. The observed decrease in relative permittivity is attributed to the dielectric relaxation of the P(VDF-TrFE) matrix. On the other hand, the dielectric loss showed a minimal difference between the nanocomposite and the pure polymer thin films, attesting to the good quality of the nanocomposite layers fabricated. In general, with an increase in frequency, the tanδ increases due to the higher energy dissipation from polymer dielectric relaxation at higher frequencies[103]. The reported dielectric loss findings in this study align closely with previous research on P(VDF-TrFE)-based nanocomposites loaded with BTO@PDA nanofillers[144].

Further analysis at 100 Hz as a function of temperature was performed to study the dielectric permittivity behaviour of the material. Using the climate chamber VCL 4006, described in Chapter 5.4, the permittivity was measured from representative samples as a function of temperature and plotted as presented in Fig. 7.12. As expected in polymers, the

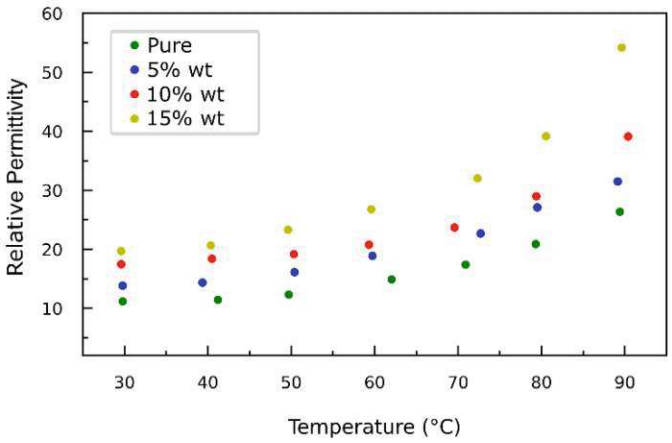

Figure 7.12. Relative permittivity of pure and nanocomposite P(VDF-TrFE) thin films measured at 100 Hz in the climate chamber VCL 4006 as a function of temperature. In polymers, heating increases the mobility of the chains, allowing the dipoles to orient more easily in the direction of the electric field.

dielectric permittivity showed a proportional relation with temperature: increasing the temperature enhances the mobility of the molecular chains, allowing the dipoles to be more easily oriented in the direction of the electric field. The similar trend showed by both the pure and the nanoparticles loaded samples further indicates the quality and stability of the fabricated nanocomposite thin films.

7.4.2 Electric breakdown field

For testing the energy storage performance of the nanocomposite thin films, MFM capacitors were subjected to dielectric strength characterization. As discussed in Chapter 3.2.1, the electric breakdown field is a crucial factor for determining the energy storage characteristics of a material. Initially, pure P(VDF-TrFE) thin films were tested to establish a baseline using capacitor-type test structures with diameters ranging from 6 to 8 mm. Following the characterization technique described in Chapter 5.6, an I/V curve, as shown in Fig. 7.13a, was obtained. It is important to highlight that the measured values are limited by the resolution of the minimum and maximum current range; therefore, the appearance of a signal at a certain voltage, approximately 650 V in this case, determined the breakdown point. Since the P(VDF-TrFE) thin film was approximately 2 μm thick, the electric breakdown field measured was calculated around 325 $V \cdot \mu m^{-1}$, in good agreement with previous research[103,231]. When the CCNF-BTO@PDA mixture was introduced into the polymer thin film, as expected, a significant reduction of the dielectric strength was observed. Scientific

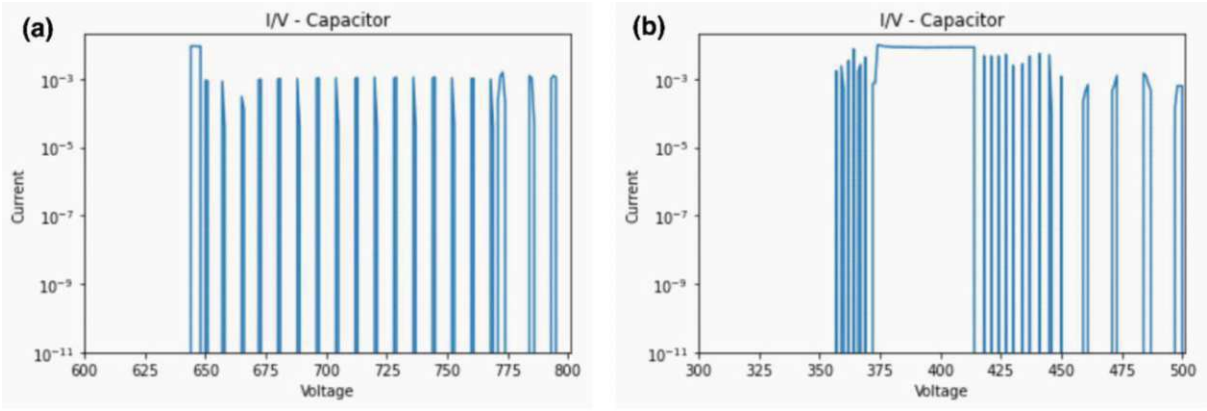

Figure 7.13. I/V curves representing the dielectric breakdown voltage of **(a)** pure and **(b)** 5% weight-loaded nanocomposite P(VDF-TrFE) thin films, both approximately 2 μm thick, obtained using capacitor-type test structures with diameters ranging between 6 to 8 mm. The introduction of CCNF-BTO@PDA nanoparticles within the polymer matrix significantly reduced the breakdown strength of the material of approximately 50%.

literature focusing on the energy storage characteristics of fluoropolymer-based nanocomposites has primarily studied polymer films with a thickness ranging between 10 and 40 μm[98,120,146,147,148]. In general, thinner films exhibit a higher density of surface and bulk defects (e.g. pits, dimples, contaminants, roughness, wrinkles, and variable thickness), making them more susceptible to localized breakdown. Since the MEMS devices based on ferroelectric polymer fabricated in our research group have an upper limit in their thickness due to the fabrication process and in the voltage supply of our setup, this study embraced the challenge of characterizing nanocomposite thin films with a thickness of around 2 μm, significantly thinner than those typically found in literature. Fig. 7.13b presents the I/V curve for a P(VDF-TrFE)-based nanocomposite thin film with a 5% weight fraction of nanofiller loading, showing a breakdown field of 175 V·μm^{-1}. This value, although way lower than that of pure P(VDF-TrFE) thin films, is nonetheless comparable to the approximately 200 V·μm^{-1} typically found in thicker film[103,144]. However, the result shown in Fig. 7.13b was found to be an outlier. Most measurements showed breakdowns occurring at significantly lower voltages, often half of the value presented in Fig. 7.13b, resulting in much lower breakdown strengths than those reported in literature. In some cases, measurements did not even take place due to

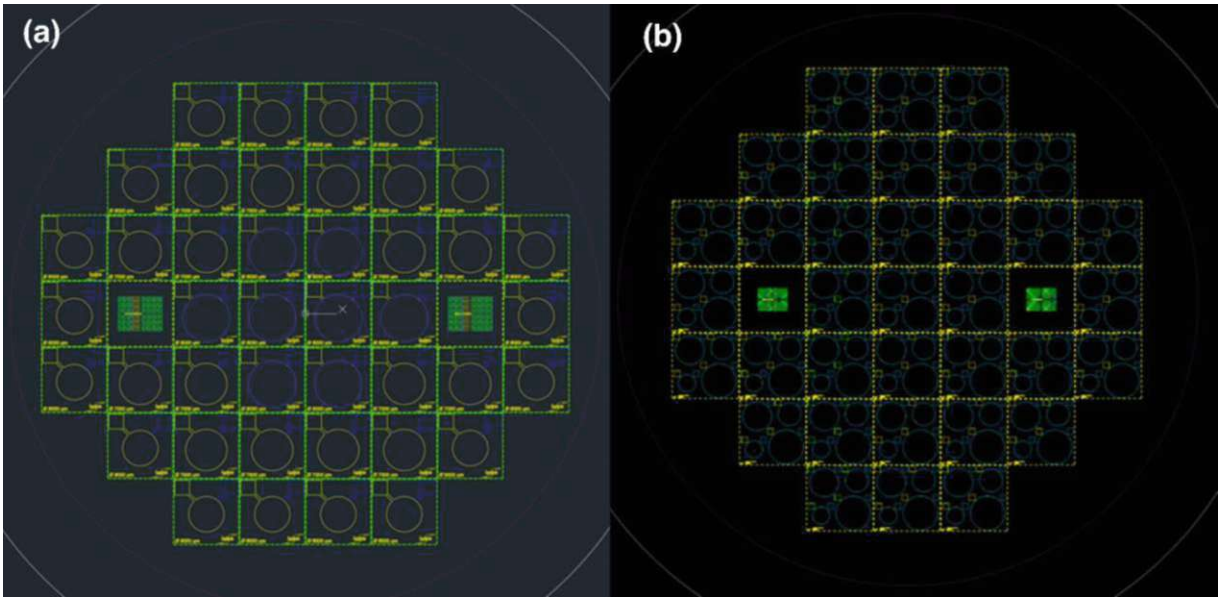

Figure 7.14. Design of the photolithography masks used for **(a)** pure and **(b)** nanocomposite P(VDF-TrFE) thin films electrical characterization. The use of a mask with reduced capacitor diameter was intended for the nanocomposites to increase the likelihood of finding electrically characterizable capacitors while maintaining low leakage current, which is essential for high quality ferroelectric characterization. However, even this adjustment did not facilitate a robust Weibull distribution for an in-depth dielectric breakdown strength analysis.

premature breakdown at the beginning of the tests, likely caused by the high density of defects within the thin film. To accurately study and determine the electric breakdown field of a material, the Weibull distribution is widely used as a statistical and modeling method. However, a robust statistical analysis requires a high number of measurements, which was not possible in these conditions.

The thin films approximately 2 μm thick used in this study can have their performance easily compromised by even a small cluster of nanoparticles, which are on average 145 nm in size (see Fig. 4.8b). To address this issue, a potential solution was proposed, previously mentioned in Chapter 4.2.3 and explained in detail in the following. Considering that nanoparticle clusters are randomly formed and distributed within the polymer thin film, it was hypothesized that reducing the electrode surface area would have increased the likelihood of finding clean and electrically characterizable capacitors. Initially, capacitors with diameters of 1 and 2 mm were designed. However, this reduction in size led to side effects, such as lower capacitance, which hindered the electrical characterization of the material. The low capacitance impeded proper ferroelectric characterization, and reducing the diameter showed to not significantly improve dielectric strength measurements enough to compensate for the poor ferroelectric performances. A compromise between these conflicting requirements was found with capacitor diameters between 3 and 5 mm in diameter, enabling effective ferroelectric characterization. Figs. 7.14a and b presents the two photolithography masks used within this work to fabricate micromachined capacitors, with diameters of 6 to 8 mm and 3 to 5 mm, respectively. While pure ferroelectric polymer thin films have been well characterized using capacitors of 6 to 8 mm in diameter, the 3 to 5 mm capacitors, with a preference for 5 mm, were used for nanocomposite thin films. However, despite these adjustments, the dielectric strength characterization of the nanocomposite thin films remained challenging, with persistent issues affecting the quality and reliability of the results. The inconsistent outcomes obtained in this study prevented the development of a robust Weibull distribution study for the dielectric strength in P(VDF-TrFE) nanocomposite thin films.

7.4.3 Energy density, energy loss, and energy efficiency

Even though a dielectric strength characterization was not possible, the thin nanocomposite films could still withstand enough electric fields to undergo polarization reversal. Therefore, the ferroelectric characterization to determine the impact of the nanofillers

on energy density, energy loss, and energy efficiency was possible. Using the 5 mm diameter micromachined capacitors, the hysteretic response of the electric displacement *D* as a function of electric field *E* was measured. *D-E* loops of representative samples of the pure and nanocomposite thin films, each with varying CCNF-BTO@PDA loadings, were fitted applying the empirical model developed by Miller *et al.*[196], as shown in Fig. 7.15. The quality of the fit with respect to the raw data is illustrated in Fig. 7.16. The fitting served the extraction of parameters such as E_c and P_r whose values are reported in Table 6 and further illustrated in Fig. 7.17a with error bars. Due to the randomized distribution of nanoparticles within the polymer thin films, an analysis across multiple samples was conducted to determine the ferroelectric properties. Because of the robust background data from previous research, multiple analysis was not performed on pure P(VDF-TrFE) thin films. Table 6 reports the E_c and P_r values obtained with their respective uncertainties. Notably, an increase in nanoparticle content resulted in a simultaneous decrease in both remnant polarization and coercivity mean values, with the former decreasing more significantly than the latter. The trend is observed despite the error bars. This observation aligns with the XRD pattern, which indicated a decrease in the ferroelectric β-phase content with increasing nanofiller loadings. In general, the E_c mean values remained relatively constant (see Table 6) up to a weight fraction of 10%, consistent with the value of pure P(VDF-TrFE) thin films[41,48,52]. A noticeable drop to a mean value of 49.8 V·μm^{-1} was instead observed at 15%. However, some level of uncertainty in E_c data should be considered, as certain error bars show overlap. The more significant decrease was found instead in P_r, with a reduction from 5.6 μC·cm^{-2} in pure P(VDF-TrFE), in good agreement with values from literature[52,41,48], to a mean value of 3.9 μC·cm^{-2} at a

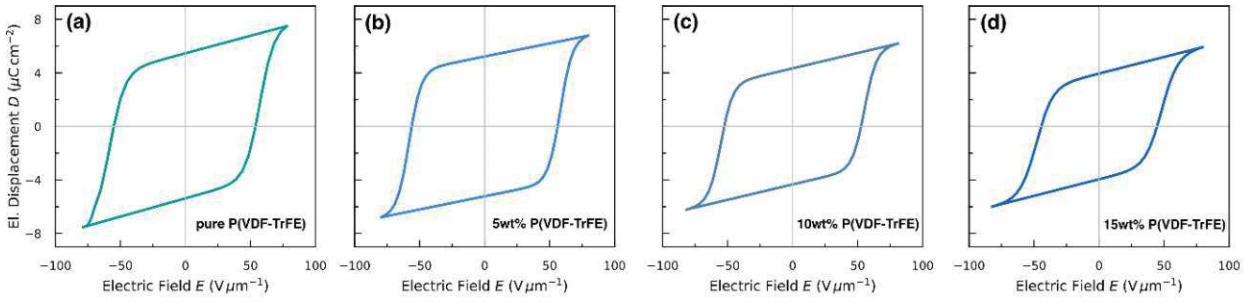

Figure 7.15. Electric displacement as a function of the electric field (*D-E* hysteresis) fitted with the Miller model of representative samples of pure P(VDF-TrFE) (**a**) and nanocomposite thin films at various CCNF-BTO@PDA loadings (**b)(c)(d).** The introduction of the nanofillers resulted in a shrinkage of the loops, leading to a consequent reduction in the remnant polarization value and coercivity[150].

15% weight fraction (Table 6 and Fig. 7.17a). The decrease in P_r, combined with an optimized dielectric permittivity, contributed to an improved energy density in the material[26], as presented in Fig. 7.17b. Here the error bars presented a more consistent behaviour. The energy density was calculated by integrating the area between the discharge curve (indicated by a

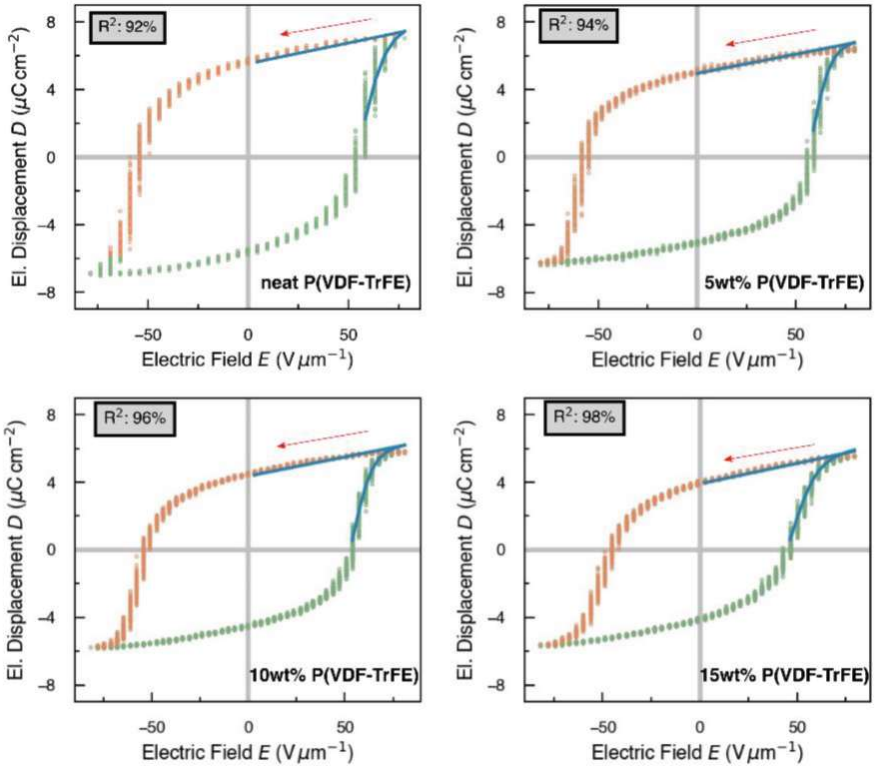

Figure 7.16. Example of collected data for the electric displacement D as a function of the electric field E of pure and nanocomposite P(VDF-TrFE) thin films (orange and green dots) fitted with the Miller model (blue line). The R^2 values of the fitting procedure are reported on the top left[150].

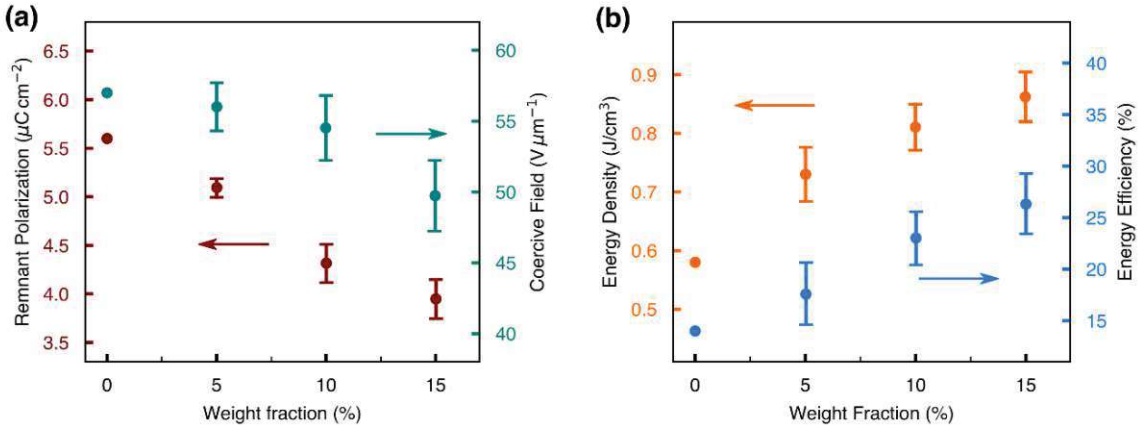

Figure 7.17. (**a**) Variation of E_c and P_r (**b**) energy density and energy efficiency with corresponding error bars of P(VDF-TrFE) thin films at different CCNF-BTO@PDA loadings from 0% to 15% weight fraction. In these two plots, the impact of the CCNF-BTO@PDA on the polymer matrix is shown through the changes in ferroelectricity, resulting in improved energy-related properties[150].

red arrow in Figure 7.16) and the ordinate axis. These calculations were performed by fitting the data limited to the first quadrant of the chart (see Figure 7.16). The reported coefficients of determination (R^2) ranged between 92% and 95%, indicating a high quality of the fit. Next, the energy efficiency was calculated as the ratio between discharged and charged energy values. However, due to the inability to apply extremely high electric fields, the energy stored by the capacitors in this study showed significantly lower values compared to those reported in literature for thicker films, which can withstand higher electric fields and store up to 5 $J \cdot cm^{-3}$ in P(VDF-TrFE)-based nanocomposite[103,105,148]. Nevertheless, this study aims to demonstrate that substantial improvements in energy storage properties can be achieved through the introduction of nanofillers, even in extremely thin layers. Furthermore, these findings offer valuable insights for applications that operate at lower voltages and explore a new nanofiller mixture that has not yet been investigated. Fig. 7.17b illustrates the energy density and energy efficiency values of the pure and nanocomposite P(VDF-TrFE) thin films at different CCNF-BTO@PDA loadings with the corresponding error bars. Starting from an initial value in the pure P(VDF-TrFE) of 0.58 $J \cdot cm^{-3}$ energy density and 14% energy efficiency, these parameters increased to a mean value of 0.86 $J \cdot cm^{-3}$ and 26.5%, respectively. Remarkably, the P(VDF-TrFE) based nanocomposite with a 15% weight fraction of CCNF-BTO@PDA demonstrated a nearly 50% improvement in energy density and almost a twofold increase in energy efficiency. The statistical analysis generally showed a wide range of values, with some overlaps between different weight fractions. Results outside the main range were excluded. Overall an improvement greater than the uncertainty was observed in energy density and efficiency correlated with the introduction of nanoparticles.

Following the study of the permittivity behaviour as a function of temperature (see Fig. 7.12), an analysis of the ferroelectric response, and thus of the energy density and efficiency, of the pure and nanocomposite P(VDF-TrFE) thin films of representative samples was conducted using the climate chamber VCL 4006. Analogous to the dielectric permittivity study, the temperature was ramped from room temperature up to 90 °C, with data for plotting the hysteresis curve collected at every 10 °C increment. Fig. 7.18 shows these data, displaying the different hysteresis loops with colours ranging from green to red, thus indicating the increasing temperature. In general, similar behaviour by a shrinking of the hysteretic response was observed in all the samples. This effect is attributed to the approach towards the Curie

temperature of P(VDF-TrFE), at which the material transitions into a paraelectric state. In this state, the electroactive crystalline domains become embedded in a soft amorphous matrix[52], leading to a decrease in electroactivity and remnant polarization. Notably, the stability of the *D-E* loop with increasing temperature differed between the samples. In pure P(VDF-TrFE), the remnant polarization decreased slightly at first, with a more pronounced drop from 4 μC·cm^{-2} to 2.2 μC·cm^{-2} observed at 90 °C. In contrast, the introduction of the CCNF-BTO@PDA nanofillers into the polymer matrix increased the sensitivity of the thin films to temperature changes, resulting in a more gradual and linear decrease in both remnant polarization and coercive field as the temperature rose. Fig. 7.19 reports the energy density,

% weight fraction	0%	5%	10%	15%
E_c (V·μm^{-1})	57	56 ± 1.8	54.5 ± 2.4	49.8 ± 2.6
P_r (μC·cm^{-2})	5.6	5.1 ± 0.1	4.3 ± 0.2	3.9 ± 0.25

Table 6. Coercive field and remnant polarization of pure and nanocomposite P(VDF-TrFE) thin films as a function of the nanofiller weight fraction with their uncertainties[150].

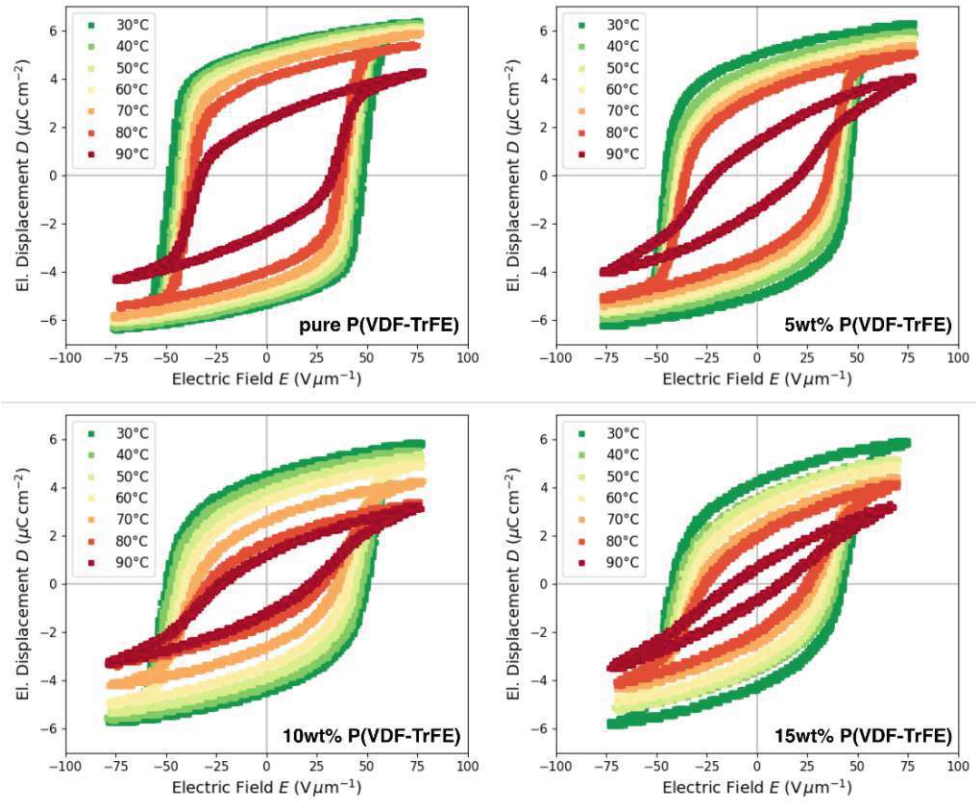

Figure 7.18. *D-E* loops of pure and nanocomposite P(VDF-TrFE) thin films as a function of temperature, ranging from 30 °C to 90 °C. A shrinking of the hysteretic response is observed as the temperature approaches the Curie point, more markedly in the nanocomposite samples.

energy loss, and energy efficiency of the samples as a function of temperature. The temperature significantly impacted the energy storage properties, particularly affecting the energy loss due to the shrinkage of the hysteresis loops observed in Fig. 7.18. The energy loss, which is represented by the area within the hysteresis curve, decreased up to 80% in value as the temperature increased. In contrast, the energy density increased by 40% at 90 °C from room temperature. With both energy loss decreasing and energy density increasing, energy efficiency also benefited, reaching up to 66% at 90 °C with 15% by weight of nanofillers. Overall, comparing the pure P(VDF-TrFE) thin film to those loaded with 5%, 10%, and 15 % by weight of the CCNF-BTO@PDA nanoparticle mixture, as previously illustrated in Fig. 7.17b, revealed significant enhancements in both energy density and energy efficiency, highlighting the advantages of using the nanoparticles mixture presented in this work to improve the energy storage performance of P(VDF-TrFE) thin films.

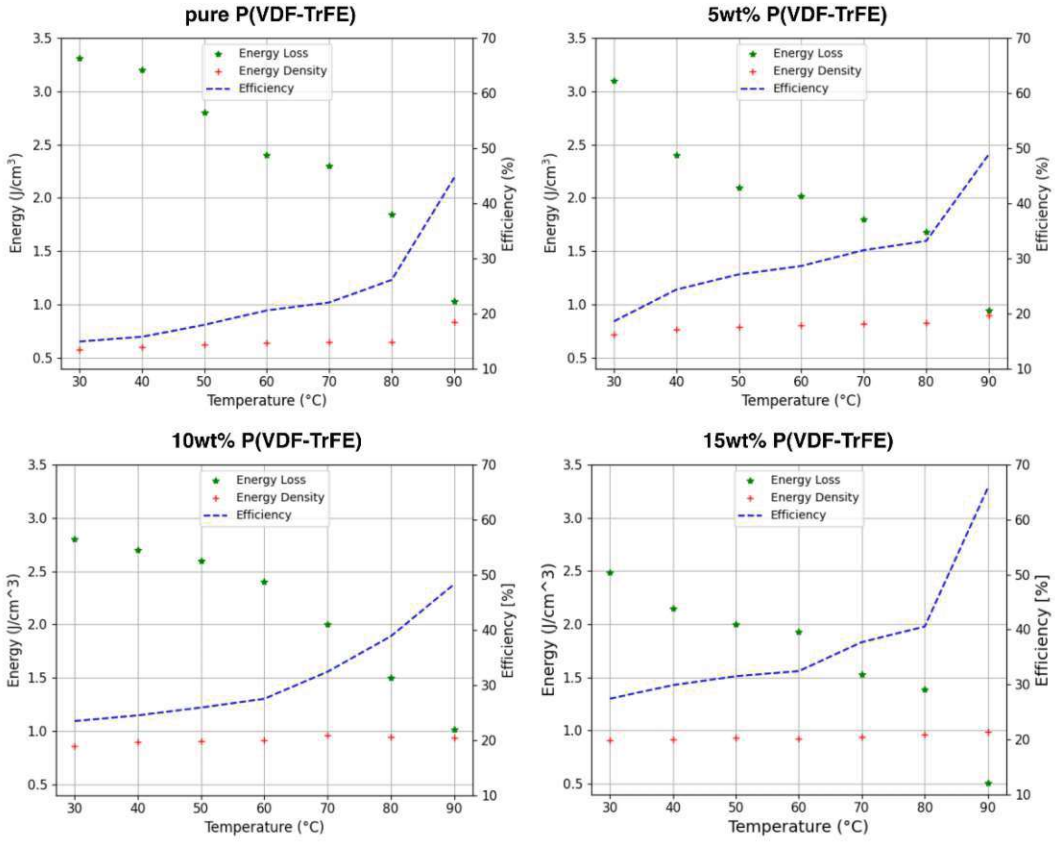

Figure 7.19. Representation of the energy density, energy loss, and energy efficiency as a function of temperature, calculated from the *D-E* loops of pure and nanocomposite P(VDF-TrFE) thin films shown in Fig. 7.18. The temperature significantly affects mainly the energy loss, leading to an increase in the energy efficiency of the MFM, which reaches up to 66 % for the sample with 15% by weight of CCNF-BTO@PDA at 90 °C. The impact on energy density is positive, but less pronounced.

8 Conclusion and Outlook

8.1 Conclusion

This thesis explores two closely related studies for MEMS applications: the ferroelectric characterization of the electroactive polymers PVDF and P(VDF-TrFE), and the energy storage properties of P(VDF-TrFE) when applied as nanocomposite thin films.

The preliminary focus of this work was the synthesis, fabrication of capacitor-type test structures, and fundamental characterization of these materials. PVDF and P(VDF-TrFE) thin films, as well as P(VDF-TrFE)-based nanocomposite thin films, were deposited by spin-coating, a cost-effective, scalable industrial technique that offers precise control over film thickness and uniformity. Chapter 4 details the process of synthesizing solution-processed ferroelectric polymer thin films.

As discussed subsequently in Chapter 6, the fabrication process is crucial for achieving the desired crystalline phase and microstructure, the effects of which on the overall performance of the polymer thin films are investigated. For instance, successful electromechanical characterization of PVDF requires high-temperature substrates preheated to 170 °C before spin-coating. This process enabled the deposition of high-quality α-PVDF thin films, allowing for high-resolution AFM surface imaging and direct observation of the polymer chains. The measured unit-cell characteristics of α-PVDF through AFM were found to closely match established literature values, confirming the quality of this study. Additionally, the ferroelectric characteristic *D-E* of the electro-formed δ-PVDF was thoroughly investigated, with results showing an E_c = 113 V·µm^{-1} and a P_r = 4.7 µC·cm^{-2}, which are in good agreement with previous findings. This thesis also presents a study on the electrostrain behavior *S-E* of δ-PVDF under both high and low electric fields, demonstrating consistent values in the electrostrictive coefficient (Q_{33} = -2.4 m^4·C^{-2}) and piezoelectric coefficients (d_{33} = -39 pm·V^{-1} at high fields and d_{33} = -42.8 pm·V^{-1} at low fields), aligning with values reported in literature.

Unlike PVDF, P(VDF-TrFE) thin films did not require substrate pre-treatment but were demonstrated to be highly sensitive to annealing temperature. A morphological transition

from a rice-like to a spherulite-like microstructure was observed when the thin films were annealed at or above 145 °C. The spherulite-like microstructure, named for its resemblance to that of α-PVDF, exhibits distinct characteristics at the nanometre scale. AFM analysis revealed highly irregular lamellae with winding-like conformations and needle-shaped crystals, contrasting the high degree of regularity and packing of α-PVDF spherulites. XRD analysis confirmed the presence of the ferroelectric β-phase in spherulite-like samples, but revealed a substrate-dependent behaviour that contrasts with the rice-like thin films, showing a more pronounced peak on gold substrates compared to silicon. Subsequent ferroelectric analysis using MFM capacitors determined an E_c = 53 V·µm^{-1} and P_r = 4.7 µC·cm^{-2}, consistent with the results from rice-like thin films. Additionally, the *S-E* characteristic was measured, yielding a Q_{33} = - 2.4 m^4·C^{-2} and a d_{33} = -29.8 pm·V^{-1} at high fields, and a d_{33} = -31.8 pm·V^{-1} at low fields, still in good match with rice-like results. This study demonstrated that, despite the microstructural change, the electromechanical properties of the low-temperature phase of P(VDF-TrFE) remained largely unaffected. However, exposing both microstructures to thermal loading, where the samples were heated to nearly 90 °C and then cooled to room temperature, showed differing thermal stability. Specifically, after the first thermal loading, the spherulite-like microstructure experienced a 15 % decrease in remnant polarization, whereas no reduction was observed in the rice-like samples. XRD analysis revealed a partial crystalline phase shift from the strong ferroelectric β-phase to the γ-2b phase. While partial restoration of ferroelectric properties was observed by applying an electric field up to ± 150 Vµm^{-1}, which induced a transition back from the γ-2b phase to the β-phase, further thermal loading cycles a continued decline in the ferroelectric properties of the spherulite-like microstructure. After the third cycle, the remnant polarization had decreased by approximately 20%, in contrast to the rice-like samples which demonstrated stable electric performance under similar thermal conditions.

The energy storage characteristics of P(VDF-TrFE)-based nanocomposite thin films are investigated in Chapter 7. This chapter addresses the challenge of fabricating MFM capacitors with nanocomposite thin films approximately 2 µm thick, loaded up to 15% by weight of CCNF-BTO@PDA nanoparticle mixture, and subsequently electrically characterizing them. Despite the inherent difficulties associated with thinner films, such as potential surface and bulk defects that can significantly impact the device performance compared to thicker films,

which *de facto* limited the electric breakdown strength studies in this work precluding a robust Weibull distribution analysis, a comprehensive evaluation of the ferroelectric and energy storage properties is presented. The results demonstrated that the dielectric permittivity increases with CCNF-BTO@PDA loading, and combined with a reduction in remnant polarization, this led to improved energy storage characteristics. Compared to pure P(VDF-TrFE) thin films, which exhibited an energy density of 0.58 $J \cdot cm^{-3}$ and an energy efficiency of 14%, the 15% weight fraction CCNF-BTO@PDA nanocomposite thin films achieved an enhanced energy density of 0.92 $J \cdot cm^{-3}$ and an energy efficiency of 28%. Overall, this represents a doubling of energy efficiency and a 60% improvement in energy density.

8.2 Outlook – Future perspectives

The findings of this thesis open up several promising investigations for further research and technological advancement in the field of electroactive polymers. Specifically, the electromechanical studies on δ-PVDF have expanded the limited number of reports on this electro-formed phase, demonstrating its potential in spin-cast thin films. The piezoelectric coefficient obtained for δ-PVDF indicates that this phase could serve as a viable alternative to the more commonly studied ferroelectric β-phase for piezoelectric applications. However, the delicate processing conditions, particularly the need for high substrate temperatures, pose challenges that currently limit the practical exploration of δ-PVDF. Further research is essential to address these processing challenges and assess the feasibility of industrial-scale applications for δ-PVDF thin films.

The investigations into the rice-like and spherulite-like microstructures in P(VDF-TrFE) thin films underscored the critical role of the annealing temperature in the fabrication process. Achieving ferroelectric polymer with thermal and ferroelectric stability at high temperatures, particularly above current melting points, has long been a key objective in the field. However, it is equally crucial to expand the scientific understanding of applications operating below these temperatures, where different challenges may arise. The relationship between polymer thin films, the nature of the deposition substrate, and temperature is complex and multifaceted, often leading to unpredictable outcomes, such as changes in mechanical properties or phase transitions. Consequently, the impact of temperature variations and substrate materials in both application or fabrication environments on

ferroelectric polymers like P(VDF-TrFE) deserves further investigation. A deeper understanding of these factors will enable the optimization of these materials for specific uses, ultimately enhancing their performance and expanding their applicability.

In conclusion, the study on P(VDF-TrFE)-based nanocomposite thin films demonstrated the potential for significantly enhanced energy storage characteristics in 2 μm thick thin films with up to 15% weight fraction of CCNF-BTO@PDA nanoparticles. These findings suggest a promising direction for advancing practical applications involving micrometer-range thin films in energy storage devices, marking a notable shift from the current literature. However, a major limitation of this thesis was the significant drop in dielectric breakdown strength, which prevented a full characterization of the material. To address this challenge, future research should focus on improving techniques for nanoparticle dispersion and functionalization, as thinner films are more susceptible to the effects of sub-micrometer nanoparticle clusters, which could compromise the micromachined devices. Beyond this, the ability to fabricate nanocomposite fluoropolymer-based thinner films engineered for energy storage offers an innovative solution for applications where high voltages, usually required in the kV range, are not feasible. All in all, while nanocomposite materials remain a leading approach for developing advanced energy storage devices, overcoming challenges such as preventing significant reductions in dielectric strength and optimizing the nature and functionalization of nanofillers, while balancing the desired performance, remain critical areas for further studies.

Abbreviations

Abbreviation	Definition
AC	Alternating current
AFM	Atomic force microscopy
APS	Ammonium persulfate
BG	Grain boundary
CCNF	Carboxymethyl cellulose nanofibers
CNF	Cellulose nanofibers
DC	Direct current
DMF	Dimethylformamide
DSC	Differential scanning calorimetry
EDX	Energy dispersive x-ray analysis
FTIR	Fourier-transform infrared spectroscopy
GPIB	General purpose interface bus
HDPE	High-density polyethylene
InvOLS	Inverse optical lever sensitivity
MFM	Metal-ferroelectric-metal
MEMS	Microelectromechanical systems
MEK	Methyl ethyl ketone (2-butanone)
MFM	Metal-ferroelectric-metal
MMT	Montmorillonite
NC	Central nucleation point
NSC	Needle-shaped crystals
PDA	Polydopamine
PDMS	Polydimethylsiloxane
PMMA	Poly(methyl-methacrylate)
PP	Polypropylene

P(VDF-CTFE)	Poly(vinylidene fluoride-chlorotrifluoroethylene)
P(VDF-HFP)	Poly(vinylidene fluoride-co-hexafluoropropylene)
P(VDF-TrFE)	Poly(vinylidene fluoride and trifluoroethylene)
PVDF	Poly(vinylidene fluoride)
PVP	Polyvinylpyrrolidone
RH	Relative humidity
SEM	Scanning electron microscopy
TC-2	Titanate coupling agent
TEM	Transmission electron microscopy
VIPS	Vapor-induced phase separation
XRD	X-ray Diffraction

Nomenclature

Symbol	Definition	Unit
A	Area MFM capacitor	m^2
C_R	Reference capacitance	F
C_S	Sample capacitance	F
d	Lattice distance	m
D	Electric displacement	$\mu C \cdot cm^{-2}$
d_{31}	Transverse piezoelectric coefficient	$pm \cdot V^{-1}$
d_{33}	Longitudinal piezoelectric coefficient	$pm \cdot V^{-1}$
E	Electric field	$V \cdot \mu m^{-1}$
E_c	Coercive field	$V \cdot \mu m^{-1}$
E_{max}	Maximum electric field	$V \cdot \mu m^{-1}$
G	Gibbs potential	$kJ \cdot mol^{-1}$
I	Current	A
M	Field-related electrostrictive coefficient	$m^2 \cdot V^{-2}$
n	Integer number	1
P_i	Induced polarization	$\mu C \cdot cm^{-2}$
P_{max}	Maximum electric polarization	$\mu C \cdot cm^{-2}$
P_r	Remnant polarization	$\mu C \cdot cm^{-2}$
P_s^+	Polarization negative to positive E	$\mu C \cdot cm^{-2}$
P_s^-	Polarization positive to negative E	$\mu C \cdot cm^{-2}$
P_s	Spontaneous polarization	$\mu C \cdot cm^{-2}$
Q	Polarization-related electrostrictive coefficient	$m^4 \cdot C^{-2}$
Q_R	Electric charge stored in the reference capacitor	C
Q_S	Electric charge stored in the sample	C
R_1	Resistor 1 (Sawyer-Tower Circuit)	$k\Omega$
R_2	Resistor 2 (Sawyer-Tower Circuit)	$k\Omega$

S	Strain	1
t	Distance between the capacitor plates	μm
T	Mechanical stress	N
T_c	Curie temperature	$°C$
T_m	Melting temperature	$°C$
U_{CH1}	Voltage at CH1 of the oscilloscope	V
U_{CH2}	Voltage at CH2 of the oscilloscope	V
U_R	Voltage drop across the reference capacitor	V
U_S	Voltage drop across the sample	V
$tan\delta$	Loss tangent	1
U_e	Energy density	$J \cdot cm^{-3}$
U_l	Energy loss	$J \cdot cm^{-3}$
V	Voltage	V
v_f	Volume fraction	1
w_f	Weight fraction	1
ε	Dielectric permittivity	$F \cdot m^{-1}$
ε_0	Vacuum permittivity	$F \cdot m^{-1}$
ε_r	Relative permittivity	1
η	Energy efficiency	1
θ	Incident angle	1
λ	Wavelength	m
χ	Electric susceptibility	$C^2 \cdot N^{-1} m^{-2}$

References

(1) Curie, J.; Curie, P. *Développement Par Compression de l'électricité Polaire Dans Les Cristaux Hémièdres à Faces Inclinées* [Development by Compression of Polar Electricity in Hemihedral Crystals with Inclined Faces]. *Bull. la Société minéralogique Fr.* **1880**, *3* (4), 90–93.

(2) Eom, C. B.; Trolier-McKinstry, S. Thin-Film Piezoelectric MEMS. *MRS Bull.* **2012**, *37* (11), 1007–1017. https://doi.org/10.1557/mrs.2012.273.

(3) Heywang, W.; Lubitz, K.; Wersing, W. *Piezoelectricity*; Springer, Ed.; Springer Series in Materials Science; Springer Berlin Heidelberg: Berlin, Heidelberg, 2008; Vol. 114. https://doi.org/10.1007/978-3-540-68683-5.

(4) Rupitsch, S. J. *Piezoelectric Sensors and Actuators*, 2008th ed.; Topics in Mining, Metallurgy and Materials Engineering; Springer Berlin Heidelberg: Berlin, Heidelberg, 2019. https://doi.org/10.1007/978-3-662-57534-5.

(5) Valasek, J. Piezo-Electric and Allied Phenomena in Rochelle Salt. *Phys. Rev.* **1921**, *17* (4), 475–481. https://doi.org/10.1103/PhysRev.17.475.

(6) Markys, C. G. *Characterisation of Ferroelectric Bulk Materials and Thin Films*; Gmbh, S. B. H., Ed.; 2014.

(7) Kim, S. G.; Priya, S.; Kanno, I. Piezoelectric MEMS for Energy Harvesting. *MRS Bull.* **2012**, *37* (11), 1039–1050. https://doi.org/10.1557/mrs.2012.275.

(8) Newnham, R. E. *Piezoelectric Sensors and Actuators: Smart Materials*; Heiderlberg, 1992. https://doi.org/10.1109/freq.1992.269973.

(9) Muralt, P. Recent Progress in Materials Issues for Piezoelectric MEMS. *J. Am. Ceram. Soc.* **2008**, *91* (5), 1385–1396. https://doi.org/10.1111/j.1551-2916.2008.02421.x.

(10) Judy, J. W. Microelectromechanical Systems (MEMS): Fabrication, Design and Applications. *Smart Mater. Struct.* **2001**, *10* (6), 1115–1134. https://doi.org/10.1088/0964-1726/10/6/301.

(11) Tadigadapa, S.; Mateti, K. Piezoelectric MEMS Sensors: State-of-the-Art and Perspectives. *Meas. Sci. Technol.* **2009**, *20* (9). https://doi.org/10.1088/0957-0233/20/9/092001.

(12) Damjanovic, D.; Newnham, R. E. Electrostrictive and Piezoelectric Materials for Actuator Applications. *J. Intell. Mater. Syst. Struct.* **1992**, *3* (2), 190–208. https://doi.org/10.1177/1045389X9200300201.

(13) Kanno, I. Piezoelectric Thin Films for MEMS Applications. *Integr. Microsystems Electron. Photonics, Biotechnol.* **2017**, 679–698. https://doi.org/10.1201/b11205.

(14) Kawai, H. The Piezoelectricity of Poly (Vinylidene Fluoride). *Jpn. J. Appl. Phys.* **1969**, *8* (7), 975. https://doi.org/10.1143/jjap.8.975.

(15) Uchino, K.; Nomura, S. New Electromechanical Materials and Their Applications. *Jpn. J. Appl. Phys.* **1981**, *20*, 225–228. https://doi.org/10.7567/JJAPS.20S4.225.

(16) Taylor, P.; Furukawa, T. Phase Transitions : A Multinational Ferroelectric Properties of Vinylidene Fluoride Copolymers. *Phase Transitions* **1989**, *18* (January, 1989), 143–211.

(17) Liu, C. Recent Developments in Polymer MEMS. *Adv. Mater.* **2007**, *19* (22), 3783–3790. https://doi.org/10.1002/adma.200701709.

(18) Ramadan, K. S.; Sameoto, D.; Evoy, S. A Review of Piezoelectric Polymers as Functional Materials for Electromechanical Transducers. *Smart Mater. Struct.* **2014**, *23* (3). https://doi.org/10.1088/0964-1726/23/3/033001.

(19) Asadi, K.; De Leeuw, D. M.; De Boer, B.; Blom, P. W. M. Organic Non-Volatile Memories from Ferroelectric Phase-Separated Blends. *Nat. Mater.* **2008**, *7* (7), 547–550. https://doi.org/10.1038/nmat2207.

(20) Liu, K.; Ouyang, B.; Guo, X.; Guo, Y.; Liu, Y. Advances in Flexible Organic Field-Effect Transistors and Their Applications for Flexible Electronics. *npj Flex. Electron.* **2022**, *6* (1). https://doi.org/10.1038/s41528-022-00133-3.

(21) Garcia, V.; Bibes, M. Ferroelectric Tunnel Junctions for Information Storage and Processing. *Nat. Commun.* **2014**, *5*. https://doi.org/10.1038/ncomms5289.

(22) Mahapatra, S. Das; Mohapatra, P. C.; Aria, A. I.; Christie, G.; Mishra, Y. K.; Hofmann, S.; Thakur, V. K. Piezoelectric Materials for Energy Harvesting and Sensing Applications: Roadmap for Future Smart Materials. *Adv. Sci.* **2021**, *8* (17). https://doi.org/10.1002/advs.202100864.

(23) Li, C.; Wu, P. M.; Lee, S.; Gorton, A.; Schulz, M. J.; Ahn, C. H. Flexible Dome and Bump Shape Piezoelectric Tactile Sensors Using PVDF-TrFE Copolymer. *J. Microelectromechanical Syst.* **2008**, *17* (2), 334–341. https://doi.org/10.1109/JMEMS.2007.911375.

(24) Edqvist, E.; Hedlund, E. Design and Manufacturing Considerations of Low-Voltage Multilayer P(VDF-TrFE) Actuators. *J. Micromechanics Microengineering* **2009**, *19* (11). https://doi.org/10.1088/0960-1317/19/11/115019.

(25) Bhat, A.; Budholiya, S.; Raj, S. A.; Sultan, M. T. H.; Hui, D.; Shah, A. U. M.; Safri, S. N. A. Review on Nanocomposites Based on Aerospace Applications. *Nanotechnol. Rev.* **2021**, *10* (1), 237–253. https://doi.org/10.1515/ntrev-2021-0018.

(26) Prateek; Thakur, V. K.; Gupta, R. K. Recent Progress on Ferroelectric Polymer-Based Nanocomposites for High Energy Density Capacitors: Synthesis, Dielectric Properties, and Future Aspects. *Chem. Rev.* **2016**, *116* (7), 4260–4317. https://doi.org/10.1021/acs.chemrev.5b00495.

(27) Behera, R.; Elanseralathan, K. A Review on Polyvinylidene Fluoride Polymer Based Nanocomposites for Energy Storage Applications. *J. Energy Storage* **2022**, *48* (January). https://doi.org/10.1016/j.est.2021.103788.

(28) Wang, Y.; Yao, M.; Ma, R.; Yuan, Q.; Yang, D.; Cui, B.; Ma, C.; Liu, M.; Hu, D. Design Strategy of Barium Titanate/Polyvinylidene Fluoride-Based Nanocomposite Films for High Energy Storage. *J. Mater. Chem. A* **2020**, *8* (3), 884–917. https://doi.org/10.1039/c9ta11527g.

(29) Lovinger, A. J. Ferroelectric Polymers. *Adv. Phys.* **1992**, *41* (1), 1–57. https://doi.org/10.1080/00018739200101463.

(30) Li, M.; Wondergem, H. J.; Spijkman, M. J.; Asadi, K.; Katsouras, I.; Blom, P. W. M.; De Leeuw, D. M. Revisiting the δ-Phase of Poly(Vinylidene Fluoride) for Solution-Processed Ferroelectric Thin Films. *Nature Materials*. 2013, pp 433–438. https://doi.org/10.1038/nmat3577.

(31) Disnan, D.; Hafner, J.; Benaglia, S.; Teuschel, M.; Schneider, M.; Garcia, R.; Schmid, U. Nanostructural and Piezoelectric Characterization of Electro-Formed δ-Phase Poly(Vinylidene

Fluoride) Thin Films. *Materials Research Letters*. 2023, pp 296–303. https://doi.org/10.1080/21663831.2022.2150096.

(32) Costa, P.; Nunes-Pereira, J.; Pereira, N.; Castro, N.; Gonçalves, S.; Lanceros-Mendez, S. Recent Progress on Piezoelectric, Pyroelectric, and Magnetoelectric Polymer-Based Energy-Harvesting Devices. *Energy Technol.* **2019**, *7* (7), 1–19. https://doi.org/10.1002/ente.201800852.

(33) Martins, P.; Lopes, A. C.; Lanceros-Mendez, S. Electroactive Phases of Poly(Vinylidene Fluoride): Determination, Processing and Applications. *Prog. Polym. Sci.* **2014**, *39* (4), 683–706. https://doi.org/10.1016/j.progpolymsci.2013.07.006.

(34) Sarkar, L.; Singh, S. G.; Vanjari, S. R. K. Preparation and Optimization of PVDF Thin Films for Miniaturized Sensor and Actuator Applications. *Smart Mater. Struct.* **2021**, *30* (7). https://doi.org/10.1088/1361-665X/abff15.

(35) Yin, Z.; Tian, B.; Zhu, Q.; Duan, C. Characterization and Application of PVDF and Its Copolymer Films Prepared by Spin-Coating and Langmuir-Blodgett Method. *Polymers (Basel).* **2019**, *11* (12). https://doi.org/10.3390/polym11122033.

(36) Chen, B. T. Investigation of the Solvent-evaporation Effect on Spin Coating of Thin Films. *Polym. Eng. Sci.* **1983**, *23* (7), 399–403. https://doi.org/10.1002/pen.760230706.

(37) Weill, A.; Dechenaux, E. The Spin-coating Process Mechanism Related to Polymer Solution Properties. *Polym. Eng. Sci.* **1988**, *28* (15), 945–948. https://doi.org/10.1002/pen.760281502.

(38) Sakai, Y. Growth Shape Observed in Two-Dimensional Poly(Ethylene Terephthalate) Spherulites. *Macromolecules* **1996**, *29* (27), 8830–8834. https://doi.org/10.1021/ma9601427.

(39) Hikoeaka, M.; Amano, K.; Rastogi, S.; Keller, A. Lamellar Thickening Growth of an Extended Chain Single Crystal of Polyethylene. 1. Pointers to a New Crystallization Mechanism of Polymers. *Macromolecules* **1997**, *30* (7), 2067–2074. https://doi.org/10.1021/ma960746a.

(40) Sommer, J. U.; Reiter, G. Crystallization in Ultra-Thin Polymer Films: Morphogenesis and Thermodynamical Aspects. *Thermochim. Acta* **2005**, *432* (2), 135–147. https://doi.org/10.1016/j.tca.2005.04.017.

(41) Disnan, D.; Hafner, J.; Schneider, M.; Schmid, U. Spherulite-like Microstructure Observed for Spin-Cast P(VDF-TrFE) Thin Films and Their Ferroelectric Characteristics. *Polymer (Guildf).* **2023**, *272* (March), 125840. https://doi.org/10.1016/j.polymer.2023.125840.

(42) Naegele, D.; Yoon, D. Y.; Broadhurst, M. G. Formation of a New Crystal Form (α p) of Poly(Vinylidene Fluoride) under Electric Field. *Macromolecules* **1978**, *11* (6), 1297–1298. https://doi.org/10.1021/ma60066a051.

(43) Park, J. H.; Kurra, N.; AlMadhoun, M. N.; Odeh, I. N.; Alshareef, H. N. A Two-Step Annealing Process for Enhancing the Ferroelectric Properties of Poly(Vinylidene Fluoride) (PVDF) Devices. *J. Mater. Chem. C* **2015**, *3* (10), 2366–2370. https://doi.org/10.1039/c4tc02079k.

(44) Martín, J.; Zhao, D.; Lenz, T.; Katsouras, I.; De Leeuw, D. M.; Stingelin, N. Solid-State-Processing of δ-PVDF. *Mater. Horizons* **2017**, *4* (3), 408–414. https://doi.org/10.1039/c7mh00007c.

(45) Qian, J.; Jiang, S.; Wang, Q.; Zheng, S.; Guo, S.; Yi, C.; Wang, J.; Wang, X.; Tsukagoshi, K.; Shi, Y.; Li, Y. Unveiling the Piezoelectric Nature of Polar α-Phase P(VDF-TrFE) at Quasi-Two-Dimensional Limit. *Scientific Reports*. 2018. https://doi.org/10.1038/s41598-017-18845-2.

(46) Davis, G. T.; McKinney, J. E.; Broadhurst, M. G.; Roth, S. C. Electric-Field-Induced Phase

Changes in Poly(Vinylidene Fluoride). *J. Appl. Phys.* **1978**, *49* (10), 4998–5002. https://doi.org/10.1063/1.324446.

(47) Hafner, J. Ferroelectric Polymer Thin Films for MEMS Applications : Towards Soft and High-Speed AFM Probes, 2021.

(48) Katsouras, I.; Asadi, K.; Li, M.; Van Driel, T. B.; Kjær, K. S.; Zhao, D.; Lenz, T.; Gu, Y.; Blom, P. W. M.; Damjanovic, D.; Nielsen, M. M.; De Leeuw, D. M. The Negative Piezoelectric Effect of the Ferroelectric Polymer Poly(Vinylidene Fluoride). *Nat. Mater.* **2016**, *15* (1), 78–84. https://doi.org/10.1038/nmat4423.

(49) Disnan, D.; Bacher, F.; Berger, S.; Schneider, M.; Schmid, U. Microstructural Influence on Thermal Stability of Ferroelectric Properties in P(VDF-TrFE) Spin Cast Thin Films. *Polymer (Guildf).* **2024**, 126894. https://doi.org/10.1016/j.polymer.2024.126894.

(50) Hafner, J.; Disnan, D.; Benaglia, S.; Garcia, R.; Schmid, U. Solution-Processed Ferroelectric Polymer Nanocrystals. *Polymer (Guildf).* **2023**, *281* (March), 126115. https://doi.org/10.1016/j.polymer.2023.126115.

(51) Hafner, J.; Teuschel, M.; Schneider, M.; Schmid, U. Origin of the Strong Temperature Effect on the Piezoelectric Response of the Ferroelectric (Co-)Polymer P(VDF 70 -TrFE 30). *Polymer (Guildf).* **2019**, *170* (March), 1–6. https://doi.org/10.1016/j.polymer.2019.02.064.

(52) Hafner, J.; Benaglia, S.; Richheimer, F.; Teuschel, M.; Maier, F. J.; Werner, A.; Wood, S.; Platz, D.; Schneider, M.; Hradil, K.; Castro, F. A.; Garcia, R.; Schmid, U. Multi-Scale Characterisation of a Ferroelectric Polymer Reveals the Emergence of a Morphological Phase Transition Driven by Temperature. *Nat. Commun.* **2021**, *12* (1), 1–9. https://doi.org/10.1038/s41467-020-20407-6.

(53) Hafner, J.; Teuschel, M.; Disnan, D.; Schneider, M.; Schmid, U. Large Bias-Induced Piezoelectric Response in the Ferroelectric Polymer P(VDF-TrFE) for MEMS Resonators. *Mater. Res. Lett.* **2021**, *9* (4), 195–203. https://doi.org/10.1080/21663831.2020.1868593.

(54) Tashiro, K.; Tanaka, R. Structural Correlation between Crystal Lattice and Lamellar Morphology in the Ferroelectric Phase Transition of Vinylidene Fluoride-Trifluoroethylene Copolymers as Revealed by the Simultaneous Measurements of Wide-Angle and Small-Angle X-Ray Scatterings. *Polymer (Guildf).* **2006**, *47* (15), 5433–5444. https://doi.org/10.1016/j.polymer.2005.06.128.

(55) Tashiro, K. *Ferroelectric Polymers*, 1st editio.; Nalwa, H. S., Ed.; CRC Press, 1995. https://doi.org/10.1201/9781482295450.

(56) Broadhurst, M. G.; Davis, G. T. Physical Basis for Piezoelectricity in PVDF. *Ferroelectrics* **1984**, *60* (1), 3–13. https://doi.org/10.1080/00150198408017504.

(57) García-Gutiérrez, M.-C.; Linares, A.; Martín-Fabiani, I.; Hernández, J. J.; Soccio, M.; Rueda, D. R.; Ezquerra, T. A.; Reynolds, M. Understanding Crystallization Features of P(VDF-TrFE) Copolymers under Confinement to Optimize Ferroelectricity in Nanostructures. *Nanoscale* **2013**, *5* (13), 6006. https://doi.org/10.1039/c3nr00516j.

(58) Kim, J. H.; Khang, D. Y. High-Performance Needle-Shaped Crystals in Thin and Ultrathin P(VDF-TrFE) Films Formed by Melt Recrystallization. *Eur. Polym. J.* **2014**, *59*, 78–83. https://doi.org/10.1016/j.eurpolymj.2014.07.017.

(59) Lee, J. S.; Prabu, A. A.; Kim, K. J. Annealing Effect upon Chain Orientation, Crystalline Morphology, and Polarizability of Ultra-Thin P(VDF-TrFE) Film for Nonvolatile Polymer Memory Device. *Polymer (Guildf).* **2010**, *51* (26), 6319–6333.

https://doi.org/10.1016/j.polymer.2010.10.053.

(60) Guo, D.; Stolichnov, I.; Setter, N. Thermally Induced Cooperative Molecular Reorientation and Nanoscale Polarization Switching Behaviors of Ultrathin Poly(Vinylidene Fluoride-Trifluoroethylene) Films. *J. Phys. Chem. B* **2011**, *115* (46), 13455–13466. https://doi.org/10.1021/jp2061442.

(61) Singh, D.; Garg, A.; Deepak. Cooling Rate Controlled Microstructure Evolution and Reduced Coercivity in P(VDF-TrFE) Devices for Memory Applications. *Org. Electron.* **2014**, *15* (1), 82–90. https://doi.org/10.1016/j.orgel.2013.10.024.

(62) Ng, C. Y. B.; Gan, W. C.; Velayutham, T. S.; Goh, B. T.; Hashim, R. Structural Control of the Dielectric, Pyroelectric and Ferroelectric Properties of Poly(Vinylidene Fluoride-: Co - Trifluoroethylene) Thin Films. *Phys. Chem. Chem. Phys.* **2020**, *22* (4), 2414–2423. https://doi.org/10.1039/c9cp01556f.

(63) Tamura, M.; Ogasawara, K.; Ono, N.; Hagiwara, S. Piezoelectricity in Uniaxially Stretched Poly(Vinylidene Fluoride). *J. Appl. Phys.* **1974**, *45* (9), 3768–3771. https://doi.org/10.1063/1.1663857.

(64) Chen, S.; Yao, K.; Tay, F. E. H.; Chew, L. L. S. Comparative Investigation of the Structure and Properties of Ferroelectric Poly(Vinylidene Fluoride) and Poly(Vinylidene Fluoride-Trifluoroethylene) Thin Films Crystallized on Substrates. *J. Appl. Polym. Sci.* **2010**, NA-NA. https://doi.org/10.1002/app.31794.

(65) Furukawa, T.; Seo, N. Electrostriction as the Origin of Piezoelectricity in Ferroelectric Polymers. *Jpn. J. Appl. Phys.* **1990**, *29* (4 R), 675–680. https://doi.org/10.1143/JJAP.29.675.

(66) Abdolmaleki, H.; Haugen, A. B.; Buhl, K. B.; Daasbjerg, K.; Agarwala, S. Interfacial Engineering of PVDF-TrFE toward Higher Piezoelectric, Ferroelectric, and Dielectric Performance for Sensing and Energy Harvesting Applications. *Adv. Sci.* **2023**, *10* (6). https://doi.org/10.1002/advs.202205942.

(67) Lu, S. G.; Rozic, B.; Kutnjiak, Z.; Zhang, Q. M. Electrocaloric Effect in Ferroelectric P(VDF-TrFE) Copolymers. *Integr. Ferroelectr.* **2011**, *125* (1), 176–185. https://doi.org/10.1080/10584587.2011.574491.

(68) You, L.; Zhang, Y.; Zhou, S.; Chaturvedi, A.; Morris, S. A.; Liu, F.; Chang, L.; Ichinose, D.; Funakubo, H.; Hu, W.; Wu, T.; Liu, Z.; Dong, S.; Wang, J. Origin of Giant Negative Piezoelectricity in a Layered van Der Waals Ferroelectric. *Sci. Adv.* **2019**, *5* (4), 1–10. https://doi.org/10.1126/sciadv.aav3780.

(69) Abbasipour, M.; Khajavi, R.; Akbarzadeh, A. H. A Comprehensive Review on Piezoelectric Polymeric and Ceramic Nanogenerators. *Adv. Eng. Mater.* **2022**, *24* (6). https://doi.org/10.1002/adem.202101312.

(70) Dallaev, R.; Pisarenko, T.; Sobola, D.; Orudzhev, F.; Ramazanov, S.; Trčka, T. Brief Review of PVDF Properties and Applications Potential. *Polymers (Basel).* **2022**, *14* (22), 1–29. https://doi.org/10.3390/polym14224793.

(71) Saxena, P.; Shukla, P. A Comprehensive Review on Fundamental Properties and Applications of Poly(Vinylidene Fluoride) (PVDF). *Adv. Compos. Hybrid Mater.* **2021**, *4* (1), 8–26. https://doi.org/10.1007/s42114-021-00217-0.

(72) Zheng, Z.; Wang, X.; Hang, G.; Duan, J.; Zhang, J.; Zhang, W.; Liu, Z. Recent Progress on Flexible Poly(Vinylidene Fluoride)-Based Piezoelectric Nanogenerators for Energy Harvesting and Self-Powered Electronic Applications. *Renew. Sustain. Energy Rev.* **2024**, *193*, 114285.

https://doi.org/10.1016/j.rser.2024.114285.

(73) Chauhan, S. S.; Bhatt, U. M.; Gautam, P.; Thote, S.; Joglekar, M. M.; Manhas, S. K. Fabrication and Modeling of β-Phase PVDF-TrFE Based Flexible Piezoelectric Energy Harvester. *Sensors Actuators A Phys.* **2020**, *304*, 111879. https://doi.org/10.1016/j.sna.2020.111879.

(74) Feng, Z.; Zhao, Z.; Liu, Y.; Liu, Y.; Cao, X.; Yu, D.; Wang, K. Piezoelectric Effect Polyvinylidene Fluoride (PVDF): From Energy Harvester to Smart Skin and Electronic Textiles. *Adv. Mater. Technol.* **2023**, *8* (14). https://doi.org/10.1002/admt.202300021.

(75) Hu, X.; Yi, K.; Liu, J.; Chu, B. High Energy Density Dielectrics Based on PVDF-Based Polymers. *Energy Technol.* **2018**, *6* (5), 849–864. https://doi.org/10.1002/ente.201700901.

(76) Goff, J. M.; Marques dos Santos Vieira, F.; Keilbart, N. D.; Okada, Y.; Dabo, I. Predicting the Pseudocapacitive Windows for MXene Electrodes with Voltage-Dependent Cluster Expansion Models. *ACS Appl. Energy Mater.* **2021**, *4* (4), 3151–3159. https://doi.org/10.1021/acsaem.0c02910.

(77) Roy, K.; Ghosh, S. K.; Sultana, A.; Garain, S.; Xie, M.; Bowen, C. R.; Henkel, K.; Schmeißer, D.; Mandal, D. A Self-Powered Wearable Pressure Sensor and Pyroelectric Breathing Sensor Based on GO Interfaced PVDF Nanofibers. *ACS Appl. Nano Mater.* **2019**, *2* (4), 2013–2025. https://doi.org/10.1021/acsanm.9b00033.

(78) Yan, X.; Guo, Z. Introduction to Nanocomposites. In *Multifunctional Nanocomposites for Energy and Environmental Applications*; Wiley, 2018; pp 1–5. https://doi.org/10.1002/9783527342501.ch1.

(79) Hafeez, M. Recent Progress and Overview of Nanocomposites. In *Nanocomposite Materials for Biomedical and Energy Storage Applications*; IntechOpen, 2022. https://doi.org/10.5772/intechopen.102469.

(80) Toro, C.; Skrabalak, S. E. Revisiting the Early Literature on Nanocomposites and the Path to Transformative Technologies: An Interview with Rupali Gangopadhyay for Chemistry of Materials ' 1k Club. *Chem. Mater.* **2022**, *34* (21), 9305–9306. https://doi.org/10.1021/acs.chemmater.2c02936.

(81) *Composite Materials*, 1st Editio.; Sachdeva, A., Singh, P. K., Rhee, H. W., Eds.; CRC Press: First edition. | Boca Raton, FL : CRC Press, 2021., 2021. https://doi.org/10.1201/9781003080633.

(82) Ahmad, N.; Ahmad, S. I.; Ahmedi, S.; Yadav, P.; Manzoor, N.; Parwaz, M.; Khan, Z. H. Structural, Optical and Antifungal Properties of the PMMA-ZnO Nanocomposites: Potential Applications in Odontology. *Mater. Chem. Phys.* **2023**, *309* (April), 128382. https://doi.org/10.1016/j.matchemphys.2023.128382.

(83) Pawar, D.; Kanawade, R.; Kumar, A.; Rao, C. N.; Cao, P.; Gaware, S.; Late, D.; Kale, S. N.; Navale, S. T.; Liu, W. J.; Zhu, D. L.; Lu, Y. M.; Sinha, R. K. High-Performance Dual Cavity-Interferometric Volatile Gas Sensor Utilizing Graphene/PMMA Nanocomposite. *Sensors Actuators, B Chem.* **2020**, *312* (November 2019). https://doi.org/10.1016/j.snb.2020.127921.

(84) Rafiefard, N.; Fardindoost, S.; Karimi Kisomi, M.; Shooshtari, L.; Irajizad, A.; Seddighi, S.; Mohammadpour, R.; Vashaee, D. High-Performance Flexible and Stretchable Self-Powered Surface Engineered PDMS-TiO2 Nanocomposite Based Humidity Sensors Driven by Triboelectric Nanogenerator with Full Sensing Range. *Sensors Actuators B Chem.* **2023**, *378* (November 2022), 133105. https://doi.org/10.1016/j.snb.2022.133105.

(85) Bodian, S.; Colchester, R. J.; Macdonald, T. J.; Ambroz, F.; Briceno de Gutierrez, M.; Mathews, S. J.; Fong, Y. M. M.; Maneas, E.; Welsby, K. A.; Gordon, R. J.; Collier, P.; Zhang, E. Z.; Beard, P.

C.; Parkin, I. P.; Desjardins, A. E.; Noimark, S. CuInS 2 Quantum Dot and Polydimethylsiloxane Nanocomposites for All-Optical Ultrasound and Photoacoustic Imaging. *Adv. Mater. Interfaces* **2021**, *8* (20). https://doi.org/10.1002/admi.202100518.

(86) Bai, W.; Lu, Y.; Hu, Z.; Xiao, G.; Zhao, H.; Zhu, J.; Liu, Z. Photoluminescence, Thermal and Surface Properties of Triarylimidazole-Containing Polyimide Nanocomposite Films. *RSC Adv.* **2021**, *11* (57), 36066–36077. https://doi.org/10.1039/d1ra07147e.

(87) Tian, M.; Wei, Z.; Zan, X.; Zhang, L.; Zhang, J.; Ma, Q.; Ning, N.; Nishi, T. Thermally Expanded Graphene Nanoplates/Polydimethylsiloxane Composites with High Dielectric Constant, Low Dielectric Loss and Improved Actuated Strain. *Compos. Sci. Technol.* **2014**, *99*, 37–44. https://doi.org/10.1016/j.compscitech.2014.05.004.

(88) Shevchenko, V. G.; Polschikov, S. V.; Nedorezova, P. M.; Klyamkina, A. N.; Shchegolikhin, A. N.; Aladyshev, A. M.; Muradyan, V. E. In Situ Polymerized Poly(Propylene)/Graphene Nanoplatelets Nanocomposites: Dielectric and Microwave Properties. *Polymer (Guildf).* **2012**, *53* (23), 5330–5335. https://doi.org/10.1016/j.polymer.2012.09.018.

(89) El Hasnaoui, M.; Triki, A.; Graça, M. P. F.; Achour, M. E.; Costa, L. C.; Arous, M. Electrical Conductivity Studies on Carbon Black Loaded Ethylene Butylacrylate Polymer Composites. *J. Non. Cryst. Solids* **2012**, *358* (20), 2810–2815. https://doi.org/10.1016/j.jnoncrysol.2012.07.008.

(90) Theravalappil, R.; Svoboda, P.; Vilcakova, J.; Poongavalappil, S.; Slobodian, P.; Svobodova, D. A Comparative Study on the Electrical, Thermal and Mechanical Properties of Ethylene–Octene Copolymer Based Composites with Carbon Fillers. *Mater. Des.* **2014**, *60*, 458–467. https://doi.org/10.1016/j.matdes.2014.04.029.

(91) Daugaard, A. E.; Jankova, K.; Marín, J. M. R.; Bøgelund, J.; Hvilsted, S. Poly(Ethylene-Co-Butylene) Functionalized Multi Walled Carbon Nanotubes Applied in Polypropylene Nanocomposites. *Eur. Polym. J.* **2012**, *48* (4), 743–750. https://doi.org/10.1016/j.eurpolymj.2012.02.006.

(92) Chang, J.; Liang, G.; Gu, A.; Cai, S.; Yuan, L. The Production of Carbon Nanotube/Epoxy Composites with a Very High Dielectric Constant and Low Dielectric Loss by Microwave Curing. *Carbon N. Y.* **2012**, *50* (2), 689–698. https://doi.org/10.1016/j.carbon.2011.09.029.

(93) Schumacher, B.; Geßwein, H.; Haußelt, J.; Hanemann, T. Temperature Treatment of Nano-Scaled Barium Titanate Filler to Improve the Dielectric Properties of High-k Polymer Based Composites. *Microelectron. Eng.* **2010**, *87* (10), 1978–1983. https://doi.org/10.1016/j.mee.2009.12.018.

(94) Padalia, D.; Bisht, G.; Johri, U. C.; Asokan, K. Fabrication and Characterization of Cerium Doped Barium Titanate/PMMA Nanocomposites. *Solid State Sci.* **2013**, *19*, 122–129. https://doi.org/10.1016/j.solidstatesciences.2013.02.002.

(95) AL-Baradi, A. M.; Al-Shehri, S. F.; Badawi, A.; Merazga, A.; Atta, A. A. A Study of Optical, Mechanical and Electrical Properties of Poly(Methacrylic Acid)/TiO2 Nanocomposite. *Results Phys.* **2018**, *9*, 879–885. https://doi.org/10.1016/j.rinp.2018.03.039.

(96) Tjong, S. C.; Liang, G. D. Electrical Properties of Low-Density Polyethylene/ZnO Nanocomposites. *Mater. Chem. Phys.* **2006**, *100* (1), 1–5. https://doi.org/10.1016/j.matchemphys.2005.11.029.

(97) M., D.; Guillaume, E.; Chivas-Joly, C. Properties of Nanofillers in Polymer. In *Nanocomposites and Polymers with Analytical Methods*; InTech, 2011. https://doi.org/10.5772/21694.

(98) Bi, M.; Hao, Y.; Zhang, J.; Lei, M.; Bi, K. Particle Size Effect of BaTiO3 Nanofillers on the Energy Storage Performance of Polymer Nanocomposites. *Nanoscale* **2017**, *9* (42), 16386–16395. https://doi.org/10.1039/c7nr05212j.

(99) Zhang, L.; Shan, X.; Wu, P.; Cheng, Z.-Y. Dielectric Characteristics of CaCu3Ti4O12/P(VDF-TrFE) Nanocomposites. *Appl. Phys. A* **2012**, *107* (3), 597–602. https://doi.org/10.1007/s00339-012-6836-3.

(100) Silakaew, K.; Thongbai, P. Suppressed Loss Tangent and Conductivity in High-Permittivity Ag-BaTiO3/PVDF Nanocomposites by Blocking with BaTiO3 Nanoparticles. *Appl. Surf. Sci.* **2019**, *492*, 683–689. https://doi.org/10.1016/j.apsusc.2019.06.262.

(101) Kim, H.; Johnson, J.; Chavez, L. A.; Garcia Rosales, C. A.; Tseng, T.-L. B.; Lin, Y. Enhanced Dielectric Properties of Three Phase Dielectric MWCNTs/BaTiO3/PVDF Nanocomposites for Energy Storage Using Fused Deposition Modeling 3D Printing. *Ceram. Int.* **2018**, *44* (8), 9037–9044. https://doi.org/10.1016/j.ceramint.2018.02.107.

(102) Zhou, T.; Zha, J. W.; Cui, R. Y.; Fan, B. H.; Yuan, J. K.; Dang, Z. M. Improving Dielectric Properties of BaTiO3/Ferroelectric Polymer Composites by Employing Surface Hydroxylated BaTiO3 Nanoparticles. *ACS Appl. Mater. Interfaces* **2011**, *3* (7), 2184–2188. https://doi.org/10.1021/am200492q.

(103) Zhang, X.; Wang, Y.; Sheng, Y.; Ye, H.; Xu, L.; Wu, H. Enhanced Energy Density in Hydroxyl-Modified Barium Titanate/Poly(Fluorovinylidene-Co-Trifluoroethylene) Nanocomposites with Improved Interfacial Polarization. *Chem. Phys. Lett.* **2019**, *723* (January), 89–95. https://doi.org/10.1016/j.cplett.2019.03.027.

(104) Chang, S. J.; Liao, W. S.; Ciou, C. J.; Lee, J. T.; Li, C. C. An Efficient Approach to Derive Hydroxyl Groups on the Surface of Barium Titanate Nanoparticles to Improve Its Chemical Modification Ability. *J. Colloid Interface Sci.* **2009**, *329* (2), 300–305. https://doi.org/10.1016/j.jcis.2008.10.011.

(105) Hu, P.; Gao, S.; Zhang, Y.; Zhang, L.; Wang, C. Surface Modified BaTiO3 Nanoparticles by Titanate Coupling Agent Induce Significantly Enhanced Breakdown Strength and Larger Energy Density in PVDF Nanocomposite. *Compos. Sci. Technol.* **2018**, *156*, 109–116. https://doi.org/10.1016/j.compscitech.2017.12.025.

(106) Gao, L.; He, J.; Hu, J.; Li, Y. Large Enhancement in Polarization Response and Energy Storage Properties of Poly(Vinylidene Fluoride) by Improving the Interface Effect in Nanocomposites. *J. Phys. Chem. C* **2014**, *118* (2), 831–838. https://doi.org/10.1021/jp409474k.

(107) Kim, P.; Jones, S. C.; Hotchkiss, P. J.; Haddock, J. N.; Kippelen, B.; Marder, S. R.; Perry, J. W. Phosphonic Acid-Modified Barium Titanate Polymer Nanocomposites with High Permittivity and Dielectric Strength. *Adv. Mater.* **2007**, *19* (7), 1001–1005. https://doi.org/10.1002/adma.200602422.

(108) Kim, P.; Doss, N. M.; Tillotson, J. P.; Hotchkiss, P. J.; Pan, M.-J.; Marder, S. R.; Li, J.; Calame, J. P.; Perry, J. W. High Energy Density Nanocomposites Based on Surface-Modified BaTiO 3 and a Ferroelectric Polymer. *ACS Nano* **2009**, *3* (9), 2581–2592. https://doi.org/10.1021/nn9006412.

(109) Fu, J.; Hou, Y.; Zheng, M.; Wei, Q.; Zhu, M.; Yan, H. Improving Dielectric Properties of PVDF Composites by Employing Surface Modified Strong Polarized BaTiO 3 Particles Derived by Molten Salt Method. *ACS Appl. Mater. Interfaces* **2015**, *7* (44), 24480–24491. https://doi.org/10.1021/acsami.5b05344.

(110) Liao, W.; Gu, A.; Liang, G.; Yuan, L. New High Performance Transparent UV-Curable Poly(Methyl Methacrylate) Grafted ZnO/Silicone-Acrylate Resin Composites with Simultaneously Improved Integrated Performance. *Colloids Surfaces A Physicochem. Eng. Asp.* **2012**, *396*, 74–82. https://doi.org/10.1016/j.colsurfa.2011.12.044.

(111) Ye, H. J.; Shao, W. Z.; Zhen, L. Tetradecylphosphonic Acid Modified BaTiO3 Nanoparticles and Its Nanocomposite. *Colloids Surfaces A Physicochem. Eng. Asp.* **2013**, *427*, 19–25. https://doi.org/10.1016/j.colsurfa.2013.02.068.

(112) Lee, H.; Dellatore, S. M.; Miller, W. M.; Messersmith, P. B. Mussel-Inspired Surface Chemistry for Multifunctional Coatings. *Science (80-.).* **2007**, *318* (5849), 426–430. https://doi.org/10.1126/science.1147241.

(113) Waite, J. H.; Tanzer, M. L. Polyphenolic Substance of Mytilus Edulis : Novel Adhesive Containing L-Dopa and Hydroxyproline. *Science (80-.).* **1981**, *212* (4498), 1038–1040. https://doi.org/10.1126/science.212.4498.1038.

(114) Liu, Y.; Ai, K.; Lu, L. Polydopamine and Its Derivative Materials: Synthesis and Promising Applications in Energy, Environmental, and Biomedical Fields. *Chem. Rev.* **2014**, *114* (9), 5057–5115. https://doi.org/10.1021/cr400407a.

(115) Ding, Y. H.; Floren, M.; Tan, W. Mussel-Inspired Polydopamine for Bio-Surface Functionalization. *Biosurface and Biotribology* **2016**, *2* (4), 121–136. https://doi.org/10.1016/j.bsbt.2016.11.001.

(116) Park, J.; Brust, T. F.; Lee, H. J.; Lee, S. C.; Watts, V. J.; Yeo, Y. Polydopamine-Based Simple and Versatile Surface Modification of Polymeric Nano Drug Carriers. *ACS Nano* **2014**, *8* (4), 3347–3356. https://doi.org/10.1021/nn405809c.

(117) Zeng, Y.; Liu, W.; Wang, Z.; Singamaneni, S.; Wang, R. Multifunctional Surface Modification of Nanodiamonds Based on Dopamine Polymerization. *Langmuir* **2018**, *34* (13), 4036–4042. https://doi.org/10.1021/acs.langmuir.8b00509.

(118) Wang, Z.; Wang, T.; Wang, C.; Xiao, Y.; Jing, P.; Cui, Y.; Pu, Y. Poly(Vinylidene Fluoride) Flexible Nanocomposite Films with Dopamine-Coated Giant Dielectric Ceramic Nanopowders, Ba(Fe0.5Ta0.5)O3, for High Energy-Storage Density at Low Electric Field. *ACS Appl. Mater. Interfaces* **2017**, *9* (34), 29130–29139. https://doi.org/10.1021/acsami.7b08664.

(119) Cai, W.; Wang, J.; Pan, Y.; Guo, W.; Mu, X.; Feng, X.; Yuan, B.; Wang, X.; Hu, Y. Mussel-Inspired Functionalization of Electrochemically Exfoliated Graphene: Based on Self-Polymerization of Dopamine and Its Suppression Effect on the Fire Hazards and Smoke Toxicity of Thermoplastic Polyurethane. *J. Hazard. Mater.* **2018**, *352* (March), 57–69. https://doi.org/10.1016/j.jhazmat.2018.03.021.

(120) Ruan, M.; Yang, D.; Guo, W.; Zhang, L.; Li, S.; Shang, Y.; Wu, Y.; Zhang, M.; Wang, H. Improved Dielectric Properties, Mechanical Properties, and Thermal Conductivity Properties of Polymer Composites via Controlling Interfacial Compatibility with Bio-Inspired Method. *Appl. Surf. Sci.* **2018**, *439*, 186–195. https://doi.org/10.1016/j.apsusc.2017.12.250.

(121) Jia, L.; Han, F.; Wang, H.; Zhu, C.; Guo, Q.; Li, J.; Zhao, Z.; Zhang, Q.; Zhu, X.; Li, B. Polydopamine-Assisted Surface Modification for Orthopaedic Implants. *J. Orthop. Transl.* **2019**, *17*, 82–95. https://doi.org/10.1016/j.jot.2019.04.001.

(122) Li, S.; Scheiger, J. M.; Wang, Z.; Dong, Z.; Welle, A.; Trouillet, V.; Levkin, P. A. Substrate-Independent and Re-Writable Surface Patterning by Combining Polydopamine Coatings, Silanization, and Thiol-Ene Reaction. *Adv. Funct. Mater.* **2021**, *31* (50).

https://doi.org/10.1002/adfm.202107716.

(123) Wang, Y.; Li, J.; Deng, Y. Enhanced Ferroelectricity and Energy Storage in Poly(Vinylidene Fluoride)-Clay Nanocomposite Films via Nanofiller Surface Charge Modulation. *RSC Adv.* **2015**, *5* (104), 85884–85888. https://doi.org/10.1039/c5ra13456k.

(124) Kausar, A. *Nanocellulose in Polymer Nanocomposite*; INC, 2020. https://doi.org/10.1016/B978-0-12-816789-2.00017-1.

(125) Rincón-Iglesias, M.; Lizundia, E.; Correia, D. M.; Costa, C. M.; Lanceros-Méndez, S. The Role of CNC Surface Modification on the Structural, Thermal and Electrical Properties of Poly(Vinylidene Fluoride) Nanocomposites. *Cellulose* **2020**, *27* (7), 3821–3834. https://doi.org/10.1007/s10570-020-03067-z.

(126) Zheng, W.; Lv, R.; Na, B.; Liu, H.; Jin, T.; Yuan, D. Nanocellulose-Mediated Hybrid Polyaniline Electrodes for High Performance Flexible Supercapacitors. *J. Mater. Chem. A* **2017**, *5* (25), 12969–12976. https://doi.org/10.1039/c7ta01990d.

(127) Chen, G.; Zhang, C.; Wang, X.; Liu, H.; Guo, Y.; Qi, H. Fabrication of Tailored Carboxymethyl-Functionalized Cellulose Nanofibers via Chemo-Mechanical Process from Waste Cotton Textile. *Cellulose* **2021**, *28* (12), 7663–7673. https://doi.org/10.1007/s10570-021-03969-6.

(128) Kono, H.; Tsukamoto, E.; Tajima, K. Facile Post-Carboxymethylation of Cellulose Nanofiber Surfaces for Enhanced Water Dispersibility. *ACS Omega* **2021**, *6* (49), 34107–34114. https://doi.org/10.1021/acsomega.1c05603.

(129) Zhang, Z.; Wu, Q.; Song, K.; Lei, T.; Wu, Y. Poly(Vinylidene Fluoride)/Cellulose Nanocrystals Composites: Rheological, Hydrophilicity, Thermal and Mechanical Properties. *Cellulose* **2015**, *22* (4), 2431–2441. https://doi.org/10.1007/s10570-015-0634-y.

(130) Lee, J.-E.; Shin, Y.-E.; Lee, G.-H.; Kim, J.; Ko, H.; Chae, H. G. Polyvinylidene Fluoride (PVDF)/Cellulose Nanocrystal (CNC) Nanocomposite Fiber and Triboelectric Textile Sensors. *Compos. Part B Eng.* **2021**, *223*, 109098. https://doi.org/10.1016/j.compositesb.2021.109098.

(131) Wu, Z.; Ji, X.; He, Q.; Gu, H.; Zhang, W.; Deng, Z. Nanocelluloses Fine-Tuned Polyvinylidene Fluoride (PVDF) Membrane for Enhanced Separation and Antifouling. *Carbohydr. Polym.* **2024**, *323*, 121383. https://doi.org/10.1016/j.carbpol.2023.121383.

(132) Fu, R.; Chen, S.; Lin, Y.; Zhang, S.; Jiang, J.; Li, Q.; Gu, Y. Improved Piezoelectric Properties of Electrospun Poly(Vinylidene Fluoride) Fibers Blended with Cellulose Nanocrystals. *Mater. Lett.* **2017**, *187* (June 2016), 86–88. https://doi.org/10.1016/j.matlet.2016.10.068.

(133) Lasrado, D.; Ahankari, S.; Kar, K. Nanocellulose-Based Polymer Composites for Energy Applications—A Review. *J. Appl. Polym. Sci.* **2020**, *137* (27), 1–14. https://doi.org/10.1002/app.48959.

(134) Ramakoti, I. S.; Panda, A. K.; Gouda, N. A Brief Review on Polymer Nanocomposites: Current Trends and Prospects. *J. Polym. Eng.* **2023**, *43* (8), 651–679. https://doi.org/10.1515/polyeng-2023-0103.

(135) Jow, T. R.; Cygan, P. J. Dielectric Breakdown of Polyvinylidene Fluoride and Its Comparisons with Other Polymers. *J. Appl. Phys.* **1993**, *73* (10), 5147–5151. https://doi.org/10.1063/1.353789.

(136) Tiantian Yan; Wen, Y.; Liu, J.; Liao, H.; Zhang, J. A Brief Overview of the Optimization of Dielectric Properties of PVDF and Its Copolymer-Based Nanocomposites as Energy Storage Materials. *Polym. Sci. Ser. A* **2022**, *64* (5), 393–405.

https://doi.org/10.1134/S0965545X22700146.

(137) Steeman, P. A. M.; Maurer, F. H. J.; van Es, M. A. Dielectric Monitoring of Water Absorption in Glass-Bead-Filled High-Density Polyethylene. *Polymer (Guildf).* **1991**, *32* (3), 523–530. https://doi.org/10.1016/0032-3861(91)90460-Z.

(138) Huang, X.; Jiang, P.; Tanaka, T. A Review of Dielectric Polymer Composites with High Thermal Conductivity. *IEEE Electr. Insul. Mag.* **2011**, *27* (4), 8–16. https://doi.org/10.1109/MEI.2011.5954064.

(139) Ramalingam, V. S.; Kanagasabai, M.; Sundarsingh, E. F. Transit Time Dependent Condition Monitoring of PCBs During Testing for Diagnostics in Electronics Industry. *IEEE Trans. Ind. Electron.* **2018**, *65* (1), 553–560. https://doi.org/10.1109/TIE.2017.2716876.

(140) Xie, L.; Huang, X.; Huang, Y.; Yang, K.; Jiang, P. Core@Double-Shell Structured BaTiO 3 – Polymer Nanocomposites with High Dielectric Constant and Low Dielectric Loss for Energy Storage Application. *J. Phys. Chem. C* **2013**, *117* (44), 22525–22537. https://doi.org/10.1021/jp407340n.

(141) Gross, S.; Camozzo, D.; Di Noto, V.; Armelao, L.; Tondello, E. PMMA: A Key Macromolecular Component for Dielectric Low-κ Hybrid Inorganic–Organic Polymer Films. *Eur. Polym. J.* **2007**, *43* (3), 673–696. https://doi.org/10.1016/j.eurpolymj.2006.12.012.

(142) Molberg, M.; Crespy, D.; Rupper, P.; Nüesch, F.; Månson, J. E.; Löwe, C.; Opris, D. M. High Breakdown Field Dielectric Elastomer Actuators Using Encapsulated Polyaniline as High Dielectric Constant Filler. *Adv. Funct. Mater.* **2010**, *20* (19), 3280–3291. https://doi.org/10.1002/adfm.201000486.

(143) Li, W.; Meng, Q.; Zheng, Y.; Zhang, Z.; Xia, W.; Xu, Z. Electric Energy Storage Properties of Poly(Vinylidene Fluoride). *Appl. Phys. Lett.* **2010**, *96* (19). https://doi.org/10.1063/1.3428656.

(144) Song, Y.; Shen, Y.; Liu, H.; Lin, Y.; Li, M.; Nan, C. W. Enhanced Dielectric and Ferroelectric Properties Induced by Dopamine-Modified BaTiO 3 Nanofibers in Flexible Poly(Vinylidene Fluoride-Trifluoroethylene) Nanocomposites. *J. Mater. Chem.* **2012**, *22* (16), 8063–8068. https://doi.org/10.1039/c2jm30297g.

(145) Claude, J.; Lu, Y.; Li, K.; Wang, Q. Electrical Storage in Poly(Vinylidene Fluoride) Based Ferroelectric Polymers: Correlating Polymer Structure to Electrical Breakdown Strength. *Chem. Mater.* **2008**, *20* (6), 2078–2080. https://doi.org/10.1021/cm800160r.

(146) Hou, Y.; Deng, Y.; Wang, Y.; Gao, H. L. Uniform Distribution of Low Content BaTiO3 Nanoparticles in Poly(Vinylidene Fluoride) Nanocomposite: Toward High Dielectric Breakdown Strength and Energy Storage Density. *RSC Adv.* **2015**, *5* (88), 72090–72098. https://doi.org/10.1039/c5ra10438f.

(147) Xie, Y.; Yu, Y.; Feng, Y.; Jiang, W.; Zhang, Z. Fabrication of Stretchable Nanocomposites with High Energy Density and Low Loss from Cross-Linked PVDF Filled with Poly(Dopamine) Encapsulated BaTiO3. *ACS Appl. Mater. Interfaces* **2017**, *9* (3), 2995–3005. https://doi.org/10.1021/acsami.6b14166.

(148) Zhang, L.; Wang, Y.; Xu, M.; Wei, W.; Deng, Y. Multiple Interfacial Modifications in Poly(Vinylidene Fluoride)/Barium Titanate Nanocomposites via Double-Shell Architecture for Significantly Enhanced Energy Storage Density. *ACS Appl. Energy Mater.* **2019**, *2* (8), 5945–5953. https://doi.org/10.1021/acsaem.9b01052.

(149) Men, T.; Liu, X.; Jiang, B.; Long, X.; Guo, H. Ferroelectric β-Crystalline Phase Formation and Property Enhancement in Polydopamine Modified BaTiO3/Poly (Vinylidene Fluoride-

Trifluoroethylene) Nanocomposite Films. *Thin Solid Films* **2019**, *669*, 579–587. https://doi.org/10.1016/j.tsf.2018.11.051.

(150) D. Disnan, M. Schneider, X. Zhang, K. Qian, F. Bacher, Y. Zhao, X. Feng, U. Schmid, (under review). P(VDF-TrFE) Nanocomposite Thin Films with Cellulose Nanofibers and Dopamine-Modified BaTiO3 Nanoparticles for Enhanced Energy Storage (under Review).

(151) Singh, N. B.; Agarwal, S. Nanocomposites: An Overview. *Emerg. Mater. Res.* **2016**, *5* (1), 5–43. https://doi.org/10.1680/jemmr.15.00025.

(152) Mahmood, T.; Ullah, A.; Ali, R. Improved Nanocomposite Materials and Their Applications. In *Nanocomposite Materials for Biomedical and Energy Storage Applications*; IntechOpen, 2022. https://doi.org/10.5772/intechopen.102538.

(153) Jow, T. R.; MacDougall, F. W.; Ennis, J. B.; Yang, X. H.; Schneider, M. A.; Scozzie, C. J.; White, J. D.; MacDonald, J. R.; Schalnat, M. C.; Cooper, R. A.; Yen, S. P. S. Pulsed Power Capacitor Development and Outlook. In *2015 IEEE Pulsed Power Conference (PPC)*; IEEE, 2015; pp 1–7. https://doi.org/10.1109/PPC.2015.7297027.

(154) SARJEANT, W.; ZIRNHELD, J.; MACDOUGALL, F.; BOWERS, J.; CLARK, N.; CLELLAND, I.; PRICE, R.; HUDIS, M.; KOHLBERG, I.; MCDUFF, G. Capacitors—Past, Present, and Future. In *Handbook of Low and High Dielectric Constant Materials and Their Applications*; Elsevier, 1999; pp 423–491. https://doi.org/10.1016/B978-012513905-2/50023-6.

(155) Ribeiro, P. F.; Johnson, B. K.; Crow, M. L.; Arsoy, A.; Liu, Y. Energy Storage Systems for Advanced Power Applications. *Proc. IEEE* **2001**, *89* (12), 1744–1756. https://doi.org/10.1109/5.975900.

(156) Tolbert, L. M.; Fang Zheng Peng; Habetler, T. G. Multilevel Converters for Large Electric Drives. *IEEE Trans. Ind. Appl.* **1999**, *35* (1), 36–44. https://doi.org/10.1109/28.740843.

(157) Zeng, W.; Shu, L.; Li, Q.; Chen, S.; Wang, F.; Tao, X. Fiber-Based Wearable Electronics: A Review of Materials, Fabrication, Devices, and Applications. *Adv. Mater.* **2014**, *26* (31), 5310–5336. https://doi.org/10.1002/adma.201400633.

(158) Baoyuan, S.; Jiantong, W.; Jun, Z.; Min, Q. A New Model Describing Physical Effects in Crystals: The Diagrammatic and Analytic Methods for Macro-Phenomenological Theory. *J. Mater. Process. Technol.* **2003**, *139* (1–3), 444–447. https://doi.org/10.1016/S0924-0136(03)00546-6.

(159) Robert E. Newnham. *Properties of Materials: Anisotropy, Symmetry, Structure*; OUP Oxford, 2005, Ed.; 2005.

(160) Baker, J., Haider, M. F., Raihan, R., & Reifsnider, K. Effect of Manufacturing on the Dielectric Properties of Composite Materials; American Society for Composites 30th Technical Conference.

(161) C. J. F. Böttcher, P. B. *Theory of Electric Polarization / Vol. 2, Dielectrics in Time-Dependent Fields*, 2nd ed.; Elsevier, Amsterdam, 1978, Ed.; 1978.

(162) Kwan Chi Kao. *Dielectric Phenomena in Solids*, 1st Editio.; Elsevier, 2004. https://doi.org/10.1016/B978-0-12-396561-5.X5010-5.

(163) A.J. Dekker. *Electrical Engineering Materials*, 1st ed.; 1959.

(164) Deborah D. L. Chung. *Composite Materials Functional Materials for Modern Technologies*, 1st ed.; Gmbh, S. B. H., Ed.; 2003.

(165) A. R. Blythe, D. B. *Electrical Properties of Polymers*, 2nd ed.; 2008.

(166) Chanmal, C.; Jyoti, J. *Characterization Techniques for Polymer Nanocomposites*; Wiley-VC Verlag GmbH & Co. KGaA:Weinheim, 2012.

(167) Li, F.; Jin, L.; Xu, Z.; Zhang, S. Electrostrictive Effect in Ferroelectrics: An Alternative Approach to Improve Piezoelectricity. *Appl. Phys. Rev.* **2014**, *1* (1). https://doi.org/10.1063/1.4861260.

(168) Sundar, V.; Newnham, R. E. Electrostriction and Polarization. *Ferroelectrics* **1992**, *135* (1), 431–446. https://doi.org/10.1080/00150199208230043.

(169) Newnham, R. E.; Sundar, V.; Yimnirun, R.; Su, J.; Zhang, Q. M. Electrostriction: Nonlinear Electromechanical Coupling in Solid Dielectrics. *J. Phys. Chem. B* **1997**, *101* (48), 10141–10150. https://doi.org/10.1021/jp971522c.

(170) Cross, L. E.; Jang, S. J.; Newnham, R. E.; Nomura, S.; Uchino, K. Large Electrostrictive Effects in Relaxor Ferroelectrics. *Ferroelectrics* **1980**, *23* (1), 187–191. https://doi.org/10.1080/00150198008018801.

(171) Fundamentals of Piezoelectricity. In *Lead-Free Piezoelectric Materials*; Wiley, 2021; pp 1–18. https://doi.org/10.1002/9783527817047.ch1.

(172) Caliò, R.; Rongala, U.; Camboni, D.; Milazzo, M.; Stefanini, C.; de Petris, G.; Oddo, C. Piezoelectric Energy Harvesting Solutions. *Sensors* **2014**, *14* (3), 4755–4790. https://doi.org/10.3390/s140304755.

(173) Osman, R. A. M.; Idris, M. S.; Zahid Jamal, Z. A.; Taking, S.; Sabki, S. N.; Poopalan, P. A. L.; Norizan, M. N.; Mohamad, I. S. Ferroelectric and Relaxor Ferroelectric to Paralectric Transition Based on Lead Magnesium Niobate (PMN) Materials. *Adv. Mater. Res.* **2013**, *795*, 658–663. https://doi.org/10.4028/www.scientific.net/AMR.795.658.

(174) Jan Tichý , Jiří Erhart , Erwin Kittinger, J. P. *Fundamentals of Piezoelectric Sensorics: Mechanical, Dielectric, and Thermodynamical Properties of Piezoelectric Materials*; Springer Berlin Heidelberg, 2010.

(175) Vizdrik, G.; Ducharme, S.; Fridkin, V. M.; Yudin, S. G. Kinetics of Ferroelectric Switching in Ultrathin Films. *Phys. Rev. B* **2003**, *68* (9), 094113. https://doi.org/10.1103/PhysRevB.68.094113.

(176) Hoffmann, M.; Fengler, F. P. G.; Herzig, M.; Mittmann, T.; Max, B.; Schroeder, U.; Negrea, R.; Lucian, P.; Slesazeck, S.; Mikolajick, T. Unveiling the Double-Well Energy Landscape in a Ferroelectric Layer. *Nature* **2019**, *565* (7740), 464–467. https://doi.org/10.1038/s41586-018-0854-z.

(177) Jin, L.; Li, F.; Zhang, S. Decoding the Fingerprint of Ferroelectric Loops: Comprehension of the Material Properties and Structures. *J. Am. Ceram. Soc.* **2014**, *97* (1), 1–27. https://doi.org/10.1111/jace.12773.

(178) Andersen, B., Ringgaard, E., Bove, T., Albareda, A., & Pérez, R. Performance of Piezoelectric Ceramic Multilayer Components Based on Hard and Soft PZT. *Proc. Actuator* **2000**, *2000*, 419–422.

(179) Schomann, K. D. Electric Breakdown of Barium Titanate: A Model. *Appl. Phys.* **1975**, *6* (1), 89–92. https://doi.org/10.1007/BF00883554.

(180) Basantakumar Sharma, H.; Sarma, H. N. K.; Mansingh, A. Ferroelectric and Dielectric Properties of Sol-Gel Processed Barium Titanate Ceramics and Thin Films. *J. Mater. Sci.* **1999**, *34* (6), 1385–1390. https://doi.org/10.1023/A:1004578905297.

(181) Beier, C. W.; Sanders, J. M.; Brutchey, R. L. Improved Breakdown Strength and Energy Density in Thin-Film Polyimide Nanocomposites with Small Barium Strontium Titanate Nanocrystal Fillers. *J. Phys. Chem. C* **2013**, *117* (14), 6958–6965. https://doi.org/10.1021/jp312519r.

(182) Li, J.; Meng, Q.; Li, W.; Zhang, Z. Influence of Crystalline Properties on the Dielectric and Energy Storage Properties of Poly(Vinylidene Fluoride). *J. Appl. Polym. Sci.* **2011**, *122* (3), 1659–1668. https://doi.org/10.1002/app.34020.

(183) P S, L. P.; Swain, B.; Rajput, S.; Behera, S.; Parida, S. Advances in P(VDF-TrFE) Composites: A Methodical Review on Enhanced Properties and Emerging Electronics Applications. *Condens. Matter* **2023**, *8* (4), 105. https://doi.org/10.3390/condmat8040105.

(184) Pan, J.; Li, K.; Chuayprakong, S.; Hsu, T.; Wang, Q. High-Temperature Poly(Phthalazinone Ether Ketone) Thin Films for Dielectric Energy Storage. *ACS Appl. Mater. Interfaces* **2010**, *2* (5), 1286–1289. https://doi.org/10.1021/am100146u.

(185) Zhang, Z.; Chung, T. C. M. The Structure−Property Relationship of Poly(Vinylidene Difluoride)-Based Polymers with Energy Storage and Loss under Applied Electric Fields. *Macromolecules* **2007**, *40* (26), 9391–9397. https://doi.org/10.1021/ma071561e.

(186) Bottino, A.; Capannelli, G.; Munari, S.; Turturro, A. Solubility Parameters of Poly(Vinylidene Fluoride). *J. Polym. Sci. Part B Polym. Phys.* **1988**, *26* (4), 785–794. https://doi.org/10.1002/polb.1988.090260405.

(187) Li, M.; Katsouras, I.; Piliego, C.; Glasser, G.; Lieberwirth, I.; Blom, P. W. M.; De Leeuw, D. M. Controlling the Microstructure of Poly(Vinylidene-Fluoride) (PVDF) Thin Films for Microelectronics. *J. Mater. Chem. C* **2013**, *1* (46), 7695–7702. https://doi.org/10.1039/c3tc31774a.

(188) Zhu, Y.; Ye, H.; Yang, L.; Jiang, L.; Zhen, L.; Huang, J.; Jiao, Z.; Sun, J. Effect of Annealing Temperatures and Time on Structural Evolution and Dielectric Properties of PVDF Films. *Polym. Polym. Compos.* **2016**, *24* (2), 167–172. https://doi.org/10.1177/096739111602400213.

(189) Ye, S.; Yu, H. Y.; Wang, D.; Zhu, J.; Gu, J. Green Acid-Free One-Step Hydrothermal Ammonium Persulfate Oxidation of Viscose Fiber Wastes to Obtain Carboxylated Spherical Cellulose Nanocrystals for Oil/Water Pickering Emulsion. *Cellulose* **2018**, *25* (9), 5139–5155. https://doi.org/10.1007/s10570-018-1917-x.

(190) Jin, F.; Xue, X.; Zhao, Y.; Shi, L.; Wang, Z.; Zhang, M.; Wang, Y.; Zhu, J.; Yuan, S. Enhanced Rate Capability and High-Voltage Cycling Stability of Single-Crystal Nickel-Rich Cathode by Surface Anchoring Dielectric BaTiO3. *J. Colloid Interface Sci.* **2022**, *619*, 65–74. https://doi.org/10.1016/j.jcis.2022.03.064.

(191) Garcia, R. *Amplitude Modulation Atomic Force Microscopy*; Wiley-VC Verlag GmbH & Co. KGaA:Weinheim, 2010.

(192) Korolkov, V. V.; Summerfield, A.; Murphy, A.; Amabilino, D. B.; Watanabe, K.; Taniguchi, T.; Beton, P. H. Ultra-High Resolution Imaging of Thin Films and Single Strands of Polythiophene Using Atomic Force Microscopy. *Nat. Commun.* **2019**, *10* (1), 1537. https://doi.org/10.1038/s41467-019-09571-6.

(193) Zhao, D. Polarization Dynamics in Ferroelectric Thin Films, Max-Planck Institute for Polymer Research, Johannes Gutenberg University, Mainz, 2012.

(194) Yoshimura, T.; Fujimura, N. Polarization Hysteresis Loops of Ferroelectric Gate Capacitors Measured by Sawyer-Tower Circuit. *Jpn. J. Appl. Phys.* **2003**, *42* (Part 1, No. 9B), 6011–6014.

https://doi.org/10.1143/JJAP.42.6011.

(195) Pecherskaya, E. A. Radio Measurements - The Use of the Sawyer-Tower Method and Its Modifications to Measure the Electrical Parameters of Ferroelectric Materials. *Meas. Tech.* **2007**, *50* (10), 1101–1107.

(196) Miller, S. L.; Nasby, R. D.; Schwank, J. R.; Rodgers, M. S.; Dressendorfer, P. V. Device Modeling of Ferroelectric Capacitors. *J. Appl. Phys.* **1990**, *68* (12), 6463–6471. https://doi.org/10.1063/1.346845.

(197) Christman, J. A.; Woolcott, R. R.; Kingon, A. I.; Nemanich, R. J. Piezoelectric Measurements with Atomic Force Microscopy. *Appl. Phys. Lett.* **1998**, *73* (26), 3851–3853. https://doi.org/10.1063/1.122914.

(198) Toprak, A.; Tigli, O. Comprehensive Characterization of PVDF-TrFE Thin Films for Microelectromechanical System Applications. *J. Mater. Sci. Mater. Electron.* **2017**, *28* (21), 15877–15885. https://doi.org/10.1007/s10854-017-7482-5.

(199) Benz, M.; Euler, W. B.; Gregory, O. J. The Role of Solution Phase Water on the Deposition of Thin Films of Poly(Vinylidene Fluoride). *Macromolecules*. 2002, pp 2682–2688. https://doi.org/10.1021/ma011744f.

(200) Arrigoni, A.; Brambilla, L.; Bertarelli, C.; Serra, G.; Tommasini, M.; Castiglioni, C. P(VDF-TrFE) Nanofibers: Structure of the Ferroelectric and Paraelectric Phases through IR and Raman Spectroscopies. *RSC Adv.* **2020**, *10* (62), 37779–37796. https://doi.org/10.1039/d0ra05478j.

(201) Wang, T. T.; West, J. E. Polarization of Poly(Vinylidene Fluoride) by Application of Breakdown Fields. *J. Appl. Phys.* **1982**, *53* (10), 6552–6556. https://doi.org/10.1063/1.330075.

(202) Das Gupta, D. K.; Doughty, K. Changes in X-Ray Diffraction Patterns of Polyvinylidene Fluoride Due to Corona Charging. *Applied Physics Letters*. 1977, pp 585–587. https://doi.org/10.1063/1.89788.

(203) Das-Gupta, D. K.; Doughty, K. Corona Charging and the Piezoelectric Effect in Polyvinylidene Fluoride. *Journal of Applied Physics*. 1978, pp 4601–4603. https://doi.org/10.1063/1.325441.

(204) Matsuyama, H.; Teramoto, M.; Nakatani, R.; Maki, T. Membrane Formation via Phase Separation Induced by Penetration of Nonsolvent from Vapor Phase. II. Membrane Morphology. *J. Appl. Polym. Sci.* **1999**, *74* (1), 171–178. https://doi.org/10.1002/(SICI)1097-4628(19991003)74:1<171::AID-APP21>3.0.CO;2-R.

(205) Matsuyama, H.; Teramoto, M.; Nakatani, R.; Maki, T. Membrane Formation via Phase Separation Induced by Penetration of Nonsolvent from Vapor Phase. I. Phase Diagram and Mass Transfer Process. *J. Appl. Polym. Sci.* **1999**, *74* (1), 159–170. https://doi.org/10.1002/(SICI)1097-4628(19991003)74:1<159::AID-APP20>3.0.CO;2-S.

(206) Scheinbeim, J. I.; Yoon, C. H.; Pae, K. D.; Newman, B. A. Poling-Time Dependence of the Field-Induced Phase Transition and Piezoelectric Response of Poly(Vinylidene Fluoride) Films. *J. Polym. Sci. Polym. Phys. Ed.* **1980**, *18* (11), 2271–2276. https://doi.org/10.1002/pol.1980.180181111.

(207) Dvey-Aharon, H.; Taylor, P. L.; Hopfinger, A. J. Dynamics of the Field-Induced Transition to the Polar α Phase of Poly(Vinylidene Fluoride). *J. Appl. Phys.* **1980**, *51* (10), 5184–5187. https://doi.org/10.1063/1.327422.

(208) Hasegawa, R.; Takahashi, Y.; Chatani, Y.; Tadokoro, H. Crystal Structures of Three Crystalline Forms of Poly(Vinylidene Fluoride). *Polymer Journal*. 1972, pp 600–610.

https://doi.org/10.1295/polymj.3.600.

(209) Bachmann, M. A.; Lando, J. B. A Reexamination of the Crystal Structure of Phase II of Poly(Vinylidene Fluoride). *Macromolecules*. 1981, pp 40–46. https://doi.org/10.1021/ma50002a006.

(210) Lovinger, A. J. Molecular Mechanism for α-γ Transformation in Electrically Poled Poly(Vinylidene Fluoride). *Macromolecules* **1981**, *14* (1), 225–227. https://doi.org/10.1021/ma50002a053.

(211) Bachmann, M.; Gordon, W. L.; Weinhold, S.; Lando, J. B. The Crystal Structure of Phase IV of Poly(Vinylidene Fluoride). *J. Appl. Phys.* **1980**, *51* (10), 5095–5099. https://doi.org/10.1063/1.327425.

(212) Guo, D.; Setter, N. Impact of Confinement-Induced Cooperative Molecular Orientation Change on the Ferroelectric Size Effect in Ultrathin P(VDF-TrFE) Films. *Macromolecules* **2013**, *46* (5), 1883–1889. https://doi.org/10.1021/ma302377q.

(213) Mao, D.; Quevedo-Lopez, M. A.; Stiegler, H.; Gnade, B. E.; Alshareef, H. N. Optimization of Poly(Vinylidene Fluoride-Trifluoroethylene) Films as Non-Volatile Memory for Flexible Electronics. *Org. Electron.* **2010**, *11* (5), 925–932. https://doi.org/10.1016/j.orgel.2010.02.012.

(214) Chung, T. C.; Petchsuk, A. Synthesis and Properties of Ferroelectric Fluoroterpolymers with Curie Transition at Ambient Temperature. *Macromolecules* **2002**, *35* (20), 7678–7684. https://doi.org/10.1021/ma020504c.

(215) Li, M.; Katsouras, I.; Asadi, K.; Blom, P. W. M.; De Leeuw, D. M. Low Voltage Extrinsic Switching of Ferroelectric δ-PVDF Ultra-Thin Films. *Applied Physics Letters*. 2013. https://doi.org/10.1063/1.4818626.

(216) Kodama, H.; Takahashi, Y.; Furukawa, T. Effects of Annealing on the Structure and Switching Characteristics of VDF/TrFE Copolymers. *Ferroelectrics* **1997**, *203* (1–4), 433–455. https://doi.org/10.1080/00150199708012865.

(217) Hossain, I. Z.; Khan, A.; Hossain, G. A Piezoelectric Smart Textile for Energy Harvesting and Wearable Self-Powered Sensors. *Energies* **2022**, *15* (15). https://doi.org/10.3390/en15155541.

(218) Remškar, M.; Iskra, I.; Jelenc, J.; Škapin, S. D.; Višić, B.; Varlec, A.; Kržan, A. A Novel Structure of Polyvinylidene Fluoride (PVDF) Stabilized by MoS 2 Nanotubes. *Soft Matter* **2013**, *9* (36), 8647–8653. https://doi.org/10.1039/c3sm51279g.

(219) Peng, G.; Zhao, X.; Zhan, Z.; Ci, S.; Wang, Q.; Liang, Y.; Zhao, M. New Crystal Structure and Discharge Efficiency of Poly(Vinylidene Fluoride-Hexafluoropropylene)/Poly(Methyl Methacrylate) Blend Films. *RSC Adv.* **2014**, *4* (32), 16849–16854. https://doi.org/10.1039/c3ra47462c.

(220) Zhao, X.; Li, C.; Qi, R.; Yin, F.; Fu, Y.; Guo, H.; Gao, R.; Peng, G. Dielectric Relaxation Process of SiC Nanowires/Poly(Vinylidene Fluoride-Chlorotrifluoroethylene) Composites. *J. Polym. Res.* **2023**, *30* (6), 1–14. https://doi.org/10.1007/s10965-023-03606-9.

(221) Su, Y.; Li, W.; Yuan, L.; Chen, C.; Pan, H.; Xie, G.; Conta, G.; Ferrier, S.; Zhao, X.; Chen, G.; Tai, H.; Jiang, Y.; Chen, J. Piezoelectric Fiber Composites with Polydopamine Interfacial Layer for Self-Powered Wearable Biomonitoring. *Nano Energy* **2021**, *89* (PA), 106321. https://doi.org/10.1016/j.nanoen.2021.106321.

(222) Tao, J.; Cao, S. A.; Feng, R.; Deng, Y. High Dielectric Thin Films Based on Barium Titanate and Cellulose Nanofibrils. *RSC Adv.* **2020**, *10* (10), 5758–5765. https://doi.org/10.1039/c9ra10916a.

(223) Zhang, K.; Sun, P.; Liu, H.; Shang, S.; Song, J.; Wang, D. Extraction and Comparison of Carboxylated Cellulose Nanocrystals from Bleached Sugarcane Bagasse Pulp Using Two Different Oxidation Methods. *Carbohydr. Polym.* **2016**, *138*, 237–243. https://doi.org/10.1016/j.carbpol.2015.11.038.

(224) Yang, Y.; Pan, H.; Xie, G.; Jiang, Y.; Chen, C.; Su, Y.; Wang, Y.; Tai, H. Flexible Piezoelectric Pressure Sensor Based on Polydopamine-Modified BaTiO3/PVDF Composite Film for Human Motion Monitoring. *Sensors Actuators, A Phys.* **2020**, *301*, 111789. https://doi.org/10.1016/j.sna.2019.111789.

(225) Sehaqui, H.; Kulasinski, K.; Pfenninger, N.; Zimmermann, T.; Tingaut, P. Highly Carboxylated Cellulose Nanofibers via Succinic Anhydride Esterification of Wheat Fibers and Facile Mechanical Disintegration. *Biomacromolecules* **2017**, *18* (1), 242–248. https://doi.org/10.1021/acs.biomac.6b01548.

(226) Zhang, H.; Shi, L.; Feng, X. Use of Chitosan to Reinforce Transparent Conductive Cellulose Nanopaper. *J. Mater. Chem. C* **2018**, *6* (2), 242–248. https://doi.org/10.1039/c7tc03980h.

(227) Teuschel, M. Herstellung Und Charakterisierung von Ferroelektrischen P(VDF-TrFE) Dünnfilmen. *Bacherlorarbeit, TU Wien* **2017**.

(228) Roosz, N.; Euvard, M.; Lakard, B.; Buron, C. C.; Martin, N.; Viau, L. Synthesis and Characterization of Polyaniline-Silica Composites: Raspberry vs Core-Shell Structures. Where Do We Stand? *J. Colloid Interface Sci.* **2017**, *502*, 184–192. https://doi.org/10.1016/j.jcis.2017.04.092.

(229) Zhang, R.; Li, L.; Long, S.; Lou, H.; Wen, F.; Hong, H.; Shen, Y.; Wang, G.; Wu, W. Enhanced Energy Storage Performance of PVDF Composite Films with a Small Content of BaTiO3. *J. Mater. Sci. Mater. Electron.* **2021**, *32* (19), 24248–24257. https://doi.org/10.1007/s10854-021-06890-7.

(230) Hafner, J.; Schrattenholzer, J.; Teuschel, M.; Schneider, M.; Platz, D.; Schmid, U. Modelling the Distribution of BaTiO3 Nanoparticles in a P(VDF70-TrFE30) Polymer Matrix for Permittivity Calculation. *Polymer (Guildf).* **2019**, *180* (July), 121682. https://doi.org/10.1016/j.polymer.2019.121682.

(231) Ding, Y.; Zhang, W.; Zou, X.; Wang, Z. Enhancement of the Dielectric Energy Storage Performance of <scp>PVDF-TrFE</Scp> Composite Film via Core-shell Structured (1-x)Ba(Ti $_{0.8}$ Zr $_{0.2}$)O $_{3}$ -x(Ba $_{0.7}$ Ca $_{0.3}$)TiO $_{3}$ @TiO <sub>2</Sub. *J. Appl. Polym. Sci.* **2023**, *140* (28). https://doi.org/10.1002/app.54045.

Publications – Scientific Works

- **D. Disnan**, F. Bacher, S. Berger, M. Schneider, U. Schmid "Microstructural influence on thermal stability of ferroelectric properties in P(VDF-TrFE) spin cast thin films", *Polymer* **2024**, Volume 298, 126894.
- **D. Disnan**, J. Hafner, M. Schneider, U. Schmid "Spherulite-like microstructure observed for spin-cast P(VDF-TrFE) thin films and their ferroelectric characteristics", *Polymer* **2023**, Volume 272, 125840.
- **D. Disnan**, J. Hafner, S. Benaglia, M. Teuschel, M. Schneider, R. Garcia, U. Schmid, "Nanostructural and piezoelectric characterization of electro-formed δ-phase poly(vinylidene fluoride) thin films", *Materials Research Letters* **2023**, Volume 11, pp. 296-303.
- J. Hafner, **D. Disnan (co-first author)**, S. Benaglia, R. Garcia, U. Schmid, "Solution-processed ferroelectric polymer nanocrystals", *Polymer* **2023**, Volume 281, 126115.
- **D. Disnan**, M. Schneider, X. Zhang, K. Qian, F. Bacher, Y. Zhao, X. Feng, U. Schmid, "P(VDF-TrFE) nanocomposite thin films with cellulose nanofibers and dopamine-modified $BaTiO_3$ nanoparticles for enhanced energy storage", ***(in peer review)***
- M. David, **D. Disnan**, E. Arigliani, A. Lardschneider, G. Marschick, H. T. Hoang, H. Detz, B. Lendl, U. Schmid, G. Strasser, B. Hinkov, "Advanced mid-infrared plasmonic waveguides for on-chip integrated photonics", Photonics Research 2023, Volume 11, pp. 1694-1702.
- M. David, **D. Disnan**, A. Lardschneider, D. Wacht, H. T. Hoang, G. Ramer, H. Detz, B. Lendl, U. Schmid, G. Strasser, B. Hinkov, "Structure and mid-infrared optical properties of spin-coated polyethylene films developed for integrated photonics applications", *Optical Materials Express* **2022**, Volume 12, pp. 2168-2180.
- J. Hafner, M. Teuschel, **D. Disnan**, M. Schneider, U. Schmid, "Large bias-induced piezoelectric response in the ferroelectric polymer P(VDF-TrFE) for MEMS resonators", *Materials Research Letters* **2021**, Volume 9, pp. 195-203